Doctoral Dissertation

Quantum Engineering Design of Diamond Surfaces: Surface Facet Dependence in Oxidation and Thermal Degradation and Effectiveness of Dangling Bond Saturation on Graphitization Suppression and Control

ダイヤモンド表面の量子工学によるデザイン:

酸化および熱劣化における表面構造依存性および

ダングリングボンド飽和によるグラファイト化の抑制と制御

John Isaac Guinto Enriquez

May 2024

Graduate School of Engineering,

Osaka University

ABSTRACT

Diamond materials possess unique properties and are well-suited for cutting-edge technologies. Oxidation and thermal degradation are two fundamental reactions that occur on diamond surfaces. These properties exhibit surface facet dependence, and the atomistic mechanism remains unclear. Understanding surface facet-dependent properties of diamonds will pave the way for improving etching, polishing, and device fabrication techniques. Graphitization is one of the primary wear mechanisms of diamond tools. One potential approach to mitigate graphitization involves saturating the surface dangling bonds. I investigated these subjects by performing density functional theory (DFT) and machine learning molecular dynamics (MLMD) simulations.

First, I simulated the oxidation process of the C(100) surface, starting from the adsorption of O_2 to the etching of the first layer atoms and subsequent surface stabilization using DFT calculations. The bridge site is the most energetically stable adsorption configuration on an ideal surface, forming ether. However, the top site is the most stable adsorption site on surfaces with vacancies, forming carbonyl. Carbonyl groups are detrimental for electronic and quantum devices as they lead to Fermi pinning and magnetic noise. I propose that atomically flat polishing of the C(100) surface before oxygen exposure can reduce carbonyl groups and increase ether groups, enhancing the performance of diamond devices.

Second, I extended my study of the oxidative etching mechanism to include the C(111) surface. The C(111) surface exhibits lower O_2 molecular and dissociative adsorption energies than the C(100) surface. As the C(111) surface is oxidized, carbonyl groups are formed with the C=O bonding with atoms on different layers, causing inclined carbonyl orientation and high steric repulsion. When a neighboring atom is removed through CO desorption, the remaining atoms in the vicinity stabilize. This leads to the surface being etched in a staggered order. In

contrast, the C=O of the carbonyl on the C(100) surface remains upright, causing less steric repulsion. The CO desorption activation energy is lower near an existing vacancy, leading to row-wise etching order. These observations will directly impact the CVD growth and diamond device fabrication methods.

Third, I investigated the thermal degradation mechanism of the C(111) and C(100) surfaces by performing MLMD simulations using graph neural network interatomic potential constructed from DFT calculation data. The C(111) surface is more susceptible to thermal degradation than the C(100) surface, which is caused by the difference in the number of interlayer bonds. Moreover, the stepped surfaces are more susceptible to thermal degradation than the flat surfaces because of the dangling bonds at the step edges, facilitating sp^2-sp^3 rehybridization. The results highlight the possible role of dangling bonds in suppressing graphitization.

Finally, in the last section of this study, I tested this possibility by simulating the C(111) surface with and without surface terminations. Saturating the dangling bond of the C(111) surface by terminating H, O, and OH is an effective strategy for suppressing graphitization. Furthermore, saturating the dangling bonds at the C(111)-Ni(111) interface reduces the interlayer interaction energy and smooths the potential energy surface, thus lubricating the interface. I propose a novel technique for self-assembling epitaxial graphene on C(111) surfaces through graphitization control, which could offer higher precision, increased robustness, and simpler production over conventional graphene-on-diamond device fabrication.

I dedicate this study to my Papa Ric, Mama Tess, and Ate Charity.

Soli Deo Gloria

ACKNOWLEDGEMENT

I would like to express my most sincere gratitude to my supervisor, Prof. Yoshitada Morikawa, without whom I would not have been able to complete this study. His unwavering patience, encouragement, and guidance were invaluable to me. Under his mentorship, I had the extraordinary opportunity to collaborate with esteemed experts in both academia and industry. I am deeply thankful to Prof. Kouji Inagaki and Prof. Masaaki Geshi of Osaka University, as well as Dr. Masato Michiuchi and Dr. Yamasaki Takahiro of Sumitomo Electric Industry, for their guidance and support in this project. I would also like to express my most sincere appreciation to Prof. Ikutaro Hamada, Prof. Satoshi Hamaguchi, and Prof. Kazuya Yamamura of Osaka University for accepting to be referees during my defense and for their invaluable insights and suggestions.

I would also like to extend my heartfelt gratitude to the Japan International Cooperation Agency (JICA), the Japanese Government Ministry of Education, Culture, Sports, Science and Technology (MEXT), the Marubun Research Promotion Foundation, and the Japan Society for the Promotion of Science (JSPS) for the generous scholarship and fellowship grants that have been instrumental in supporting my academic pursuits and research endeavors in Japan over the past years. I would also like to acknowledge the support of the Sumitomo Electric Industry, "Hyper-Ordered Structure Science" (grant no. JP20H05883) and Scientific Research (B) (grant no. JP20H02569) from JSPS, and Grant-in-Aid for JSPS Fellows (project no. JP23KJ1431).

Finally, I wish to acknowledge the Cybermedia Center, Osaka University, the Research Institute for Information Technology at Kyushu University, and the Institute for Solid State Physics at the University of Tokyo for generously providing the supercomputer resources necessary for conducting the calculations in this study. The invaluable contribution of these resources has significantly contributed to the successful completion of this research.

List of Publications

1. **Oxidative Etching Mechanism of the Diamond (100) Surface**

   Enriquez, J.I., Muttaqien, F., Michiuchi, M., Inagaki, K., Geshi, M., Hamada, I., Morikawa, Y.

   Carbon 174 36–51 (2021)

   Special Issue: Diamond: Synthesis, Electrochemistry, Electronics, Sensing, Defects and Quantum Applications

   https://doi.org/10.1016/j.carbon.2020.11.057

2. **Origin of the Surface Facet Dependence in the Oxidative Etching of the Diamond (111) and (100) Surfaces from First-Principles Calculations**

   Enriquez, J.I.G., Yamasaki, T., Michiuchi, M., Inagaki, K., Geshi, M., Hamada, I., Morikawa, Y.

   J. Phys. Chem. C 128 15 6294–6308 (2024)

   Special Issue: Jens K. Norskov Festschrift

   https://doi.org/10.1021/acs.jpcc.3c08378

3. **Origin of the Surface Facet Dependence in the Thermal Degradation of the Diamond (111) and (100) Surfaces in Vacuum Investigated by Machine Learning Molecular Dynamics Simulations**

   Enriquez, J.I.G., Halim, H.H., Yamasaki, T., Michiuchi, M., Inagaki, K., Geshi, M., Hamada, I., Morikawa, Y.

   Carbon 226 119223 (2024)

   Special Issue: Frontiers in Carbon Science and Technology

   https://doi.org/10.1016/j.carbon.2024.119223

List of Conference Presentations

1. **Graphitization and Oxidation of Diamond Surfaces Studied by Graph Neural Network Molecular Dynamics**

   Oral Presentation

   33rd International Conference on Diamond and Carbon Materials

   10-14 September 2024, Mallorca, Spain

2. **Temperature-driven Graphitization of the Diamond (111) and (100) Surfaces Studied by Graph Neural Network Molecular Dynamics**

   Poster Presentation

   34th IUPAP Conference on Computational Physics, 2023

   4-8 August 2023, Kobe, Japan

3. **Graph Neural Network Molecular Dynamics Study of Thermal Degradation of the Diamond (111) and (100) Surfaces With and Without Oxygen**

   Poster Presentation

   Materials Research Meeting (MRM) 2023 / International Union of Materials Research Societies (IUMRS) - International Conference in Asia (ICA), 2023

   11-16 December 2023, Kyoto, Japan

4. **Diamond Quantum Engineering Design: Oxidation, Graphitization Suppression, and Epitaxial Graphene Self-Assembly**

   Oral Presentation (accepted)

   34th International Conference on Diamond and Carbon Materials

   1-5 September 2024, Dresden, Germany

List of Scholarships and Grants

1. **Top Global University Project Scholarship**

   Ministry of Education, Culture, Sports, Science and Technology, Japan (MEXT)

   2021-2022

2. **Exchange Research Grant**

   Marubun Research Promotion Foundation

   2022-2023

3. **Research Fellowship DC2**

   Japan Society for the Promotion of Science (JSPS)

   2023-2025

TABLE OF CONTENTS

Abstract		i
Dedication		iii
Acknowledgment		v
List of Publications		vii
List of Conference Presentations		ix
List of Scholarships and Grants		xi
Table of Contents		xiii
List of Figures		xxi
List of Tables		xxvii
Chapter 1	INTRODUCTION	1
1.1	Background of the Study	1
1.2	Problem Statement	3
1.3	Objectives of the Study	5
1.4	Scope and Limitation of the Study	6
1.5	Significance of the Study	7
Chapter 2	REVIEW OF RELATED LITERATURE	9
2.1	Diamond Overview	9
2.1.1	Structure of Diamond	10
2.1.2	Classification of Diamond	11
2.1.3	Properties of Diamond	12
2.1.3.1	Mechanical Property	12

2.1.3.2	Thermal Property	12
2.1.3.3	Optical Property	13
2.1.3.4	Electronic Property	13
2.2	Synthetic Production of Diamond	15
2.2.1	High-Temperature High-Pressure Method	15
2.2.2	Chemical Vapor Deposition Method	17
2.2.3	Detonation Method	18
2.3	Industrial and Technological Applications of Diamond	20
2.3.1	Diamond Tools	20
2.3.2	Photonics and Biotechnology Applications	23
2.3.3	Electronics	25
2.3.4	Quantum Technology	28
2.4	Diamond Device Fabrication	30
2.4.1	Plasma Etching	31
2.4.2	Thermochemical Etching	32
2.5	Oxidation of Diamond (111) and (100) Surfaces	34
2.6	Graphitization of Diamond	38
Chapter 3	THEORETICAL FRAMEWORK – ELECTRONIC AND ATOMIC-LEVEL SIMULATIONS USING DENSITY FUNCTIONAL THEORY AND MACHINE LEARNING MOLECULAR DYNAMICS	41
3.1	Many-Body Schrodinger Equation and Born-Oppenheimer Approximation	41

3.2	Variation Theorem, Hartree Fock Approximation and Self-Consistent Field Method	44
3.3	Hohenberg-Kohn Theorems and Density Functional Theory	47
3.4	Kohn-Sham Equations	44
3.5	Exchange Correlation Functional	55
3.6	Iterative Solution to Kohn-Sham Equations	61
3.7	Plane-Wave Basis Function	63
3.8	Pseudopotential Approach	64
3.9	Semiempirical van der Waals Correction	66
3.10	Transition State Search using Nudged Elastic Band Method	68
3.11	Molecular Dynamics	70
3.11.1	Classical Molecular Dynamics	71
3.11.2	Ab initio Molecular Dynamics	74
3.11.3	Machine Learning Molecular Dynamics	75
3.12	Machine Learning Molecular Dynamics Based on Neural Network Model	75
3.12.1	Artificial Neural Network	75
3.12.2	Neural Network Interatomic Potentials	80
3.12.2.1	High-Dimensional Neural Network	80
3.12.2.2	Graph Neural Network	82
Chapter 4	METHODOLOGY	85
4.1	Density Functional Theory Calculations	85
4.2	Surface Energy and Surface Stabilization Energy	86

4.3	Adsorption Energies	87
4.4	Desorption Reaction Energy and Activation Energy	87
4.5	Crystal Orbital Overlap Population Analysis	88
4.6	Vibrational Properties	89
4.7	Graph Neural Network Interatomic Potential Construction	91
4.8	Graph Neural Network Interatomic Potential Fine-tuning and Evaluation	93
4.9	Graph Neural Network Interatomic Potential Pre-Production Validation	96
4.10	Machine Learning Molecular Dynamics Simulations	96
4.11	Machine Learning Analysis of the Molecular Dynamics Data	96
Chapter 5	OXIDATIVE ETCHING MECHANISM OF THE DIAMOND (100) SURFACE	99
5.1	Model of the Diamond (100) Surface	100
5.2	Adsorption of Gas-Phase O_2 on 2×1 Reconstructed C(100) Surface	100
5.3	Oxygen-Induced Surface Dereconstruction and Oxygenation at Monolayer Coverage	104
5.4	Electronic analysis of diamond (100) surface with monolayer oxygen coverage	107
5.5	Vibrational frequency analysis of clean and oxygenated diamond (100) surfaces	114
5.6	Oxidation and etching of diamond (100) surface	118

5.7	Co-existence of carbonyl and ether on oxidized C(100) surface	125
Chapter 6	ORIGIN OF THE SURFACE FACET DEPENDENCE IN THE OXIDATIVE ETCHING OF THE DIAMOND (111) AND (100) SURFACES	129
6.1	Model of the Diamond (111) and (100) Surfaces	130
6.2	Adsorption of Gas-Phase O2 on the C(111) Surface	132
6.3	Oxygen-Induced Surface Dereconstruction and Oxygenation at Monolayer Coverage	135
6.4	Comparison of the O_2 Adsorption on the C(111) and C(100) Surfaces	142
6.5	Oxidative Etching of the Diamond (111) and (100) Surfaces	145
6.6	Static Steady-State Oxidative Etching Simulation of the Diamond (111) and (100) Surfaces	152
Chapter 7	Origin of the Surface Facet Dependence in the Thermal Degradation of the Diamond (111) and (100) Surfaces	159
7.1	Graph Neural Network Interatomic Potential Model for Production Simulations	160
7.2	Model of the Flat and Stepped Diamond (111) and (100) Surfaces for Thermal Degradation Simulations	162
7.3	Thermal Degradation of the Flat and Stepped Diamond (111) and (100) Surfaces	164

7.4	Hybridization of Carbon Atoms on the Thermally Degraded Diamond Surfaces	172
Chapter 8	Suppression and Control of Diamond Graphitization and Lubrication by Dangling Bond Saturation	177
8.1	Effect of Surface Termination on the Geometry of the C(111) Surface	178
8.2	Graph Neural Network Interatomic Potential for Diamond Surfaces with H, O, and OH	182
8.3	Comparison of GNN and ReaxFF Interatomic Potentials in Describing the Oxidative Etching of Diamond (111) and (100) Surfaces	184
8.4	Effect Of Dangling Bond Saturation in Suppressing the C(111) Graphitization	187
8.5	Thermal Degradation of C(111) Surface with Triangular Island and Pit	190
8.6	Preferential Graphitization of Non-Terminated C(111) Surface Atoms	194
8.7	Effect of Dangling Bond Saturation in the Interfacial Interaction of the Diamond (111) and Nickel (111) Surfaces	199
Chapter 9	SUMMARY, CONCLUSIONS, FUTURE WORKS, AND RECOMMENDATIONS	205
9.1	Summary	205

9.1.1	On the Oxidative Etching Mechanism of the Diamond (100) Surface	205
9.1.2	On the Origin of the Surface Facet Dependence in the Oxidative Etching of the Diamond (111) and (100) Surfaces	207
9.1.3	On the Origin of the Surface Facet Dependence in the Thermal Degradation of the Diamond (111) and (100) Surfaces	208
9.1.4	On the Suppression and Control of Diamond Graphitization and Lubrication by Dangling Bond Saturation	209
9.2	Conclusions	210
9.3	Future Works	210
9.4	Recommendations	212
Appendix		213
A1	Convergence Test of Adsorption Energy for Slab Thickness	213
A2	Band Structure Calculations for Different Slab Thickness	215
A3	CO Desorption Reaction from Flat and Etched Diamond Surfaces on Various Sites	216
A4	Learning Database of the Graph Neural Network Interatomic Potential	220
References		223

LIST OF FIGURES

Chapter 2

2.1	Diamond unit cell	14
2.2	Hardness of diamond compared to other hard materials	14
2.3	Pressure-temperature diagram of diamond-graphite	19
2.4	Isotropic and anisotropic plasma etching	33
2.5	Diamond (100) and (111) surfaces	37

Chapter 3

3.1	DFT calculation of total energy using self-consistent field method	62
3.2	Two-layer neural network	79
3.3	Behler-Parrinello high dimensional neural network potential	81
3.4	The NequIP network architecture	84

Chapter 4

4.1	GNN-IP construction workflow	92

Chapter 5

5.1	Model of the 2×1 reconstructed C(100) surface	102
5.2	Potential energy surface of O_2 adsorption on the top site using PBE, PBE+D2, optb86b-vdW, and rev-vdw-DF2	102
5.3	Reaction path of the adsorption of gas phase triplet and singlet O_2 on the top site of the C(100)-(2×1) surface	103
5.4	Reaction path of the adsorption of gas phase triplet and singlet O_2 on the bridge site of the C(100)-(2×1) surface	103
5.5	Oxygen-induced surface dereconstruction following O_2 adsorption on the top site of the C(100)-(2×1) surface.	105

5.6	Oxygen-induced surface dereconstruction following O_2 adsorption on the bridge site of the C(100)-(2×1) surface	106
5.7	Optimized structures for monolayer O adsorption on the top and bridge sites of the C(100) surface	106
5.8	Band structures of the clean C(100)-(2×1) surface and oxygenated C(100)-(1×1):O_{top} and C(100)-(1×1):O_{bridge} surfaces	109
5.9	Highest occupied molecular orbital (HOMO) of the C(100)-(1×1):O_{top} and C(100)-(1×1):O_{bridge} surfaces	110
5.10	Density of states of bulk diamond and clean C(100)-(2×1) surface projected onto 2s and 2p orbitals	110
5.11	Density of states of oxygenated C(100)-(1×1):O_{top} and C(100)-(1×1):O_{bridge} surfaces projected onto 2s and 2p orbitals	111
5.12	Density of states weighed by gross population (GPOP) of the 2s and 2p orbitals of O and corresponding crystal orbital overlap population (COOP) curve with respect to the bond between O and C(100) surface for top and bridge site adsorption	112
5.13	Electron charge density difference of oxygen adsorption reaction for monolayer coverage	113
5.14	EELS spectra and calculated vibrational spectra of the clean 2×1 reconstructed and oxygen-terminated C(100) surfaces.	116
5.15	Vibrational modes of the clean and oxygen-terminated C(100) surfaces	117
5.16	Desorption of CO and CO_2 from the C(100) surface	121
5.17	Successive CO desorption from the C(100) surface	122
5.18	Mechanism of preferred etching along [011] direction	123
5.19	Gross population (GPOP) and crystal orbital overlap population (COOP) analysis of the CO and C(100) surface.	123
5.20	Desorption of CO_2 from the C(100)-(1×1):O_{bridge} surface and C(100)-(1×1):O_{bridge} surfaces with 1, 2, and 3 desorbed CO	124

5.21	Optimized structures of etched C(100) surface with O atoms adsorbed on vacant sites	126
5.22	Reaction path of first and second O_2 adsorption on etched C(100) trough	127

Chapter 6

6.1	Model of the C(111)-(1×1) surface, reconstructed C(111)(2×1) surface, and reconstructed C(100)-(2×1) surface	131
6.2	Reaction path of the molecular adsorption of gas phase triplet and singlet O_2 on the top site of the C(111)-(2×1) surface	133
6.3	Reaction path of the molecular adsorption of gas phase triplet and singlet O_2 on the bridge site of the C(111)-(2×1) surface	144
6.4	Adsorption of two O_2 molecules on the C(111)-(2×1) surface (first reaction path)	138
6.5	Total and projected density of states plot of the surface atom before and after O_2 adsorption on an adjacent site	139
6.6	Adsorption of two O_2 molecules on the C(111)-(2×1) surface (second reaction path)	140
6.7	Adsorption of two O_2 molecules on the C(111)-(2×1) surface (third reaction path)	141
6.8	Differential adsorption energy of O_2 molecule on the C(111)-(2×1) and C(100)-(2×1) surfaces	144
6.9	Etching of the top-layer atoms of the carbonyl pair-terminated C(111)-(1×1) surface through successive CO desorption	149
6.10	Comparison of the carbonyl angles and CO desorption activation energy and reaction energy on carbonyl pairs and diamond islands	150

6.11	Etching of the top-layer atoms of the ether-terminated C(100)-(1×1) surface through successive CO desorption	151
6.12	Steady-state oxidative etching of the carbonyl pair-terminated C(111)(1×1) surface through successive CO desorption and O_2 adsorption	156
6.13	Steady-state oxidative etching of the ether-terminated C(100)-(1×1) surface through successive CO desorption and O_2 adsorption	158

Chapter 7

7.1	Comparison of DFT and GNN energies and forces for the pre-production validation dataset	161
7.2	Flat and stepped C(111) and C(100) surface models used in production simulations	163
7.3	Constant heating rate simulations of the flat and stepped C(111) and C(100) surfaces	169
7.4	Snapshots of (2×1) π-bonded reconstruction of the flat and stepped C(111) surfaces	170
7.5	Variation of thermal degradation temperatures with heating rate for the flat and stepped C(111) surfaces	171
7.6	Coordination and hybridization analysis of carbon atoms on the thermally degraded diamond surfaces	174

Chapter 8

8.1	Optimized geometries of the non-terminated and H-, O-, and OH-terminated C(111) surfaces	180
8.2	Definition of the three tripod angles of a given central atom	181
8.3	Pre-production validation dataset	183
8.4	Comparison of DFT and GNN energies and forces for pre-production validation dataset	183

8.5	CO desorption activation and reaction energies on the C(111)(1×1):O_{ML} surface calculated using DFT, GNN, and ReaxFF	186
8.6	CO desorption activation and reaction energies on the C(100)(1×1):O_{ML} surface calculated using DFT, GNN, and ReaxFF	186
8.7	Constant heating rate simulation of the clean, H-, O-, and OH-terminated stepped C(111) surfaces	188
8.8	Comparison of the H-, O-, and OH-terminated stepped C(111) surface at T = 2000 K	189
8.9	SEM images of diamond microcrystals with overgrowth, hollow octahedral faces, and oxidized diamond (111) surface with triangular etched pits	192
8.10	Comparison of surface morphologies of the clean and H-terminated surface islands heated up to 1500 K	193
8.11	Self-assembly of epitaxial graphene on the partially H-terminated C(111) surface	197
8.12	Activation energies of bilayer exfoliation reaction, and H_2 desorption reactions from unreconstructed and reconstructed C(111) surfaces	198
8.13	Proposed method of graphene-on-diamond device fabrication by self-assembly of epitaxial graphene	198
8.14	Optimized geometries of the clean, H-, O-, and OH-terminated C(111)-Ni(11) interface	201
8.15	Optimized geometries of the clean, H-, O-, and OH-terminated C(111)-Ni(11) interface with the 2-dimensional potential energy surface	202
8.16	Reaction path of Ni(111) sliding on the clean and H-terminated C(111) surfaces along the $[\bar{1}2\bar{1}]$ and $[\bar{1}01]$ directions	203

Appendix

A1	Band structures of the clean C(100)-(2×1) surface and oxygenated C(100)-(1×1):O_{top} and C(100)-(1×1):O_{bridge} surfaces for 8, 12, 16, and 20-layer slab models	215
A2	Alternate reaction path to the CO desorption reactions D to F described in Fig. 6.9	216
A3	CO desorption activation energies and reaction energies from various locations on the C(111)-(1×1):O surface with 1 CO desorbed	217
A4	CO desorption activation energies and reaction energies from various locations on the C(111)-(1×1):O surface with 4 CO desorbed and 2 O_2 adsorbed (Fig. 6.12H)	217
A5	CO desorption activation energies and reaction energies from various locations on the C(111)-(1×1):O surface with 5 CO desorbed and 2 O_2 adsorbed (Fig. 6.12J)	218
A6	CO desorption activation energies and reaction energies from various locations on the C(111)-(1×1):O surface with 6 CO desorbed and 3 O_2 adsorbed (Fig. 6.12K)	218
A7	CO desorption activation energies and reaction energies from various locations on the C(111)-(1×1):O surface with 7 CO desorbed and 3 O_2 adsorbed (Fig. 6.12L)	219
A8	CO desorption activation energies and reaction energies from various locations on the C(111)-(1×1):O surface with 8 CO desorbed and 3 O_2 adsorbed (Fig. 6.12M)	219
A9	CO desorption activation energies and reaction energies from various locations on the C(100)-(1×1):O surface with 4 CO desorbed and 2 O_2 adsorbed	220
A10	Equilibrium structures used in training the GNN interatomic potential	221

LIST OF TABLES

Chapter 2

2.1	Selected electronic and thermal properties of diamond and other semiconductors	19

Chapter 6

6.1	Comparison of CO and CO_2 desorption activation and reaction energies	148
6.2	CO desorption activation and reaction energies	157

Chapter 7

7.1	Diamond surface models for pre-production validation and production simulations	161
7.2	GNN predicted interatom separation in graphite and diamond crystals compared with DFT and experiment	162
7.3	GNN predicted diamond surface energies compared with DFT	163
7.4	Comparison of relevant surface properties calculated using 12-layer and 16-layer slab models	164
7.5	Comparison of thermal degradation temperatures of the diamond surfaces for slow and fast heating rates	171

Chapter 8

8.1	Effect of surface termination on the geometry of the C(111) surface	181
8.2	Effect of surface termination on the interface distance and energy of the C(111)-Ni(111) interface	201

Appendix

A1	O_2 molecular adsorption energies on clean C(100)(2×1) surface for slab models with various thickness	213
A2	O_2 metastable adsorption energies on clean C(100)(2×1) surface for slab models with various thickness	214
A3	Adsorption energy per O atom on C(100)(1×1):O_{top} for slab models with various thickness	214
A4	Adsorption energy per O atom on C(100)(1×1):O_{bridge} for slab models with various thickness	214
A5	Database of structures and target energies and forces used in training the GNN interatomic potential	221

CHAPTER 1

INTRODUCTION

1.1. Background of the Study

Diamond is an ideal material for cutting-edge applications because it possesses a unique combination of exceptional properties. It has the highest dielectric breakdown field, saturated electron drift velocity, and thermal conductivity of all semiconductors. This makes diamond materials suitable for next-generation electronics expected to outperform current systems in operating frequency and power handling capacity (Wort and Balmer 2008). Beyond electronics, diamonds also possess color centers that serve as bright single-photon sources (SPS) at room temperatures, offering exciting prospects for quantum metrology and quantum information science (Prawer and Greentree, 2008). In recent years, diamonds have found increasing use in biotechnology, playing a role in drug delivery, gene transfection, fluorescence imaging, and magnetic resonance imaging (Chen and Zhang, 2017; Hébert et al., 2014). Moreover, diamond materials are utilized in precision cutting (Bryan, 1979; Brinksmeier and Preuss, 2012; Lucca et al., 2020), photonics (Greentree et al., 2008; Aharonovich et al., 2011; Bradac et al., 2019), microelectromechanical systems (Björkman et al., 1999; Toros et al., 2018; Z. Zhang et al., 2019), and coating and lubrication (Bobzin, 2017; Zhai et al., 2017; Erdemir and Martin, 2018; Chen and Li, 2020) . The most technologically important diamond facets are the (111) and (100) surfaces (Koizumi et al., 2018).

Oxidation and graphitization are the two primary chemical processes on diamond surfaces. Oxidation involves the chemical reaction of diamonds with oxygen or oxygen-containing molecules. Currently, oxidation-based methods such as plasma and thermochemical etching are the primary techniques used for fabricating diamond devices (Toros et al., 2020; Hicks et al., 2019; Nagai et al., 2018, 2020). On the other hand, graphitization, or more generally thermal degradation, occurs as diamond transforms to graphite or amorphous carbon when heated to sufficiently high temperatures. This transformation occurs in several industrial and device fabrication processes such as diamond tool wear, catalytic etching, polishing, laser ablation, and plasma treatment (Thornton and Wilks, 1980; J. Wang et al., 2015; Liu et al., 2022; Mildren et al., 2011; Yan et al., 2021).

Among the various technological uses of diamonds, the cutting tool industry represents the largest market, with an annual value amounting to billions of dollars ("Market Study on Diamond Tools," n.d.). This illustrates the effectiveness and demand of diamond as a cutting material. However, premature wear makes diamond tools unsuitable for cutting steel and other ferrous metals. Various mechanisms have been proposed, such as graphitization and the dissolution of carbon atoms into the metal. A surface modification that prevents graphitization and promotes chemical passivation of the diamond surface at the diamond-metal interface could potentially improve diamond wear resistance. One potential approach is saturating the dangling bonds through H-termination, which has shown promise in materials similar to diamonds. For example, simulations of nanodiamonds have demonstrated that the C(111) facets transform to graphite after geometry relaxations, but this transformation can be prevented by saturating the dangling bonds on the surface (Li and Zhao, 2011). Additionally, friction experiments on diamond-like-carbon (DLC) films have indicated that friction wear is reduced when sliding occurs in hydrogen-rich environments (Fontaine et al., 2004; Okubo et al., 2015).

1.2. Problem Statement

There are still many aspects of diamond surface oxidation that need to be clarified. For instance, experiments have shown that while the C(100) surface can be oxygenated at monolayer coverage at room temperature, the C(111) surface requires high temperature to achieve the same coverage (Loh et al., 2002; Thomas et al., 1992; Hossain et al., 1999). In addition, the oxidized diamond surface facets have different morphologies. When etched with pure oxygen, the C(111) surface has a rough morphology without a well-defined crystallographic orientation while the C(100) surface has a flat morphology characterized by small steps (de Theije et al., 2000).

The process of diamond graphitization remains inadequately understood. Although the formation of graphitic structures from diamond has been well studied, the formation of amorphous carbon and sp^1-bonded carbon chains reported in experiments has yet to be elucidated on the atomic level. Notably, graphitization also shows surface facet dependence, with the C(111) surface being more vulnerable to graphitization compared to the C(100) surface (Bokhonov et al., 2021).

While the surface termination with hydrogen shows some promise in graphitization suppression and lubrication of nanodiamonds and DLC, respectively, its effectiveness on diamond surfaces is uncertain Despite some similarities between nanodiamonds and the C(111) surface, the latter is considerably more stable, particularly after reconstruction. Therefore, whether hydrogen termination will work or not in suppressing the graphitization of the C(111) surface at high temperatures has yet to be demonstrated. Furthermore, the reduction of friction

by hydrogen is not universally applicable. Specifically, when diamond slides with graphene, the addition of hydrogen increases the frictional forces (Dong et al., 2013).

In this context, it is imperative to address the following questions:

1. What are the reasons behind the differences in the oxygen adsorption behavior and oxidized surface morphology of the (111) and (100) surfaces?

2. What factors contribute to the differences in thermal degradation susceptibility between the (111) and (100) surfaces?

3. How does the saturation of dangling bonds impact the suppression of graphitization and the improvement of lubrication at the diamond-metal interface?

4. In what ways can the understanding of diamond oxidation, graphitization, and the effects of dangling bond saturation be applied in diamond device technologies?

1.3. Objectives of the Study

The study aims to address the aforementioned issues by performing electronic and atomic-level quantum simulations. Spin-polarized density functional theory will be utilized for electronic property calculations and reaction path simulations, while molecular dynamics with interatomic potentials trained from quantum simulation data will be used for finite-temperature dynamical simulations.

The specific objectives of the study are as follows:

1. To investigate the origins of surface facet dependence in the oxidative etching of diamond (111) and (100) surfaces.

2. To investigate the origins of surface facet dependence in the thermal degradation of diamond (111) and (100) surfaces.

3. To evaluate the effectiveness of dangling bond saturation in suppressing graphitization and enhancing lubrication at the diamond-metal interface

4. To utilize quantum engineering and design in developing strategies and innovative insights to enhance diamond device technologies.

1.4. Scope and Limitations of the Study

1. Although synthetic diamond is typically hydrogen-terminated, this research focuses on the oxidative etching of oxygen-terminated surfaces due to its relevance to diamond device fabrication. Simulations indicate that during the early exposure to oxygen plasma, the surface will become predominantly hydrogen-free as most hydrogen atoms are removed (Paci et al., 2011).

2. The machine learning interatomic potential is trained using DFT data with electrons calculated at zero temperature. Earlier studies have shown that this approximation is valid for the simulation conditions in this study (Correa et al., 2006; Willman et al., 2022).

3. The simulations of graphitization suppression by dangling bond termination are only performed on the stepped C(111) surface. This is because this surface is the most vulnerable to thermal degradation. Experimental evidence suggests that graphitization of nanodiamonds initiates on the C(111) surface and spreads to the C(100) surface (Bokhonov et al., 2021). Therefore, it is reasonable to assume that by suppressing graphitization on the C(111) surface, thermal degradation on other facets will also be mitigated.

1.5. Significance of the Study

The use of diamond materials in advanced technologies will have a positive impact across various sectors of society. By gaining insight into the surface facet dependence in the oxidation and graphitization of diamonds, we can fine-tune the properties of diamond materials for applications in electronics, quantum technology, and biotechnology. This understanding will also contribute to improved precision in the fabrication and polishing of diamond devices. Additionally, by preventing graphitization and enhancing lubrication, we can develop strategies to minimize wear on diamond cutting tools, thereby reducing industrial cutting costs and enhancing cutting precision. Moreover, by employing preferential graphitization through selective dangling bond saturation, graphene can be formed directly on the diamond surface, opening up the potential for the microfabrication of all-carbon devices and circuits. This novel concept will help facilitate the transition from silicon-based to carbon-based electronics, offering a promising route to achieve carbon neutrality, promote sustainability, and enhance environmental safety.

CHAPTER 2. REVIEW OF RELATED LITERATURE

2.1. Diamond Overview

Diamond is a mineral of pure carbon known for its hardness and ability to disperse light. The term "diamond" comes from the Greek word ἀδάμας (adamas), which means unbreakable. Its remarkable brilliance has established the diamond as the most desired gemstone. The ornamental use of diamonds dates back to ancient times when they were exclusively mined in India until their discovery in Brazil in the 1700s. Large diamond mining operations are currently active in Russia, Australia, and various parts of Africa. Diamonds are highly valuable. In a typical mine, one hundred tons of kimberlite, the primary diamond-bearing ore, yields as little as 32 carats (6.4 g) of diamond. The high cost of diamonds has driven efforts to produce them synthetically. The first successful synthesis of diamonds using high-pressure methods was achieved in 1955, nearly simultaneously but independently, in the United States, Sweden, and the former Soviet Union. Substantial advancements have been made in synthetic diamond production over the past few decades, resulting in the availability of highly pure, single-crystal diamonds measuring up to several millimeters. Synthetic diamonds represent over 99% of the total annual production by weight. Although synthetic diamonds have not yet replaced natural diamonds in jewelry, they are used in various industrial applications such as grinding, polishing, and cutting. More recently, significant progress has been made in synthesizing diamonds using chemical vapor deposition (CVD) in low-pressure environments. This method has shown the potential to grow diamond wafers measuring up to 10 centimeters, opening up numerous applications in electronics, optics, and photonics (Pierson, 1993).

2.1.1 Structure of Diamond

In 1772, the French chemist Antoine Lavoisier conducted an experiment in which he burned diamonds in a pure oxygen atmosphere and discovered that the only combustion product was carbon dioxide. This finding indicated that diamonds consist of pure carbon. Building on Lavoisier's work, the English chemist Smithson Tennant furthered the experiment and proved that diamond and graphite release the same amount of gas when burned. This experiment demonstrated that diamond and graphite are chemically equivalent despite their significant differences in appearance and hardness.

The atomic structure of a diamond is formed by sp^3 hybridized carbon atoms that form regular tetrahedrons with equal angles of 109.5 degrees. In contrast, graphite, another carbon allotrope, is composed of sp^2 hybridized carbon atoms. Diamond crystallizes with cubic symmetry, featuring a bond length of 1.54 angstroms and a bond energy of approximately 5 eV. A diamond's unit cell has eight atoms located in the corners (1/8 x 8), faces (1/2 x 6), and inside the cell (4) (see Figure 2.1). Additionally, a naturally occurring diamond with hexagonal symmetry, known as lonsdaleite, exists, although it is much less common. While cubic diamond exhibits a {111} plane stacking sequence of ABCABC, meaning every third layer is identical, hexagonal diamond has a stacking sequence of ABAB.

2.1.2 Classification of Diamond

One quantitative means to distinguish diamond from graphite is through the use of Raman spectroscopy, where diamond has a characteristic peak at 1332 cm^{-1} while graphite peaks at 1570 cm^{-1}. But even within diamonds, whether it is natural or synthetic, differences do exist. Diamonds can form with varying amounts of defects, such as elemental impurities and crystallographic faults. Therefore, no two diamonds have exactly the same composition and properties. Diamond gems are graded in terms of 4 C's: cut, color, clarity, and carat weight. For scientific and industrial applications, diamonds are classified based on the level and type of impurities. Type 1 diamonds have significant nitrogen atom impurities in small aggregates (Type 1a) or dispersed within the lattice (Type 1b). Type 2 diamonds have minimal nitrogen impurities (Type 2a). Type 2b diamonds are extremely rare and are characterized by boron impurity, giving them a characteristic blue color. The impurities alter several properties of diamond. For example, Type 2a single-crystal diamonds produced using the HPHT method have the best optical transparency. Nitrogen-doped Type 1a and 1b diamonds are n-type semiconductors, while boron-doped Type 2b diamonds are p-type semiconductors (Pierson, 1993).

2.1.3. Properties of Diamond

2.1.3.1. Mechanical Property

Diamonds are extremely hard. In the Mohs scale of relative hardness, a diamond has a maximum hardness of 10, which means that a diamond can only be scratched by another diamond. There have been several reports on new materials that claim to be harder than diamonds. However, none of these materials have been used for industrial or scientific applications. Therefore, for all practical purposes, diamond is still the hardest known material (Sumiya et al., 2015). The hardness of crystalline materials can be accurately measured using indentation techniques such as the Knoop hardness test. Figure 2.2 shows the Knoop hardness of the diamond compared with other hard materials.

2.1.3.2. Thermal Property

Pure, single-crystal diamonds have an extremely high thermal conductivity of at least 2000 W/mK, five times higher than the best metals, such as silver and copper (Table 1). Thermal conductivity in diamonds occurs through lattice vibrations. In contrast, the thermal conductivity in metals occurs by electron transport. Diamonds' unusually high thermal conductivity results from the high bond energy between light carbon atoms. In addition, this also results in a low linear expansion coefficient of 0.8×10^{-6} °C^{-1} (Pierson, 1993).

2.1.3.3. Optical Property

Diamond is an ideal optical material as it can transmit radiant energy over a wide range of optical wavelengths, making it optically transparent from deep ultraviolet (UV) up to far infrared (IR). Theoretically, pure diamond has only two minor intrinsic adsorption bands at 230 nm (UV) and 650 nm (IR). Impurities such as nitrogen dopants lower the transmittance by introducing additional adsorption bands. In addition, its high band gap prevents thermal generation of charge carriers, making it transparent even at high temperatures and radiation intensities. Moreover, diamond has a moderately high refractive index of 2.4 (Pierson, 1993).

2.1.3.4. Electronic Property

Diamond has an indirect bandgap of 5.47 eV. Among other wide-bandgap semiconductors, diamond has the highest electron and hole mobility, with respective values of 4500 $cm^2V^{-1}s^{-1}$ and 3800 $cm^2/V^{-1}s^{-1}$ measured from single-crystal CVD diamond at room temperature. It also has high electron and hole saturation velocity, which can be reached at a relatively low electric field of 10 kV/cm. On top of this, diamond has the highest predicted breakdown field of all semiconductors with values between 5-10 MV/cm. Table 2.1 shows the electronic properties of diamond in comparison with other wide-bandgap semiconductors (Wort and Balmer, 2008).

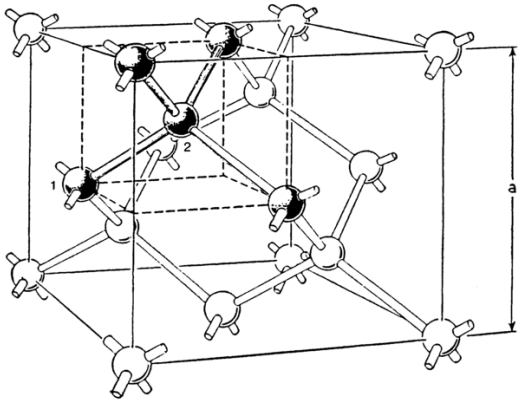

Figure 2.1. Diamond unit cell with dimensions a × a × a showing tetrahedral coordination and two inequivalent atoms (1 and 2) (Shockley, 1976).

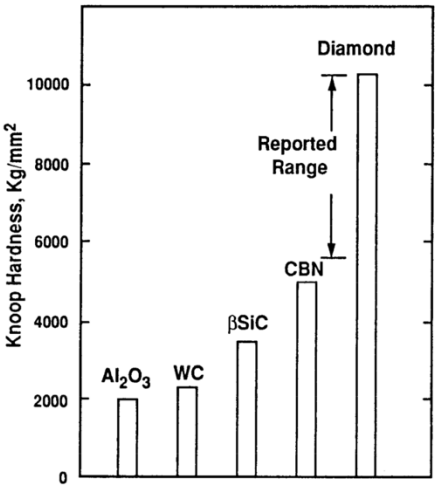

Figure 2.2. Hardness of diamond and other hard materials (Pierson, 1993).

2.2. Production of Synthetic Diamonds

Natural diamond is produced in high-pressure and high-temperature environments. Most of the natural diamonds in commercial diamond deposits come from the Earth's mantle, which is then delivered to the Earth's surface through kimberlite magma by volcanic eruptions. The entire process of natural diamond formation takes about 1-3 billion years. Diamond's extreme rarity, coupled with its much-desired properties, led to an over century-long sustained effort to produce diamond synthetically, using much cheaper carbon-containing substances such as graphite and methane. Today, three methods of synthetic diamond production have been developed, each of which produces distinct diamond forms. These are (1) the high-pressure high-temperature (HPHT) method that forms the bulk, gem-like diamond shapes, (2) the chemical vapor deposition (CVD) method which grows diamond thin films and wafers, and (3) the detonation method that produces nanodiamonds.

2.2.1. High-Pressure High-Temperature Method

Diamond production by HPHT is an attempt to replicate the conditions of natural diamond formation. Figure 2.3 shows the pressure-temperature diagram of carbon, showing the extreme conditions required to achieve graphite-diamond transformation. The first successful attempt of General Electric USA to synthesize diamond in 1955 implements a solvent-catalyst reaction where graphite is completely dissolved up to individual atoms in metals such as iron, cobalt, chromium, nickel, platinum, and palladium to provide a reaction path with lower activation energy. The required pressure is obtained in a hydraulic press using a tungsten-carbide piston (Pierson, 1993). The solvent-catalyst reaction has been found to have limited practical

applicability because of two factors. First, the growth rate is very slow, thus making the process very costly. Second, a lot of solvent metals would be included in the crystal's growth, which leads to decreased crystal quality, known as skeletonization.

Several improvements in the HPHT method have been developed over the succeeding decades. One of the most notable is the successful synthesis of high-purity Type 2a diamond crystals at a high growth rate of 3-4 mg/h by Sumitomo Japan in 1990 using the temperature-gradient method. Two features made this method unique compared to earlier methods. First, they focus on addressing the problem of nitrogen impurities by adding titanium to the solvent metal, which leads to the formation of TiC and traps nitrogen metal inclusions. Impurities of less than 0.1 ppm can be achieved, which improves the diamond's properties, including its absorbance. The second feature is their discovery that good-quality diamond crystals only form on a very narrow temperature width of less than 10 ℃. This method allows the growth of 8-10 carat diamond crystals with dimensions of 10-12 mm (Sumiya et al., 2015).

Small diamond crystals with dimensions between 5 to 20 micrometers can be bonded together under high pressure and temperature to form polycrystalline diamond (PCD). Typical binders are cobalt and nickel. Unlike single-crystal diamonds with direction-dependent hardness, the grain boundaries of PCD make its hardness orientation-independent and generally less brittle. However, grain boundaries negatively affect the optical transparency of PCD by introducing several adsorption bands. In 2003, Sumitomo successfully synthesized binder-less nanopolycrystalline diamond (NPD) using a Kawai-type multi-anvil apparatus (KMA), which uses eight tungsten carbide anvils with edges truncated to form a regular triangle shape in the corner. Recently, the 6000-ton BOTCHAN in Ehime University can produce 1-cm length and

diameter NPD rods by generating a press load of as much as 4700 tons. NPD is harder than single crystal diamond and PCD, making it suitable for many industrial applications (Irifune and Sumiya, 2014).

2.2.2. Chemical Vapor Deposition Method

Diamonds can be grown using the CVD method, a type of low-pressure vapor-phase synthesis. This method uses hydrocarbon to grow diamonds in various substrates. The main advantages of CVD over the HPHT method are the simplicity of setup, the ability to grow diamonds over large areas, and fine control of chemical impurities. Recently, boron and nitrogen impurities at the parts-per-billion level were reported. At pressures used in the CVD method, the stable phase of carbon is graphite and not a diamond. Therefore, the growth is driven by kinetics and not by equilibrium thermodynamics (Aharonovich et al., 2011). Specifically, this is accomplished through continuous activation of the surface carbon species to assimilate the carbon atoms from the feed gas. Surface carbon atoms and gas-phase hydrocarbons are activated by high temperature or plasma.

In addition to hydrocarbons, CVD feed gas always includes hydrogen atoms. According to Gicquel et al., depositing diamond of very high purity at an ultrahigh growth rate simplifies to “producing as much as possible hydrogen atoms in a very clean system, and prevent their loss until they get to the growing surface” (Gicquel et al., 2014). The mechanism of hydrogen’s role in CVD diamond growth is as follows. First, hydrogen stabilizes the sp^3 dangling bonds of surface carbon atoms. Without this stabilization, the (111) surface carbon atoms will tend to change to sp^2 bonding and flatten out to a graphitic structure. Second, hydrogen atoms activate

the diamond surface to capture carbon from gas-phase hydrocarbon. This is illustrated in the two-step deposition model by Frenklach and Spear. In the first step, atomic hydrogen removes the adsorbed hydrogen, making the surface reactive. In the second step, the activated surface-carbon radical reacts with hydrocarbon species, such as C_2H_2, and becomes a site for carbon addition. Finally, atomic hydrogen selectively etches graphite impurities from the grown diamond (Frenklach and Spear, 1988).

For many years, CVD diamonds existed only in polycrystalline form. In early 2000, the availability of larger HPHT diamonds made it possible to use high-quality single-crystal diamonds as a substrate for CVD diamonds. The fusion of these two diamond synthesis methods led to the production of single-crystal CVD diamond (Amaratunga, 2002). Since then, CVD diamonds' quality, growth rate, and size have steadily progressed.

2.2.3. Detonation Method

Detonation nanodiamonds (DND) can be produced from molecules of explosives such as trinitrotoluene, also known as TNT ($C_6H_2(NO_2)_3CH_3$) and hexogen ($C_3H_6N_6O_6$). The explosives are the source of carbon atoms and energy to heat and compress carbon into diamonds. A 60/40 ratio of TNT and hexogen can be detonated in a closed metallic chamber in an atmosphere of nitrogen, carbon dioxide, and water to produce a 4-5 nm diameter diamond nanoparticles. DNDs are hydrophilic and can be functionalized for various applications (Shenderova, 2014; Chen and Zhang, 2017).

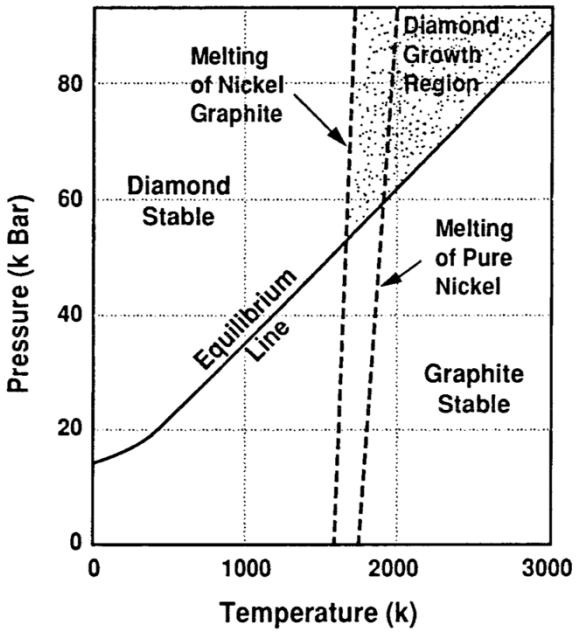

Figure 2.3. Pressure-temperature diagram of diamond-graphite (Pierson, 1993)

Table 2.1. Selected electronic and thermal properties of diamond and other semiconductors (Wort and Balmer, 2008)

	Si	4H-SiC	GaN	Natural Diamond	CVD Diamond
Bandgap (eV)	1.1	3.2	3.44	5.47	5.47
Breakdown field ($MVcm^{-1}$)	0.3	3	5	10	10
Electron saturation velocity ($\times 10^7$ cm s^{-1})	0.86	3	2.5	2	2
Hole saturation velocity ($\times 10^7$ cm s^{-1})	n/a	n/a	n/a	0.8	0.8
Electron mobility (cm^2 V^{-1} s^{-1})	1450	900	440	200-2800	4500
Hole mobility (cm^2 V^{-1} s^{-1})	480	120	200	1800-2100	3800
Thermal conductivity (W cm^{-1} K^{-1})	1.5	5	1.3	22	24

2.3. Industrial and Technological Applications of Diamond

2.3.1. Diamond Tools

The industrial applications of diamonds depend on the crystal size. Small crystals (< 1mm) are used as powder and grit for grinding, lapping, and polishing applications. In addition, they are used in the manufacture of PCD and NPD. On the other hand, larger crystals (> 1mm) are polished and shaped into drill bits, single-point turning tools, cutting tools, and wire-drawing dies. There are three requirements for materials used in cutting and grinding. These are hardness, toughness, and chemical stability. Being the hardest of all materials, diamonds meet the first requirement excellently. However, single crystal diamond is brittle and has low toughness. In addition, diamonds react readily with metals such as Fe, Co, Ni, Cr, and V. This limits the application of diamond tools to certain materials. In particular, diamond tools are well suited to processing stone, concrete, glass, gemstones, ceramics, carbide alloys, and non-ferrous metals such as aluminum and copper. However, diamond tools are unsuitable for steel processing (Pierson, 1993).

Diamond-cutting tools have limited applicability for the machining of ferrous metals. Diamonds react chemically with ferrous metals, causing premature tool wear and surface deterioration (Li et al., 2013). Several studies have been performed to understand the mechanism of diamond tool wear in cutting ferrous metals. These studies are motivated by the possibility of developing methods to reduce the wear, which could lead to ultra-precision machining of hardened steel.

The wear mechanism of diamond tools can be divided into four groups (Evans and Bryan, 1991):

1. Adhesion and formation of built-up edge
2. Abrasion, microchipping, fracture and fatigue
3. Tribothermal
4. Tribochemical

One notable difference between diamond turnable materials and ferrous metals is the absence of the accumulated material that adheres to the tooltip, known as a built-up edge (BUE). The BUE accumulates and eventually becomes part of the tool itself. This changes the tool geometry and rake stiffness, which causes premature tool wear and poor surface finish. An experiment on the friction between diamond and steel in vacuum shows that above a critical sliding speed, the metal is smeared over the surface of the diamond. However, the load and speeds applied on diamonds and metals in actual turning are lower than those where BUE and adherent transfer were reported. Therefore, this mechanism should not be dominant (Evans and Bryan, 1991).

The wear of diamond tools, which appears to be abrasive, has been observed. However, since diamonds are extremely hard and have negligible plasticity below 1900 K, typical abrasive wear through plastic deformation and shear should not be the cause. The wear is likely due to microchipping and cleavage along the stable (111) plane. Diamond tools also show fatigue behavior, where fracture strength decreases with increasing stress cycles. While this explains the wear behavior of diamonds when turning diamond-turnable materials, it cannot

explain the high wear rate of diamond tools when turning pure iron, which occurs even for relatively low-stress cycles (Evans and Bryan, 1991).

Since diamond is a metastable allotrope of carbon, the increased temperature in the tool-work interface can lead to tool degradation as diamond reverts into graphite (Komanduri and Shaw, 1975). This phase transformation occurs above 1800 K in vacuum or inter gas, 1100 K in an oxygen atmosphere, and 1000 K in the presence of iron. However, the temperatures of both the rake and cutting edge of diamond tools during single-point turning were found to be well below those for which rapid thermal graphitization could occur.

Tribochemical wear can be divided into graphitization, diffusion of carbon into the metal, carbide formation, and oxidation. Graphitization is generally considered the primary chemical wear mechanism. One of the first pieces of evidence of the catalytic role of iron in diamond tool graphitization is the observed higher wear as the carbon content of ferrous metal decreases (Shimada et al., 2004). Moreover, since bulk diamond and steel do not react, the wear must be due to the increased chemical activity of clean metal surfaces generated during machining.

The diffusion of diamond into the material has also been observed (Komanduri and Shaw, 1975). Molecular dynamics simulations of the nanometric cutting of iron with a diamond show that diffusion occurs when there is a graphite interlayer and is accompanied by the transformation of iron into a hexagonal structure (Narulkar et al., 2009). Correlation studies

suggest that the d-electrons in metal workpieces break the diamond lattice, promoting graphitization. In addition, it was suggested that graphitization involves the formation of transition state carbides (Paul et al., 1996). Direct evidence of dissociation of carbon from the diamond surface was observed in an erosion test involving diamond and heated steel wire at temperatures above 1000 K. Interestingly, at temperatures less than 900 K, Erosion is caused by the deoxidation of iron and the oxidation of diamonds (Shimada et al., 2004). This experiment shows that the mechanism of diamond wear in ferrous metals is temperature-dependent.

Ultrasonic vibration cutting in oxygen gas has been shown to suppress the wear of diamond tools (X. Zhang et al., 2019). The effects of hydrogen-containing gases such as methane on the wear of diamond tools when cutting metal are unclear. Casstevens reported that methane gas reduces the wear of diamond tools when cutting steel, while Hitchner and Wilks reported contradictory results (Casstevens, 1983; Hitchiner and Wilks, 1984). Uemura attributed the desorption of hydrogen from the diamond surface as the trigger of the thermochemical graphitization of diamonds when cutting ferrous metals (Uemura, 2004).

2.3.2. Photonics and Biotechnology

In addition to industrial applications, diamond has several niche applications that employ its unique optical, electrical, and thermal properties. The chemical resistance, low thermal expansion, and robustness of diamond make it a suitable window material for extreme environments. For example, diamond windows were used to protect the cameras of some Russian Venera probes from Venus' corrosive and high-pressure environment. These properties

make diamonds suitable for a wide range of applications such as high-energy particle detection (Mainwood, 2000), photodetection (Kleimeier et al., 2010), UV and IF LEDs (Koizumi et al., 2001; Zaitsev et al., 2006), Raman lasers (Mildren et al., 2008), and miniature photonic optical elements (Aharonovich et al., 2011).

Diamond nanoparticles and vertically aligned diamond nanostructures have been applied in chromatography, proteomics, mass spectrometry, catalysis, lubrication, energy storage, capacitors, and batteries. Moreover, because of the diamond's biocompatibility, diamond nanoparticles and nanostructures have been used as tissue scaffolds and surgical implants. Boron-doped diamond micro-electrode arrays have been used to build neural prostheses such as retinal implants (Hébert et al., 2014).

Diamonds also possess optically active color centers, the most prominent of which are the nitrogen-vacancy emission centers that are highly photostable and extremely sensitive to magnetic fields, temperatures, ion concentrations, and spin densities. This has led to several biotechnological applications. Diamond nanoparticles have been widely employed for fluorescence imaging to understand transmembrane pathways through diffusion in cells such as HeLa cells (Fu et al., 2007; Chen and Zhang, 2017). Diamond nanoparticles have been shown to have high brightness and photostability, which make them trackable over long durations. In particular, it has been used to track breast cancer cells for over 20 days (Lin et al., 2015). Diamond nanoparticles have been recently employed for magnetic resonance imaging (MRI). This made it possible to sense the oscillating magnetic field generated by nuclear spins in addition to electron spins. As a result, this improves the spatial resolution of conventional MRI from tens of micrometers to nanometer level. Finally, diamond nanoparticles have been

used in drug delivery. Diamond nanoparticles can be functionalized with carboxyl groups to adsorb various drug molecules and help facilitate the dispersion of these medicines in an aqueous solution (Chen et al., 2009). In addition, diamond nanoparticles have been shown to enhance drug efficacy and be used to deliver a combination of several drugs in a single treatment for a synergistic effect (Chow et al., 2011; H. Wang et al., 2015).

2.3.3. Electronics

Diamond's excellent electrical properties, such as high band gap, high charge-carrier mobilities, and high breakdown field strength, coupled with an unusually high thermal conductivity, make it well-suited as a semiconductor material for high-power and high-frequency applications (Wort and Balmer, 2008).

Maximizing efficiency in power semiconductors requires a device that minimizes conduction loss and switching loss. Current silicon unipolar power devices such as Schottky diodes and metal-oxide-semiconductor field effect transistors (MOSFET) have near-zero switching losses because of the absence of stored charge. However, because of conduction losses, these devices are limited to operation to within 250 V and 600 V for Schottky diodes and MOSFETs, respectively. Bipolar devices such as isolated gate bipolar transistors (IGBTs) reduce conduction losses at high voltages. However, the design of bipolar devices involves charge injection, leading to high switching loss. Therefore, a growing interest has been in developing unipolar devices suitable for high-voltage applications. This could be accomplished by using wide-bandgap (WBG) semiconductors. Silicon carbide (SiC) power modules using Schottky barrier diodes (SBD) have reached commercialization and have been successfully

installed in various industrial equipment and home appliances. SiC power modules are 20% smaller and 15% lighter, allowing the system to achieve 30% less power loss (Shikata, 2016). Because diamond has superior properties compared to SiC, many researchers saw the potential to further improve the efficiency of power electronics by developing diamond power devices. Recently, diamond devices such as pseudo-vertical Schottky barrier diodes (pVSBD) have demonstrated high forward-current density and long-term stability at 400 °C and lossless fast turn-off operation with high blocking capability of > 10kV (Umezawa et al., 2010; Umezawa, 2018). As for switching devices, diamond metal-semiconductor field effect transistors (MESFET) and MOSFET have achieved high blocking voltages of more than 2kV (Kitabayashi et al., 2017). However, this value is still far from the theoretical limit of diamonds (Umezawa, 2018; Wort and Balmer, 2008).

In addition to power applications, diamond devices are also being developed for high-frequency applications such as radio frequency (RF) transistors. Diamond could replace the traveling-wave vacuum tubes (TWT) still being used in broadcasting stations, communication satellites, and radar systems. This can lead to smaller, lighter, lower operational voltage and more robust RF systems. However, unlike diodes and switches, conventional Si device designs are unlikely to work well for diamond transistors. This is because p-type boron-doped diamonds have high ionization energy. Therefore, new types of devices should be developed (Kasu, 2016). In many diamond RF devices, the standard design element utilizes the two-dimensional hole gas (2DHG) on hydrogen-terminated diamonds (Strobel et al., 2004; Ueda et al., 2006; Kasu, 2016; Inaba et al., 2016). This surface conductivity allows charge carrier drift velocity saturation at relatively low fields (Wort and Balmer, 2008). One such new device is the metal-insulator-semiconductor field effect transistor (MOSFET) that uses Al_2O_3 as gate dielectric (Kawarada et al., 2014; Fujii et al., 2023). The current power density record for

operation at 1 GHz is 3.8 W/mm (Imanishi et al., 2019). For 10 GHz frequency, a power density of 182 mW/mm has been recently reported (Yu et al., 2019). As with the current benchmarks in diamond power devices, these values show that the current technology barely taps diamond's potential in high-frequency applications, and there is still a lot of research and development work that needs to be done.

Finally, the graphene-on-diamond structure has been attracting considerable attention due to the unique possibility of having an all-carbon, sp^2-sp^3 technology application (Wu et al., 2011; Ogawa et al., 2012; Yu et al., 2012). The composite structure of graphene and diamond has been shown to improve the performance of graphene devices. Conventional graphene field-effect transistors are built on SiO_2/Si substrates. There are several advantages of using diamond as a substrate. First, the lattice mismatch between diamond and graphene is lower by 2%. Second, the graphene contamination is lower since the substrate is composed of the same type of atom. Finally, the band gap of a diamond is larger; thus, the leakage current of a graphene channel FET is lower (Ogawa et al., 2012). Using a diamond substrate can increase the device's current carrying capacity (Yu et al., 2012).

Graphene-on-diamond devices can be fabricated using the transfer method and direct formation using a catalyst. In the transfer method, the graphene is first adhered to a transfer medium, followed by the delamination of graphene from the growth substrates, and finally, the delamination of graphene onto the target substrates. However, this process is very tedious and can usually lead to cracks in the graphene membrane, transfer-induced doping, wrinkles, and surface contamination (Song et al., 2021). An alternative is to grow graphene directly on the diamond. Kanada et al. fabricated graphene layers on diamond (111) surfaces by annealing at

900 °C for 1 min under an Ar atmosphere with Ni. While the method is much less complicated, the obtained mobility value was lower than that of high-quality graphene on nanocrystalline diamond. The lower performance is possibly due to the imperfections in the graphene and the thick graphene layers formed using this method (Kanada et al., 2017).

2.3.4. Quantum Technology

The term “first and second quantum revolutions” has been increasing recently. The first quantum revolution, or the so-called “quantum 1.0,” refers to the surge of inventions over the past century, including lasers, transistors, semiconductors, and MRI, made possible by our understanding of quantum phenomena. Over the past decades, quantum physicists have laid the theoretical groundwork for detecting and controlling individual quantum states. Today, experimentalists have caught up and demonstrated that manipulating quantum effects such as superposition and entanglement is possible. The foreseen next wave of innovations, such as quantum computing, simulation, communication, and sensing, is called the second quantum revolution or “quantum 2.0” (Markham and Twitchen, 2020).

Quantum states, also known as qubits, are the building blocks of quantum 2.0 technology. It must satisfy two basic requirements. First, it must be sufficiently isolated from external disturbance to prevent the loss of quantum information, and second, it must be interactable and controllable. One of the most technologically advanced solutions is the qubits based on the spins of ions trapped in an electromagnetic field. However, this approach requires ultrahigh vacuum and complex trapping architectures to hold individual particles in place, which is very challenging. An alternative approach is to use a solid-state system, which is easier

to integrate into devices. However, controlling individual spin and maintaining quantum information in a solid-state system requires operation at cryogenic temperatures, which could be as low as a fraction of a Kelvin (Awschalom et al., 2007; Prawer and Greentree, 2008).

In 1997, it was discovered that diamonds possess nitrogen-vacancy (NV) defect centers that can be manipulated and provide optical output at room temperature in a process called optically detected magnetic resonance (ODMR) (Gruber et al., 1997). These optically active centers are bright enough to be detected individually with conventional microscopy (Prawer and Greentree, 2008). The NV center causes an electron from a neighboring nitrogen substitutional defect to occupy the dangling bonds around the vacancy site. The energy states of this electron behave similarly to a trapped ion without the need for a complex trapping mechanism. The diamond has several intrinsic properties, making it an ideal host to quantum defects. First, its wide band gap excites the electrons without entirely knocking them to the conduction band. Diamond's band gap is also wide enough to accommodate defect center excitations along the optical spectrum, which can be induced with readily available lasers. In addition, the NV defects are very well isolated from any interference within the diamond. Because of carbon's low atomic mass and strong sp3 bonding, the diamond has a high Debye temperature, resulting in weak interaction of the NV center with the vibrational mode of the diamond lattice. In addition, diamond has a naturally low concentration of carbon-13 that has intrinsic nuclear spin. Thus, the likelihood of NV state and nuclear interaction is low. Furthermore, the spin-orbit coupling of the NV defect is weak. Because of these, the NV center can retain its quantum character sufficiently long to perform calculations. Recently, a ten-qubit solid-state spin register was developed based on an electron spin on the NV center and nine diamond nuclear spins. This system can hold a single-qubit state for up to 75 seconds and preserve two-qubit entanglement for at least 10 seconds (Bradley et al., 2019).

Despite these desirable features, several challenges must be overcome before we see practical diamond quantum computers and information processing devices. Fortunately, researchers have found several alternative "quantum diamond" applications with less stringent technological requirements than quantum computing. The NV center of diamond has been found to have applications in biological fluorescence imaging and improving the resolution of MRI. Quantum mechanically entangled quantum repeater nodes based on diamond NV centers have demonstrated 100% secure internet communication (Markham and Twitchen, 2020). A new generation of room-temperature masers (microwave amplification by stimulated emission of radiation) has been developed, lighter, more compact, and less complex than conventional masers (Breeze et al., 2018). As a final example, Lockheed Martin, an American aerospace company, and Element Six, a leading commercial CVD diamond producer, have recently teamed up to develop a jam-resistant global positioning system (GPS). Known as dark ice, this GPS operates without any external signals and relies entirely on a diamond magnetometer to sense the strength and direction of Earth's magnetic field. This works under the principle that a diamond's NV center can form in four different orientations, which gives the diamond magnetometer an intrinsic vector capability (Markham and Twitchen, 2020).

2.4. Diamond Device Fabrication

The ability to engineer diamonds into various forms with nanoscale precision will profoundly affect electronics and quantum technologies (Awschalom et al., 2007). Typical electronic device fabrication involves flatting the surface and forming trench structures. Forming atomically flat surfaces is very important in semiconductors and semiconductor-metal

heterostructure devices. This is because imperfections, even at the atomic scale, can result in charge-carrier scattering, which will affect device performance (Tokuda et al., 2016). Trench structures with a depth of tens up to a few hundred micrometers are required for the fabrication of MEMS, MOSFETS, and Schottky diodes (Inaba et al., 2016; Toros et al., 2018; Hicks et al., 2019). As for quantum technology devices, there is a growing trend favoring all-diamond systems, which involves fabricating waveguides and resonators from diamond bulk. In addition, photonic emitters from vertical nanostructures have been shown to have an order of magnitude increase in efficiency compared to diamond bulk (Babinec et al., 2010).

2.4.1. Plasma Etching

In many of these applications, the precision structuring of diamond has been achieved using fabrication based on plasma etching. A plasma is a collection of free-charged particles moving in random directions in a quasineutral state. This means that, on average, plasmas are electrically neutral, while at smaller scales, the flux of charged particles leads to charged regions and electric fields. One important consequence of quasineutrality is forming a positively charged sheath layer between the plasma and a grounded wall surface. Within the sheath, ions are accelerated toward the walls in the ion bombardment process. The specific plasma etching method used to manufacture many electronic devices is called reactive ion etching (RIE). RIE works through the combination of chemical reaction of the material with neutral species and ion bombardment (Fig. 2.4). The chemical reaction generally results in isotropic etching, wherein the material is etched equally in every direction. On the other hand, ion bombardment allows anisotropic etching or etching along a preferred direction, usually

perpendicular to the substrate. The desired features of the material are implemented through the deposition of a protective mask (Lieberman and Lichtenberg, 2005).

The traditional fabrication methods used in the semiconductor industry cannot be directly applied to diamond because of its hardness and chemical inertness. Therefore, several modifications have been made to plasma processing to achieve satisfactory results. For instance, the masks used for Si have insufficient lifetimes in plasma to achieve significant depth in diamonds. Therefore, the main masking options for diamonds are metals or metal oxides. However, these masks generate sputtered mask materials across the etched surface, known as micromasking. This has been addressed by cycling the plasma that effectively etches the diamond with the plasma that effectively etches the micromask (Yamada et al., 2007). Recently, this technique has been shown to effectively fabricate a high-quality 10-micrometer deep trench structure, which uses Ar/O_2 to etch the diamond and Ar/Cl_2 to clean the aluminum micromask (Hicks et al., 2019).

2.4.2. Thermochemical Etching

While considerable progress has been made in developing plasma etching methods tailor-made for diamond device fabrication, plasma etching still suffers from two difficulties: low diamond/mask selectivity of etchant (Tran et al., 2010) and plasma-induced damage of diamond (Kawabata et al., 2004; Yamazaki et al., 2007). For this reason, an alternative, non-plasma diamond etching process based on thermochemical reaction has been developed.

This novel etching method was inspired by the same reaction that made diamond-cutting tools ineffective in processing ferrous metals such as iron, cobalt, and nickel (Furushiro et al., 2010; Zou et al., 2018). This reaction is employed by using metals to pattern on the surface of a diamond while heating under high-temperature gas. Etching rates comparable to plasma processes have been achieved on thermochemical reactions between Ni and diamond under high-temperature air (Morofushi et al., 2011). However, significantly slower rates were reported when the reaction was carried out under non-oxidative gases such as N_2 (Morofushi et al., 2011), Ar (Nakanishi et al., 2016), and H_2 (Mehedi et al., 2013; Aida et al., 2016). Therefore, oxidation by high-temperature O_2 is necessary for a high etching rate. To improve etching selectivity between diamond and Ni, Nagai et al. have performed thermochemical etching of diamond using Ni under water vapor. This modification results in the 46-micrometer-deep trench with an etching rate that is considerably faster than other diamond etching processes, including the plasma process. In addition, anisotropic etching similar to Si etching by KOH was observed. The (100) surface under Ni film was etched with an inverted pyramid and truncated pyramid-shaped trenches with (111) surface side walls functioning as stopping planes. In comparison, (111) surface was atomically flattened, albeit no trench was formed (Nagai et al., 2018).

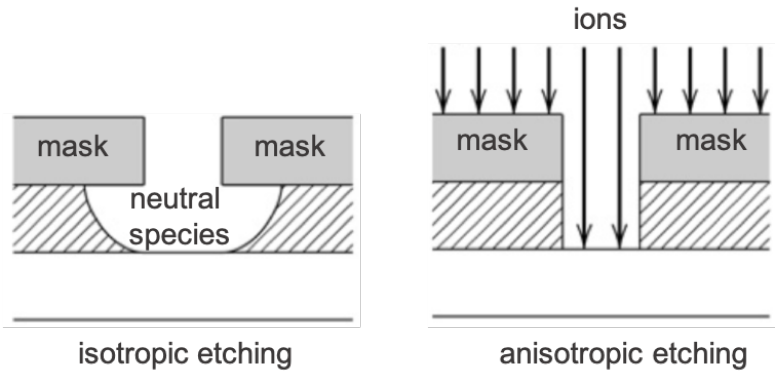

Figure 2.4. Isotropic and anisotropic plasma etching

2.5. Oxidation of Diamond (111) and C(100) Surfaces

The number of researchers developing diamond devices has increased over the past years. However, most diamond applications have yet to deliver the anticipated technological impact. In electronics, the device performance is still a fraction of its theoretical limits, while in quantum technologies such as quantum computers, practical devices have yet to be developed. One of the main hurdles is the effective and efficient device fabrication method. While both plasma and thermochemical etching have shown considerable progress in the past years, these methods are still in their infancy compared to the matured tools available for processing conventional semiconductor materials. Oxygen plays a significant role in both plasma and thermochemical etching. Thus, a detailed understanding of the interaction between oxygen and the diamond surface will improve these fabrication methods.

The most technologically relevant surface facets of diamond are the (111) and (100) surfaces. The C(111) surface has one dangling bond per surface carbon atom in its as-cleaved configuration. It reconstructs to achieve a 2×1 periodicity by producing a π-bonded chain structure, saturating the dangling bonds, and lowering the surface energy. On the other hand, in its as-cleaved state, the C(100) surface has two dangling bonds per surface carbon atom and reconstructs to achieve a 2×1 periodicity by the formation of π-bonded dimers. This reconstruction reduces the number of dangling bonds per surface atom by 1, lowering the surface energy (Fig. 2.5).

Of the two surfaces, the C(100) surface is most frequently employed in producing electronic devices such as Schottky diodes and MOSFET. Additionally, it grows the easiest

with the CVD process (Koizumi et al., 2018). In comparison, the C(111) surface possesses a distinct set of properties, including higher electron and hole mobility and the capacity to create more homogeneous nitrogen-vacancy (NV) centers, making it more suitable for quantum devices (Reed et al., 2022).

The adsorption of oxygen on the C(100) surface has been studied extensively. Electron energy loss spectra (EELS) of C(100) surface exposed to atomic O have shown peaks corresponding to both bridge and on-top adsorption (Hossain et al., 1999). High-resolution x-ray photoelectron spectroscopy (XPS) of diamond (100) surface oxidized in dry O_2 has also demonstrated that diamond (100) surface is terminated with both carbonyl (on top) and ether (bridge), with surface coverage of up to a monolayer (John et al., 2002). Electron diffraction measurements have revealed that oxygen adsorption induced the breaking of the surface carbon dimer bond, which led to the deconstruction of (100) surface (Zheng et al., 2001). In comparison, there are fewer studies on oxygenated C(111) surfaces. Using Auger electron spectroscopy (AES), it has been shown that the uptake of oxygen on the C(111) surface saturates at room temperature. Full coverage can only be attained once the surface is heated to 400 degrees (Loh et al., 2002).

Several studies investigated diamond etching using dry oxygen at high temperatures. Diamond (100) surfaces etched with oxygen were generally flat with very low steps whose sides are along the {110} directions. In contrast, the etched (111) surfaces were morphologically rough (de Theije et al., 2000). Moreover, atomic force microscopy (AFM) images of diamond (100) have shown that the surface roughness has no appreciable change after the removal of 480 nm of carbon (John et al., 2002). Analysis of thermal desorption

spectra (TDS) revealed that the oxidative etching of diamond surface is mainly by desorption of CO, although much smaller amounts of desorbed CO_2 were also detected (Hossain et al., 1999; Thomas et al., 1992). The most puzzling feature of the TDS data is that the peak of CO desorption was extremely wide. From the peak temperature of TDS, Frenklach et al. estimated the CO desorption energy to be 45.0 kcal/mol (1.95 eV) (Frenklach et al., 1993). Using temperature-programmed desorption (TPD), it has been observed that the oxidative etching of the C(111) surface is also by desorption of CO with an estimated desorption energy of 59 kcal/mol (2.56 eV) (Loh et al., 2002).

The oxidation of the C(100) surface has been studied theoretically. The most energetically stable adsorption site at monolayer is the bridge site forming ether followed by the top site forming carbonyl (Frenklach et al., 1993; Skokov et al., 1994; Rutter and Robertson, 1998; Sque et al., 2006; Petrini and Larsson, 2007). Based on these results, calculations predicted that the C(100) surface is terminated by ether groups at monolayer coverage. As for the C(111) surface, Loh et al. proposed that at low O coverage, the epoxy configuration (bridge) is more stable, while at high coverage, the surface reconstructs to form a carbonyl-type oxygen species (Loh et al., 2002). The molecular and dissociative adsorption of O_2 on the C(100) and C(111) surface has been compared by Tran et al., and reported that the O_2 adsorption on the C(100) surface is stronger compared to the C(111) surface (Tran and Righi, 2022).

Frenklach et al. performed semi-empirical quantum chemical potential energy calculations to investigate the CO desorption mechanism. The largest potential energy barrier is 38.4 kcal/mol (1.67 eV), corresponding to the breaking of the final C-CO bond. While the calculated potential energy barrier agreed reasonably with their estimate from TDS data, their

simulation was not able to explain the observed wide desorption peak (Frenklach et al., 1993). Tran et al. also simulated the CO desorption reaction from the C(111) and C(100) surfaces from a single O_2 adsorption. The calculated activation energy for the C(111) and C(100) surfaces are 6.43 eV and 3.24 eV, respectively (Tran and Righi, 2022)The calculated values are much higher than those in experiments and earlier calculations. This suggests that a more physical oxidative etching model is necessary to accurately predict the activation energies.

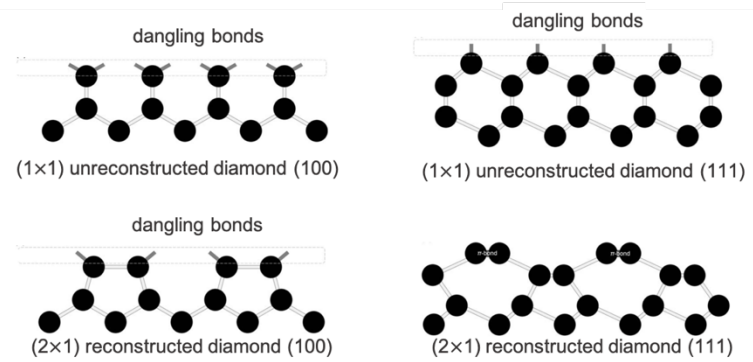

Figure 2.5. Diamond (100) and (111) surfaces (Tokuda 2018)

2.6. Graphitization of Diamond

Diamond is a thermodynamically unstable form of carbon, and when heated to sufficiently high temperatures, changes into graphite (Seal, 1958). This thermal degradation process, which is commonly referred to as graphitization, typically produces not just crystalline graphite but also amorphous carbon (Ali et al., 2021; Yan et al., 2021).

Despite the extensive history of diamond graphitization research, theoretical and experimental work in this field is ongoing. This is because the atomistic mechanism of graphitization, particularly the dependency of graphitization rate on surface facet, is still not fully understood (Bokhonov et al., 2021).

David and Evans investigated the graphitization of diamond by heating diamond octahedrons, which consist of (111) planes. They reported that the graphitization rate increased rapidly from 0.2% mass loss per minute when heated at 1850 C to 5% mass loss per minute when heated at 2000C. They also heated a brick-shaped diamond with two (100) facets and two (110) facets at 1875 C for 5 minutes. They reported that while the (110) surfaces were coated with a black coating of graphite, the (100) surface showed only small, isolated regions of graphitization. They estimated that the rate of graphitization follows the order (110) > (111) > (100). They proposed a graphitization mechanism in which single carbon atoms detach from the surface and re-condense into graphite (Davies et al., 1997). This graphitization mechanism is also proposed in other experiments, including the graphitization of diamonds in the presence of H_2O (Grenville-Wells, 1952; Evans and James, 1964; Bundy, 1980; O'Bannon et al., 2020).

In contrast, several theoretical studies have proposed an alternative mechanism where direct graphitization of C(111) occurs by heating and pulsed laser treatment. Kern et al. use ab initio molecular dynamics to study the graphitization of the C(100) surface when heated at high temperatures and predicted that the flat and stepped surface will graphitize at 3500K-3900K and 2500K, respectively, within a few picoseconds (Kern and Hafner, 1998). A similar mechanism is also reported in the ab initio molecular dynamics simulations of Vita et al. but with lower predicted graphitization temperature for flat C(111) surface (2500 K) (De Vita et al., 1996). Wang et al. use ab-initio tight-binding simulations with finite electronic temperature to investigate the laser-induced graphitization of the (111) surface. Using femtosecond laser pulses, their simulations show that layer-by-layer graphitization is possible (Wang et al., 2000).

Recent experiments have shown the possibility of this mechanism, as proven by fabricating epitaxial graphitic layers in diamonds. Rubanov et al. implanted diamonds with Ga ions and annealed the specimen at high pressure and temperature. The annealing resulted in the production of high-quality graphite planes (Rubanov et al., 2016). More recently, an experiment on synthetic diamond microcrystals has shown that epitaxial growth of graphene on diamond with parallel and vertical orientation is possible even without ion implantation. Moreover, they have reported that the diamond (111) surface [C(111)] is more susceptible to graphitization compared to the (100) surface and that the graphitization of microcrystals starts from the vertices and edges (Bokhonov et al., 2021).

CHAPTER 3. THEORETICAL FRAMEWORK

ELECTRONIC AND ATOMIC-LEVEL SIMULATIONS USING DENSITY FUNCTIONAL THEORY AND MACHINE LEARNING MOLECULAR DYNAMICS

3.1. Many-body Schrödinger Equation and Born-Oppenheimer Approximation

The time-independent, non-relativistic Schrödinger equation can be expressed in the form

$$\hat{H}\Psi = E\Psi \tag{3.1}$$

where Ψ is the particle's wavefunction, $\hat{\mathrm{H}}$ is the Hamiltonian operator, and E is the energy eigenvalue (Schrödinger, 1926). The Born interpretation of quantum mechanics states that the square modulus of the wavefunction Ψ at any given position $\vec{\mathrm{r}}$ is proportional to the probability P of finding the particle at that position (Born and Jordan, 1925; Fedak and Prentis, 2009)

$$P \propto |\Psi|^2 \tag{3.2}$$

The consequence of this interpretation is that the integral of $|\Psi|^2$ over all space must equal to unity

$$\int |\Psi|^2 d\vec{r} = 1 \tag{3.3}$$

For a system consisting of multiple electrons and nuclei, $\widehat{H}$ is represented by Coulomb Hamiltonian

$$\widehat{H} = \hat{T}_n + \hat{T}_e + \widehat{U}_{en} + \widehat{U}_{ee} + \widehat{U}_{nn} \tag{3.4}$$

where

$$\hat{T}_n = -\frac{1}{2}\sum_i \frac{1}{M_i}\nabla^2_{\vec{R}_i} \tag{3.5}$$

$$\hat{T}_e = -\frac{1}{2}\sum_i \nabla^2_{\vec{r}_i} \tag{3.6}$$

$$\widehat{U}_{en} = -\sum_i \sum_j \frac{Z_i}{\left|\vec{R}_i - \vec{r}_j\right|} \tag{3.7}$$

$$\widehat{U}_{ee} = \sum_i \sum_{j>i} \frac{1}{\left|\vec{r}_i - \vec{r}_j\right|} \tag{3.8}$$

$$\widehat{U}_{nn} = \sum_i \sum_{j>i} \frac{Z_i Z_j}{\left|\vec{R}_i - \vec{R}_j\right|} \tag{3.9}$$

Eq. 3.5 and 3.6 describes the sums of the kinetic energies of the nuclei and the electrons respectively, while Eq. 3.7, 3.8, and 3.9 describes the sums of electrical potential energies

associated with attractive electron-nuclei interaction, and repulsive electron-electron and nucleus-nucleus interactions.

Born-Oppenheimer approximation suggest that the motion of the nuclei and electrons can be treated separately, allowing us to separate the wavefunction into its electronic $\Psi_e(\vec{r},\vec{R})$ and nuclear $\Psi_n(\vec{R})$ components (Born and Oppenheimer, 1927; Tully, 2000) (Born and Oppenheimer, 1927; Tully, 2000).

$$\Psi = \Psi_e(\vec{r},\vec{R})\Psi_n(\vec{R}) \tag{3.10}$$

The electronic wavefunction $\Psi_e(\vec{r},\vec{R})$ satisfy the eigenvalue equation

$$\hat{H}_e\Psi_e(\vec{r},\vec{R}) = E_e\Psi_e(\vec{r},\vec{R}) \tag{3.11}$$

Here, $\hat{\mathrm{H}}_\mathrm{e}$ is the Hamiltonian operator given by

$$\hat{H}_e = \hat{T}_e + \hat{U}_{en} + \hat{U}_{ee} \tag{3.12}$$

and $\mathrm{E_e}$ is the total energy of the electrons.

Due to the large difference between the masses of electrons and nucleus, we can simplify the system and consider the electrons moving in a fixed nucleus. Thus, the sum of kinetic energies $\hat{T}_n$ of nuclei is zero, and the total nuclear potential energy reduces to a constant

$$E_n = \sum_i \sum_{j>i} \frac{Z_i Z_j}{|\vec{R}_i - \vec{R}_j|} = \text{const.} \tag{3.13}$$

The total energy of the system simplifies to

$$E = E_e + E_n \tag{3.14}$$

3.2. Variation Theorem, Hartree Fock Approximation and Self-Consistent Field Method

The ground state energy E_0 can be exactly determined whenever the corresponding wavefunction Ψ_0 is known using the equation

$$E_0 = \frac{\int \Psi_0^* \hat{H} \Psi_0 \, d\vec{r}}{\int \Psi_0^* \Psi_0 d\vec{r}} \tag{3.15}$$

The exact ground state wavefunction is seldom known. However, approximate wave function Ψ_{trial} may be used giving us an approximate ground state energy E_{trial}, which according to Variation Theorem is always greater than or equal to the true ground state energy

$$E_{trial} = \frac{\int \Psi_{trial}^{*} \hat{H} \Psi_{trial} \, d\vec{r}}{\int \Psi_{trial}^{*} \Psi_{trial} d\vec{r}} \geq E_0 \tag{3.16}$$

To minimize E_{trial}, we are required, in principle, to search over all acceptable N-electron wavefunctions. The task may be simplified by defining a suitable subset. Recall that any reasonable electronic wavefunction must reflect the indistinguishability of electrons, and since electrons are fermions, Pauli exclusion principle requires all electronic wavefunctions to be antisymmetric. This is accomplished by expressing the wavefunction as Slater determinant (Slater, 1951)

$$\Psi(1, 2, 3, \dots, N) = \frac{1}{\sqrt{N}} \begin{vmatrix} \chi_1(1) & \chi_2(1) & \cdots & \chi_N(1) \\ \chi_1(2) & \chi_2(2) & \cdots & \chi_N(2) \\ \cdots & \cdots & \cdots & \cdots \\ \chi_1(N) & \chi_2(N) & \cdots & \chi_N(N) \end{vmatrix} \tag{3.17}$$

where $\chi_i(\vec{r})$ are the spin orbitals, which are composed of the spatial orbitals $\phi_i(\vec{r})$ and one of the two spin functions $\alpha(s)$ and $\beta(s)$.

$$\chi_i(\vec{r}) = \phi_i(\vec{r})\sigma(s), \sigma = \alpha, \beta \tag{3.18}$$

Hartree and Fock gave a prescription for finding a single Slater determinant that gives the lowest ground state energy for multi-electron system. This was made by assuming that electrons are uncorrelated in such a way that a single electron is affected only by the spatially averaged electron charge distribution of the remaining $N - 1$ electrons. This approach, known

as Hartree-Fock approximation, leads to a set of differential equations known as Hartree-Fock equations:

$$\hat{f}\chi_i(\vec{r}) = \varepsilon_i\chi_i(\vec{r}),\ i = 1,2,\dots,N \tag{3.19}$$

where ε_i are orbital energies and $\hat{f}$ is the Fock operator

$$\hat{f} = -\frac{1}{2}\nabla_i^2 - \sum_i \frac{Z_i}{|\vec{R}_i - \vec{r}_j|} + V_{HF}(\vec{r}) \tag{3.20}$$

The Hartree-Fock potential V_{HF} is the average repulsive potential experienced by a single electron due to the remaining $N-1$ electrons.

$$V_{HF} = \int \frac{n(\vec{r}')}{|\vec{r} - \vec{r}'|} d\vec{r} \tag{3.21}$$

where $n(\vec{r}')$ is the electron density given by

$$n(\vec{r}') = 2\sum_i |\Psi_i(\vec{r}')|^2 \tag{3.22}$$

The above equations can be transformed into a set of algebraic equations by treating multi-electron spin orbitals as a linear combination of atomic orbitals (LCAO approximation)

$$\chi_i = \sum_{\mu i} c_{\mu i} \varphi_\mu \tag{3.23}$$

where φ are basis functions and μ is the number of basis set. As $\mu \to \infty$, LCAO approximation is exact at Hartree-Fock level.

Finding spin orbitals requires solving single-electron equations (Eq. 3.18) and defining Hartree-Fock potential for single-electron equations (Eq. 3.19 and 3.20) requires knowledge of electron density (Eq. 21), which in turn requires electron wavefunction (Eq. 22). Therefore, the spin orbital calculations necessitate an iterative approach. The procedure is repeated for all electrons until the solutions for the energies and orbitals do not change significantly in a further iteration, an algorithm that is called self-consistent field method (Giustino, 2014).

3.3. Hohenberg-Kohn Theorems and Density Functional Theory

Assume there exist two different external potentials $\widehat{U}(\vec{r})$ and $\widehat{U}'(\vec{r})$ that give rise to two electronic systems having equal ground state electron density $n(\vec{r})$. Because of Variation Theorem, no wavefunction Ψ' can give an energy E' that is less than the energy E of wavefunction Ψ given the Hamiltonian $\widehat{H}$

$$E = \langle \Psi | \hat{H} | \Psi \rangle < \langle \Psi' | \hat{H} | \Psi' \rangle \tag{3.24.a}$$

Conversely

$$E' = \langle \Psi' | \hat{H}' | \Psi' \rangle < \langle \Psi | \hat{H}' | \Psi \rangle \tag{3.24.b}$$

Because $\hat{H}$ and $\hat{H}'$ gave identical n($\vec{r}$), the above expressions for expectation values can be rewritten as

$$E < \langle \Psi' | \hat{H} | \Psi' \rangle = \langle \Psi' | \hat{H}' | \Psi' \rangle + \int [\hat{U}(\vec{r}) - \hat{U}'(\vec{r})] n(\vec{r}) d\vec{r} \tag{3.25.a}$$

$$E' < \langle \Psi | \widehat{H'} | \Psi \rangle = \langle \Psi | \hat{H} | \Psi \rangle + \int [\hat{U}'(\vec{r}) - \hat{U}(\vec{r})] n(\vec{r}) d\vec{r} \tag{3.25.b}$$

Adding Eq. 3.25.a and 3.25.b,

$$E + E' < \langle \Psi' | \hat{H}' | \Psi' \rangle + \int [\hat{U}(\vec{r}) - \hat{U}'(\vec{r})] n(\vec{r}) d\vec{r} + \langle \Psi | \hat{H} | \Psi \rangle$$

$$+ \int [\hat{U}'(\vec{r}) - \hat{U}(\vec{r})] n(\vec{r}) d\vec{r}$$

$$E + E' < \langle \Psi' | \hat{H}' | \Psi' \rangle + \langle \Psi | \hat{H} | \Psi \rangle + \int [\hat{U}(\vec{r}) - \hat{U}'(\vec{r})] n(\vec{r}) d\vec{r}$$

$$- \int [\hat{U}(\vec{r}) - \hat{U}'(\vec{r})] n(\vec{r}) d\vec{r}$$

$$E + E' < \langle \Psi' | \hat{H}' | \Psi' \rangle + \langle \Psi | \hat{H} | \Psi \rangle$$

$$E + E' < E' + E \tag{3.26}$$

which is absurd. This argument leads to the First Hohenberg-Kohn Theorem (Hohenberg and Kohn, 1964):

> "*The full many-particle ground state is a unique functional of electron density.*"

Since electron density uniquely determines the ground state wavefunction, electron density should uniquely determine all observables of the system, including the kinetic energies. We can therefore define Hohenberg-Kohn functional $F[n(\vec{r})]$

$$F[n(\vec{r})] \equiv T[n(\vec{r})] + U_{ee}[n(\vec{r})] \tag{3.27}$$

where T and U_{ee} are kinetic and electron interaction energies which are functionals of electron density n. Using Eq. 3.12, we can construct the total energy expression of a wavefunction in terms of $F[n(\vec{r})]$

$$\langle \Psi | \hat{H} | \Psi \rangle = \langle \Psi | \hat{T}_e + \hat{U}_{en} + \hat{U}_{ee} | \Psi \rangle = T_e + U_{en} + U_{en}$$

$$\langle \Psi | \hat{H} | \Psi \rangle = F[n(\vec{r})] + U_{en} \tag{3.28}$$

Using Variation Theorem, we can form a relation between energies with exact ground state density $[n(\vec{r})]$ and trial ground state density $[n'(\vec{r})]$

$$E[n(\vec{r})] \leq \langle \Psi' | \hat{H} | \Psi' \rangle = F[n'(\vec{r})] + U'_{en}$$

$$E[n(\vec{r})] \leq F[n'(\vec{r})] + U'_{en} = E[n'(\vec{r})] \tag{3.29}$$

The results suggest that the electron density that minimizes the energy of the Hohenberg-Kohn functional is the electron density that will give the ground state energy. This argument, known as the Second Hohenberg-Kohn Theorem can be restated as follows (Hohenberg and Kohn, 1964)

> *"The problem of determining the ground-state energy and density in a given external potential would be rather easy since it requires merely the minimization of a functional of the three-dimensional density function."*

The two Hohenberg-Kohn theorems laid the foundation for a quantum mechanical modeling which determines the properties of many-electron systems using functionals of electron density now known as the Density Functional Theory (DFT).

3.4. Kohn-Sham Equations

The derivation of Kohn-Sham equations (Kohn and Sham, 1965) starts by defining a non-interacting reference system having Hamiltonian $\hat{H}_S$

$$\hat{H}_S = \hat{T}_e + \hat{V}_{eff} \tag{3.30}$$

where $\hat{T}_e$ is the same kinetic energy defined in Eq. 3.6 and $\hat{V}_{eff}$ is the effective local potential. This reference system is described by wavefunction Θ_S. Similar to Hartree-Fock methods, this system requires to be in a form of Slater determinants to satisfy Pauli exclusion principle

$$\Theta_S(1,2,3,\dots,N) = \frac{1}{\sqrt{N}} \begin{vmatrix} \kappa_1(1) & \kappa_2(1) & \cdots & \kappa_N(1) \\ \kappa_1(2) & \kappa_2(2) & \cdots & \kappa_N(2) \\ \cdots & \cdots & \cdots & \cdots \\ \kappa_1(N) & \kappa_2(N) & \cdots & \kappa_N(N) \end{vmatrix} \tag{3.31}$$

In the above expression, κ_i is the corresponding set of spin orbitals known as Kohn-Sham orbitals. The Kohn-Sham analog of Hartree-Fock equations, i.e. Eq. 3.19 and 3.20 are as follows

$$\hat{f}_{KS}\kappa_i(\vec{r}) = \varepsilon_i\kappa_i(\vec{r}),\ i = 1,2,\dots,N \tag{3.32}$$

$$\hat{f}_{KS}(\vec{r}) = -\frac{1}{2}\nabla_i^2 + \hat{V}_{eff}(\vec{r}) \tag{3.33}$$

Notice that the $\hat{f}_{KS}$ entirely assumes zero electron-electron interaction, in contrast with $\hat{f}$ that includes V_{HF} which is the interaction between an electron and the average potential due to the remaining N-1 electrons. To relate this fictitious non-interacting system to the realistic system that we are concerned with, Hohenberg-Kohn Theorems assure that all we need to do is to choose $\hat{V}_{eff}$ such that the ground state density n_S of non-interacting system equals the ground state density n of the real system.

$$n_S(\vec{r}) = \sum_i \sum_s |\kappa_i(\vec{r}, s)|^2 = n(\vec{r}) \tag{3.34}$$

The next task is to define an expression for the ground state energy in terms of functionals of electron density. First, we define the kinetic energy T_S

$$T_S[n(\vec{r})] = \langle \kappa_i | \hat{T}_e | \kappa_i \rangle \tag{3.35}$$

which is obviously not equivalent to the true kinetic energy $T[n(\vec{r})]$ because of the approximations that we made. Next, we define the Coulomb interaction $J[n(\vec{r})]$, which is the classical electrostatic potential energy due to the interaction of charge distribution with itself.

$$J[n(\vec{r})] \equiv \frac{1}{2}\iint \frac{n(\vec{r})n(\vec{r}')}{|\vec{r}-\vec{r}'|}d\vec{r}d\vec{r}' = \frac{1}{2}\sum_{i}^{N}\sum_{j}^{N}\iint \frac{|\kappa_i(\vec{r})|^2|\kappa_j(\vec{r}')|^2}{|\vec{r}-\vec{r}'|}d\vec{r}d\vec{r}' \tag{3.36}$$

Again, the expression for $J[n(\vec{r})]$ is not equivalent to the true electron-electron interaction energy $U_{ee}[n(\vec{r})]$ since it includes self-interaction. As a correction to the errors introduced by Eq. 3.35 and 3.36, we introduce the exchange correlation energy $E_{XC}[n(\vec{r})]$

$$E_{XC}[n(\vec{r})] = T[n(\vec{r})] - T_S[n(\vec{r})] + U_{ee}[n(\vec{r})] - J[n(\vec{r})] \tag{3.37}$$

We can also express the nuclei-electron interaction as a function of electron density

$$U_{en}[n(\vec{r})] = \langle\kappa_i|\widehat{U}_{en}|\kappa_i\rangle \tag{3.38}$$

Using Eq. 3.35-3.38, the exact ground state energy E[n($\vec{r}$)] of our real, interacting system can be expressed as

$$E[n(\vec{r})] = T_S[n(\vec{r})] + J[n(\vec{r})] + E_{XC}[n(\vec{r})] + U_{en}[n(\vec{r})]$$

$$E[n(\vec{r})] = -\sum_{i}\frac{1}{2}\langle\kappa_i|\nabla^2_{\vec{r}_i}|\kappa_i\rangle + \frac{1}{2}\sum_{i}^{N}\sum_{j}^{N}\iint \frac{|\kappa_i(\vec{r})|^2|\kappa_j(\vec{r}')|^2}{|\vec{r}-\vec{r}'|}d\vec{r}d\vec{r}' \tag{3.39}$$

$$+E_{XC}[n(\vec{r})] - \sum_i \sum_j \frac{Z_i}{|\vec{R}_i - \vec{r}_j|} |\kappa_i(\vec{r})|^2$$

All energies can be expressed explicitly in terms Kohn-Sham orbital κ except for E_{XC}. Minimizing $E[n(\vec{r})]$ by getting its functional derivative with respect to κ (Par and Yang 2015) gives the Kohn-Sham Equation

$$\left[-\sum_i \frac{1}{2} \nabla_{\vec{r}_i}^2 + \hat{V}_{eff}(\vec{r}) \right] \kappa_i(\vec{r}) = \varepsilon_i \kappa_i(\vec{r}) \tag{3.40}$$

where

$$\hat{V}_{eff}(\vec{r}) = \int \frac{n(\vec{r})}{|\vec{r} - \vec{r}'|} d\vec{r} + V_{XC}(\vec{r}) - \sum_i \sum_j \frac{Z_i}{|\vec{R}_i - \vec{r}_j|} \tag{3.41}$$

$$V_{XC}(\vec{r}) \equiv \frac{\partial E_{XC}[n(\vec{r})]}{\partial n(\vec{r})} \tag{3.42}$$

The ε_i in Eq. 3.40 are Lagrange multipliers for the constraint

$$\int \kappa_i^*(\vec{r}) \kappa_j(\vec{r}) d\vec{r} = \delta_{ij} \tag{3.43}$$

and the total energy in terms of ε_i is given by

$$E = \sum_i \varepsilon_i - \frac{1}{2}\iint \frac{n(\vec{r})n(\vec{r}')}{|\vec{r}-\vec{r}'|} d\vec{r}d\vec{r}' - \int V_{XC}(\vec{r})n(\vec{r})d\vec{r} \tag{3.44}$$

Here

$$\sum_i \varepsilon_i = \sum_i \left\langle \kappa_i \middle| -\sum_i \frac{1}{2}\nabla_{\vec{r}_i}^2 + \hat{V}_{eff}(\vec{r}) \middle| \kappa_i \right\rangle \tag{3.45}$$

Like Hartree-Fock approach, Kohn-Sham equations can be solved iteratively. Complete description of $\hat{V}_{eff}(\vec{r})$ requires knowledge of electron density $n(\vec{r})$. If we know $\hat{V}_{eff}(\vec{r})$ we can solve Eq. 3.32 for Kohn-Sham orbitals κ_i, which we can then use with Eq. 3.34 to determine the ground state electron density of the system. Since ground state electron density is a unique functional of the ground state wavefunction, we can determine the ground state energy using Eq. 3.39 or 3.44, and in principle any information about the system.

3.5. Exchange Correlation Functional

The formalism that Kohn and Sham introduced can be used to determine the exact ground state energy of multi-electron systems, provided that the exchange correlation functional $E_{XC}[n(\vec{r})]$ is known. However, except for overly simplified systems, explicit form of $E_{XC}[n(\vec{r})]$ cannot be solved. Thus, the central goal of density functional theory research is to develop more accurate approximations of this quantity. In this section, some of the most commonly applied exchange correlation functional in solid state physics will be discussed.

The model system in which virtually all approximate exchange correlation functionals are based assumes a uniform electron gas. This functional, known as the Local Density Approximation (LDA) assumes that the exchange correlation functional E_{XC}^{LDA} depends only on the density and the coordinate where the functional is evaluated

$$E_{XC}^{LDA}[\, n(\vec{r})] = \int n(\vec{r})\varepsilon_{XC}[n(\vec{r})]\, d\vec{r} \tag{3.46}$$

$$\varepsilon_{XC} = \varepsilon_X + \varepsilon_C \tag{3.47}$$

where ε_{XC} is the sum of exchange energy ε_X and correlation energy ε_C per particle. Bloch and Dirac shown that ε_X for uniform electron gas system takes the form (Dirac, 1930)

$$\varepsilon_X = -\frac{3}{4}\sqrt[3]{\frac{3n(\vec{r})}{\pi}} \tag{3.48}$$

No explicit expression for ε_C is known. However, highly accurate approximations do exist as a result of numerical quantum Monte-Carlo simulations of homogeneous electron gas (Ceperley and Alder, 1980).

An extension of LDA assumes unrestricted case, such that instead of electron density, the central input would be two spin densities $n_\alpha(\vec{r})$ and $n_\beta(\vec{r})$. This method is called Local Spin Density Approximation (LSD) and because of the flexibility of having two variables, LSD generally provided more accurate results than LDA (Barth and Hedin, 1972). The expression for exchange correlation energy is

$$E_{XC}^{LSD}\left[\, n_\alpha(\vec{r}),\, n_\beta(\vec{r})\right] = \int n(\vec{r})\varepsilon_{XC}\left[\, n_\alpha(\vec{r}),\, n_\beta(\vec{r})\right] d\vec{r} \tag{3.49}$$

LSD approximation can be used to deal with spin polarized cases, where the relative spin polarization ξ is determined using the equation

$$\xi = \frac{n_\alpha(\vec{r}) - n_\beta(\vec{r})}{n(\vec{r})} \tag{3.50}$$

Another extension considers the non-uniformity of real electron density. This is accomplished by treating LDA as the first term in Taylor expansion for uniform density and assuming to obtain better approximation by considering the second term of the series, which contains the gradient of electron density. Because of this, the method is called Gradient Expansion Approximation (GEA).

$$\begin{aligned} E_{XC}^{GEA}\left[\, n_\alpha(\vec{r}),\, n_\beta(\vec{r})\right] &= \int n(\vec{r})\varepsilon_{XC}\left[n_\alpha(\vec{r}),\, n_\beta(\vec{r})\right] d\vec{r} \\ &+ \sum_{\sigma\sigma'} \int C_{XC}^{\sigma\sigma'}\left[\, n_\alpha(\vec{r}),\, n_\beta(\vec{r})\right] \frac{\nabla n_\sigma(\vec{r})}{n_\sigma(\vec{r})^{2/3}} \frac{\nabla n_{\sigma'}(\vec{r})}{n_{\sigma'}(\vec{r})^{2/3}} d\vec{r} + \cdots \end{aligned} \tag{3.51}$$

where σ and σ′ indicate α or β spin. Corrections to the GEA is necessary for it to describe physical system with an accuracy beyond than that of LSD. Such modifications include

enforcing restrictions to the exchange correlation holes. The resulting functional is called Generalized Gradient Approximation (GGA). Several functionals related to this approach were developed, and all of them can be expressed in the form

$$E_{XC}^{GGA}\left[\, n_\alpha(\vec{r}),\, n_\beta(\vec{r})\right] = \int f\left[\, n_\alpha(\vec{r}),\, n_\beta(\vec{r}), |\nabla n_\alpha(\vec{r})|, \left|\nabla n_\beta(\vec{r})\right|\right] d\vec{r} \tag{3.52}$$

In comparison with LSD, GGA tend to improve total energies (Perdew et al., 1992), atomization energies (Becke, 1992; Perdew et al., 1992; Proynov et al., 1995), energy barriers, and structural energy differences (Hammer and Scheffler, 1995; Hamann, 1996; Zupan et al., 1997).

The exchange correlation energy for GGA is usually split into its exchange and correlation contribution

$$E_{XC}^{GGA}\left[\, n_\alpha(\vec{r}),\, n_\beta(\vec{r})\right] = E_X^{GGA}\left[\, n_\alpha(\vec{r}),\, n_\beta(\vec{r})\right] + E_C^{GGA}\left[\, n_\alpha(\vec{r}),\, n_\beta(\vec{r})\right] \tag{3.53}$$

One of the most popular GGA exchange correlation functional is the functional developed by Perdew, Burke, and Ernzerhof (PBE), in which all parameters are fundamental physical constants (Perdew et al., 1996). The correlation contribution is in the form

$$E_C^{GGA}\left[\, n_\alpha(\vec{r}),\, n_\beta(\vec{r})\right] = \int n\left[\varepsilon_c^{unif}(r_s, \xi\,) + H(r_s, \xi\,, t)\right] d^3r \tag{3.54}$$

where ε_c^{unif} is the correlation energy of uniform electron gas, r_s is the local Seitz radius, ξ is the relative spin polarization, and t is the dimensionless density gradient given by

$$t = \frac{|\nabla n|}{2\phi k_s n} \tag{3.55}$$

Here, ϕ is a spin-scaling factor

$$\phi(\xi) = \frac{\left[(1+\xi)^{2/3} + (1-\xi)^{2/3}\right]}{2} \tag{3.56}$$

and k_s is the Thomas-Fermi screening wave number

$$k_s = \sqrt{\frac{4k_F}{\pi a_0}} \tag{3.57}$$

where k_F and a_0 are the Fermi wave number and Bohr radius, respectively. The gradient contribution H is given by

$$H = \left(\frac{e^2}{a_0}\right)\gamma\phi^3 \times ln\left[1 + \frac{\beta}{\gamma}t^2\left(\frac{1+At^2}{1+At^2+A^2t^4}\right)\right] \tag{3.58}$$

and here

$$A = \frac{\beta}{\gamma}\left(e^{-\frac{\varepsilon_c^{unif} a_0}{\gamma \phi^3 e^2}} - 1 \right) \tag{3.59}$$

where β and γ are constants having values of 0.066725 and 0.031091, respectively. On the other hand, the exchange contribution is in the form

$$E_X^{GGA} = \int n\, \varepsilon_X^{unif}(n) F_X(s) d^3r \tag{3.60}$$

The gradient contribution F_X is given by

$$F_X(s) = 1 + k - \frac{k}{1 + \frac{\mu}{k} s^2} \tag{3.61}$$

where k and μ are constants having values of 0.804 and 0.21951, respectively, and s is given by

$$s = \left(\frac{r_s}{a_0}\right)^{1/2} \frac{\phi t}{c} \tag{3.62}$$

in which c is another constant equal to 1.2277.

3.6. Iterative Solution to Kohn-Sham Equations

Kohn-Sham equations are solved iteratively using the self-consistent field method. The steps are outlined below and illustrated on Figure 3.1.

1. Choose an initial set of expansion coefficients C_{in} for Kohn-Sham orbitals.
2. Use Eq. 63 to construct an initial set of Kohn Sham orbitals κ_i.
3. Calculate the density $n(\vec{r})$ using Eq. 3.34.
4. Determine the V_{XC} and $\hat{V}_{eff}$ that corresponds to the calculated $n(\vec{r})$ using Eq. 3.41 and 3.42.
5. Construct H_{mn} using Eq. 3.65.
6. Use Eq. 3.64 to solve for new set of C_{in}.
7. Repeat steps 2 and 3.
8. If the new density equals the previous, calculate the total energy using Eq. 3.39 or 3.44. Else, proceed to step 4.

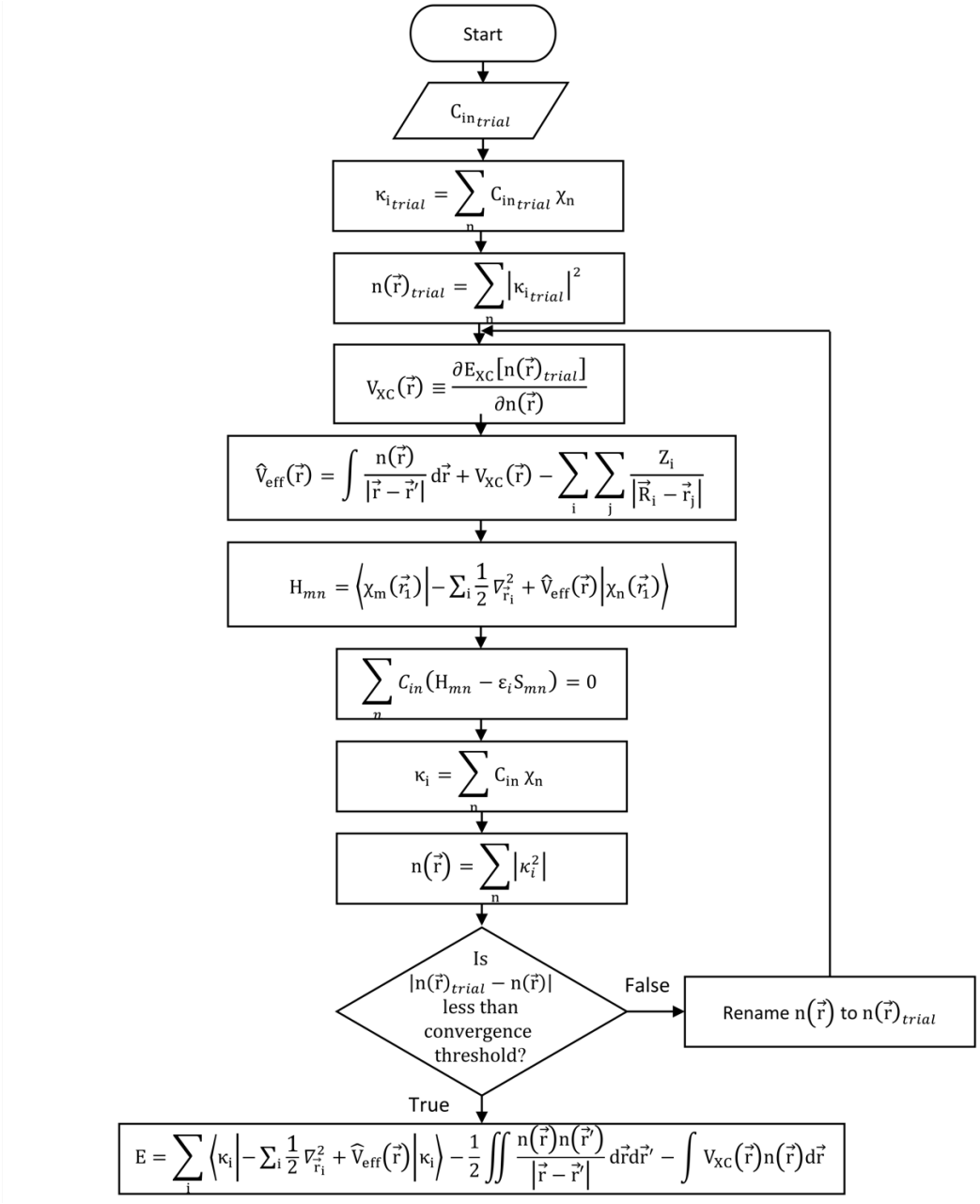

Figure 3.1. DFT calculation of total energy using self-consistent field method

3.7. Plane-wave Basis Function

In actual calculations of Eq. 3.32, it is convenient to expand the Kohn-Sham orbitals in terms of plane-wave basis functions $\Psi_{n,k}(\vec{r})$

$$\Psi_{n,k}(\vec{r}) = \sum_{\vec{G}} c_{n,\vec{k}+\vec{G}}(\vec{r}) \frac{1}{\sqrt{\Omega}} \exp\left[i\left(\vec{k}+\vec{G}\right)\cdot\vec{r}\right] \tag{3.63}$$

where n is the band index, Ω is the unit cell volume, $\vec{G}$ is the reciprocal lattice vector, and $c_{n,\vec{k}+\vec{G}}(\vec{r})$ is the Fourier transform of $\Psi_{n,k}(\vec{r})$

$$c_{n,\vec{k}+\vec{G}}(\vec{r}) = \frac{1}{\sqrt{\Omega}} \int_{\Omega}^{\infty} \exp\left[-i\left(\vec{k}+\vec{G}\right)\cdot\vec{r}\right] \Psi_{n,k}(\vec{r}) d^3\vec{r} \tag{3.64}$$

In principle, the required number of reciprocal points $\vec{G}$ is infinite. But in practice, a cutoff wave number $\vec{G}_{max}$ is used, which satisfies

$$\left|\vec{k}+\vec{G}\right| \leq \left|\vec{G}_{max}\right| \tag{3.65}$$

Using plane-wave basis functions, Kohn-Sham equations can be expressed in form of matrices

$$\boldsymbol{Hc} = \boldsymbol{\varepsilon c} \tag{3.66}$$

$$\sum_{\vec{G}} \left[\frac{1}{2}\left|\vec{k}+\vec{G}\right|^2 + \widehat{\mathrm{V}}_{\mathrm{eff}}\left(\vec{G}-\vec{G}'\right)\right] c_n\left(\vec{k}+\vec{G}'\right) = \varepsilon_{n,k} c_n\left(\vec{k}+\vec{G}\right) \tag{3.67}$$

where the terms in the sum are the kinetic energy and effective potential, respectively.

3.8. Pseudopotential Approach

The electronic states of an atom can be classified into core states, which are highly localized and are not involved in chemical bonding, and valence states, which are extended and responsible for chemical bonding. The core and valence states are separated by some cutoff radius r_c. The pseudopotential approach implements the frozen core approximation, which restricts the relaxation of core states. Core electrons are replaced with simplified analytic or numerical form which can be calculated in advance. The interaction of the valence electrons with the nucleus and core states is replaced by an effective, screened potential. The full ionic core-electron interaction is replaced by softer pseudopotential which is constructed in such as way that its scattering properties are the same as those of the all-electron potential.

The main requirement of the pseudopotential approach is that it reproduces the valence charge density associated with chemical bonds. It has been shown (Hamann et al., 1979) that for pseudo Ψ_{PP} and all-electron Ψ_{AE} wavefunctions to be identical beyond the core radius, it is necessary for the integrals of squared amplitudes of the two functions be the same.

$$\int_0^{r_c} |\Psi_{PP}(\vec{r})|^2 d\vec{r} = \int_0^{r_c} |\Psi_{AE}(\vec{r})|^2 d\vec{r} \tag{3.68}$$

This is equivalent to requiring norm-conservation from pseudo wavefunctions, i.e. that each of them should carry exactly one electron. This condition ensures that the scattering properties of the pseudopotential are reproduced correctly. Accurate DFT calculations of solid-state properties using plane-wave basis and norm-conserving pseudopotentials have been demonstrated. However, norm-conserving condition proves difficult to produce practical pseudopotentials for systems containing highly-localized valence orbitals, such as p states in first-row elements and d states in second row transition metals, e.g. O 2p or Cu 3d. The wavefunctions of these states have large amplitudes close to nuclei which requires larger number of basis functions which increases the computational cost. An alternative approach is to remove the norm-conserving condition and replace with generalized norm-conserving condition (Vanderbilt, 1990)

$$Q_{i,j} = \langle \Psi_{AE}^i | \Psi_{AE}^j \rangle_{r_c} - \langle \Psi_{PP}^i | S | \Psi_{PP}^j \rangle \tag{3.69}$$

$$\langle \Psi_{AE}^i | \Psi_{AE}^j \rangle_{r_c} = \langle \Psi_{PP}^i | S | \Psi_{PP}^j \rangle \tag{3.70}$$

$$S = 1 + \sum_{i,j} Q_{i,j} \, |\beta_i\rangle\langle\beta_j| \tag{3.71}$$

where S is a non-local overlap operator and $|\beta_i\rangle$ is a set of local wavefunctions which satisfies

$$\langle \Psi_{PP}^{i} | \beta_j \rangle = \delta_{i,j} \tag{3.72}$$

By removing the norm-conserving condition, the charge associated with the large amplitude can be removed which lead to "soft" pseudo wavefunctions in core region. Pseudopotentials of this type are called Ultra-soft Pseudopotentials (USPP). To recover the full electronic charge, the electron density given by the square moduli of wavefunctions is augmented in the core regions.

$$n(\vec{r}) = \sum_{n} |\Psi_r(\vec{r})|^2 + \sum_{l} \sum_{i,j} \rho_{i,j}^{l} Q_{i,j}^{l}(\vec{r}) \tag{3.73}$$

where $\rho_{i,j}^{l}$ are the occupied states and $Q_{i,j}^{l}(\vec{r})$ are the augmentation functions.

3.9. Semiempirical van der Waals Correction

Van der Waals interactions are nonlocal, long-range electron correlation effect. It has a significant role in many chemical systems, such as structures of DNA and proteins, packing of crystals, formation of aggregates, supramolecular systems, and orientation of molecules on surfaces. While gradient-corrected DFT includes electron correlation effects, it was not able to properly describe dispersive interactions. Inclusion of van der Waals interactions within Kohn-Sham DFT formalism has been made, but these non-empirical corrections lead to a large increase in computational cost. An alternative way is to restrict the use of DFT energy in short-range electron correlations and replace the medium and larger range interactions by an empirical damped atom-pairwise dispersion correction in the form of $C_6 R^{-6}$, where R is the

interatomic distance and C is the dispersion coefficient (Grimme, 2004, 2006). The corrected dispersion part of the total energy E_{DFT-D} has the form

$$E_{DFT-D} = E_{DFT} + E_{disp} \tag{3.74}$$

where E_{DFT} is the energy obtained from standard DFT calculations and E_{disp} is the empirical dispersion correction given by

$$E_{disp} = -s_6 \sum_{i=1}^{N_{at}-1} \sum_{j=i+1}^{N_{at}} \frac{C_6^{ij}}{R_{ij}^6} f_{dmp}(R_{ij}) \tag{3.75}$$

Here, s_6 is a global scaling factor, N_{at} is the number of atoms in the system, and C_6^{ij} and R_{ij} are the dispersion coefficient and interatomic distance for atom pair ij, respectively. A damping function is used to avoid singularities for small R

$$f_{dmp}(R_{ij}) = \frac{1}{1 + e^{-d(R_j/R_r - 1)}} \tag{3.76}$$

where R_r is the sum of atomic van der Waals radii.

3.10. Transition State Search Using Nudged Elastic Band Method

The identification of a minimum energy path (MEP) for a chemical process from one stable configuration to another is a common and important problem in chemistry and condensed matter physics. The transition state (TS) of a chemical process is on the saddle point of the potential energy maximum along MEP which determines the activation energy barrier of the process. One of the ways to calculate the MEP is through the chain-of-states method which uses a set of atomic coordinates known as images as an initial estimate for MEP. The images are then assumed to be connected with springs of zero natural length. This requires that the images along the MEP should use the lowest amount of energy to define a path between two minima and that the images should be evenly spaced along the path. This is implemented through the minimization of the objective function $M(\vec{r}_1, \vec{r}_2, \dots, \vec{r}_P)$

$$M(\vec{r}_1, \vec{r}_2, \dots, \vec{r}_P) = \sum_{i=1}^{P-1} E(\vec{r}_i) + \sum_{i=1}^{P} \frac{K}{2} (\vec{r}_i - \vec{r}_{i-1})^2 \tag{3.77}$$

where $\vec{r}_1, \vec{r}_2, \dots, \vec{r}_P$ are the set of images, $E(\vec{r}_i)$ is the total energy of the ith image, and K is a constant that defines the stiffness of the harmonic springs or the elastic bands. For plane-wave DFT calculations, the most widely used method for the minimization of the objective function is the nudged elastic band (NEB) method (Jonsson et al., 1998). In NEB method, the minimization involves the calculation of the perpendicular component of the true force $\vec{F}_i = -\nabla V(\vec{r}_i)$ and component of the spring force $\vec{F}_{i,spring}$ parallel to the MEP on an image i.

$$\vec{F}_i^{\perp} = -\nabla V(\vec{r}_i)_{\perp} = -[\nabla V(\vec{r}_i) - \nabla V(\vec{r}_i) \cdot \hat{\tau}_{\parallel}\hat{\tau}_{\parallel}] \tag{3.78}$$

$$\vec{F}_{i,spring}^{\parallel} = \vec{F}_{i,spring} \cdot \hat{\tau}_{\parallel}\hat{\tau}_{\parallel} \tag{3.79}$$

where $\hat{\tau}_{\parallel}$ is the unit tangent to the MEP path. The total force on the image is given by the sum of these forces

$$\vec{F}_i^0 = \vec{F}_i^{\perp} + \vec{F}_{i,spring}^{\parallel} \tag{3.80}$$

The MEP condition will be satisfied when $\vec{F}_i^{\perp} = 0$, while the $\vec{F}_{i,spring}^{\parallel}$ assures that the images are evenly spread out along the path. For situations where the energy of the system changes rapidly along the path, but the restoring force on the images perpendicular to the path is weak, the paths can get kinky which leads to slow convergence. An effective remedy is to introduce a switching function $f(\phi_i)$ which goes from 0 for a straight path to 1 if adjacent segments of the path form a right angle. The position of each image is updated based on the NEB force $\vec{F}_i^{NEB}$

$$\vec{F}_i^{NEB} = \vec{F}_i^0 + f(\phi_i)\left(\vec{F}_{i,spring} - \vec{F}_{i,spring} \cdot \hat{\tau}_{\parallel}\hat{\tau}_{\parallel}\right) \tag{3.81}$$

After few iterations, the image with the highest energy i_{max} is identified, which is not affected by the spring force. The force on this image is given by

$$\vec{F}_{i_{max}} = -\nabla V\left(\vec{r}_{i_{max}}\right) + 2\nabla V\left(\vec{r}_{i_{max}}\right) \cdot \hat{\tau}_{\parallel}\hat{\tau}_{\parallel} \tag{3.82}$$

Replacing the force on one image with Eq. 3.82 will turn it into a climbing image which moves up the potential energy surface along the elastic band and down the potential surface perpendicular to the band. This modification to the standard NEB is called Climbing Image NEB (Henkelman et al., 2000).

3.11. Molecular Dynamics

Molecular dynamics is an atomic-level simulation of molecules and materials. It assumes Born-Oppenheimer approximation in which the motion of the nuclei and electrons can be treated separately (Section 3.1). Under this assumption, as the nuclei of atom i accelerates due to the potential energy, the position of the electrons of atom i relative to this nuclei will be fixed. The forces **F** on the atomic nuclei i are calculated from the potential energy U

$$\mathbf{F} = -\nabla U \tag{3.83}$$

and the position $\boldsymbol{r}$ an atomic nuclei i after some timestep dt is calculated from Newton's Second law of motion using Verlet algorithm

$$\mathbf{F} = m\boldsymbol{a} = m\frac{d^2\boldsymbol{r}}{dt^2} = -\frac{dU}{d\boldsymbol{r}} \tag{3.84}$$

$$\boldsymbol{r}(t + \Delta t) = 2\boldsymbol{r}(t) - \boldsymbol{r}(t + \Delta t) + \boldsymbol{a}(t)\Delta t^2 \tag{3.85}$$

There are three types of molecular dynamics simulations based on how the potential energy between atoms is constructed or calculated. These are (1) classical, (2) ab-initio, and (3) machine learning.

3.11.1. Classical Molecular Dynamics

In classical molecular dynamics, a function of predefined form is used to calculate the interatomic potential which is a function of relative atomic positions (Lee, 2016). One of the simplest potential is the Lennard-Jones potential U_{LJ}

$$U_{LJ}(\boldsymbol{r}) = 4\varepsilon\left[\left(\frac{\sigma}{r}\right)^{12} - \left(\frac{\sigma}{r}\right)^{6}\right] \tag{3.86}$$

where ε and σ are parameters that determine the lowest energy of the potential energy curve and the interatomic distance at which the potential energy between two atoms is zero.

Another type of interatomic potential is based on embedded atom method (EAM) which is especially suited for metals where the electrons are delocalized. This potential considers the effective electron density as the sum of pair potentials $U_{ij}(r_{ij})$ and embedded atom energy

$$U_{EAM}(\boldsymbol{r}) = \sum_{i<j} U_{ij}(r_{ij}) + \sum_{i} F_i(\rho_i) \tag{3.87}$$

where $F_i(\rho_i)$ is the embedding energy function.

For covalent solids, the Tersoff potential which considers the bond order between two atoms is more suitable (Tersoff, 1988). The Tersoff potential has the form

$$U_{Tersoff}(\boldsymbol{r}) = \frac{1}{2}\sum_{i\neq j} U_R(r_{ij}) + \frac{1}{2}\sum_{i} B_{ij} U_A(\rho_i) \tag{3.88}$$

where U_R and U_A are repulsive and attractive potentials, and B_{ij} is the bond order which is a function that decreases with the number of nearest neighbor or coordination N_{coor}

$$B_{ij} \propto \frac{1}{\sqrt{N_{coor}}} \tag{3.89}$$

Traditional classical interatomic potentials are unable to simulate chemical reactions because they require all bonds to be defined explicitly. Hence, the bond breaking and bond forming cannot be described. This issue is addressed with the development of ReaxFF force field. In this method, the total energy E_{system} is defined as the sum of bond energy E_{bond},

energies associated with three-body angle strain E_{angle} and four-body torsion angle strain E_{tors}, and electrostatic $E_{Coulomb}$ and dispersive $E_{vdWaals}$ forces.

$$E_{system} = E_{bond} + E_{over} + E_{angle} + E_{tors} + E_{vdWaals} + E_{Coulomb} + E_{specific} \quad (3.90)$$

The E_{over} is the energy penalty for over coordination. The central feature of ReaxFF is on the definition of bond order energy $E_{bond_{ij}}$.

$$E_{bond_{ij}} = BO_{ij}^{\sigma} + BO_{ij}^{\pi} + BO_{ij}^{\pi\pi} \quad (3.91)$$

which is the sum of bond energies with σ, π, and $\pi\pi$ bond character The bond-order energy formula is continuous and contains no discontinuities through the transition between the bond characters. Additionally, it accommodates long-distance covalent interactions characteristic in transition state structures. This allows the force-field to simulate chemical reactions and accurately predict reaction barriers.

3.11.2. Ab-initio Molecular Dynamics

Ab-initio molecular dynamics (AIMD) using DFT uses the potential energy surface obtained by solving the Kohn-Sham equation at each timestep. This is typically performed under Born-Oppenheimer approximation (Chapter 3.1) where the nuclear and electronic wavefunctions are treated separately. Typically, AIMD is performed at zero electronic temperature approximation which works well for semiconducting and insulating systems like diamond (Correa et al., 2006). The electrons can be simulated at finite temperature using Mermin's formulation of DFT where the electron density takes the form of temperature-dependent Fermi-Dirac equation (Mermin, 1965). An alternative to Born-Oppenheimer approximation is the Car-Parrinello approximation (Car and Parrinello, 1985). Using this method, the electronic Kohn-Sham equations are only solved for the initial nuclear configuration which is then used in the Lagrangian which when solved generates the nuclear velocities and the corresponding electronic ground state.

The advantage of AIMD over the classical MD is that the dynamics for systems where the forces have not been parametrized can be calculated. In addition, the bond-breaking and forming can be simulated accurately. The main disadvantage is the much higher computational cost. For this reason, the AIMD simulation is typically limited to a few hundred atoms over simulation time of a few picoseconds.

3.11.3. Machine Learning Molecular Dynamics

A machine learning interatomic potential (MLIP) is an analytic expression of the potential energy surface providing the potential energy and its derivatives as a function of atomic positions. MLMPs are constructed by training a machine learning algorithm to map the chemical environment to the forces and energies which are typically calculated using ab-initio methods such as density functional theory (DFT). Molecular dynamics simulations that use MLIP are called machine learning molecular dynamics (MLMD). MLMDs have been used to perform materials simulations with comparable accuracy with the ab-initio methods at a small fraction of computational cost. Several machine learning algorithms have been proven successful in constructing MLIPs. This includes neural networks (Behler, 2021), graph neural networks (Batzner et al., 2022), and Gaussian approximation potentials (Bartók and Csányi, 2015; Deringer et al., 2021).

3.12. Machine Learning Molecular Dynamics Based on Neural Network Model

3.12.1. Artificial Neural Network

Machine learning is a field of study concerned with developing systems and algorithms with the ability to acquire knowledge through automated extraction of patterns from raw data (Goodfellow et al., 2016). To perform machine learning, important data representations or features are first determined and extracted from the raw data. The algorithm is then used to discover the mapping from the data representation to the output or target value. Then, the

trained algorithm can be used to generalize the pattern to unseen data and perform tasks without explicit instructions. For many tasks, it is difficult to know which data representation is important for the prediction of the target value. A more advanced machine learning approach is the representation learning which automatically extracts meaningful patterns from raw data.

An artificial neural network ANN is a machine learning model inspired by the structure and function of the neurons in a brain. ANN consists of nodes connected by edges. Each node receives signals from connected nodes, then processes them and sends a signal to other connected nodes. The "signal" is a real number, and the output of each node is added and transformed using a non-linear function. The strength of the signal at each connection is determined by a weight, which adjusts during the learning process. Typically, neurons are aggregated into layers. Signals travel from the first layer (the input layer) to the last layer (the output layer), possibly passing through multiple intermediate layers (hidden layer). Deep learning is a class of ANN that has several hidden layers.

The linear model for classification and regression is based on a linear combination of fixed nonlinear basis functions $\phi_j(\mathbf{x})$ and take the form (Bishop)

$$y(\mathbf{x}, \mathbf{w}) = f\left(\sum_{j=i}^{M} w_j \phi_j(\mathbf{x})\right) \tag{3.92}$$

where y is the target value which is a function of the input $\mathbf{x}$ and the weights $\mathbf{w}$. The function $f(\cdot)$ is a nonlinear activation function or identity when the task is classification or regression, respectively.

The basic neural network model can be described by the function

$$a_j = \sum_{i=1}^{D} w_{ji}^{(1)} x_i + w_{j0}^{(1)} \tag{3.93}$$

where $x_i, \ldots, x_D$ are the input variables, $w_{ji}^{(1)}$ and $w_{j0}^{(1)}$ are the weights and biases on the neural network layer number (1). The quantity a_j is called the activation which is transformed using a differentiable nonlinear activation function $h(\cdot)$ to give

$$z_j = h(a_j) \tag{3.94}$$

The quantity z_j correspond to the output of the basis function $\phi_j(\mathbf{x})$, which will be the input for the neural network layer number (2)

$$a_k = \sum_{i=1}^{D} w_{ki}^{(2)} z_j + w_{k0}^{(2)} \tag{3.95}$$

where $k = 1, .., K$ and K is the total number of outputs.

Finally, the output unit activations are transformed using an appropriate activation function to give a set of network outputs y_k. The process of evaluating the outputs from the

inputs using the weights and biases on the hidden layers is called forward propagation. The network diagram for a two-layer neural network is shown in Fig. 3.2.

The neural network is trained by finding the weight vector $\mathbf{w}$ that minimizes the error function $E(\mathbf{w})$

$$E(\mathbf{w}) = \frac{1}{2}\sum_{n-1}^{N} \|y(\mathbf{x_n}, \mathbf{w}) - \mathbf{t}_n\| \tag{3.96}$$

$$\nabla E(\mathbf{w}) = 0 \tag{3.97}$$

where $y(\mathbf{x_n}, \mathbf{w})$ is the output of the neural network and $\mathbf{t}_n$ is the target value. The gradient of the error function is calculated using the back propagation algorithm. For each output unit, the error δ is calculated

$$\delta_k = y_k - t_k \tag{3.98}$$

For the hidden units,

$$\delta_j = \frac{\partial E_n}{\partial a_j} = \sum_{n-1}^{N} \frac{\partial E_n}{\partial a_k}\frac{\partial a_k}{\partial a_j} \tag{3.99}$$

Finaly, the gradient of error is calculated using the equation

$$\frac{\partial E_n}{\partial w_{ji}} = \frac{\partial E_n}{\partial a_j}\frac{\partial a_j}{\partial w_{ji}} \tag{3.100}$$

$$\frac{\partial E_n}{\partial w_{ji}} = \delta_j z_i \tag{3.101}$$

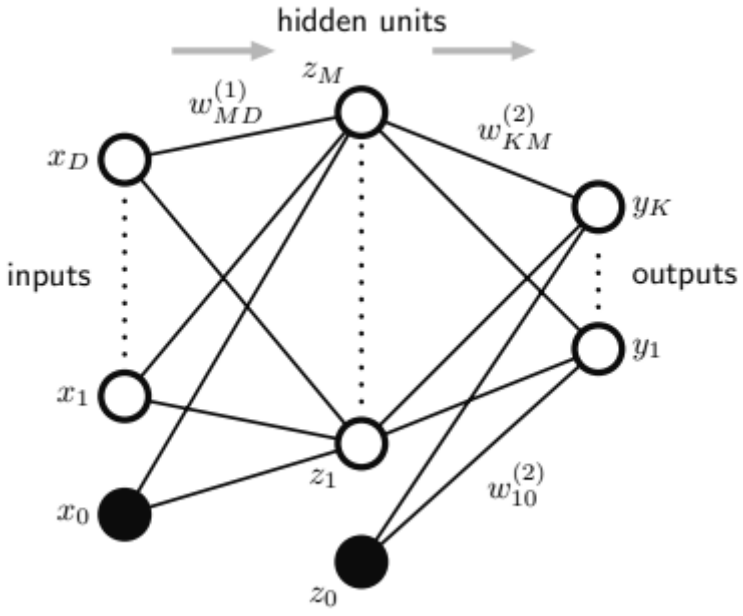

Fig. 3.2. Two-layer neural network. The arrows denote the direction of information flow through the network during the forward propagation (Bishop, 2006).

3.12.2. Neural Network Interatomic Potentials

3.12.2.1. High-Dimensional Neural Network

Behler and Parinello proposed a model where the total energy is equal to the sum of atomic energy contributions (Behler and Parrinello, 2007)

$$E = \sum_{i=1}^{N_{elem}} \sum_{j=1}^{N_{atom}^{i}} E_j^i \tag{3.102}$$

where N_{elem} is the number of the elements present in the system and N_{atom}^{i} is the number of atoms of the respective element. In their model, known as high-dimensional neural network potential (HDNNP), each atom will have a corresponding atomic neural network which will be trained to predict the atomic energy (Fig. 3.3)

The input of the HDNNP is a set of data representation or features that describes the local atomic environment. Among the most popular descriptors are the atom-centered symmetry functions G_i^{rad} and G_i^{ang} which can describe the 2-body (radial) and 3-body (angular) interactions, respectively.

$$G_i^{rad} = \sum_{j \neq i}^{N_{atom} \in R_c} e^{-\eta (R_{ij} - R_s)^2} f_c(R_{ij}) \tag{3.103}$$

$$G_i^{rad} = 2^{1-\zeta} \sum_{j \neq i}^{N_{atom} \in R_c} \sum_{k \neq i,k}^{N_{atom} \in R_c} (1 \pm \cos \theta_{ijk})^{\zeta} e^{-\eta (R_{ij} - R_{jk})^2} f_c(R_{ij}) f_c(R_{ik}) \tag{3.104}$$

where the function f_c is the polynomial cutoff function which ensures that the descriptor terminates smoothly to zero outside the predefined cutoff radius. These symmetry functions contain the hyperparameters ζ and η which has to be manually fine-tuned.

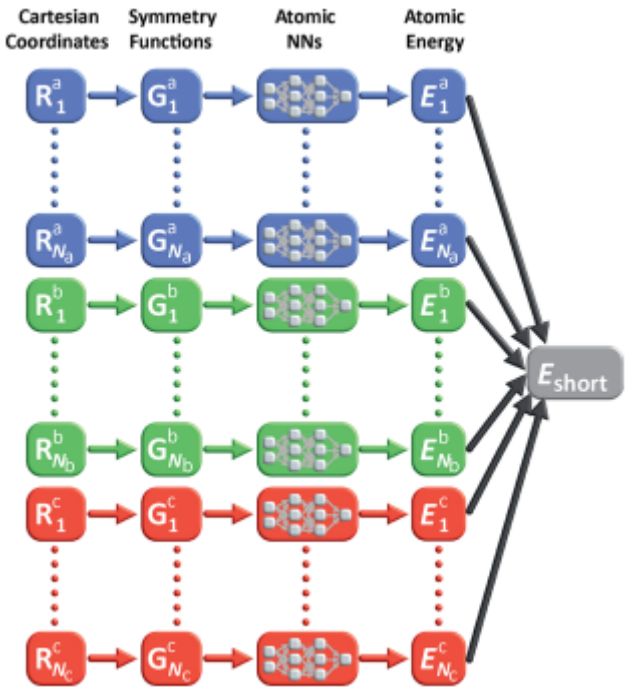

Fig. 3.3. Behler-Parrinello high dimensional neural network potential (Behler, 2021)

3.12.2.2. Graph Neural Network

One of the limiting factors of MLIP based on neural networks is the difficulty of engineering hand-crafted descriptors. Graph neural network interatomic potentials (GNN-IP) eliminates this need by incorporating a graph representation learning based on message passing scheme.

Graphs are general language for describing and analyzing entities with relations or interactions. A graph $\mathcal{G}$ is defined by a set of nodes (vertices, $\mathcal{V}$) and a set of links (edges, $\mathscr{E}$) between these nodes

$$\mathcal{G} = (\mathcal{V}, \mathcal{E}) \tag{3.105}$$

Graph neural networks are deep learning models that use graphs as input data.

Neural message passing is the defining feature of graph neural networks (Gilmer). In neural message passing, vector messages are exchanged between nodes and updated using neural networks. In GNN-IP, atomic structures are represented by collections of nodes and edges, where nodes in the graph correspond to individual atoms and edges are typically defined by simply connecting every atom to all other atoms that are closer than some cutoff distance. Every node/atom i is associated with a feature $\boldsymbol{h}_i$, which is iteratively refined via a series of convolutions over neighboring atoms j based on both the distance to neighboring atoms rij and their features $\boldsymbol{h}_i$. To calculate the features, first the hidden embedding $\mathbf{h}_u^{(0)}$ for all the nodes $\mathcal{V}$ is initialized.

$$\boldsymbol{h}_u^{(0)} = \boldsymbol{x}_u \, , \, \forall \, u \in \mathcal{V} \tag{3.106}$$

Next, the information or messages on the neighbors v are aggregated

$$\text{AGGREGATE}^{(k)} \left(\left\{ \mathbf{h}_v^{(k)}, \, \forall \, v \in \mathcal{N}(u) \right\} \right) \tag{3.107}$$

Finally, the hidden embedding is updated based on the messages that it receives.

$$\boldsymbol{h}_u^{(k+1)} = UPDATE^{(k)} \left(\text{AGGREGATE}^{(k)} \right) \tag{3.108}$$

This iterative process allows information to be propagated along the atomic graph through a series of convolutional layers (Gilmer et al., 2017).

Physical systems have properties that remain invariant under translation, reflection, and rotation of a set of atoms. The neural networks which ensure that all tensor operations, even in the internal features, retain the physical transformation properties are called equivariant neural networks. To achieve rotation equivariance, the aggregate function has to be in the form of the product of some radial function R and spherical harmonics $Y_m^{(l)}$.

$$\text{AGGREGATE}\left(\vec{r}_{ij} \right) = R\left(\vec{r}_{ij} \right) Y_m^{(l)} \left(\hat{r}_{ij} \right) \tag{3.109}$$

The Neural Equivariant Interatomic Potential (NequIP) implements the equivariant graph neural network scheme for learning interatomic potentials from ab-initio calculations for molecular dynamics simulation (Batzner et al., 2022). In NeqIP, the whole aggregate function takes the form

$$\mathcal{L}_{u,x,m_0}^{l_0,p_0,l_f,p_f,l_i,p_i}\left(\vec{r}_u, V_{u,x,m_i}^{l_i,p_i}\right) = \sum_{m_f,\, m_i} C_{l_i,m_i,l_f,m_f}^{l_o,\, m_o} \sum_{v\in\mathcal{N}(u)} \left(R(r_{uv})_{c,l_0,p_0,l_f,p_f,l_i,p_i}\right) Y_{m_f}^{l_f}(\hat{r}_{uv}) V_{v,c,m_i}^{l_i,p_i} \tag{3.110}$$

where $R(r_{uv})$ is the radial Bessel function and C is the Clebsch-Gordan coefficients. The NequIP network architecture is illustrated in Fig. 3.4. First, a set of atoms is interpreted as atomic graph (a). The atomic features are refined through a series of interaction blocks, creating scalar and higher-order tensor features (b). The detail of the interaction block is shown in (c) where it contains the convolution (d).

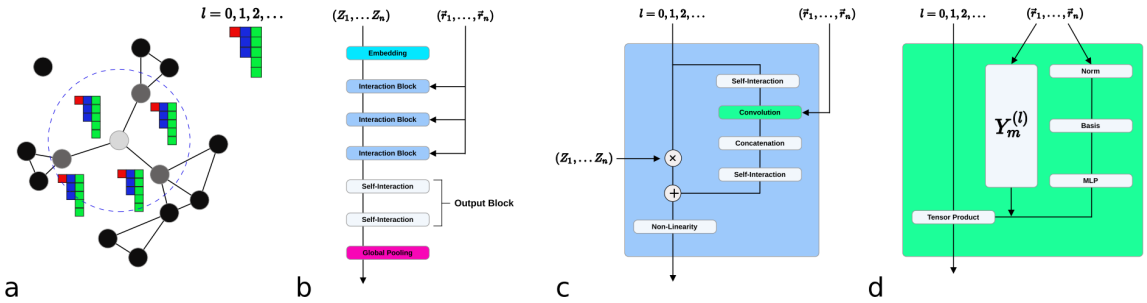

Fig. 3.4. The NequIP network architecture (Batzner et al., 2022).

CHAPTER 4. METHODOLOGY

4.1. Density Functional Theory Calculations

Density functional theory (DFT) (Kohn and Sham, 1965) calculations have been performed using STATE code package (Simulation Tool for Atom TEchnology) (Morikawa et al., 2004; "STATE Code," n.d.) with generalized gradient exchange-correlation functional (GGA) based on the work of Perdew, Burke and Ernzerhof (PBE) (Perdew et al., 1996) with the Grimme D2 dispersion correction (Grimme, 2006). Core electrons were treated using ultra-soft pseudopotentials (Vanderbilt, 1990). Wave functions were expanded using plane-wave basis with wave function and augmentation charges cutoff of 36 Ry (490 eV) and 400 Ry (5442 eV), respectively. Special points for Brillouin-zone integration were generated using Monkhorst-Pack scheme (Monkhorst and Pack, 1976). In Chapter 5, spin polarized calculations were performed whenever triplet O_2 is simulated. In Chapter 6, spin polarized calculations were used in all calculations. The convergence threshold for energy minimization is 1×10^{-9} Ha (2.72×10^{-8}eV). Geometry optimizations were performed until the forces on each atom is less than 1×10^{-3} Ha/a_0 (5.14×10^{-2}eV/Å). Reaction path search were carried out using climbing image nudge elastic band method (CINEB) (Jonsson et al., 1998; Henkelman et al., 2000). Similar calculation parameters were used in the construction of database for the machine learning interatomic potential. All calculations were performed using Born-Oppenheimer approximation with zero electronic temperature. Zero-electronic temperature approximation has been used to study carbon phase diagrams at extreme pressures and temperatures and comparison with finite-electronic temperature shows minimal error especially for insulating systems (Correa et al., 2006). Similar approximation was done on a recent MLMD study of

carbon at extreme pressures and temperatures, which shows highly accurate prediction of Hugoniot temperatures (temperature attained of a material during shockwave compression) particularly for temperatures < 10,000 K (Willman et al., 2022).

4.2. Surface energy and surface stabilization energy

The surface energies γ of the C(111)-(1×1) unreconstructed surface, C(111)-(2×1) reconstructed surface, and C(100)-(2×1) reconstructed surface are calculated by

$$\gamma = \frac{1}{2A}(2 * E_{slab1} - E_{slab2}) \tag{4.1}$$

where E_{slab1} is the total energy a 12-layer diamond slab where the bottom surface is terminated by H atoms, E_{slab2} is the total energy of a 24-layer diamond slab where the top and bottom surfaces are both terminated by H atoms, and A is the surface area of the slab. The stabilization energy of the C(111) surface per surface atom $E_{stabilization}$ after reconstruction is defined as

$$E_{stabilization} = \frac{E_{(2\times1)} - E_{(1\times1)}}{n_a} \tag{4.2}$$

where $E_{(2\times1)}$ is the total energy of the C(111)-(2×1) reconstructed surface, $E_{(1\times1)}$ is the total energy of the C(111)-(2×1) non-reconstructed surface, and n_a is the number of surface atom.

4.3. Adsorption Energies

The adsorption energy E_{ads} is defined with respect to the energies of C(111)-(2×1) π-bonded chain reconstructed surface or C(100)-(2×1) C-dimer reconstructed surface E_{surf} and isolated gas-phase triplet O_2 E_{O_2}:

$$E_{ads} = E_{sys} - \left(E_{surf} - E_{O_2}\right) \tag{4.3}$$

where E_{sys} is the energy of the system of diamond surface and adsorbed O atoms. Using this definition, a positive E_{ads} indicates repulsive interaction, while a negative E_{ads} indicates attractive interaction.

The differential adsorption energy of O_2 on the C(111) and C(100) surfaces ΔE_{O_2} is given by:

$$\Delta E_{O_2} = E_{surf+nO_2} - \left(E_{surf+(n-1)O_2} - E_{O_2}\right) \tag{4.4}$$

where $E_{surf+nO_2}$ and $E_{surf+(n-1)O_2}$ are the total energies of systems with n and $n-1$ number of O_2 adsorbed, and E_{O_2} is the total energy of gas phase O_2.

4.4. Desorption Reaction Energy and Activation Energy

The CO desorption reaction energy E_{des} is defined with respect to the energies of the relaxed final state of the system after desorption E_{sys-CO} and the isolated gas-phase CO E_{CO}:

$$E_{des} = \left(E_{sys-CO} + E_{CO}\right) - E_{sys} \tag{4.5}$$

where E_{sys} is the energy of the system before CO desorption. In this definition, the positive and negative values of E_{des} mean endothermic and exothermic reactions, respectively. The CO desorption activation energy is the energy of the transition state as calculated using the CINEB method. The CO_2 desorption reaction energy and activation energy are defined similarly.

4.5. Crystal Orbital Overlap Population Analysis

The bonding of O and CO on diamond surfaces was analyzed using a population analysis scheme for DFT calculations with plane wave basis sets (Hoffmann, 1988; Aizawa and Tsuneyuki, 1998). This scheme divides the total system into two subsystems, A and B, corresponding to CO and diamond surface, respectively. Electron wavefunction ψ_i is expressed in terms of the sum of the minimal basis sets N_A and N_B for systems A and B

$$\boldsymbol{\psi_i} = \sum_{\boldsymbol{j=1}}^{\boldsymbol{N_A}} \boldsymbol{c_{i,j}^A \chi_{i,j}^A} + \sum_{\boldsymbol{k=1}}^{\boldsymbol{N_A}} \boldsymbol{c_{i,k}^B \chi_{i,k}^B} \tag{4.6}$$

where wave functions χ_j^A and χ_k^B are calculated using the same cut-off energy and unit cell size as ψ_i. The coefficients c_j^A and c_k^B are obtained from the inverse of an overlap matrix. The gross population (GPOP) of each atomic (molecular) orbital of O (CO), $q(i;j)$, and the crystal

orbital overlap population (COOP) with respect to the bond of O (CO) and diamond surface, $p(i)$, are calculated by

$$\boldsymbol{q(i;j) = \left|c_{i,j}\right|^2 + \frac{1}{2}\sum_{k}\left(c_{i,j}^{A}\right)^{*} c_{i,k}^{B} S_{j,k}} + \text{(complex conjugate)} \tag{4.7}$$

$$\boldsymbol{p(i) = \sum_{j,k}\left(c_{i,j}^{A}\right)^{*} c_{i,k}^{B} S_{j,k}} + \text{(complex conjugate)} \tag{4.8}$$

where $S_{j,k}$ is the overlap integral between wave functions χ_j^A and χ_k^B.

4.6. Vibrational Properties

The vibrational properties were determined using a finite-difference harmonic approximation by diagonalizing the Hessian matrices to obtain vibrational eigenvalues and eigenvectors. The Hessian matrices were estimated numerically by initially displacing the O atoms and top four C layers by 0.05 a_0. The displacements of each atom were updated until the energy eigenvalues converged. Two methods were used to produce vibrational spectra from the calculated eigenvalues. Firstly, Lorentzian broadening with a full-width-half-maximum (FWHM) of 15 meV was employed to match the resolution of reported EELS data. Secondly, the intensity of vibration was calculated using the dipole scattering mechanism (Ibach et al., 1982). In this scheme, the relative intensities of the vibrational modes are assumed to be proportional to the square of the dynamic dipole moment $d\mu/dQ$

$$\frac{\boldsymbol{I_{loss}}}{\boldsymbol{I_{elastic}}} = \frac{\hbar(\mathbf{1}-\mathbf{2}\boldsymbol{\theta_E})^{\mathbf{1/2}}}{\mathbf{8}\boldsymbol{a_0}\boldsymbol{\epsilon_0}\boldsymbol{E_I}\,\boldsymbol{cos}\,\boldsymbol{\theta_I}}\left(\frac{\boldsymbol{d\mu}}{\boldsymbol{dQ}}\right)^{\mathbf{2}}\frac{\mathbf{1}}{\boldsymbol{\omega_s}}\boldsymbol{F_s}(\widehat{\boldsymbol{\theta}}_{\mathbf{0}})\boldsymbol{n_s} \tag{4.9}$$

$$\frac{\boldsymbol{I_{loss}}}{\boldsymbol{I_{elastic}}} \propto \left(\frac{\boldsymbol{d\mu}}{\boldsymbol{dQ}}\right)^{\mathbf{2}} \tag{4.10}$$

The dynamic dipole moment was determined by calculating the difference in the work function between the two sides of the simulation slab (Hayashi et al., 2001; Aizawa et al., 2002; Pham et al., 2020). Effective screening medium (ESM) based on the Green's function method was implemented to eliminate non-physical dipole and multipole interactions with image slabs (Otani and Sugino, 2006; Hamada et al., 2009). The a_0, ϵ_0, and ω_s, corresponds to the Bohr radius, vacuum permittivity, and normal frequency. The primary energy E_I, incident angle of electron beam θ_I, and acceptance angle of spectrometer θ_C, which defines $\hat{\theta}_C = \theta_C/\theta_E$, where $\theta_E = \hbar\omega_s/2E_I$ are experimental parameters. The coverage of adsorbates is given by n_s, while the function $F_s(\hat{\theta}_0)$ is given by

$$\boldsymbol{F_s}(\widehat{\boldsymbol{\theta}}_{\mathbf{0}}) = (\boldsymbol{sin^2\theta_I} - \mathbf{2}\boldsymbol{cos^2\theta_I})\frac{\widehat{\boldsymbol{\theta}}_{\boldsymbol{C}}^{\,\mathbf{2}}}{\mathbf{1}+\widehat{\boldsymbol{\theta}}_{\boldsymbol{C}}^{\,\mathbf{2}}} + (\mathbf{1}+\boldsymbol{cos^2\theta_I})\boldsymbol{ln}\left(\mathbf{1}+\widehat{\boldsymbol{\theta}}_{\boldsymbol{C}}^{\,\mathbf{2}}\right) \tag{4.11}$$

Finally, the intensity data were broadened using Gaussian with FWHM of 8 meV.

4.7. Graph Neural Network Interatomic Potential Construction

The GNN-IP construction workflow is shown in Fig. 4.1. We started by building an initial database of equilibrium structures consisting of diamond, graphite, graphene, and flat and stepped diamond (111) and (100) surfaces (Appendix A4). From the equilibrium structures, non-equilibrium structures are generated by randomizing the atomic coordinates, annealing at various temperatures using AIMD and MLMD, and performing active learning (Enriquez et al., 2024a). The non-equilibrium structures generated through the active learning include thermally degraded C(111) surfaces with exfoliated top bilayer and C(100) surfaces with amorphous carbon and carbon-chain on the surface. The forces and energies of these structures are calculated using DFT and used for training the GNN-IP model. Each structure sample i on the database consist of the atomic positions r_{ix}, r_{iy}, and r_{iz}, force components F_{ix}, F_{iy}, and F_{iz}, and total potential energy E_i of the simulation system. The database of structures used in the construction of GNN-IP are provided in the Supplementary Material.

The NequIP software is used to construct a GNN-IP that maps the atomic positions and chemical species to the potential energy of the simulation system and forces acting on the atoms (Batzner et al., 2022). In this method, the nodes in the graph represent the individual atoms while the edges are defined by connecting every atom to all other atoms within a cutoff radius. Every atom is described by a feature vector which is refined by message passing through convolution layers. Rotational equivariance is achieved by constraining the convolution to be products of radial function and spherical harmonics with learnable weights. The radial function is constructed as the product of Bessel function and polynomial cutoff function. We use a total of 8 radial basis and polynomial order of 6. The network has 32 features with 4 interaction

blocks and a max tensor rank of 1. The cutoff radius is set to 4.0 Å which is larger than the 5th nearest neighbor in bulk diamond and the distance between adjacent graphite layers. The cutoff radius is large enough to accurately describe the activation energy of bilayer exfoliation on the C(111) surface (Enriquez et al., 2024a). The predicted total potential energy is obtained by the sum of atomic contributions and the energy conservation is guaranteed by calculating the predicted force from the gradient of predicted energy. The GNN interatomic potential is trained using the loss function based on the weighed sum of the energy and force loss terms where we set both weights to 1.0. The database is split such that 90% of the data is used to training the weights and biases and the remaining 10% is used for testing.

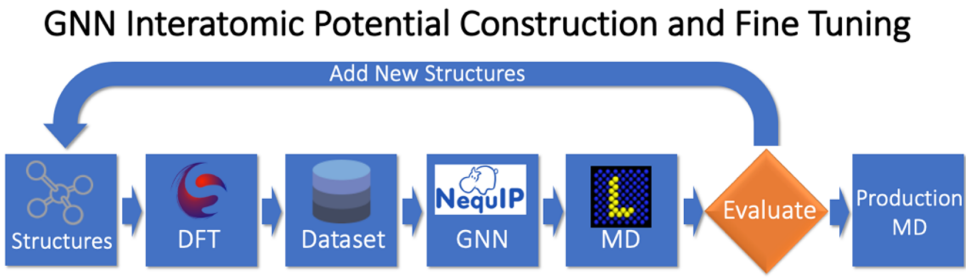

Fig. 4.1. GNN-IP construction workflow. The DFT calculations are performed using STATE code, the GNN-IP is trained using NequIP code, and the MD simulations are performed using LAMMPS software.

4.8. Graph Neural Network Interatomic Potential Fine-tuning and Evaluation

The constructed GNN-IP is evaluated based on its (1) accuracy, (2) stability, and (3) reliability.

1. The accuracy of the GNN-IP is based on the root mean square error (RMSE) of the forces and energies of the test data. Accuracies can be improved by adjusting the training hyperparameters such as the learning rate and size of the network.

2. The stability of the GNN-IP refers to the ability to simulate at the target temperature for sufficiently long timescales without misbehaving or crashing. A misbehaved simulation includes explosions of systems, temperature spikes, and formation of unphysical structures. We observe that crashes of simulations typically occur right after the formation of atomic environments that are not well represented in the database. The stability of the GNN-IP is improved by adding these new atomic environments and structures to the database.

3. Machine learning of interatomic potential is a kind of regression modelling. As with all regression methods, the predictions are more reliable in interpolating between datapoints and less reliable in extrapolating. An extrapolated atomic environment means that the atomic environment is not correlated with any atomic environment on the database. In other words, the database does not contain training data for such configuration of atoms. We use this principle in checking for extrapolated atomic environment. First, we make a database of the feature vectors of all the atomic environment in the dataset. The feature vectors were calculated using neural message passing (Gilmer et al., 2017):

$$\mathbf{h}_i^{(0)} = \mathbf{x}_i \tag{4.12}$$

$$\mathbf{h}_i^{(k+1)} = \mathrm{UPDATE}^{(k)}\left(\mathrm{AGGREGATE}^{(k)}\left(\left\{\mathbf{h}_j^{(k)},\ \forall\, j \in \mathcal{N}(i)\right\}\right)\right) \tag{4.13}$$

where $\mathbf{x}_i$ is the initial embedding chosen depending on the atomic species, $\mathbf{h}_i$ is the hidden embedding of atom i, and k is the number of message passes. The aggregate function is a function of the hidden embeddings of the neighboring atoms j, and takes the form

$$\mathrm{AGGREGATE}\left(\mathbf{h}_j^{(k)}\right) = \tanh(S_m^l) \tag{4.14}$$

$$S_m^l = \sum_{i \neq j}^{N} R(r_{ij}) f(r_{ij}, r_c)\, Y_m^l(\hat{r}_{ij}) \tag{4.15}$$

$$R(r_{ij}) = \frac{2}{r_c} \frac{\sin\left(\frac{b\pi}{r_c} r_{ij}\right)}{r_{ij}} \tag{4.16}$$

$$\begin{aligned} f(r_{ij}, r_c) = 1 &- \frac{(p-1)(p+2)}{2}\left(\frac{r_{ij}}{r_c}\right)^p + p(p+2)\left(\frac{r_{ij}}{r_c}\right)^{p+1} \\ &- \frac{p(p+1)}{2}\left(\frac{r_{ij}}{r_c}\right)^{p+2} \end{aligned} \tag{4.17}$$

Here, $R(r_{ij})$, $f(r_{ij}, r_c)$, and $Y_m^l(\hat{r}_{ij})$ are the Bessel radial basis function, polynomial cutoff function, and spherical harmonics, respectively. The feature vectors are updated using the equation

$$\mathrm{UPDATE}^{(k)}\left(\mathrm{AGGREGATE}\left(\mathbf{h}_j^{(k)}\right)\right) = \mathbf{h}_i^{(k)} + \mathrm{AGGREGATE}\left(\mathbf{h}_j^{(k)}\right) \tag{4.18}$$

Second, we use the GNN-IP to perform MD simulations. Then we calculated the feature vectors of the atomic environments on an MD snapshot. We compare each feature vector element to the database. If we found elements whose numerical value is lower or higher than the maximum value of the corresponding feature vector in the database, then we regard the atomic environment as extrapolated. The forces and energies of the structures containing the extrapolated atomic environments are calculated using DFT added to the database

After the new structures have been added into the database, a new GNN-IP is trained and used to perform MD simulations. The accuracy, stability, and reliability are evaluated using the criteria described above. We continue this cycle to improve the interatomic potential iteratively or through an active learning process, until all of the GNN-IP evaluation criterion is satisfied.

4.9. Graph Neural Network Interatomic Potential Pre-Production Validation

I implement pre-production validation where a smaller system is simulated with the same conditions such as heating rate and temperature range as that of the production simulations. The smaller system size makes it possible to calculate DFT forces and energies of sampled MD snapshots and perform a final error analysis and validation. Pre-production validations have been used in the MLIP construction in Chapter 7 and Chapter 8.

4.10. Machine Learning Molecular Dynamics Simulations

Molecular dynamics simulations with GNN-IP are performed on LAMMPS code (Thompson et al., 2022) using an NVT ensemble with Nose-Hoover thermostat and a timestep of 0.1 fs (Hoover, 1985). In this method, the temperature of the atomic nuclei is controlled by first calculating the nuclei velocities using the GNN-IP and then introducing a fictitious dynamical variable which slows or accelerates the particles until desired temperature, calculated using the equipartition function, is reached. Periodic boundary conditions are imposed along the x and y axis

4.11. Machine Learning Analysis of the Molecular Dynamics Data

The carbon atoms in graphite and diamond are sp^2- and sp^3-hybridized, respectively. An sp^2-hybridized atom has its s orbital hybridize with two p orbitals, resulting in a trigonal

planar structure with three coordination. On the other hand, an sp^3-hybridized atom has its s orbital hybridize with three p orbitals, resulting in a tetragonal structure with four coordination. However, it is also possible to have 3-coordinated sp^3 hybridized atoms on the diamond surfaces (sp^3 with 1 dangling bond), which results in a slightly flattened tetragonal structure. In molecular dynamics simulations, the 3-coordinated and 4-coordinated atoms are typically assigned to sp^2-hybridized and sp^3-hybridized atoms, respectively (Ma et al., 2007). However, since 3-coordinated atoms can either be sp^2- or sp^3-hybridized with a dangling bond, the classification is not trivial. The 3-coordinated sp^3 atoms could easily convert to 4-coordinated sp^3 when the dangling bond is saturated, hence, it should be properly distinguished from the 3-coordinated sp^2 atoms. To classify between the sp^2 and 3-coordinated sp^3 atoms, it is necessary to consider the bond lengths and the shape formed by the central atom and its nearest neighbors. To do this, we build a database of sp^2 and 3-coordinated sp^3 atoms with four features, namely the three bond lengths and the sum of the three bond angles, and either sp^2 or sp^3 as the target class. The sp^2 atoms came from graphite and graphene, while the 3-coordinated sp^3 atoms came from the first layer atoms of the diamond (111) and (100) surfaces. The coordinates of graphite, graphene, and the diamond (111) and (100) surfaces are perturbed randomly using uniform distribution to create new structures. The features are used as input to a neural network binary classifier model. The model has 3 hidden layers and an output layer where we used rectified linear unit (ReLU) and sigmoid activation function, respectively. The model is trained with binary cross-entropy loss function, and adaptive moment estimation (Adam) optimizer as implemented in PyTorch machine learning framework (Paszke et al., 2019).

CHAPTER 5

OXIDATIVE ETCHING MECHANISM OF THE DIAMOND (100) SURFACE

Publication: *Enriquez, J.I., Muttaqien, F., Michiuchi, M., Inagaki, K., Geshi, M., Hamada, I., Morikawa, Y., 2021. Oxidative etching mechanism of the diamond (100) surface. Carbon 174, 36–51. https://doi.org/10.1016/j.carbon.2020.11.057*

The diamond (100) surface [C(100)] is the easiest diamond facet to grow using CVD technology and the most widely used facet in diamond electronics. Hence, it is currently the most technologically relevant diamond surface. Understanding the oxidative etching process, from O_2 adsorption, dissociation, and surface etching through CO/CO_2 desorption, will give insights that will improve both the CVD diamond growth process and diamond device fabrication.

The main issue I intend to address in this chapter is the observed co-existence of carbonyl and ether groups in the O-terminated C(100) surface. First, I will prove the validity of my simulation models by comparing the adsorption energies, relative stabilities, and vibrational modes with the experiment and theoretical literature. After this, I will present the results of the static reaction path simulations of CO desorption and show that in physical surfaces where defects exist, the co-existence of carbonyl and ether groups will occur and give the most energetically stable configuration.

5.1. Model of the C(100) Surface

The optimized diamond lattice constant is 3.572 Å, in good agreement with the experiment (Shikata et al., 2018). The C(100) surface model consists of 8 C layers, a terminating H layer, and an 18.5 Å vacuum slab to prevent spurious interaction between repeating slab images (Fig. 5.1). The top surface atoms are dimerized to match the experimental observations (Hossain et al., 1999; Thoms and Butler, 1995). Although fewer layers are sufficient for accurate adsorption energy calculations, a thicker slab with 20 C layers is necessary for electronic band structure calculations (see Fig. A1, Table A1-A4) (Tiwari et al., 2011; Iacobucci et al., 2016). The relaxed surface exhibits a C-dimer bond length of 1.383 Å, which aligns well with experimental measurements (Krüger and Pollmann, 1995; Long et al., 2008).

5.2. Adsorption of Gas-Phase O_2 on 2×1 Reconstructed C(100) Surface

I first performed test calculations to guide the choice of method that will account for dispersion relation, comparing PBE, PBE+D2, optb86b-vdW, and rev-vdW-DF2 functionals (Fig. 5.2) (Grimme, 2004; Klimeš et al., 2011; Hamada, 2014) to account for dispersion forces. The dispersion corrections enhanced the adsorption energies by 0.241 eV, 0.354 eV, and 0.284 eV for PBE+D2, optb86b-vdW, and rev-vdW-DF2, respectively. The van der Walls corrections enhanced the adsorption energies with minimal effect on the predicted adsorption distance. I decided to use the PBE+D2 as it gives the best simulation cost and accuracy balance.

Carbonyl and ether are the two O-containing functional groups observed in electron energy loss spectroscopy (EELS) of the C(100) surface. When carbonyl forms, the O atom bonds on top of the C atom, forming a double bond. On the other hand, when ether forms, the O atom bonds on the bridge site, forming two single bonds. The carbonyl groups dominate at low surface coverages, and the ether groups dominate at high surface coverages. Nevertheless, even at monolayer, the carbonyl groups do not entirely vanish. Curiously, prior theoretical works predicted that a C(100) surface with monolayer O coverage should be terminated by ether. Hence, the existence of less energetically stable carbonyl has yet to be explained. The type of functional group on the C(100) surface directly affects its chemistry and electronic properties. To fabricate high-quality diamond devices with uniform properties, it is necessary first to reconcile the disparity between experimental observations and theoretical predictions.

To investigate this issue, I simulated the adsorption of O_2 gas on the C(100) surface. I consider two adsorption models, the first is molecular adsorption on top of the C atom, and the second is dissociative adsorption on the site bridge of two C atoms. The reaction path of O_2 molecular adsorption is illustrated in Figure 5.3 (black line), along with the reaction paths of fictitious O_2 with fixed singlet (blue) and fixed triplet (red) spin multiplicity. The transition state of the reaction occurs at the intersystem crossing point (ISC).O_2 is in a triplet state in the gas phase. When it approaches the C(100) surface, it gets trapped in a -0.78-eV metastable state. The spin conversion probability of O_2 from triplet to singlet state is low due to weak spin-orbit coupling. However, since O_2 is unlikely to escape once trapped in a metastable state, spin transition could occur because of molecular vibrations. Specifically, a part of the kinetic energy gained at a finite temperature will be converted to a rocking vibration of O_2 with one of its ends fixed at the surface. Vibrating in this manner will cause the triplet O_2 to pass at the ISC point several times until spin transition eventually occurs. Compared to the energy barrier of O_2 with

fixed triplet multiplicity (0.55 eV), undergoing spin transition paves an easier path to final adsorption as the energy barrier is lowered to 0.27 eV. A similar reaction path occurs for O_2 dissociative adsorption but with a noticeably deeper metastable state (-3.12 eV). Spin transition reduces the adsorption barrier from 0.78 eV to 0.35 eV (Fig. 5.4). Since the reaction path of triplet O_2 up to the metastable state is barrier-less for both molecular and dissociative adsorption, and since the difference between the reduced barrier height during ISC for both sites is small (0.08 eV), it is likely that both adsorption processes take place at initial oxidation.

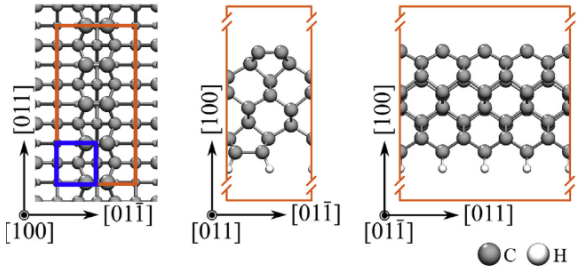

Figure 5.1. Model of the 2×1-reconstructed C(100) surface. Grey and white spheres correspond to carbon and hydrogen atoms, respectively.

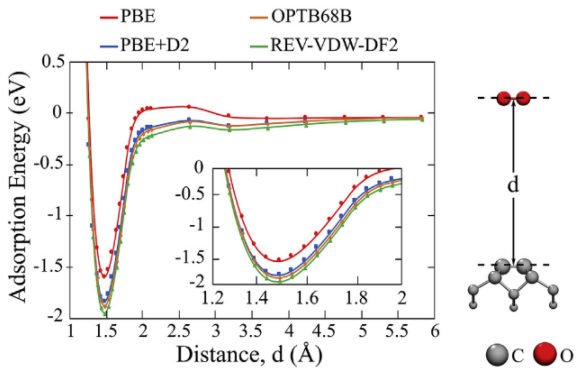

Figure 5.2. Potential energy surface of O_2 adsorption on the top site using PBE and van der Walls-corrected functionals.

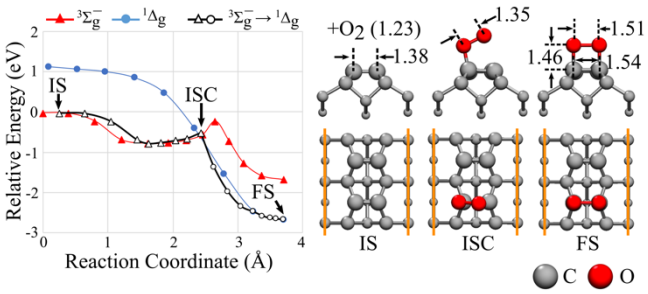

Figure 5.3. Adsorption of triplet and singlet O_2 on the top site of the reconstructed C(100) surface, showing the initial state (IS), intersystem crossing state (ISC), and final state (FS).

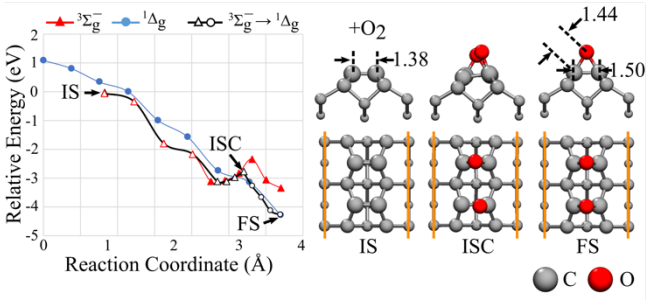

Figure 5.4. Adsorption of triplet and singlet O_2 on the bridge site of the reconstructed C(100) surface, showing the initial state (IS), intersystem crossing state (ISC), and final state (FS).

5.3. Oxygen-Induced Surface Dereconstruction and Oxygenation at Monolayer Coverage

The unrelaxed C(100) surface has two dangling bonds per surface atom. After performing geometry optimization, the surface atoms dimerize, which leads to experimentally observed 2×1 reconstruction. Experiments also observed that O adsorption on the C(100) surface causes surface dereconstruction where the surface atoms revert to the 1×1 periodicity. To understand this process, I simulated the surface dereconstruction following oxygen molecular adsorption (Fig. 5.5). The dereconstruction has an activation energy of 0.81 eV and co-occurs with the formation of carbonyl groups. The surface stabilizes further with the formation of an ether group chain.

Surface dereconstruction can also occur following a second oxygen dissociative adsorption (Fig. 5.6). As the C dimer bonds break, the ether group forms a chain structure. These calculations show that the ether chain-terminated C(100) is energetically favorable compared to the carbonyl-terminated C(100). Lastly, I simulated a C(100) surface with monolayer O coverage (Fig. 5.7). Adsorption on the bridge site forming ether is more energetically stable at 0.37 eV compared with the adsorption on the top site, which forms carbonyl, which agrees with the literature (Frenklach et al., 1993; Skokov et al., 1994; Rutter and Robertson, 1998; Sque et al., 2006; Petrini and Larsson, 2007; Lu et al., 2020).

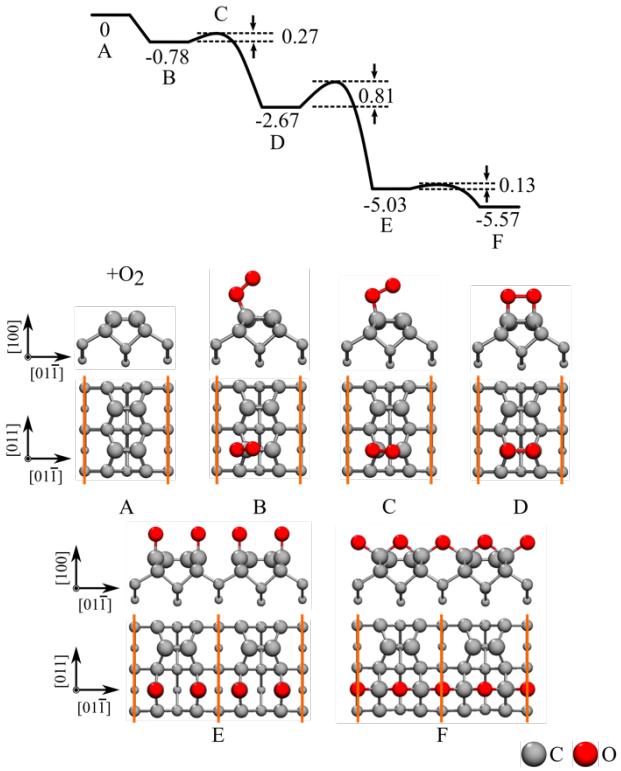

Figure 5.5. Oxygen molecule adsorption on the top site and dereconstruction of the C(100) surface.

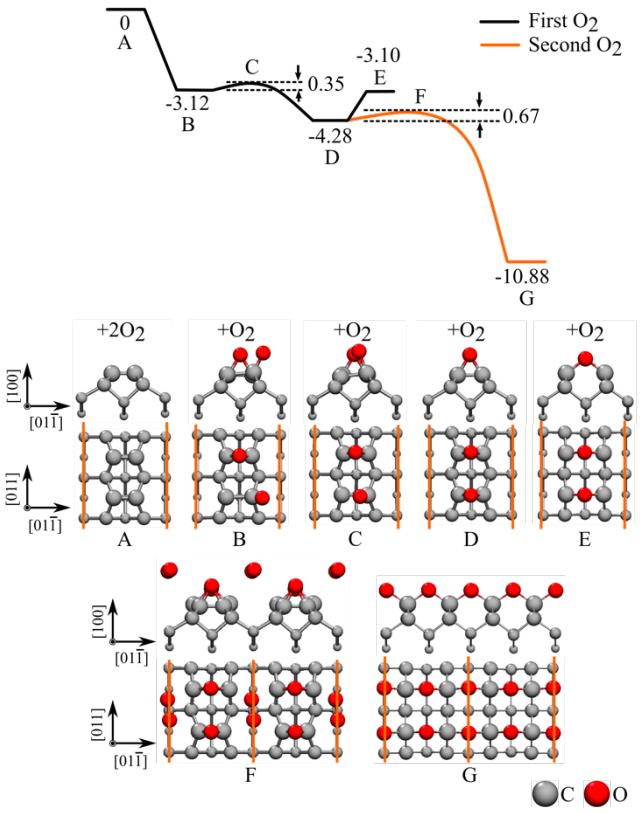

Figure 5.6. Oxygen molecule adsorption on the bridge site and dereconstruction of the C(100) surface.

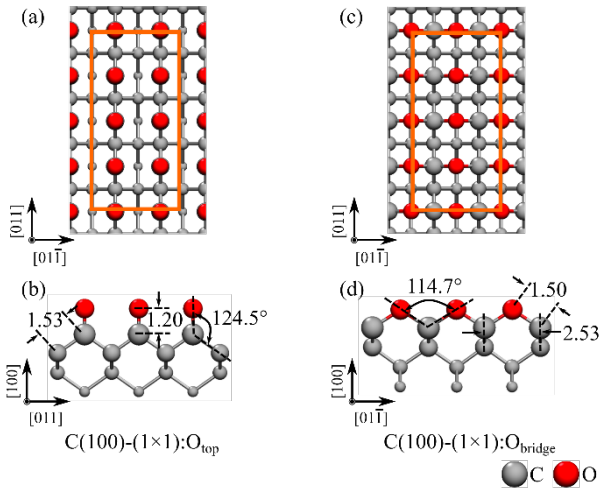

Figure 5.7. Optimized structures for monolayer O adsorption on top and bridge sites of the C(100) surface. Grey and red spheres correspond to carbon and oxygen atoms, respectively.

5.4. Electronic analysis of diamond (100) surface with monolayer oxygen coverage

I calculated the band structures of clean and oxygen-terminated C(100) surfaces (Fig. 5.8). The clean C(100) surface is an indirect band gap semiconductor, but the absorption of O on top significantly narrows the energy gap. The VBM corresponds to HOMO, characterized by O lone pair orbitals that are antibonding with respect to the σ bonding orbitals between first and second-layer C atoms (Fig. 5.9). In contrast, adsorption on the bridge site widens the energy gap and changes C(100) into a direct band-gap semiconductor. The O lone pair orbitals and the σ orbitals are farther apart; thus, their antibonding interaction is lesser.

Next, I calculated the density of states of bulk diamond and C(100)-(2×1) projected onto s and p orbitals (PDOS) (Figure 5.10). The Fermi level of each system is set to zero. For bulk diamonds, there is an energy gap region of about ~4 eV. The energy levels of px, py, and pz orbitals are completely degenerate. Hybridization of s and p orbitals can be inferred from the overlapping of peak at -13.0 eV and several others between -15 to -6 eV. Cleaving (100) surface and reconstruction of surface C atoms led to changes in the density of states, the most notable is the rise of available pz states in the energy gap region. The peak at -13.0 eV lowers and broadens as new states become available due to the splitting of p states. The density of states of C(100)-(1×1):O_{top} and C(100)-(1×1):O_{bridge} are shown in Figure 5.11. The Fermi level of each system is set to zero. The density of states projected into a single oxygen and a single surface carbon atom, and their corresponding orbitals are also shown. Adsorption on the top site gives rise to a peak at -22.0 eV which shows overlapping of $2s$ and $2pz$ states of O and C. Furthermore, a peak at -5.6 eV shows overlapping of O and C $2pz$ states. The number of states in the energy gap region increased due to hybridized O and C $2px$ states. Moreover, the

dereconstruction of the surface leads to the reemerging of the peak at around -13.0 eV. However, unlike in the bulk diamond, this peak (-12.8 eV) is mainly due to unhybridized C s states. For the adsorption on the bridge site, there are also two peaks (-21.3 and -3.7 eV) that show the hybridization of O $2s$ and C $3pz$ states. Unlike the top site adsorption, the peak at around -13.0 eV does not reemerge due to the hybridization of O and C states between -17.7 to -7.9 eV.

Figure 12 shows the crystal orbital overlap population (COOP) analysis of the bonding between the oxygen and the C(100) surface. The O on the bridge site has stronger hybridization than the top site, as shown by wider energy bands of the 2p orbital. The total overlap of the O on the bridge site is higher than the top site by 0.03, explaining the higher stability of the bridge site adsorption.

Lastly, I calculated the charge density difference $\Delta\rho$ using the equation

$$\Delta\rho = \rho_{\mathrm{sys}} - (\rho_{\mathrm{dia}} - \rho_{\mathrm{O}}) \tag{5.1}$$

where ρ_{sys}, ρ_{dia}, and ρ_{O} are the electron charge densities of dereconstructed diamond (100) with adsorbed oxygen, dereconstructed diamond (100), and isolated O atoms, respectively for monolayer oxygen coverage on the top and bridge sites. I mapped the results as isosurfaces and images of volume slice highlighting charge transfer are shown in Figure 5.13. Blue and red regions correspond to regions where electrons are gained and lost, respectively. For on-top adsorption, electrons were enriched around the oxygen atom and in the region between the

oxygen and carbon atom, while electrons were depleted around the carbon atoms and in the spaces between them. For bridge site adsorption, electrons were enriched around the oxygen atom and on the bonds joining oxygen and carbon, while electrons were depleted on top of the carbon atoms.

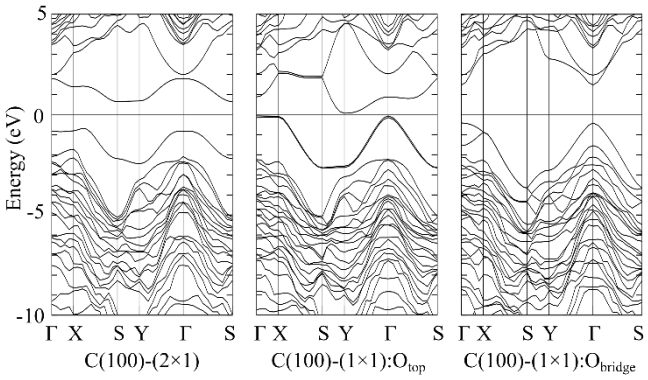

Fig. 5.8. Electronic band structures of the clean and oxygen-terminated C(100) surfaces.

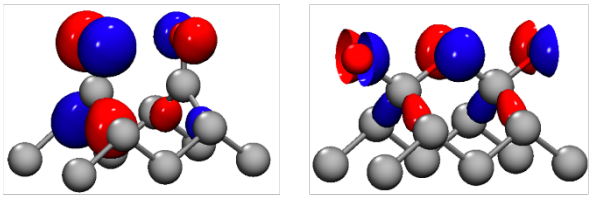

Fig. 5.9. Plot of the valence band maximum (highest occupied molecular orbital) of the C(100) surface with O atoms at the top and bridge sites

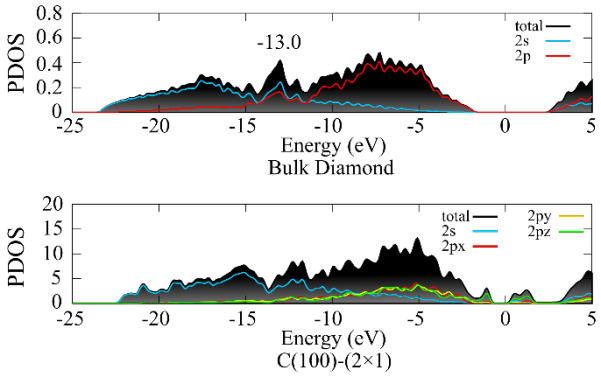

Fig. 5.10. Density of states of bulk diamond and clean C(100)-(2×1) surface projected onto 2s and 2p orbitals.

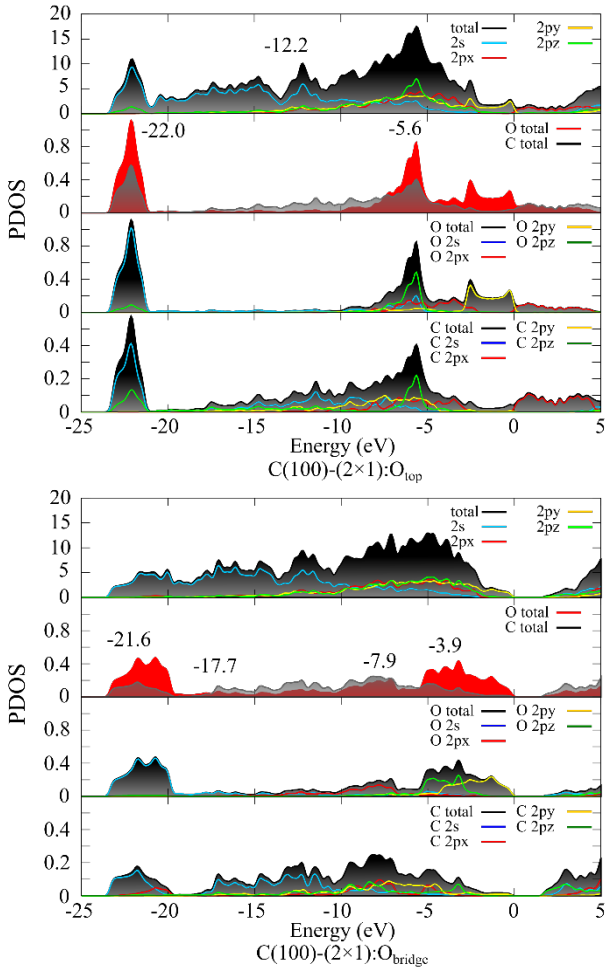

Fig. 5.11. Density of states of oxygenated C(100)-(1×1):O_{top} and C(100)-(1×1):O_{bridge} surfaces projected onto 2s and 2p orbitals. Also shown are the projections into an adsorbed O atom and a top-layer C atom.

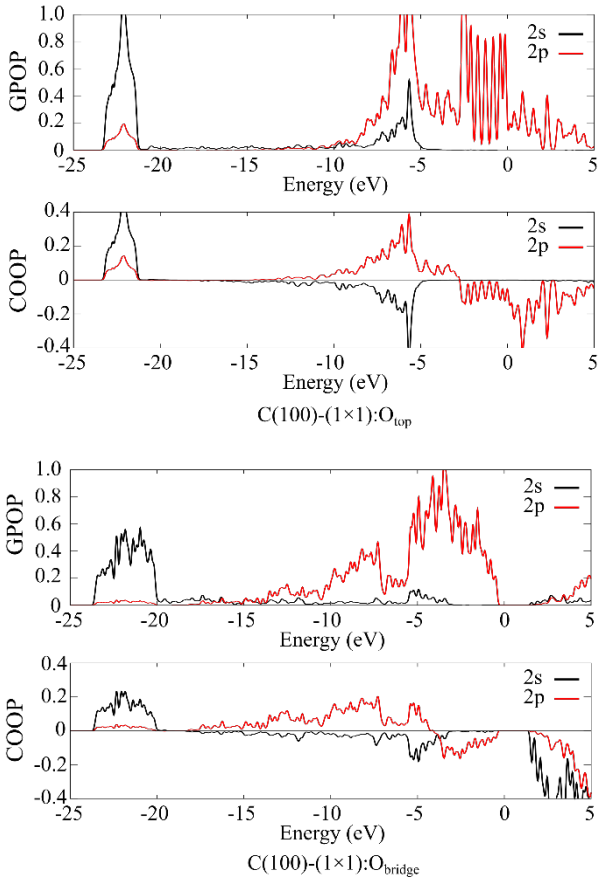

Fig. 5.12. Gross population (GPOP) and crystal orbital overlap population (COOP) analysis of the C(100) surface with O atoms at the top and bridge sites.

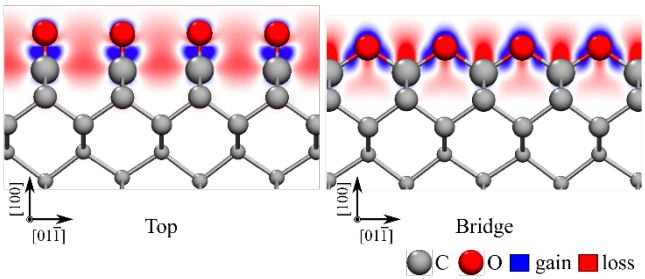

Fig. 5.13. Electron charge density difference of oxygen adsorption reaction for monolayer coverage. Grey and red spheres correspond to carbon and oxygen atom, respectively. Blue and yellow isosurfaces correspond to regions where charges are enriched and depleted, respectively.

5.5. Vibrational frequency analysis of clean and oxygenated diamond (100) surfaces

I calculated the vibrational frequencies of the clean C(100) surface and surfaces with 1 ML oxygen coverage on top and bridge sites. The vibrational eigenvalues were obtained using a finite-difference harmonic approximation involving the topmost four carbon layers for a clean surface. At the same time, the oxygenated surfaces also include the surface O layer. To match the resolution of the EELS spectrometer employed in the work of Hossain et al., the results were broadened using Lorentzian with a width of 15 meV, as shown in Figure 5.14. The calculated spectra for the clean C(100) surface exhibit broadbands below ~150 meV, with two prominent peaks at 80 and 147 meV and a minor peak at 106 meV. It is worth noting that the two main peaks correspond to the peaks in EELS data and earlier theoretical works (Lee and Apai, 1993; Alfonso et al., 1995; Frauenheim et al., 1996).

Next, I computed the vibrational intensities using the dipole scattering mechanism, as illustrated in Fig. 5.15. I examined the top-site adsorption and identified peaks at 155 and 231 meV, attributed to subsurface phonon bouncing and carbonyl stretching, respectively. This confirmation supports the assignment of the EELS peak at 215 meV to carbonyl stretching. In contrast, I observed peaks at 129 and 153 meV linked to ether bending and surface phonon bouncing for the bridge site adsorption. Since bridge site adsorption is the most stable configuration at monolayer, these peaks likely correspond to the EELS peaks at 113 and 150 meV observed in high oxygen exposure. These findings suggest the coexistence of carbonyl and ether at high surface coverage.

I conclude this section by proposing a mechanism of oxygen adsorption that combines the results of reaction path and vibration spectra calculations with the EELS data. In the gas phase, O_2 is adsorbed molecularly on the top site and dissociatively on the bridge site. Even at low O coverage, surface reconstruction occurs primarily due to oxygen adsorption on the top, leading to carbonyl formation. As the O coverage increases, isolated epoxide groups transform into ether chain groups, causing surface reconstruction. This results in the disappearance of specific peaks and the emergence of others. When the surface reaches 1 ML coverage, O atoms of the carbonyl groups move from the top to the bridge position to form the more stable ether chain. Despite high oxygen exposure, the carbonyl stretching mode does not entirely disappear, suggesting the incomplete formation of the ether chain on certain parts of the surface, potentially due to defects and vacancies along rows.

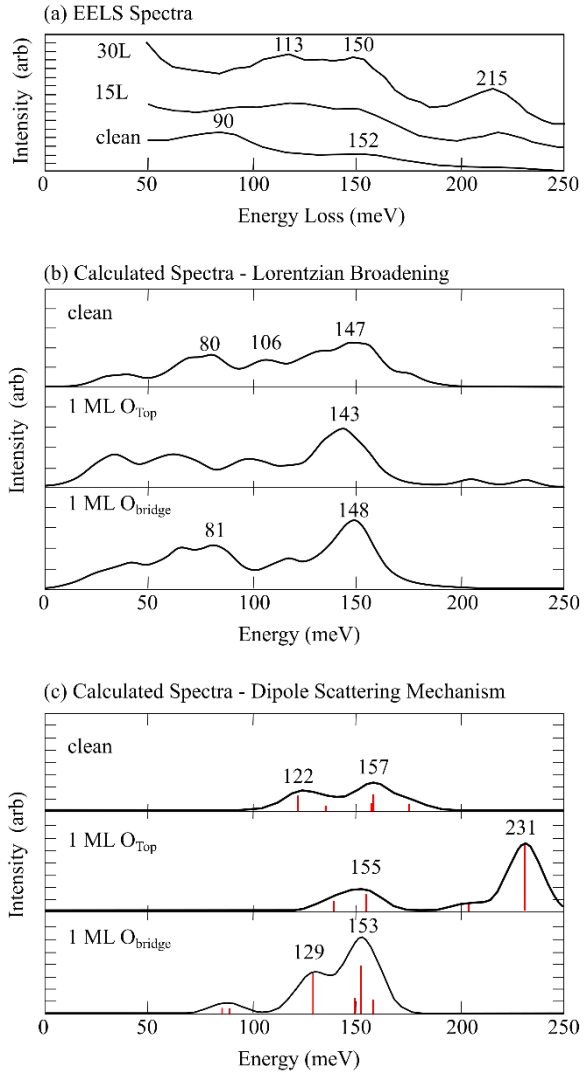

Fig. 5.14. (a) EELS spectra of diamond (100) surface exposed to oxygen at 500 K. Redrawn with permission from (Hossain et al., 1999), and calculated vibrational spectra with intensities based on (a) Lorentzian broadening and (b) dipole scattering mechanisms.

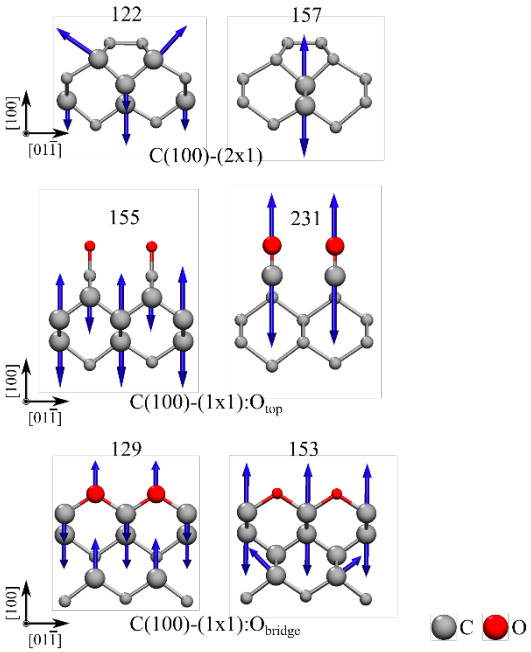

Fig. 5.15. Vibrational modes with the highest intensity of the clean and oxygen-terminated C(100) surfaces.

5.6. Oxidative Etching of the C(100) Surface

In this final section, I studied the mechanism of the oxidative etching of the C(100) surface. I choose the C(100)-(1×1):O_{bridge} model since it is the most energetically stable monolayer configuration. First, I compared the reaction paths of CO and CO_2 desorption (Fig. 5.16). The desorption of CO starts with the breaking of the C-O bonds on the surface ethers and the movement of O from the bridge site to the top site, forming a carbonyl. This is followed by the breaking of two C- CO_{bridge} bonds, requiring a total desorption activation energy ($E_{barrier}$) of 4.30 eV. On the other hand, the desorption of CO_2 follows a similar path as CO until it reaches the physisorbed state. Just before complete desorption, the physisorbed CO binds with the O atom of the adjacent CO_{bridge}, breaking the C-O bond and desorbing as CO_2. This additional step results in a higher desorption activation of 4.88 eV. This explains why CO_2 desorption is less likely than CO, consistent with experimental findings (Thomas et al. 1992, Hossain et al. 1999).

Next, I simulated the CO desorption reactions up to the complete etching of the top C layer (Fig. 5.17, Table 5.2). The succeeding CO desorption reactions along the [011] (Fig. 18 B-E) all have lower $E_{barrier}$ compared to $[01\bar{1}]$, suggesting a preferred etching direction. Initial desorption of CO along a given row in [011] direction has the highest desorption activation energy while succeeding energy barriers are lower. The initial CO desorption proceeds by the near-simultaneous breaking of two CO_{bridge}-C bonds. The point defect left by the initial desorption allows the next CO_{bridge} to break one bond with second layer C and form Ca O on top (CO_{top}) structure. The non-simultaneous bond breaking reduces the heat released by the

reaction and the desorption activation barrier. This suggests that the point defect functions as nucleation point for CO desorption along [011] direction.

I conducted simulations of CO desorption reactions leading to the complete etching of the top C layer, as shown in Fig. 5.17. The subsequent CO desorption reactions along the [011] all have lower $E_{barrier}$ compared to $[01\bar{1}]$, indicating a preferred etching direction. The initial CO desorption along the [011] direction has the highest desorption activation energy, while the following energy barriers are lower. The initial CO desorption involves the simultaneous breaking of two CO_{bridge}-C bonds. The resulting point defect allows the next CO_{bridge} to break one bond with the second layer C and form a CO on top (COtop) structure. The non-simultaneous bond breaking reduces the heat released by the reaction and the desorption activation barrier, indicating that the point defect serves as a nucleation point for CO desorption along the [011] direction (Fig. 5.18). This mechanism was initially suggested by John et al. based on their observation that the removal rate of rows of atoms is faster than that of the layers (John et al. 2002). This work is the first theoretical study to validate their prediction.

A completely etched first layer will leave a second layer with the characteristic 2×1 reconstruction along [011] direction (Fig. 5.17 I). The reaction H ⟶ I show the desorption reaction of isolated CO from the bridge site of the C dimer. I used GPOP analysis to gain insights of the bonding mechanism of CO on the C(100) surface (Fig. 5.19). The DOS weighed by GPOP shows that 5σ orbital of the CO has no distinct peak, suggesting strong hybridization with the bonding states of C(100). On the other hand, the 2π orbital have a sharp occupied peak at -1.9 eV. The adsorption of CO has a total orbital overlap of 0.53 including net bonding contributions of 0.27 and 0.32 from 5σ and 2π orbitals, respectively.

The desorption activation energy of isolated CO is 1.70 eV. This value agrees well with computational and experimental literature. Using the cluster model, Frenklach et al. have estimated the activation energy of CO desorption to be 1.66 eV. Thomas et al. and Frenklach et al. performed thermal desorption spectroscopy (TDS) and confirmed that the diamond (100) surface was oxidized by the desorption of CO and reported an activation barrier of 1.91 eV and 1.95 eV, respectively (Thomas et al., 1992; Frenklach et al., 1993). The TDS data revealed an intriguing result: the CO desorption peak was unusually wide, with a full width at half maximum (FWHM) comparable to the data presented by Thomas et al. Based on our simulation results, we hypothesize that the broad peak is a result of multiple peaks corresponding to a wide range of desorption activation energies that we have calculated.

Finally, I calculated the desorption of CO_2 from oxygenated C(100) with defects (Fig. 5.20). The CO_2 desorption following the desorption of first CO has the highest activation energy of 5.17 eV. It is significantly higher than the $E_{barrier}$ of CO desorption (3.62 eV) from the same surface (Fig. 17 B⟶C). The same is true for the two other cases, with $E_{barrier}$ of 2.39 and 3.68 eV, while the $E_{barrier}$ for the corresponding CO desorptions are 1.01 and 1.84 eV, respectively. The results indicate that diamond (100) primarily undergoes oxidation through CO desorption, even in the case of defected surfaces, consistent with experimental findings.

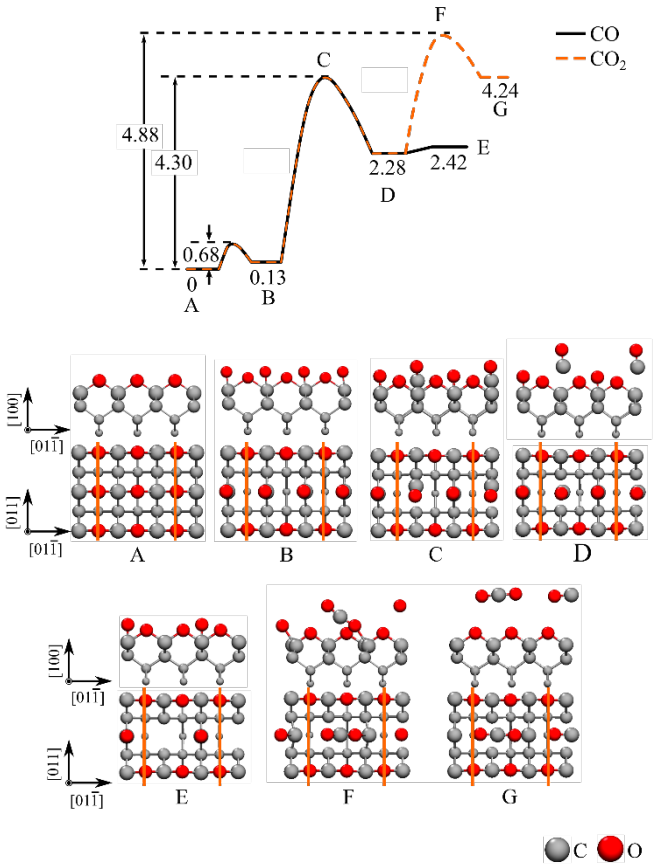

Fig. 5.16. Desorption of CO and CO_2 from the C(100) surface.

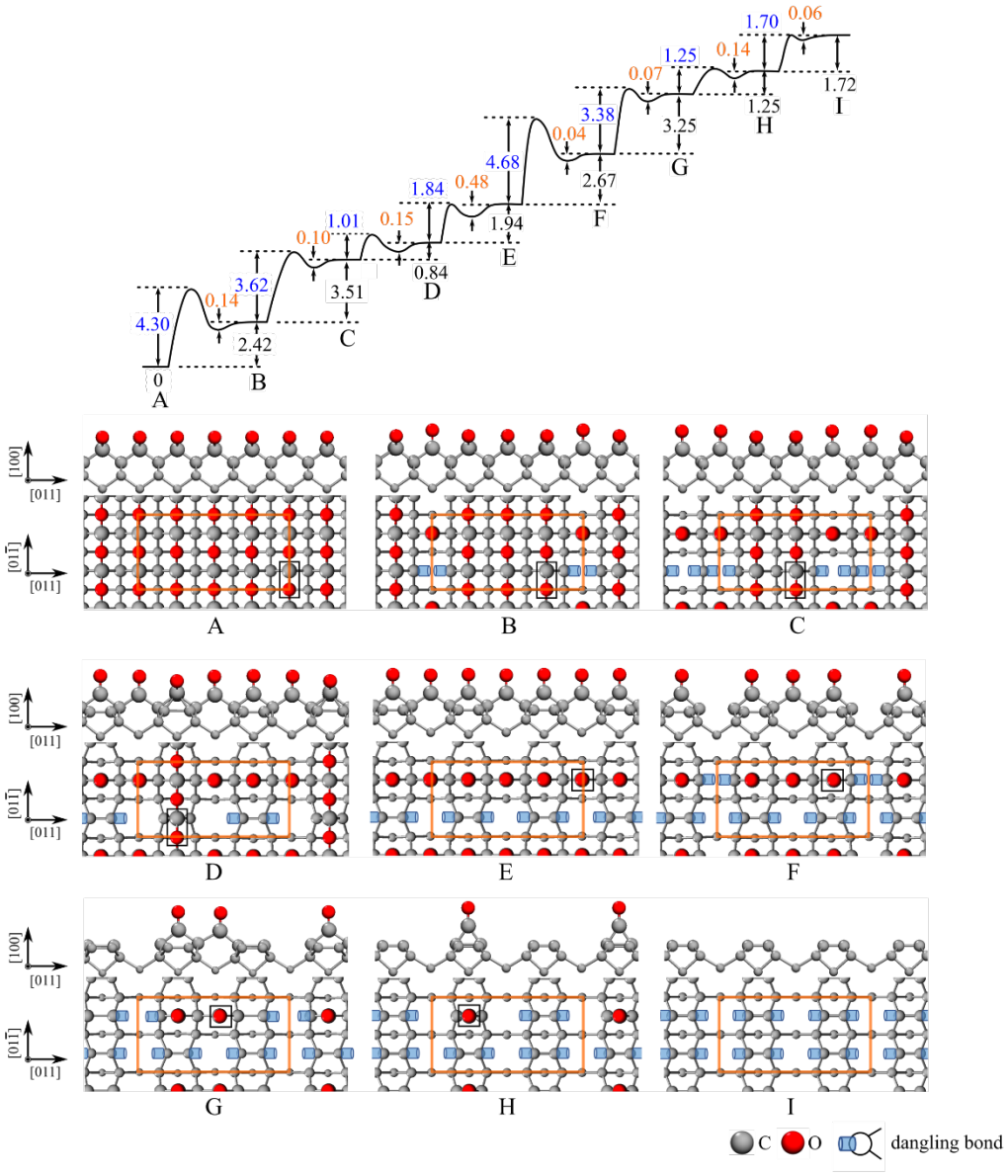

Fig. 5.17. Successive CO desorption from the C(100) surface.

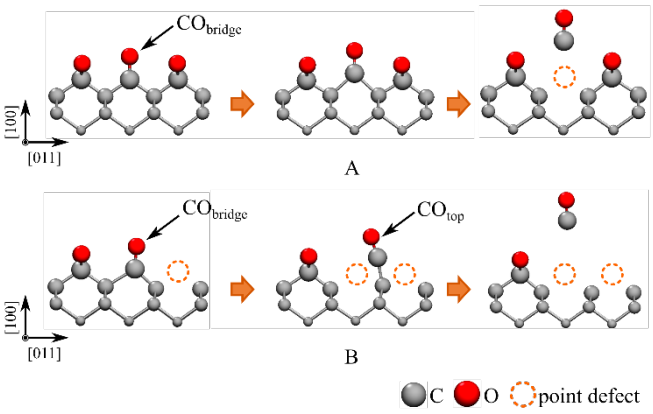

Fig. 5.18. Mechanism of preferred etching along [011] direction.

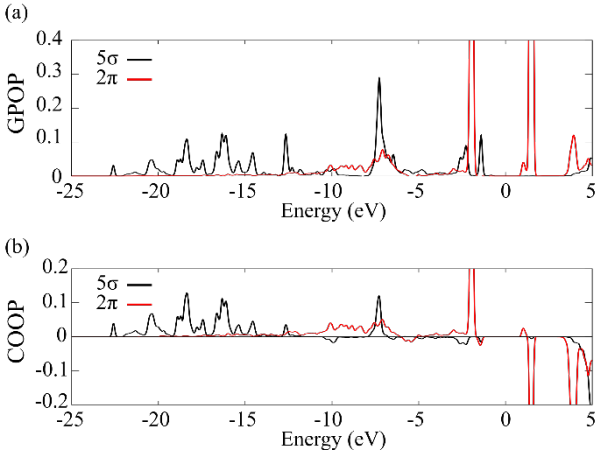

Fig. 5.19. Gross population (GPOP) and crystal orbital overlap population (COOP) analysis of the CO and C(100) surface.

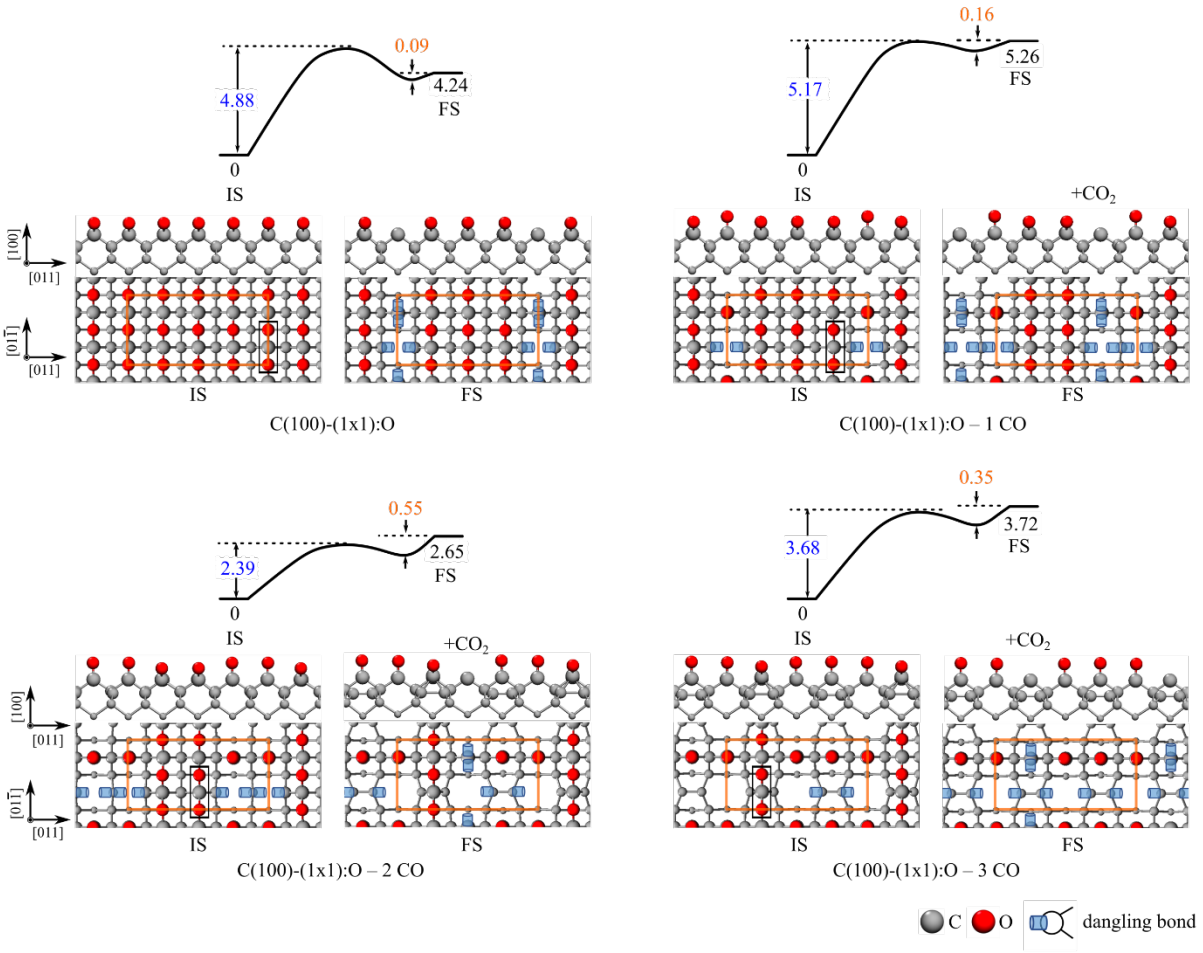

Fig. 5.20. Desorption of CO_2 from the C(100)-(1×1):O_{bridge} surface and C(100)-(1×1):O_{bridge} surfaces with 1, 2, and 3 desorbed CO.

5.7. Co-existence of carbonyl and ether on oxidized C(100) surface

Finally, in this section, I present a mechanism for the co-existence of carbonyl and ether groups on the C(100) surface (5.21). I begin with the surface with one missing carbon atom following the desorption of the first CO from the surface with monolayer coverage. The two dangling bonds left by the desorbed CO can be readily saturated by free oxygen atom to form an isolated ether. The calculated adsorption energy relative to the isolated O atom is -8.72 eV, which more stable than the average C(100)-(1×1):O_{bridge} ether adsorption energy by 1.30 eV.

Next, I simulated the adsorption of gas-phase O_2 on the oxygenated surface with two carbon vacancies. As O_2 approaches the surface, intersystem crossing occurs, and the O_2 dissociatively adsorbs with an adsorption energy of -7.89 eV. Finally, I simulated the adsorption of O_2 on a single-atom deep trough, which is formed by row-wise etching of CO along [011] direction. The reaction path and corresponding geometries for the adsorption of first and second O_2 are shown in Figure 5.22. Unlike the case of adsorption on one or two vacant sites, the adsorption on trough is an activated process because the etched surface is already partially stabilized by dimer formation. The calculated reaction path is similar in the case of O_2 adsorption on top of the reconstructed surface discussed in Section A. The etched trough is stabilized by O adsorption with an average adsorption energy per O atom of -7.69 eV, which is 0.27 eV more stable than in the case of the surface with 1 ML oxygen coverage on the bridge site.

These calculations confirm the structural stability of surfaces with monolayer oxygen coverage, consisting of carbonyl on the first layer and ether on the second layer. Additionally, we have demonstrated that these structures could form during oxidation, as oxygen is adsorbed on vacant sites left by desorbed species. It is worth noting that the stabilization of the succeeding layers by oxygen adsorption can explain the stable shallow steps formed during dry oxygen etching of the diamond (100) surface (de Theije et al. 2020).

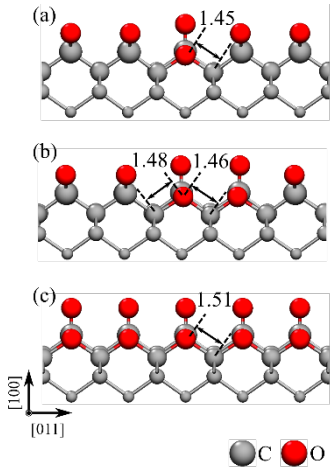

Fig. 5.21. Adsorption of oxygen on surfaces with (a) one missing C-atom, (b) two missing C-atoms, and (c) single-atom-deep trough structure.

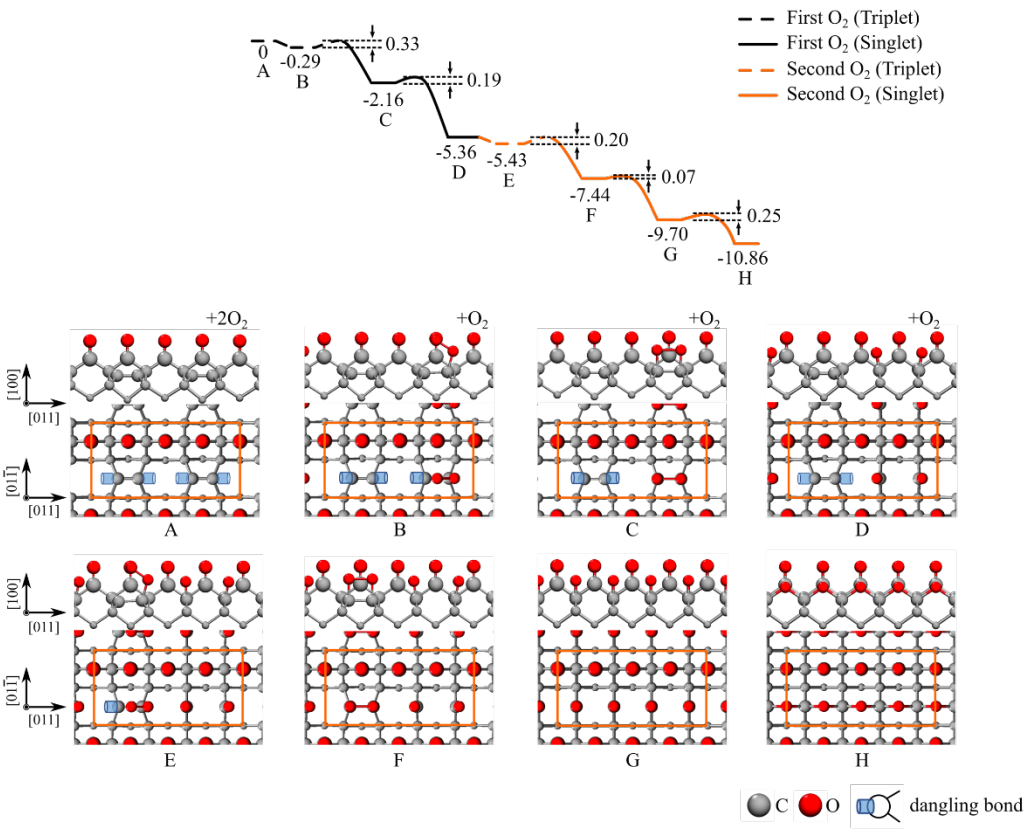

Fig. 5.22. Adsorption of O_2 on etched C(100) trough.

CHAPTER 6

ORIGIN OF THE SURFACE FACET DEPENDENCE IN THE OXIDATIVE ETCHING OF THE DIAMOND (111) AND (100) SURFACES

Publication: *Enriquez, J.I.G., Yamasaki, T., Michiuchi, M., Inagaki, K., Geshi, M., Hamada, I., Morikawa, Y., 2024. Origin of the Surface Facet Dependence in the Oxidative Etching of the Diamond (111) and (100) Surfaces from First-Principles Calculations. J. Phys. Chem. C. 128 15 6294–6308. https://doi.org/10.1021/acs.jpcc.3c08378*

The C(111) surface has unique properties which could lead to novel technological applications. Unlike the semiconducting C(100) surface, the C(111) surface is metallic because of the π-bonding between the top layer atoms. The C(111) and C(100) surfaces also have contrasting oxidation properties. Experiments have shown that the C(111) and C(100) surface have different reactivity with oxygen gas. Moreover, the oxidized surface morphology of the C(111) surface is much rougher compared to the C(100) surface when etched at similar conditions.

In the previous chapter, I presented the oxidative etching mechanism of the C(100) surface with the goal of providing insights that will be useful in diamond technology. The experiments comparing the oxidation of these two surfaces imply that the C(111) surface has unique oxidative etching mechanism. In this chapter, I will present this mechanism and propose a theory on the origins of the surface facet-dependent diamond surface oxidation.

6.1 Model of the Diamond (111) and (100) Surfaces

The calculated lattice constant for bulk diamond is $\alpha_{dia} = 3.572$ Å which agrees very well with experiment (Shikata et al., 2018).

To determine the number of layers of the surface models, we perform test calculation of O_2 adsorption on C(100) surface with 12-layers and 16-layers. The difference in the adsorption energy per atom is only 0.0069 eV, thus 12 layers is sufficient to accurately model surface reactions. In addition, we perform the following test calculations to determine the appropriate supercell size. First, using molecular O_2 on a $\sqrt{3} \times 2$ supercell as a test case, we verify that the total energy change is less than 0.0002 eV when doubling the supercell size to either x- or y- directions and 0.011 eV when doubling the supercell size to both x- and y-directions. Second, the difference in the adsorption energy of O_2 on C(111) surface at 0.5 ML coverage on a $\sqrt{3} \times 2$ supercell and $\sqrt{3} \times 4$ supercell is only 0.0072 eV. By considering these test calculations, the adsorption energy is converged within 0.011 eV with respect to the supercell size.

The C(111) surface is modeled as a slab of 12 carbon layers with a vacuum region of at least $35\ a_0$ (18.5 Å). We use an orthorhombic cell with lattice $a = \frac{\sqrt{2}\sqrt{3}}{2}\alpha_{dia}$ and $b = \frac{\sqrt{2}}{2}\alpha_{dia}$. The top bilayer is modeled as π-bonded chain (2×1) reconstructed surface. The bottom layer is terminated with H atoms. We use $\sqrt{3} \times 2$ supercell with 8×8 k-point mesh for oxygen adsorption simulations and larger $\sqrt{3} \times 4$ supercell with 8×4 k-point mesh in differential adsorption energy and oxidation simulations. The C(100) surface was modeled as a slab of 12 carbon layers with a vacuum region of at least $35\ a_0$ (18.5 Å). We use an orthorhombic cell

with lattice $a' = b' = \sqrt{2}\alpha_{dia}$. The top layer is modeled as C-dimer 2×1 reconstructed surface. The bottom layer is reconstructed in a similar manner and then terminated with H atoms. We use 2×4 supercell with 8×4 k-point mesh in differential adsorption energy and oxidation simulations. The simulation models of the C(111)-(1×1) unreconstructed surface, C(111)-(2×1) π-bonded chain reconstructed surface, and C(100)-(2×1) C-dimer reconstructed surfaces are shown in Figure 6.1.

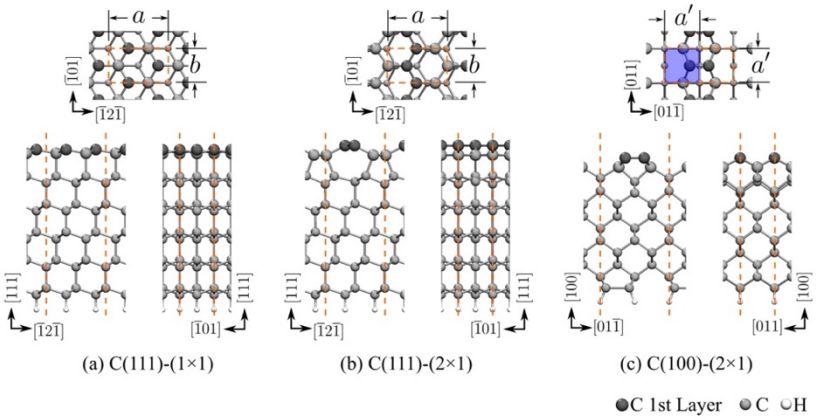

Fig. 6.1. Model of (a) the C(111)-(1×1) unreconstructed and (b) C(111)-(2×1) reconstructed surfaces. The orthorhombic cell, defined by the orange lines, has the dimensions $a = \sqrt{2}\sqrt{3}/2\,\alpha_{dia}$ and $b = \sqrt{2}/2\,\alpha_{dia}$, where α_{dia} is the lattice constant of bulk diamond. (c) Model of the C(100)-(2×1) reconstructed surface. The unit cell is shown in the blue shaded box with dimension $a' = \sqrt{2}\alpha_{dia}$. A 2×1 supercell is defined by orange lines. Grey, silver, and white spheres correspond to 1st layer carbon atoms, 2nd-12th layer carbon atoms, and hydrogen atoms, respectively.

6.2. Adsorption of Gas-Phase O_2 on the C(111) Surface

There are two possible configurations of O_2 adsorption on the clean π-bonding chain-reconstructed C(111)-(2×1) surface, namely, molecular adsorption on the top site and dissociative adsorption on the bridge site. The reaction path of O_2 molecular adsorption is illustrated in Fig. 6.2 (black line), along with the reaction paths of fictitious O_2 with fixed singlet (blue) and fixed triplet (red) spin multiplicity. The transition state of the reaction occurs at the intersystem crossing point (ISC). O_2 is in triplet state in the gas phase. When it approaches the C(111) surface, it gets physisorbed in a -0.07-eV metastable state. The adsorption well is rather shallow, thus the O_2 has some likelihood to escape the MS state. Nevertheless, spin transition could still occur, albeit at a lower probability. From the MS state, the activation energy of spin transition and subsequent adsorption is 0.9 eV. The final adsorbed state has an energy of -0.87 eV relative to the initial state. I performed similar calculations for the dissociative adsorption of O_2 on the bridge site, and the reaction paths are shown in Fig. 6.3. In this reaction, the MS, ISC, and FS are -0.08 eV, 0.85 eV, and -2.39 eV, respectively. While dissociative adsorption has more stable energy compared to molecular adsorption, the energy differences between their physisorbed energies and ISC activation barriers are small. Therefore, during the initial stages of oxidation, O_2 molecules can be both absorbed molecularly on the top site and dissociatively on the bridge site.

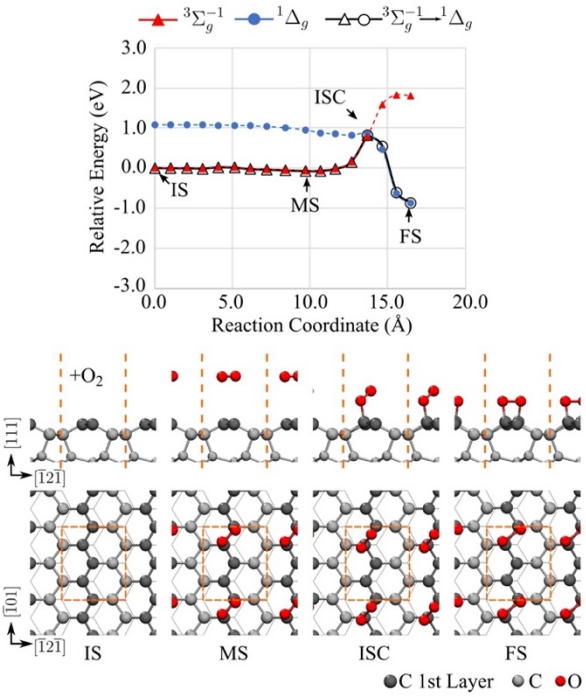

Fig. 6.2. Reaction path of the molecular adsorption of gas phase triplet $^3\Sigma_g^{-1}$ (red curve) and singlet $^1\Delta_g$ (blue curve) O_2 on the top site of the C(111)-(2×1) surface. The reaction path of triplet O_2 that underwent intersystem crossing to singlet state is shown in black curve. Structures corresponding to the initial state (IS), metastable physisorbed state (MS), intersystem crossing state (ISC) and final state (FS) are shown, with silver and red spheres corresponding to oxygen and carbon atoms, respectively.

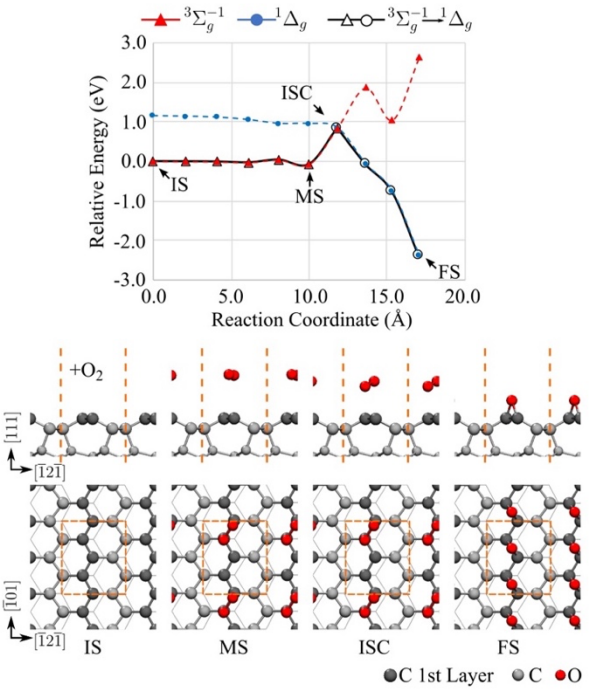

Fig. 6.3 Reaction path of the molecular adsorption of gas phase triplet $^3\Sigma_g^{-1}$ (red curve) and singlet $^1\Delta_g$ (blue curve) O_2 on the bridge site of the C(111)-(2×1) surface. The reaction path of triplet O_2 that underwent intersystem crossing to singlet state is shown in black curve. Structures corresponding to the initial state (IS), metastable physisorbed state (MS), intersystem crossing state (ISC) and final state (FS) are shown, with silver and red spheres corresponding to oxygen and carbon atoms, respectively.

6.3. Oxygen-Induced Surface Dereconstruction and Oxygenation at Monolayer Coverage

Next, I investigated the O_2 adsorption on the C(111)-(2×1) surface up to monolayer coverage. Experiments have shown that at monolayer O coverage, the C(111)-(2×1) surface reconstructs and attain (1×1) periodicity. A previously proposed model by Loh et al. was characterized by broken Pandey chains with carbonyl pairs forming a dimer, where the adjacent carbonyl units share two carbon atoms, and their oxygen atoms form double bond on top of the surface atom. We verified the energetic stability of this model, with an adsorption energy per O_2 molecule of -1.68 eV (Fig. 6.4E). We also discovered two additional stable O-terminated structures. In the first structure, oxygen atoms are adsorbed on top, on bridge, and on backbond sites, forming a mixture of carbonyl and ether groups (Fig. 6.4F). The second structure contains oxygen atoms alternately adsorbed on the bridge and the backbond sites, forming ether groups (Fig. 6.4G). The adsorption energies per O_2 molecule in these structures are -1.94 -1.84 eV and -2.08 eV, respectively.

We consider three reaction paths that will lead to O-terminated C(111) surfaces. For the first reaction path, we assume that O_2 adsorbs molecularly on the top site (Fig. 6.4). This is followed by molecular adsorption of a second O_2. The activation energy of second O_2 adsorption is 0.89 eV higher compared to the first, while the adsorption energy is 0.33 eV weaker. To gain insight, we plotted the total density of states of a surface atom before and after O_2 molecular adsorption on its neighbors (Fig. 6.5). As reported by Reed et al., the C(111)-(2×1) surface is metallic and the calculation confirms that it has $2p_z$ states at the Fermi level. Moreover, there are bonding and antibonding states near the Fermi level. Surface states existing near the Fermi level can hybridize with adsorbate orbitals, stabilizing the transition state of the adsorption process. On the other hand, a large gap at the Fermi level hinders the hybridization

of adsorbate orbitals with the surface states and destabilizes the transition state off the adsorption process. After the adsorption of the first O_2 molecule, the $2p_z$ states at the Fermi level disappear, and the $2p_z$ states below and above the Fermi level shifted to lower and higher energies, respectively. This shifting of $2p_z$ states could explain the increase of the activation energy and weakening of the adsorption energy of the second O_2 adsorption (Fig. 6.3 B-C).

The O_2-terminated C(111)-(2×1) surface can become more stable by O_2-dissociation and 2×1 to 1×1 surface reconstruction into carbonyl-terminated C(111)-(1×1):O surface (Fig. 6.4 C-E). As O_2 molecules dissociate, the π-bonded chain breaks and the surface atoms form C dimers. The C=O of the carbonyl is bonded to the first- and second-layer C atoms. This makes the carbonyl inclined relative to the surface. This transformation lowers the energy of the system by 1.97 eV. Afterwards, the surface carbon atoms reconstruct to form buckled 6-member rings with the sublayer atoms, while two of the oxygen atoms will move from the top site to the bridge and backbond site forming combined carbonyl and ether-terminated C(111)-(1×1):O_{ML} surface (Fig. 6.4 E-F). Finally, the surface reconstructs further, forming interconnected buckled 6-member rings with oxygen atoms on the bridge and backbond sites forming ether-terminated C(111)-(1×1):O surface (Fig. 6.4 F-G). While the reactions from E to G lower the energy of the system, the activation energies are high. Therefore, these surfaces may only exist in high pressure and temperature conditions.

The second reaction path is shown in Fig. 6.6. Here, we assume that O_2 dissociatively adsorbs on the bridge site (Fig. 6.6 A-B). This saturates all the dangling bonds, rendering the surface inert. Next, a second O_2 dissociatively adsorbs, and the surface undergoes 2×1 to 1×1 reconstruction forming carbonyl-terminated C(111)-(1×1):O (Fig. 6.6 B-C). The activation energy of second O_2 adsorption is 1.06 eV higher compared to the first, while the adsorption

energy is 1.42 eV weaker. This suggests that the adsorption energy of O_2 on C(111) depends on the coverage. The succeeding reactions show the reconstruction of the surface forming buckled 6-membered rings with oxygen atoms on the bridge and backbond sites (Fig. 6.6 C-E).

Finally, the third reaction path is shown in Fig. 6.7. As with the first reaction path, we assume that O_2 adsorbs molecularly on the top site (Fig. 6.7 A-B). Afterwards, O_2 dissociates, and moves to the bridge site (Fig. 6.7 B-C). The succeeding reactions are similar to the second reaction path: a second O_2 adsorbs dissociatively, forming C(111)-(1×1):O with monolayer oxygen coverage (Fig. 6.7 C-D), followed by surface reconstruction into buckled 6-membered rings with oxygen atoms on the bridge and backbond sites (Fig. 6.7 D-F).

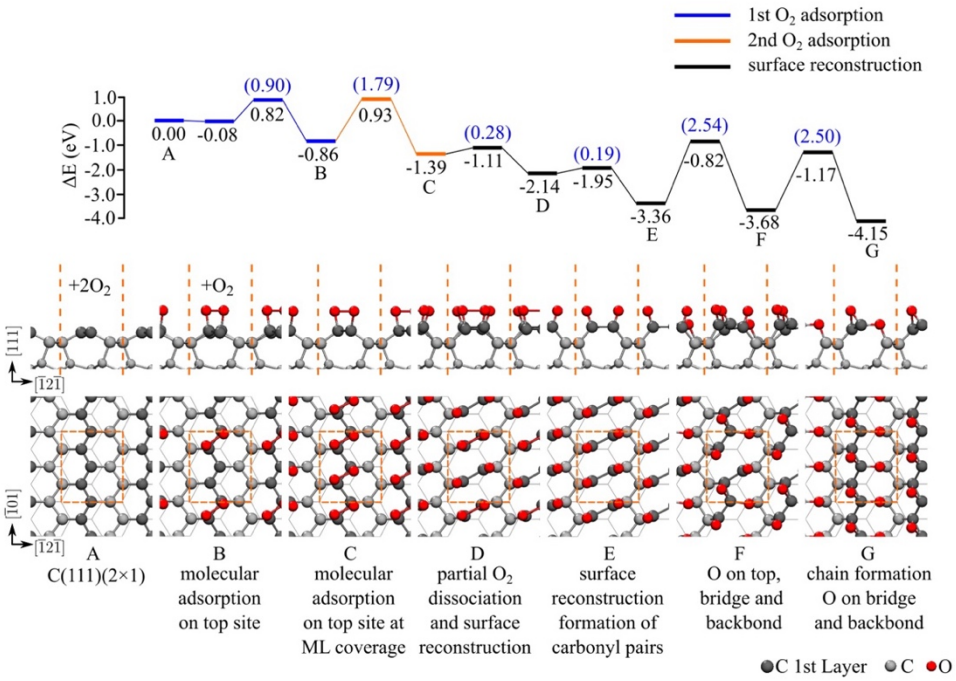

Fig. 6.4. Adsorption of two O_2 molecules on the C(111)-(2×1) surface (first reaction path). Stable structures corresponding to the labeled states are shown, with silver and red spheres corresponding to oxygen and carbon atoms, respectively. The reaction path of the first O_2 adsorption, the second O_2 adsorption, and the subsequent surface reconstructions are shown in blue, orange, and black lines, respectively. Relative energies and activation energies are labeled in black and blue texts, respectively.

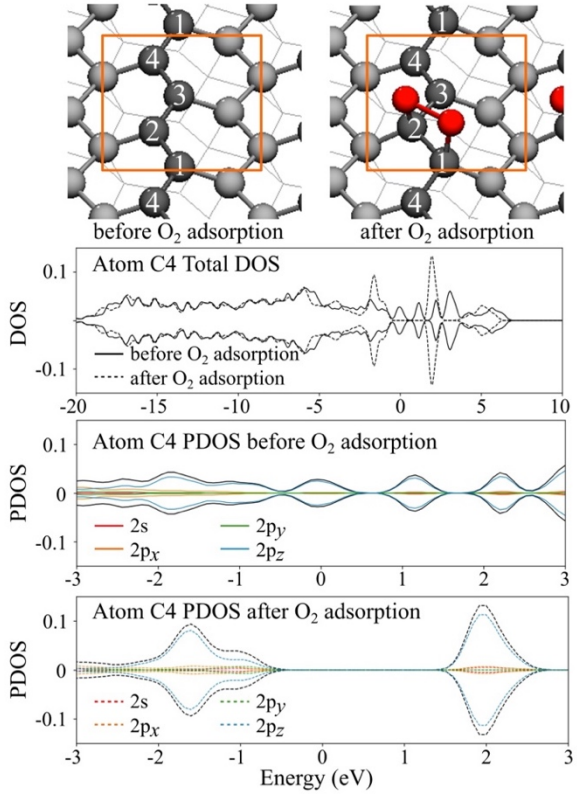

Fig. 6.5. Total and projected density of states plot of the surface atom C4 before and after O_2 adsorption on an adjacent site.

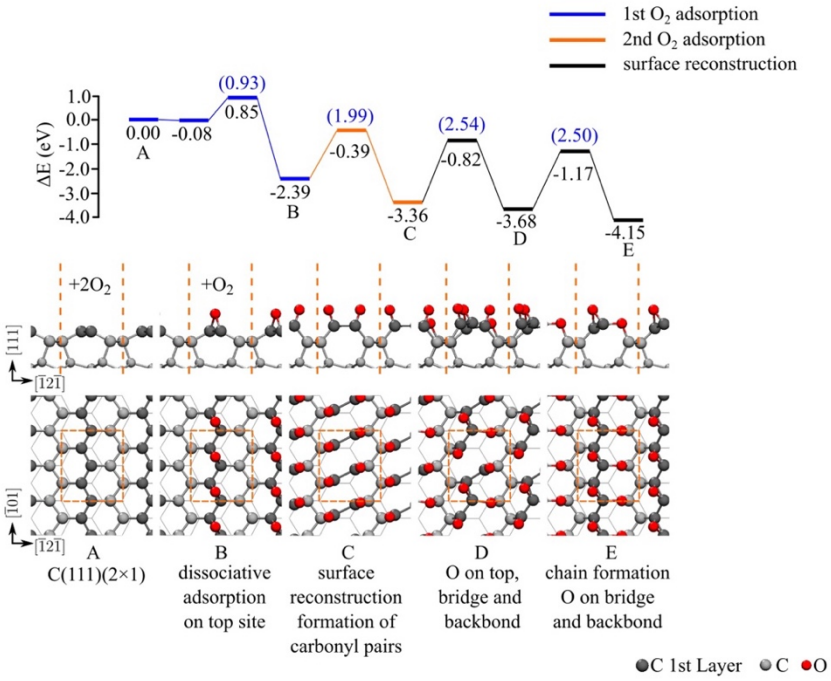

Fig. 6.6. Adsorption of two O_2 molecules on the C(111)-(2×1) surface (second reaction path). Stable structures corresponding to the labeled states are shown, with silver and red spheres corresponding to oxygen and carbon atoms, respectively. The reaction path of the first O_2 adsorption, the second O_2 adsorption, and the subsequent surface reconstructions are shown in blue, orange, and black lines, respectively. Relative energies and activation energies are labeled in black and blue texts, respectively.

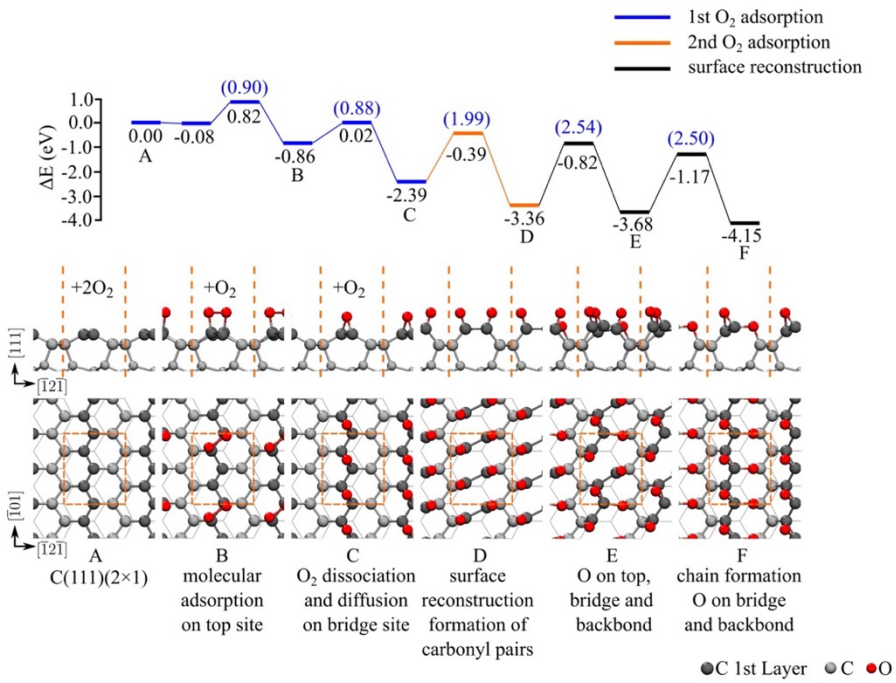

Fig. 6.7. Adsorption of two O_2 molecules on the C(111)-(2×1) surface (second reaction path). Stable structures corresponding to the labeled states are shown, with silver and red spheres corresponding to oxygen and carbon atoms, respectively. The reaction path of the first O_2 adsorption, the second O_2 adsorption, and the subsequent surface reconstructions are shown in blue, orange, and black lines, respectively. Relative energies and activation energies are labeled in black and blue texts, respectively.

6.4. Comparison of the O_2 Adsorption on the C(111) and C(100) Surfaces

The simulation results that I presented in Chapter 5.1 and 5.2 and in the beginning of this chapter have shown that there is a notable difference in the adsorption of O_2 on the C(111) and (100) surface. First, while triplet O_2 can be chemisorb on the C(100) surface, it is not possible on the C(111) surface as shown in the antibonding reaction energy curves (Fig. 6.2, 6.3). Second, the metastable adsorption of triplet O_2 on the C(111) surface is much lower compared to the C(100) surface. Therefore, a triplet O_2 metastably adsorbed on the C(111) surface could more easily escape, leading to lower spin transition and sticking probability compared to the C(100) surface. Third, the activation energy of O_2 adsorption on the C(111)-(2×1) surface is higher than that of the C(100)-(2×1) surface. The reason is that the π-bonding reconstructed C(111)-(2×1) has no dangling bonds while the C(100)-(2×1) has 1 dangling bond per surface atom. Moreover, the surface energy of the C(111)-(2×1) is lower compared to the C(100)-(2×1) surface. This shows that the C(111) is chemically less reactive compared to the C(100) surface. Fourth, the adsorption energies on the C(111) surface for both molecular and dissociative cases are lower compared to the C(100) surface.

To investigate further, I calculated the differential adsorption energy of O_2 on the C(111) and C(100) surfaces (Fig. 6.8). I consider the dissociative adsorption since it gives the most stable adsorption configurations. At 0.25 and 0.5 ML, the C(111) surface is terminated by O atoms adsorbed on the bridge site. At 0.75 ML, the C(111) surface partially reconstructs and is terminated by O atoms on top and bridge sites. At 1.0 ML, the C(111) surface fully reconstructs and is terminated by O atoms on the top site forming carbonyl pairs. These calculations show that the maximum adsorption energy is attained between 0-0.5 ML and

decrease considerably between 0.5-0.75 ML. Between 0.75-1.0 ML, the adsorption energy increases. The weakened adsorption energy at coverages greater than 0.5 ML explain the necessity of a high temperature environment to achieve monolayer coverage on the C(111) surface. In contrast, the calculated differential adsorption energy of the O_2 dissociative adsorption only has small differences for various coverages (Fig. 6.7).

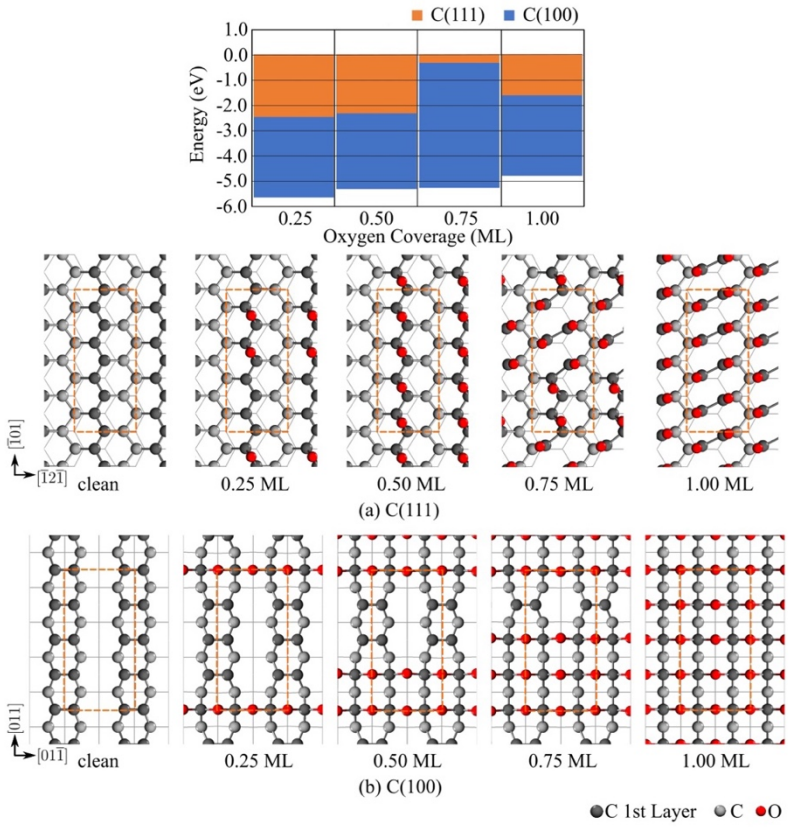

Fig. 6.8. Differential adsorption energy of O_2 molecule on the (a) C(111)-(2×1) and (b) C(100)-(2×1) surfaces with respect to gas-phase O_2. The O_2 adsorption energy on the C(111)-(2×1) surface is coverage-dependent, while for the C(100)-(2×1) surface it is virtually coverage-independent. Silver and red spheres correspond to carbon and oxygen atoms, respectively. (A color version of this figure can be viewed online.)

6.5. Oxidative Etching of the Diamond (111) and (100) Surfaces

Several experiments reported that the primary product of dry oxygen etching of the diamond (111) and (100) surfaces is CO (Hossain et al., 1999; Loh et al., 2002). To verify this observation, I calculated the activation energy of CO and CO_2 desorption from flat carbonyl pair-terminated C(111)-(1×1):O and ether terminated C(100)-(1×1):O, and various oxidized diamond (111) and (100) surfaces models. The results are shown in Table 6.1. With the exemption of flat C(111)-(1×1):O surface, the activation energies of CO desorption are all lower to that of CO_2, confirming the experimental observation. For this reason, I focus the oxidative etching simulations on etching via CO desorption.

First, I perform successive CO desorption reaction path calculations, starting with flat oxygen-terminated diamond surfaces and ending with the complete etching of the top-most layer. For each surface, I considered several CO desorption locations and used the activation energies as a criterion in selecting the most likely reaction path. The most likely reactions are presented in this chapter, while the other reactions are shown in the Appendix (A3). The test calculations have shown several surface dangling bonds present on the etched C(111) surfaces, therefore, spin-polarized calculations are necessary. To enable a direct comparison between the oxidative etching of the C(111)-(1×1):O and C(100)-(1×1):O surfaces, I recalculated the CO desorption reaction from the ether-terminated C(100)-(1×1):O surface in the previous chapter, where I used spin restricted calculations (Enriquez et al., 2021). The activation energies of CO desorption from the C(100) surfaces slightly differs for the spin polarized and spin restricted calculations, but the general conclusion in the previous chapter is unaffected.

I start with the CO desorption from the carbonyl pair-terminated C(111)-(1×1):O surface. The first CO is desorbed in a two-step reaction. First, the CO molecule detaches from the surface and attaches to two oxygen atoms of adjacent carbonyl groups with an activation energy of 0.36 eV (Fig. 6.9 A-B). Second, the CO fully desorbs with an activation energy of 2.94 eV (Fig. 6.9 B-C). Overall, the desorption of the first CO is exothermic. The next CO is desorbed from the remaining half of the carbonyl pair. This reaction is endothermic with an activation energy of 1.96 eV (Fig. 6.9 C-D). The third and fourth CO are desorbed from the carbonyl pair non-adjacent to the vacancy. The CO desorption activation energy from the first half of the carbonyl pair is 3.10 eV (Fig. 6.9 D-E). The remaining half desorbs more easily, with an activation energy of 1.24 eV (Fig. 6.9 E-F).

After the desorption of 4 CO molecules, the resulting structure has two isolated carbonyl pairs. The CO desorption activation energies from the first and second half of the isolated carbonyl pair are 3.05 eV and 1.67 eV (Fig. 6.9 F-H). The corresponding CO desorption activation energies of the remaining carbonyl pair are 3.18 eV and 1.85 eV (Fig. 6.9 H-J). The reaction path shows that following the etching of the first carbonyl pair, the CO desorption reactions are all endothermic and follow a pattern of alternating high and low activation energies, corresponding to the desorption of the first and second half of the carbonyl pair, with an average activation energy of 2.35 eV. This value agrees reasonably well with the average CO desorption energy reported in the experiment (2.56 eV) (Loh et al., 2002). The carbonyl pairs are etched in a staggered order, i.e., when a carbonyl pair is etched, the second nearest carbonyl pair will be etched next. As a neighboring carbonyl pair is etched, the O steric repulsion is reduced which causes the remaining carbonyl pair to relax. To illustrate this concept, Figure 6.10 (a)-(b) shows an array of carbonyl pairs and an isolated carbonyl pair. The carbonyl pair array exhibits an $O{=}C_{layer1}{-}C_{layer1}$ angle of 109.1°, while this increases to 115.1°

in the isolated carbonyl pair. This implies that the carbonyl pair is strained due to oxygen steric repulsion. Etching the neighboring carbonyl pair lifts this strain, as the C-O bonds of the carbonyl pair twist in opposite directions to maximize the distance between two oxygen atoms and become more planar. The relaxed carbonyl pair is more stable and has a higher CO desorption activation energy compared to that of the strained carbonyl pair. For physical systems, the staggered etching will eventually lead to the loss of long-range crystallographic order of the surface atoms.

Figure 6.11 shows the oxidative etching reaction of the ether-terminated C(100)-(1×1):O surface. The CO desorption reaction starts by the movement of the O atom from the bridge site to the top site forming carbonyl. The activation energy of the initial CO desorption is 3.88 eV (Fig. 6.10 A-B). The next CO is desorbed adjacent to the vacancy left by the previous CO desorbed. The succeeding CO desorptions follow a row-wise etching order along the [011] direction with activation energies that are lower compared to the first CO desorption, with values of 3.43 eV, 1.39 eV, and 1.77 eV (Fig. 6.10 B-E). The atoms on the etched row dimerize to attain a stability similar to the original surface. After CO desorption from the first row, the adjacent row becomes carbonyl terminated. The etching of the adjacent row follows the similar row-wise etching order as the first row, with activation energies of 4.09 eV 2.89 eV, 1.46 eV, and 1.66 eV (Fig. 6.11 E-I). The calculated desorption activation energy of an isolated CO is 1.66 eV agrees reasonably well with experiment value of $1.8 - 1.9$ eV for single crystal diamond (de Theije et al., 2000; Nimmagadda et al., 1990). Since the etching proceeds along rows, the crystallographic orientation of the surface atoms will be preserved.

Table 6.1. Comparison of CO and CO_2 desorption reaction energy and activation energies.

structure	CO		CO_2	
	Activation Energy (eV)	Reaction Energy (eV)	Activation Energy (eV)	Reaction Energy (eV)
C(111)				
flat surface 1ML (Fig. 6.9A)	0.36, 2.94	-2.35, 1.45	0.37, 1.26	-2.86, 0.20
isolated carbonyl pair (Fig. 6.9H)	3.18	3.01	5.04	4.98
non-flat surface 1ML (Fig. 6.12H)	0.64	0.70	1.85	1.07
C(100)				
flat surface 1ML (Fig. 6.11A)	3.88	2.43	4.94	4.06
1 vacancy (Fig. 6.11B)	3.43	3.27	4.89	4.62
2 vacancies (Fig. 6.11C)	1.39	1.24	2.85	2.61
3 vacancies (Fig. 6.11D)	1.77	1.92	3.77	3.24

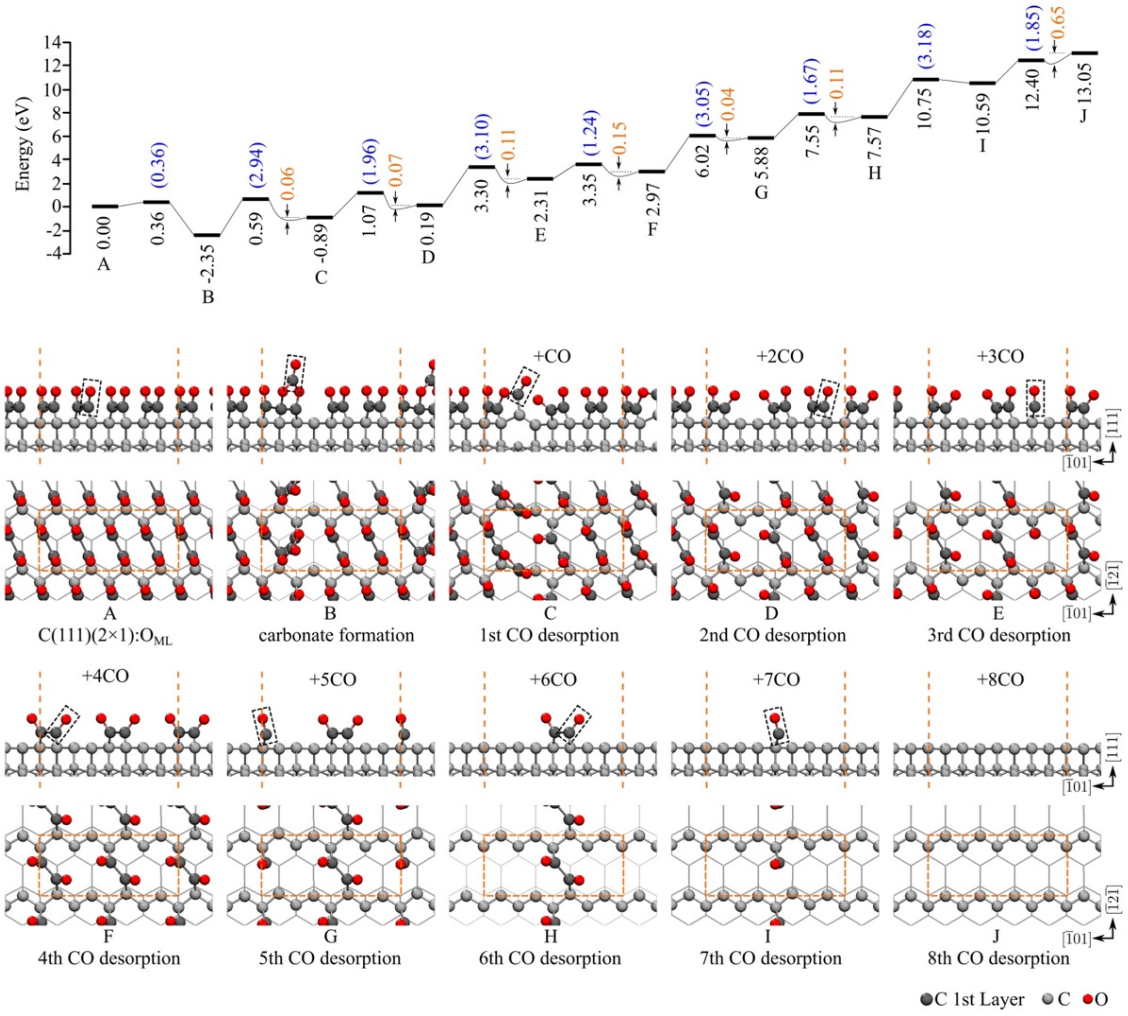

Fig. 6.9. Etching of the top-layer atoms of the carbonyl pair-terminated C(111)-(1×1):O surface through successive CO desorption. The relative energies and activation energy of reactions are labeled in black and blue texts, respectively. Physisorption energies of CO are labeled in orange text. Grey and red spheres correspond to carbon and oxygen atoms, respectively.

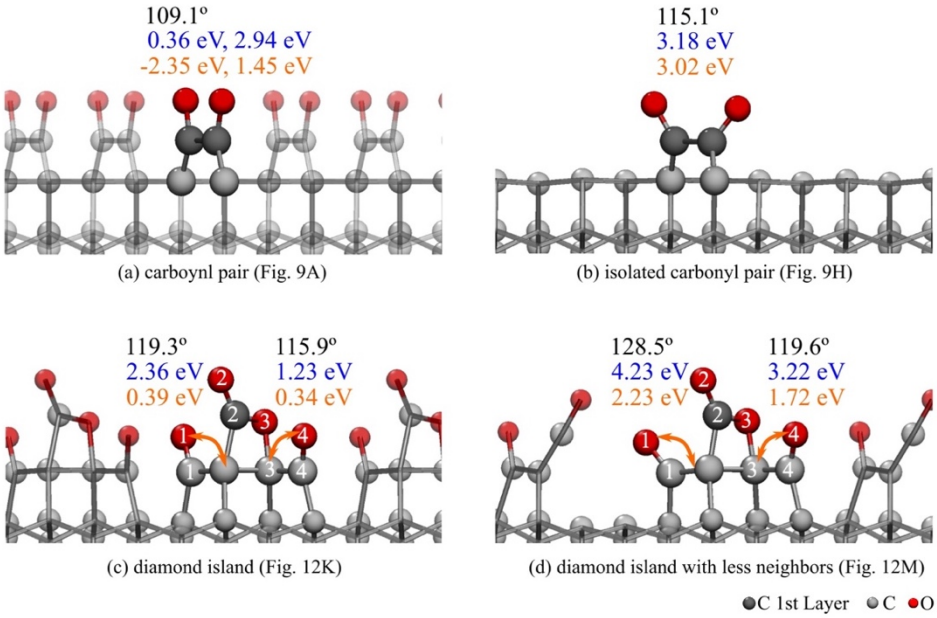

Fig. 6.10. Comparison of carbonyl angles and CO desorption activation energy (blue text) and reaction energy (orange text) on carbonyl pairs and diamond islands. Grey and red spheres correspond to carbon and oxygen atoms, respectively.

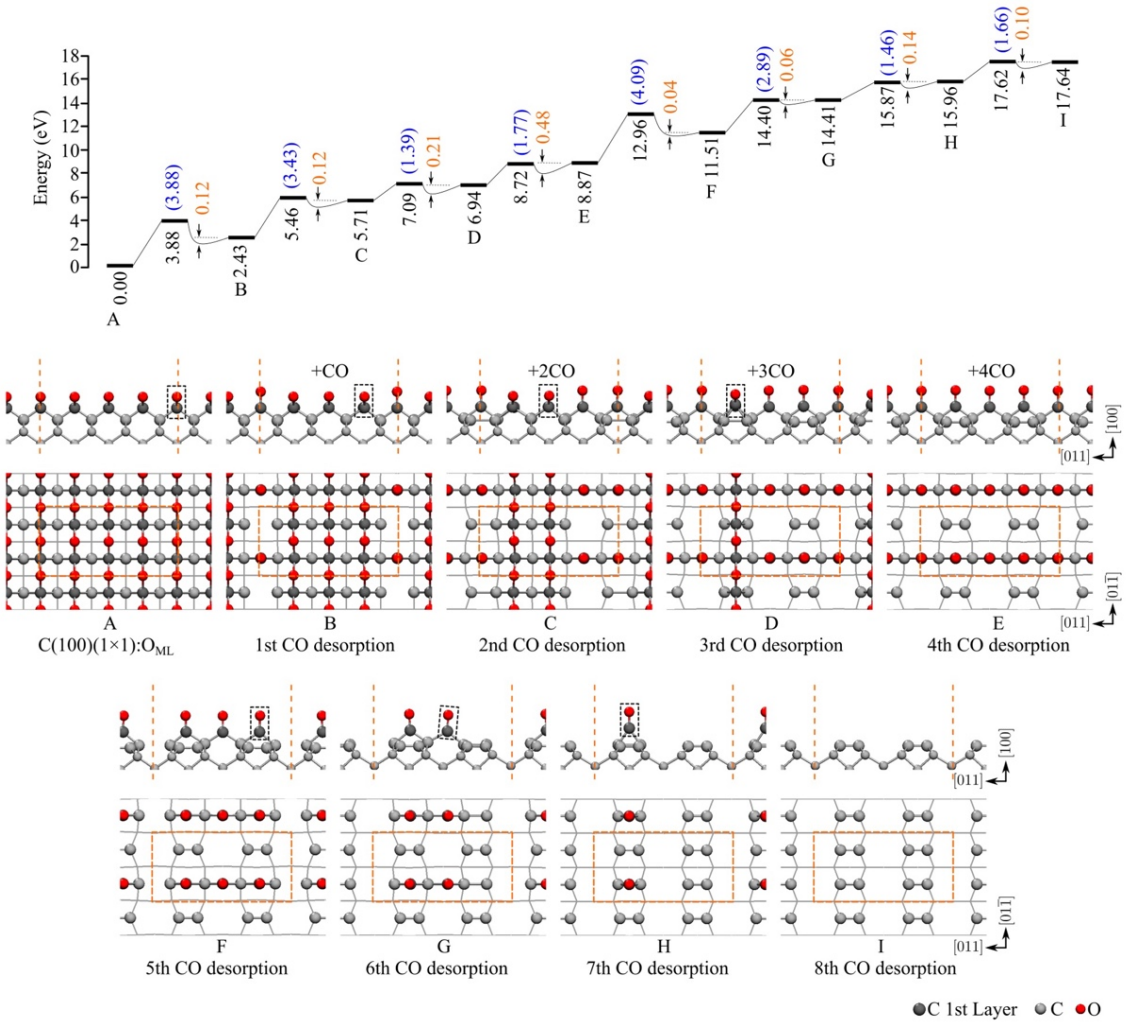

Fig. 6.11. Etching of the top-layer atoms of the ether-terminated C(100)-(1×1):O surface through successive CO desorption. The relative energies and activation energy of reactions are labeled in black and blue texts, respectively. Physisorption energies of CO are labeled in orange text. Grey and red spheres correspond to carbon and oxygen atoms, respectively.

6.6. Static Steady-State Oxidative Etching Simulation of the Diamond (111) and (100) Surfaces

In this final section, I discuss the results of static steady-state reaction path simulations of successive CO desorption and O_2 adsorption of the carbonyl pair-terminated C(111)-(1×1):O and ether terminated C(100)-(1×1):O surfaces. I performed simulations until the top layer atoms are removed and oxidative etching pattern emerges.

I start with the static steady-state oxidative etching simulations of the carbonyl pair-terminated C(111)-(1×1) surface (Fig. 6.12). The first four CO desorption reactions proceed in a staggered order leading to the formation of two isolated carbonyl pairs (Fig. 6.12 A-F). The surface has half of its the second-layer C atoms exposed. We assume that there is high probability for two O_2 molecules to dissociatively adsorb on the exposed sublayer (Fig. 6.12 F-H). As the dissociated O atoms adsorb, the C-C bond between the sublayer is broken, and carbonyls are formed. The C=O of the carbonyl bonds with second- and third-layer C atoms. This makes the carbonyl inclined relative to the surface. The average activation energy of the O_2 dissociative adsorption is 1.61 eV and average adsorption energy is -3.98 eV. This reaction transforms the surface into island structures with a carbonyl pair on the top layer and two carbonyl groups on the second layer.

The O adsorption on the second layer C atoms strains the carbonyl pairs on the first layer, reducing the O-O distance from the adjacent carbonyl pair along $[\bar{1}2\bar{1}]$ from 3.93 Å to 2.66 Å. This increases the O steric repulsion and significantly lowers the CO desorption activation energy from one of the carbonyl pairs to 0.64 eV (Fig. 6.12 H-I). The next CO is desorbed from the other carbonyl pair with an activation energy of 1.33 eV (Fig. 6.11 I-J).

The surface of the structure in Fig. 6.12-J consists of 2-layer islands in the supercell, where each island consists of two carbonyl groups and one ether group with an oxygen atom bridging the first and the second layer carbon atoms. The island is stable, with relatively high average CO desorption activation energies of 3.00 eV from every site. At this point, we assume that there is sufficient time for O_2 to dissociatively adsorb on the second layer (Fig. 6.12 J-K). The activation energy of the dissociative adsorption is 1.62 eV with an adsorption energy of 2.36 eV. The next two CO molecules desorb from the second layer of one of the islands, modeled in this simulation as the left island, reducing it to carbonyl and a ketene-like group (Fig. 6.12 K-M). Desorption of CO from this structure has a high activation energy (3.04 eV). Thus, the next CO will likely desorb on the right island. The next desorption occurs from the second right-hand most CO from the right island with an activation energy of 2.81 eV, followed by the isolated CO with an activation energy of 1.01 eV (Fig. 6.11 M-O). This forms the structure in Fig. 6.12 O, consisting of two clusters of carbonyl and ketene, and the diamond crystallographic order of the C(111) surface is no longer well defined. The CO desorption from this structure proceeds by breaking the double bond between the top layer C atom and the second layer C atom, with an average activation energy of 3.12 eV, followed by desorption of the carbonyl on the second layer, with an average activation energy of 2.50 eV (Fig. 6.12 O-S). The final structure is non-reconstructed C(111)-(1×1) surface with a single-atom asperity forming three bonds with the surface atoms. From here on, the oxidative etching of the C(111) surface is expected to proceed along different reaction pathways but form the same functional groups and follow the same etching mechanism.

It is noteworthy that the CO desorption activation energies from the diamond island with complete neighbors (Fig. 6.12 K) are higher compared to those of the diamond island with less neighbors (Fig. 6.12 M). This is illustrated in Fig. 6.10 c-d. For the diamond island with

complete neighbors, the O=C_{layer2}-C_{layer2} angle of the left-most carbonyl group (central C and O atoms labeled as C1 and O1) is 119.3°, and the CO desorption activation energy is 2.36 eV. After two CO desorption reactions from its neighboring island, the O=C_{layer2}-C_{layer2} angle increased to 128.5°, and the CO desorption activation energy is increased to 4.23 eV. In addition, the O-C_{layer2}-C_{layer2} angle of the left-most carbonyl group (central C and O atoms labeled as C4 and O4) also increased from 115.9° to 119.6°, and the CO desorption activation energy increased from 1.23 eV to 3.22 eV. Finally, the desorption of CO from the neighbors also reduces the O steric repulsion, leading to an increase in CO desorption energies of the atoms labeled C2-O2 from 2.52 eV to 3.62 eV and C3-O3 from 1.81 eV to 2.81 eV. In addition, the CO desorption reaction energies from the diamond island with complete neighbor are lower compared to those with less neighbors. A complete comparison of the change in desorption activation energy and reaction energies illustrated in Fig. 6.10 is shown in Table 6.2. These results show that the functional groups on the C(111) surface relax with less neighbors. Therefore, the next CO will desorb from areas with more neighbors and higher O steric repulsion, leading staggered etching order.

I performed similar simulations for the ether-terminated C(100)-(1×1):O surface (Fig. 6.13). Etching proceeds with row-wise CO desorption along the [011] direction. The etched row reconstructs to form carbon dimers (Fig. 6.13 A-E). The adjacent row, which has oxygen atoms at the top position, can also be viewed as carbonyl chain. CO desorption from one of these carbonyl groups has a relatively high activation energy (4.09 eV). At this point, we assume that O_2 adsorbs on the etched row. Oxygen adsorbs molecularly then it dissociates and drives surface dereconstruction with an average activation energy of 0.37 eV and adsorption energy of 4.91 eV (Fig. 6.13 E-G). The oxygen atoms then move from the top to the bridge position, forming an ether chain which further lowers the energy of the system by 1.18 eV (Fig.

6.13 G-H). The CO-desorption activation energy from the ether chain is higher (4.32 eV) compared to the CO desorption activation energy from the carbonyl chain in the first layer (4.04 eV), so we choose the first layer as the next CO desorption site. The CO in the first layer desorbs in a similar row-wise order. The etched row reconstructs and form carbon dimers (Fig. 6.13 H-L). The final structure is oxygen-terminated C(100)-(2×1) surface with half monolayer coverage. From here on, the oxidative etching of the C(100)-(2×1) surface is expected to proceed in a similar row-wise etching reaction pathway.

In summary, the steady-state etching simulation reveals another contrasting behavior between the C(111)-(2×1) and C(100)-(2×1) surfaces. For the C(111)-(2×1) surface, the adsorption of O_2 on the etched surface strains and destabilizes the adjacent carbonyl group, lowering the CO desorption activation energy. This leads to the formation of islands which follows a staggered etching order. Fragments of the island may remain as the next batch of oxygen molecules attacks the sublayer atoms. These lead to the loss of crystallographic order of the surface atoms and explain the rough surface morphology observed in the experiments. In contrast, for the C(100)-(2×1) surface, the adsorption of O on the etched surface stabilizes the structure and does not affect the geometry of the existing carbonyl groups. The row-wise etching and stable etched surface preserve the crystallographic orientation of the surface atoms and explain the flat morphology and stable steps observed in the experiment.

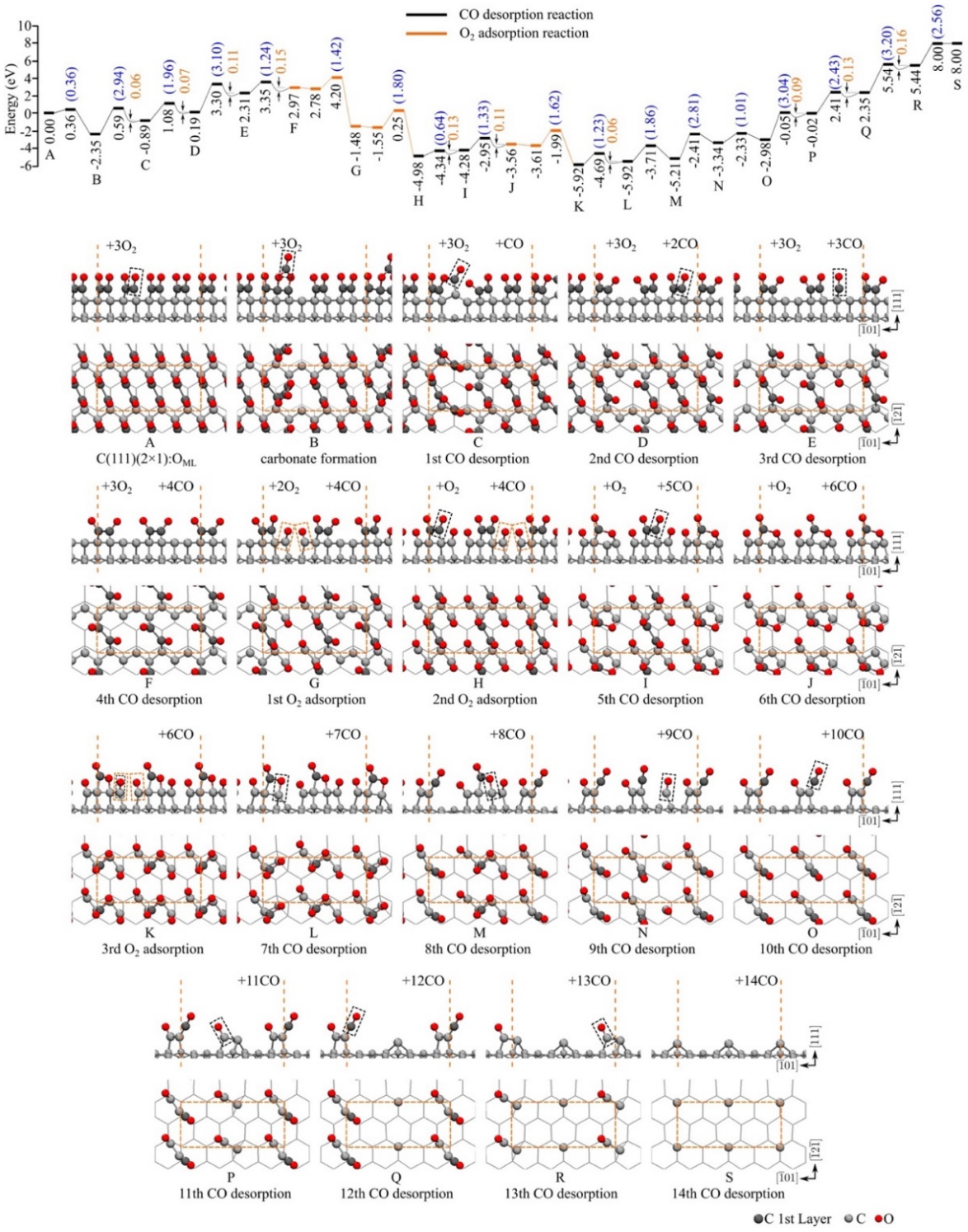

Fig. 6.12. Steady-state oxidative etching of the carbonyl pair-terminated C(111)-(1×1):O surface through successive CO desorption and O_2 adsorption. The relative energies and activation energy of reactions are labeled in black and blue texts, respectively. Physisorption energies of CO and O_2 are labeled in orange text. Grey and red spheres correspond to carbon and oxygen atoms, respectively, while the dangling bonds are represented by blue cylinder.

Table 6.2. CO desorption activation and reaction energies from array and isolated carbonyl pair and diamond island as shown in Fig. 6.10. The CO desorption activation energy and reaction energy increase when CO is desorbed from the neighboring locations.

CO Desorbed	Activation Energy (eV)	Reaction Energy (eV)
	carbonyl pair*	
(a) non-isolated	0.36, 2.94	-2.35, 1.45
(b) isolated	3.18	3.02
	diamond island†	
(c) with complete neighbors		
C1-O1	2.36	0.39
C2-O2	2.52	2.52
C3-O3	1.81	0.61
C4-O4	1.23	0.34
(d) with less neighbors		
C1-O1	4.23	2.23
C2-O2	3.62	2.98
C3-O3	2.81	1.84
C4-O4	3.22	1.72

*Fig. 10 (a) - (b)
† Fig. 10 (c) - (d)

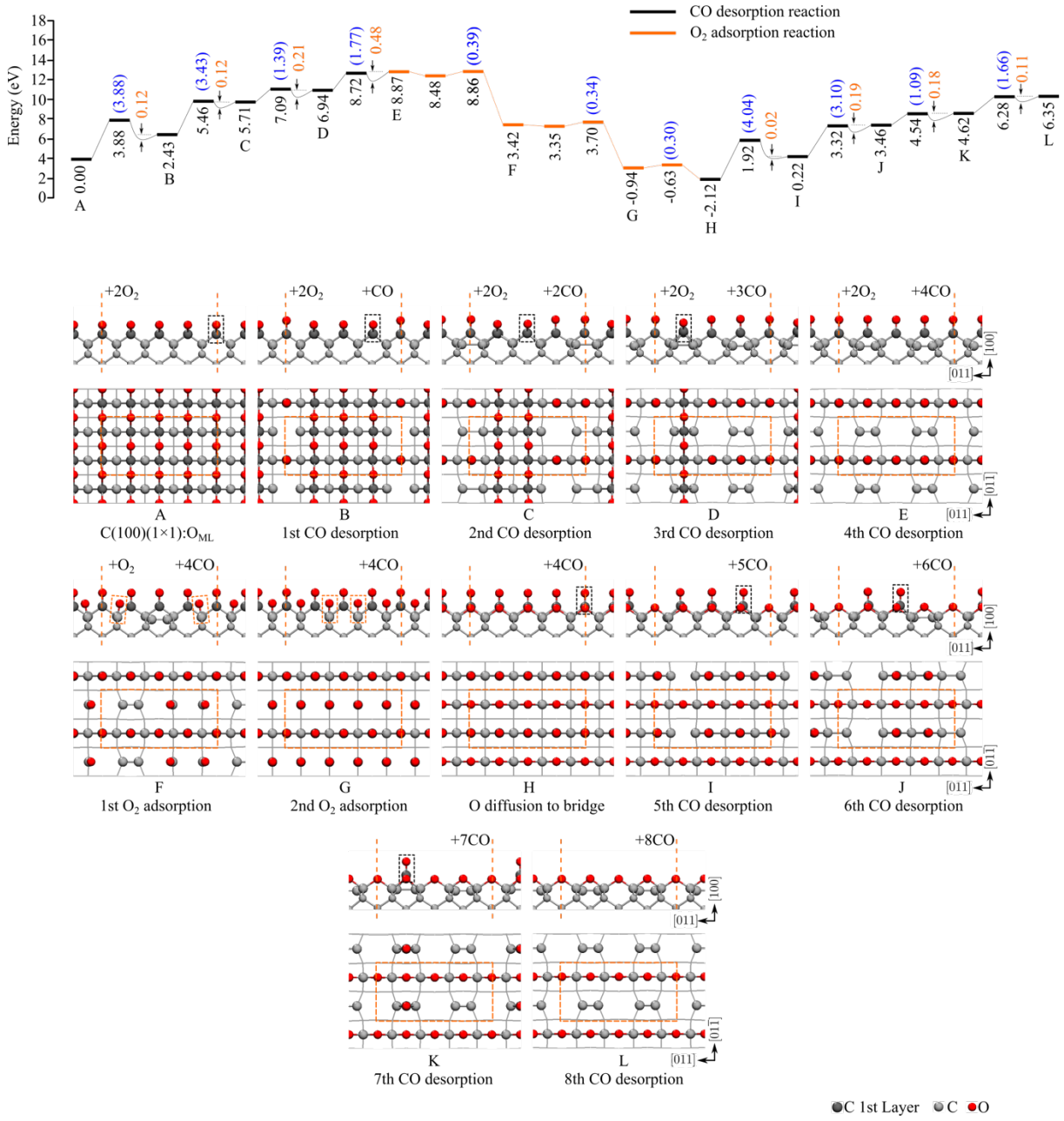

Fig. 6.13. Steady-state oxidative etching of the ether-terminated C(100)-(1×1):O surface through successive CO desorption and O_2 adsorption. The relative energies and activation energy of reactions are labeled in black and blue texts, respectively. Physisorption energies of CO and O_2 are labeled in orange text. Grey and red spheres correspond to carbon and oxygen atoms, respectively, while the dangling bonds are represented by blue cylinder.

CHAPTER 7

ORIGIN OF THE SURFACE FACET DEPENDENCE IN THE THERMAL DEGRADATION OF THE DIAMOND (111) AND (100) SURFACES

Publication: *Enriquez, J.I., Halim, H., Yamasaki, T., Michiuchi, M., Inagaki, K., Geshi, M., Hamada, I., and Morikawa, Y. 2024. Origin of the Surface Facet Dependence in the Thermal Degradation of the Diamond (111) and (100) Surfaces in Vacuum Investigated by Machine Learning Molecular Dynamics Simulations. Carbon 226 119223. https://doi.org/10.1016/j.carbon.2024.119223*

Diamond is a thermodynamically unstable form of carbon, and when heated to sufficiently high temperatures, changes into graphite. This thermal degradation process, which is commonly referred to as graphitization, typically produces not just crystalline graphite but also amorphous carbon.

Experiments have shown that the C(111) and C(100) surfaces have different thermal degradation susceptibilities. Atomistic simulations of graphitization require large system sizes and long simulation time which are not possible to do with first principles simulations. For this reason, I employed machine learning molecular dynamics (MLMD) as an alternative method. In this chapter, I present the results of my simulations and develop a theory on the origins of the surface facet-dependent diamond surface thermal degradation.

7.1. Graph Neural Network Interatomic Potential Model for Production Simulations

I constructed a machine learning interatomic potential using the graph neural network (GNN) model. The GNN interatomic potential used in the production simulations has been constructed from the database of 6,302 structures, consisting of 452,656 atomic environments with 6,302 total energy data corresponding to the structures and 1,357,968 force components. The energy and force root-mean-square errors (RMSE) of the test set are $0.003\ \mathrm{eV/atom}$ and $0.085\ \mathrm{eV/Å}$, respectively. I performed pre-production validation of the GNN-IP by simulating the C(111) and C(100) surfaces (Table 7.1) at increasing temperatures, up to $3600\ \mathrm{K}$ for the C(111) and $4400\ \mathrm{K}$ for the C(100). Comparison of the DFT and GNN energies and forces are shown in Figure 7.1. The energy and force RMSEs of the pre-production validation set are $0.005\ \mathrm{eV/atom}$ and $0.128\ \mathrm{eV/Å}$, respectively. The test and validation RMSEs that we obtained using GNN method are lower compared with the RMSE of the ML-IP for diamond and carbon materials constructed using Gaussian approximation potential (GAP) and neuro evolution potential (NEP) methods (Li and Jiang, 2023; Rowe et al., 2020). The sampled MD trajectories of the pre-production run have no extrapolated atomic environment feature vector with respect to the database. Next, we use the GNN-IP model to predict the equilibrium interatom separation in graphite and diamond crystals. The predicted interatom separation of both graphite and diamond agrees very well with DFT and experiment (Table 7.2). Finally, we used the GNN-IP model to calculate the surface energy of the diamond surfaces. The C(100) surface has higher surface energy compared to the C(111) surface, in good agreement with the DFT calculation (Table 7.3).

Table 7.1. Diamond surface models for pre-production validation and production simulations, showing the simulation box sizes x and y and the number of atoms in each structure.

Type of Surface	x (Å)	y (Å)	No. of Atoms
Pre-Production Validation			
Flat C(111) (4×4)	8.7488	10.1023	208
Flat C(100) (4×4)	10.1023	10.1023	208
Production Simulation			
Flat C(111) (8×8)	17.4977	20.2046	832
Stepped C(111) / C(665)	24.8761	20.2046	1184
Flat C(100) (8×8)	20.2046	20.2046	832
Stepped C(100) / C(1 1 10) Type A	25.5071	20.2046	1000
Stepped C(100) / C(1 1 10) Type B	25.5071	20.2046	1048

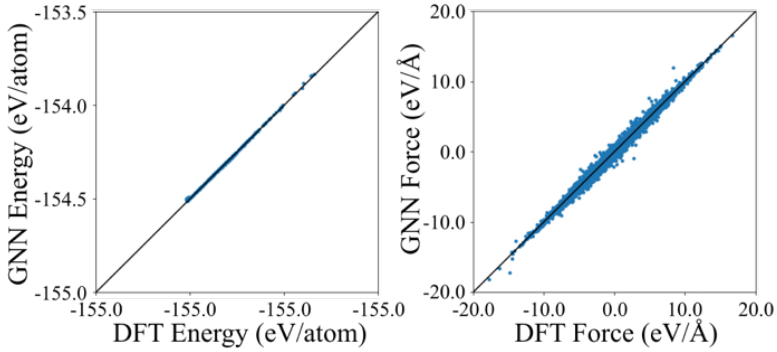

Fig. 7.1. Comparison of the DFT and GNN energies and forces for the pre-production validation dataset, with energy and force RMSEs of $0.005\ \mathrm{eV/atom}$ and $0.128\ \mathrm{eV/Å}$, respectively.

Table 7.2. GNN predicted interatom separation in graphite and diamond crystals compared with DFT and experiment.

Structure	GNN	DFT	experiment
Graphite	1.425 Å	1.424 Å	1.419 Å (Kittel, 1996)
Diamond	1.544 Å	1.546 Å (Enriquez et al., 2021)	1.545 Å (Shikata et al., 2018)

Table 7.3. GNN predicted diamond surface energies compared with DFT.

	GNN	DFT (this study)	DFT (Stekolnikov et al., 2002))
C(111)-(2×1)	3.42 J/m^2 (1.18 eV/atom)	4.09 J/m^2 (1.41 eV/atom)	4.06 J/m^2 (1.37 eV/atom)
C(100)-(2×1)	5.07 J/m^2 (2.02 eV/atom)	6.05 J/m^2 (2.41 eV/atom)	5.71 J/m^2 (2.2 eV/atom)

7.2. Model of the Flat and Stepped Diamond (111) and (100) Surfaces for Thermal Degradation Simulations

The models of the flat and stepped diamond (111) and (100) surfaces for production simulations (Table 1) are shown in Figure 7.2. The C(100) surface reconstruction by C-atom dimerization is not a thermally activated process and occurs spontaneously at 0 K (Enriquez et al., 2024b). For this reason, all simulations of the C(100) surface start with the reconstructed model . We consider two types of stepped C(100), depending on whether the dimer direction is normal (Type A) or parallel (Type B) to the step edge. The main difference between these two stepped surface models is the absence (Type A) or presence (Type B) of dangling bonds on the second layer of the step edge, similar to the stepped Si(001) models proposed by Chadi (Chadi, 1987). Test calculations show that a slab model thickness of 12 layers is sufficient to describe the surface reconstruction, bilayer exfoliation and reconstruction, which is the energy

difference between a C(111) surface and C(111) surface with graphitized top 2 layers, and the surface energies. Increasing the thickness to 16 layers have negligible effect on these properties (Table 7.4). All models have 12 C layers, and the bottom are terminated with H atoms. The bottom 2 layers and the H layer positions are fixed during the simulations.

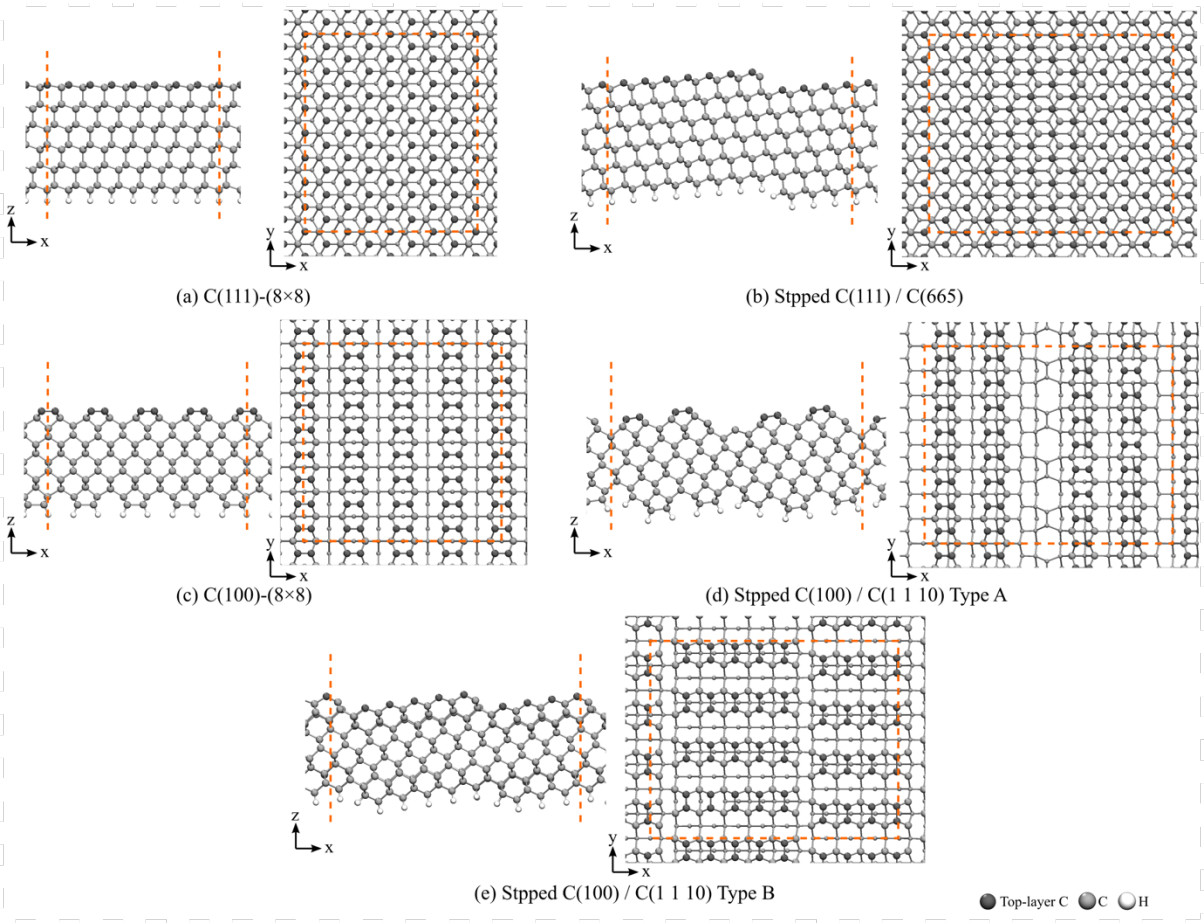

Fig. 7.2. Flat and stepped C(111) and C(100) surface models used in production simulations. Dark grey spheres correspond to top-layer carbon atoms, while grey and white spheres correspond to the other carbon and hydrogen atoms, respectively

Table 7.4. Comparison of relevant surface properties calculated using 12-layer and 16-layer slab models

Properties (eV/atom)	12 Layers	16 Layers
C(111) Reconstruction Energy	-0.756	-0.753
C(111) Bilayer Exfoliation and Reconstruction Energy	0.125	0.131
Surface Energy		
C(111) non-reconstructed	2.161	2.159
C(111) 2×1 reconstructed	1.405	1.405
C(100) 2×1 reconstructed	2.410	2.410

7.3. Thermal Degradation of the Flat and Stepped Diamond (111) and (100) Surfaces

I investigated the thermal degradation of the C(111) and C(100) surfaces by performing MD simulations with constant heating rate of 10 K/ps. I considered both flat and stepped C(111) and C(100) models (Fig. 7.3). To analyze the results of MD simulations, we monitor the changes in the number of phase-transformed atoms and their coordination. We define the phase transformed atoms as the atoms that move at least 0.8 Å away from their initial positions. The cutoff for the calculation of the coordination number is 2.0 Å. The simulation is carried out until about four layers of the surface have been phase transformed or thermally degraded.

I begin with the simulation of the flat C(111) surface (Fig 7.3a). At t = 52 ps (T ~ 520K), a number of atoms start to undergo phase transformation. The number of phase-transformed atoms is almost unchanged up to t = 260 ps (T ~ 2600K), suggesting that this phase is at least meta-stable within this temperature range. Upon examination of the snapshot at t = 60 ps, the phase transformation is characterized by the (2×1) π-bonding reconstruction of the C(111) surface (Fig. 7.4a). We investigated the temperature dependence of the π-bonding reconstruction by first performing constant heating rate simulation from 0 K up to a target

temperature, and then keeping the simulation temperature constant. When the target temperature is 500 K, the π-bonding reconstruction occurred within 4.5 ps. When the target temperature is lowered to 400 K and 300 K, the time required to reconstruct increased to 50.0 ps and 68.3 ps, respectively. I also simulated at 280 K for 500 ps but did not observe π-bonding reconstruction. The results suggest that the C(111) (2×1) π-bonding reconstruction is a thermally activated process and agrees with earlier theoretical studies using first principles calculations (Enriquez et al., 2024b; Petrini and Larsson, 2008). The thermal degradation of the surface occurs from t = 285 ps (T ~ 2850K) as shown by the sharp increase of 3-coordinated phase transformed atoms. The thermal degradation of the C(111) surface occurs through bilayer exfoliation, which starts with the breaking of bonds between the second- and third-layer C atoms. This bond breaking mechanism is similar to the cleaving of the C(111) surface which breaks one bond per atom. When attached to the surface, the top bilayer has a buckled structure with the characteristic tetrahedral geometry of diamond. After it has been detached, the top bilayer is exfoliated, and forms corrugated graphene-like sheet where the C atoms are all 3-cooridnated and form 6-membered rings. The snapshot at t = 292 ps shows a thermally degraded C(111) surface with two exfoliated bilayers. To estimate the activation energy of the bilayer exfoliation, we performed static DFT calculations and nudged elastic band reaction path search (Henkelman et al., 2000). The activation energy is 0.758 eV/atom (2.199 J/m^2). Using the GNN-IP, the calculated energy barrier is 0.717 eV/atom (2.081 J/m^2) which shows good agreement with DFT.

Figure 7.3b shows the results of the simulation of the stepped C(111) surface. The (2×1) π-bonding reconstruction starts at an earlier timestep of t = 35 ps (T ~ 350K). The completed reconstruction is shown in the snapshot at t = 50 ps. The π-bonding chain is formed at an angle of 60° across the steps (Fig. 7.4b). The thermal degradation of the stepped C(111) surface starts

to occur at an earlier timestep of t = 181 ps (T ~ 1810K) compared with the flat C(111) surface. This difference is caused by the dangling bonds already present on the second-layer atoms at the step edges which promotes bilayer exfoliation. The snapshot at t = 201.5 ps shows a thermally degraded stepped C(111) surface with the top two terraces that have been exfoliated and have combined into a single 3-coordinated C atom rippled sheet that forms graphene-like 6-membered rings. The remaining terraces contains sections with 2×1 reconstructed atoms and partially exfoliated C atom sheets.

Next, I discuss the results of the simulation of the C(100) surface (Fig. 7.3c). The thermal degradation of the surface starts at a much later timestep of t = 368 ps (T ~ 3680K) compared to the C(111) surface. This shows that the C(100) surface has higher thermal degradation resistance compared to the C(111) surface. As can be seen from the MD snapshots at t = 373 ps and t = 382 ps, unlike the C(111) surface, the thermal degradation of the C(100) surface does not proceed through the exfoliation of the top bilayer. Exfoliation of the top bilayer of the C(100) surface requires synchronous breaking of two bonds per atom which is a more stringent requirement compared to the one bond per atom requirement of cleaving the top bilayer on the C(111) surface. Instead of bilayer exfoliation, the C(100) surface degrades by breaking bonds between layers and the degradation proceeds through a small cluster of phase transformed atoms that grows until it covers the entire surface. The thermal degradation causes the surface to expand, which supports the observation in the laser ablation of diamond (Komlenok et al., 2011). The phase transformed atoms consist of 2-, 3-, and 4-coordinated C atoms. Having 2-coordinated carbon chains shows that there are more broken bonds per atom in the thermal degradation of the C(100) surface compared to the C(111) surface.

Figures 7.3d and 7.3e show the results of the simulations of the Type A and Type B stepped C(100) surfaces. The main difference between the two stepped surface models is the absence or presence of dangling bonds on the second-layer atoms on the step edges. When the C-dimer bond is normal to the step edge (Type A), there is no dangling bond on the second-layer atoms at step edge. But when the C-dimer bond is parallel to the step edge (Type B), there is 1 dangling bond per second-layer atom at the step edge. This leads to the difference in the thermal degradation mechanism of the two stepped surface models. For the Type A stepped C(100) surface, the thermal degradation of the surface starts at t = 350 ps (T ~ 3500 K) which is just slightly lower compared to the flat C(100) surface. Similar to the flat C(100) surface, the thermal degradation starts with disordered clusters of 2-, 3-, and 4-coordinated phase transformed C atoms and grows until it covers the step terrace. In contrast, for the Type B stepped C(100) surface, the thermal degradation of the surface occurs at a much earlier timestep of t = 307 ps (T ~ 3070K). Also, the rate of increase of the phase transitioned atoms is slower compared to the flat C(100) surface. Moreover, the thermally degraded structure is noticeably different. The number of thermally degraded atoms with 2-coordination is lesser, while 3-coordinated atoms with short-range order are observed. Thermal degradation starts with the formation of cylindrical and dome-like structures at the step edges. The cylindrical structure consists of 3-coordinated atoms that form 6-membered rings similar to graphene, while the dome-like structures consist of 3-coordinated atoms that form 5- and 6-membered rings similar to fullerenes. As thermal degradation progresses, the cylindrical and dome-like structures combine and become more disordered.

I also perform the same simulations at a faster heating rate of 200 K/ps. The predicted thermal degradation temperature is higher compared to the ones predicted in the slower heating rate simulation (Table 7.5). For instance, at slower heating rate of 10 K/ps, the graphitization

starts at 1810 K for the stepped C(111) surface which is close to the temperatures in the experiment, in which the graphitization of diamond microcrystals occurs within a few minutes when heated at 1600℃ (1873 K) which starts from the edges and the C(111) facet (Bokhonov et al., 2021). At faster heating rate of 200 K/ps, the predicted graphitization temperature for the same surface is higher (2840 K). Next, I calculated the thermal degradation of the flat and stepped C(111) surface for increasing heating rates and plotted thermal degradation temperatures (Fig. 7.5). The graph shows that the thermal degradation temperature converges at 10K/ps. Therefore, while 10 K/ps is still much faster compared to the one used in the experiment (15 ℃/min) (Bokhonov et al., 2021), it is still possible to predict realistic thermal degradation temperature with this value of heating rate.

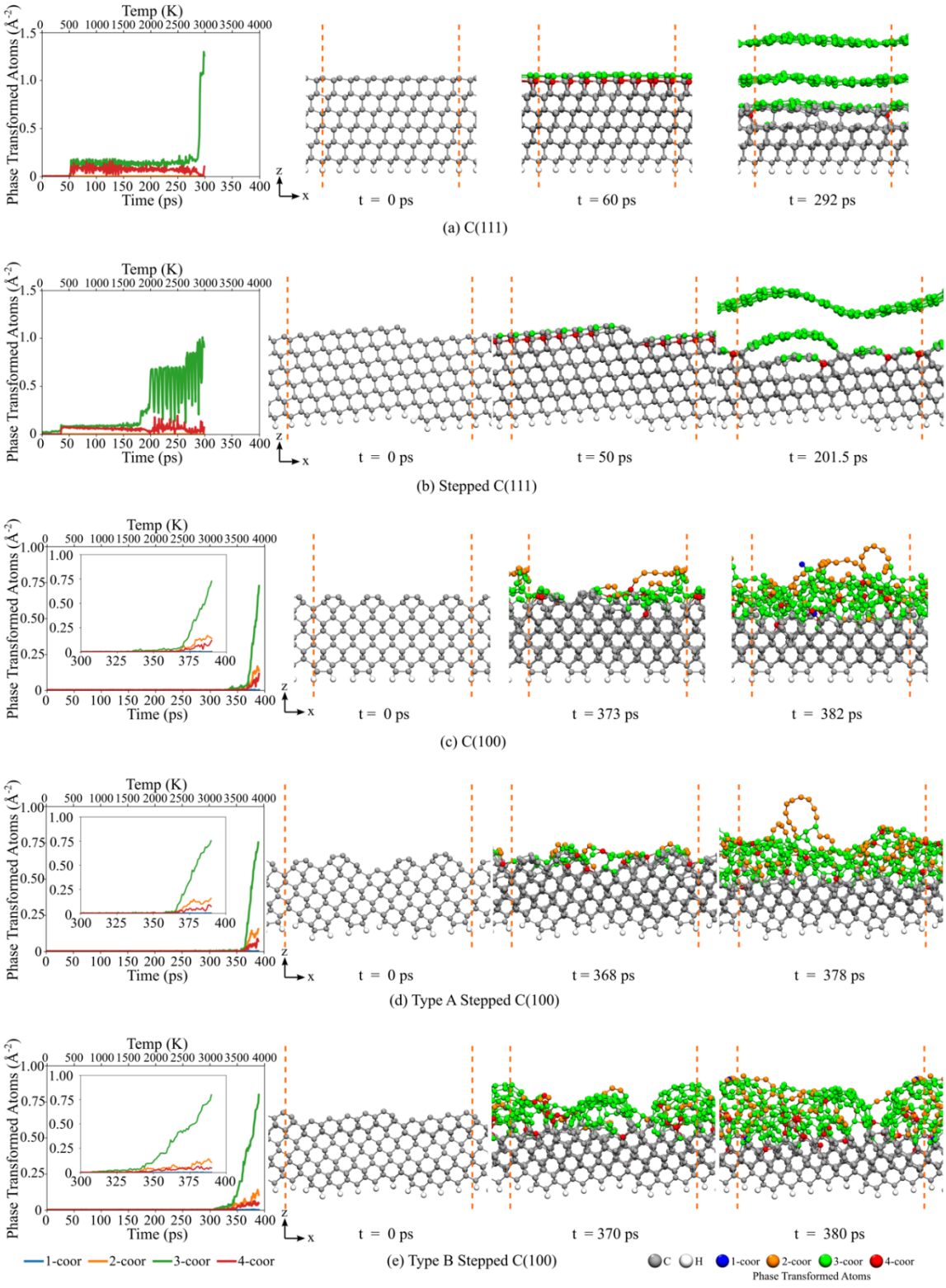

Fig. 7.3. Constant heating rate simulations of the flat and stepped C(111) and C(100) surfaces. For each surface model, the number of phase transformed atoms per Å^2 during the simulation is shown, with blue, orange, green, and red lines corresponding to 1-, 2-, 3-, and 4-coordinated

atoms, respectively. Snapshots of the MD simulation at selected timesteps are also shown with blue, orange, green, and red spheres corresponding to 1-, 2-, 3-, and 4-coordinated phase transformed atoms, respectively. Grey and white spheres correspond to non-phase transformed carbon and hydrogen atoms, respectively.

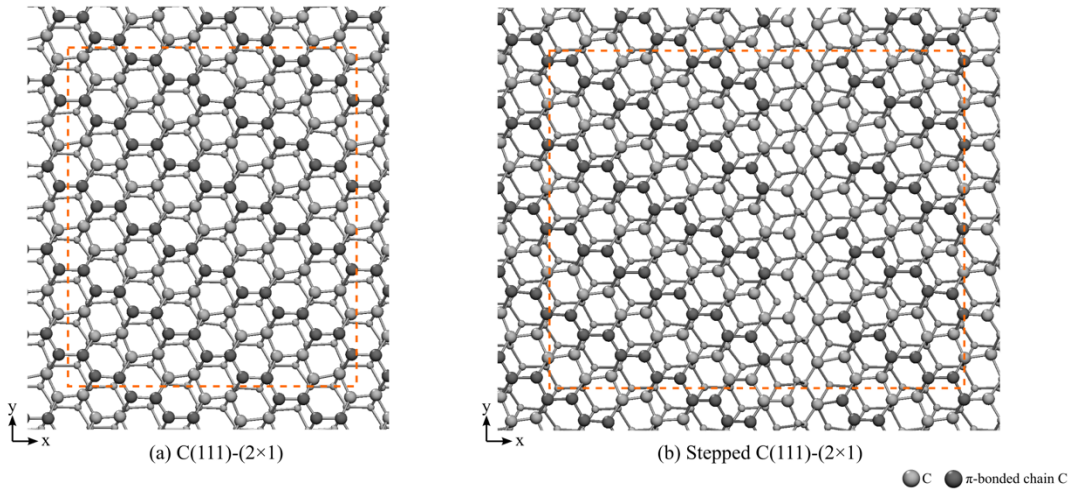

Fig. 7.4. Snapshots of (2×1) π-bonded reconstruction of the (a) C(111) surface (t = 60 ps, T ~ 600K) and (b) stepped C(111) surface (t = 50 ps, T ~ 500K). Dark grey spheres correspond to π-bonded carbon atoms while grey spheres correspond to other carbon atoms. (A color version of this figure can be viewed online.)

Table 7.5. Comparison of the thermal degradation temperatures of the diamond surfaces for slow (10 K/ps) and fast (200 K/ps) heating rates.

structure	thermal degradation temperature (K)	
	slower heating rate	faster heating rate
C(111)	2850	3240
C(111) stepped	1810	2840
C(100)	3680	4050
Stepped C(100) Type A	3500	3900
Stepped C(100) Type A	3070	3640

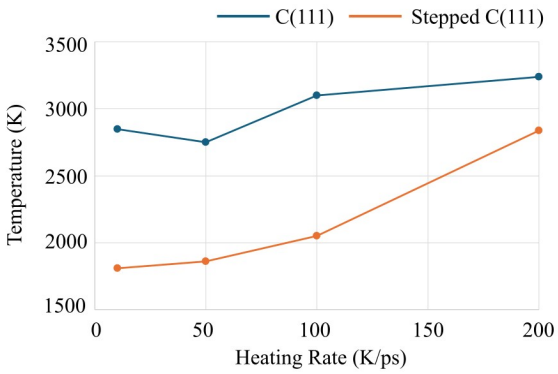

Fig. 7.5. Variation of thermal degradation temperature with heating rate for the flat and stepped C(111) surfaces.

7.4. Hybridization of Carbon Atoms on the Thermally Degraded Diamond Surfaces

To gain further insights, I classify the phase transformed atoms of the thermally degraded surfaces according to their hybridization. The 1- and 2-coordinated atoms are classified as sp^1-hybridized, and the 4-coordinated atoms are classified as sp^3-hybridized. The 3-coordinated atoms can either be sp^2 hybridized or sp^3 hybridized with a dangling bond, depending on the bond lengths and bond angles. To classify the 3-coordinated atoms whether they have sp^2 or sp^3 character, we constructed a neural network binary classifier model with bond lengths and bond angles as input features. The details of this binary classifier model are discussed in the methodology section. The classified structures of thermally degraded surfaces are shown in Figure 6 with the calculated percent composition of each hybridization type for each structure. In addition, structure analysis using the coordination number is also presented. While the coordination analysis is a good metric to contrast between the amount of 1-, 2-, and 4-coordinated thermally degraded atoms on the flat and stepped C(111) and C(100) surfaces, it gives limited insight in differentiating between the type of thermally degraded 3-coordinated atoms on the surfaces. For this task, the hybridization analysis allows further elucidation.

The exfoliated sheet on the thermally degraded C(111) surface contains sp^2 and 3-coordinated sp^3 hybridized atoms forming 6-membered rings (Fig. 7.6a). The corrugation is caused by the compressive stress due to the mismatch between the lattice parameter of the C(111) surface and graphene, which prevents the 3-coordinated sp^3 atoms to fully flatten and change into sp^2 hybridization. In physical systems, the exfoliated sheet will likely become purely sp^2-hybridized when the compressive stress is lifted. Similarly, the exfoliated rippled

sheet and the partially exfoliated sublayer of the stepped C(111) surface contain C atoms in 6-membered rings with both sp^2 and sp^3 character (Fig. 7.6b).

In contrast, the thermally degraded C(100) surface contains sp^1 hybridized carbon chains and an amorphous network of sp^2-hybridized and 3- and 4-coordinated sp^3-hybridized C atoms (Fig. 7.6c). In physical systems, the 3-coordinated sp^3-hybridized C atoms can either form bond with other atoms to saturate the dangling bond or flatten to change into sp^2 hybridization upon annealing. Also, as argued by O'Bannon et al, the sp^1-hybridized carbon will transform into zigzag chain and combine to form into more stable sp^2-hybridized carbon (O'Bannon et al., 2020). The thermally degraded structure on the Type A stepped C(100) surface is similar to the flat C(100) surface (Fig. 7.6d). In contrast, the Type B stepped C(100) surface has noticeably less sp^1 hybridized carbon chains (Fig. 7.6e). Also, unlike in the flat and the Type A stepped C(100) surface, the sp^2 and 3-coordinated sp^3 structures on the Type B stepped C(100) surface have short range order, which form into graphene-like and semi fullerene-like structures with 5- and 6-membered rings. The 3-coordinated sp^3-hybridized carbon atoms in these rings will likely flatten upon annealing. The formation of half fullerene-like structure supports the experimental observation that fullerene can form during CVD growth of diamond and that diamond can be formed from fullerene (Brazhkin et al., 1998; Chow et al., 1995).

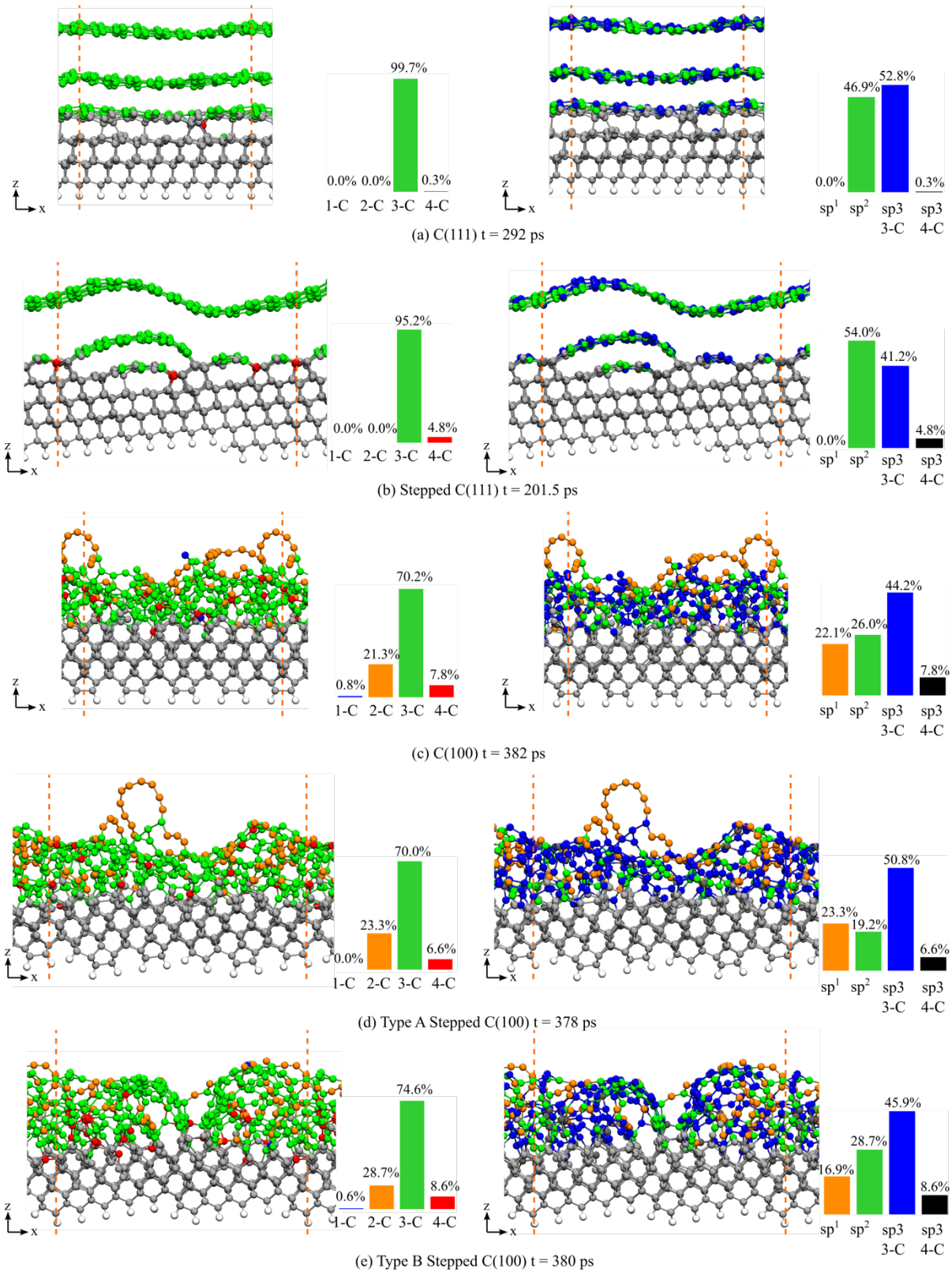

Fig. 7.6. Coordination (left) and hybridization (right) analysis of carbon atoms on the thermally degraded diamond surfaces. Snapshots of the MD simulation at selected timesteps are shown

with blue, orange, green, and red spheres corresponding to 1-coordinated, 2-coordinated, 3-coordinated, and 4-coordinated C atoms (left) and orange, green, blue, and black spheres corresponding to sp^1, sp^2, 3-coordinated sp^3, or 4-coordinated sp^3 hybridized C atoms (right). Grey and white spheres correspond to non-phase transformed diamond and hydrogen atoms. The percentage composition of each type of coordination and hybridization for each structure is calculated.

CHAPTER 8

SUPPRESSION AND CONTROL OF DIAMOND GRAPHITIZATION AND LUBRICATION BY DANGLING BOND SATURATION

Graphitization, or more generally thermal degradation, is an undesirable phenomenon in diamonds. From diamond cutting tools to diamond electronic devices intended for use in extreme conditions, the suppression of graphitization has been an active area of research. In Chapter 7, I have shown that the C(111) surfaces are more susceptible to thermal degradation compared to the C(100) surfaces. The mechanism of the degradation is also different. While the thermally degraded C(111) surface atoms form graphitic structures through bilayer exfoliation, the C(100) surface atoms become amorphous. Furthermore, the simulations indicate that the stepped surfaces are more vulnerable to graphitization when compared to the flat surfaces due to the presence of dangling bonds at the stepped edges (Enriquez et al., 2024a).

I hypothesize that by fully saturating the dangling bonds of the C(111) surface with atoms and small molecules such as H, O, and OH, it may be possible to inhibit graphitization and chemically passivate the surface, thereby reducing diamond chemical wear. Furthermore, precise control of the graphitization of the C(111) surface can be achieved through partial surface termination, presenting a promising approach for fabricating graphene-on-diamond devices. To investigate these hypotheses, I constructed models of C(111) surfaces terminated by H-, O-, and OH and performed first principles and machine learning molecular dynamics (MLMD) simulations.

8.1. Effect of Surface Termination on the Geometry of the C(111) Surface

I performed DFT simulations to optimize the geometries of the pristine and H-, O-, and OH-terminated C(111) surfaces (Fig. 8.1). The resulting average adsorption energies per atom/molecule were found to be -3.220 eV, -4.433 eV, and -3.035 eV for the H atom, O atom, and OH molecule, respectively. These findings indicate that all terminating species effectively stabilize the C(111) surface.

Moreover, the results show that surface termination significantly influences the inter-layer distances of the C(111) surface. Notably, the distance between the first- and second-layer atoms increased, while the distance between the second- and third-layer atoms decreased. Table 8.1 shows that the distance between first-layer atoms (C_{L1}) of the pristine C(111) surface measures 1.442 Å, which is shorter than the C-C distance in bulk diamond (1.546 Å) and nearly equivalent to the C-C distance in graphite (1.424 Å). To further analyze the geometry, I define the tripod angles A:(B, C, D) as the angles formed by the central atom A with the vertices (B, C, D) of the base of the tetrahedron, namely $\angle BAC$, $\angle CAD$, and $\angle DAB$ (Fig. 8.2). In the case of an ideal sp^3-hybridized C atom with perfect tetrahedral geometry, the sum of the tripod angles is 328.41°. Table 8.1 indicates that the first-layer atoms (C_{L1}) have increased tripod angles leading to a flattened geometry. These results suggest that the C_{L1} atoms exhibit an sp^2-hybridized character.

Terminating the surface with H or OH has caused a significant increase in the C1-C1 bonds. Additionally, the sums of the tripod angles of the first- and second-layer atoms (C_{L1} and C_{L2}) have increased, resulting in a less flattened geometry. Similar observations can be made

regarding the termination of O, albeit with a less pronounced effect. These findings indicate that the surface termination restores the sp^3-character of the C_{L1} and C_{L2} atoms. The most significant consequence of these changes is the decrease in the bond distance between the second- and third-layer atoms, suggesting an increase in bond strength and possibly an enhancement of graphitization resistance.

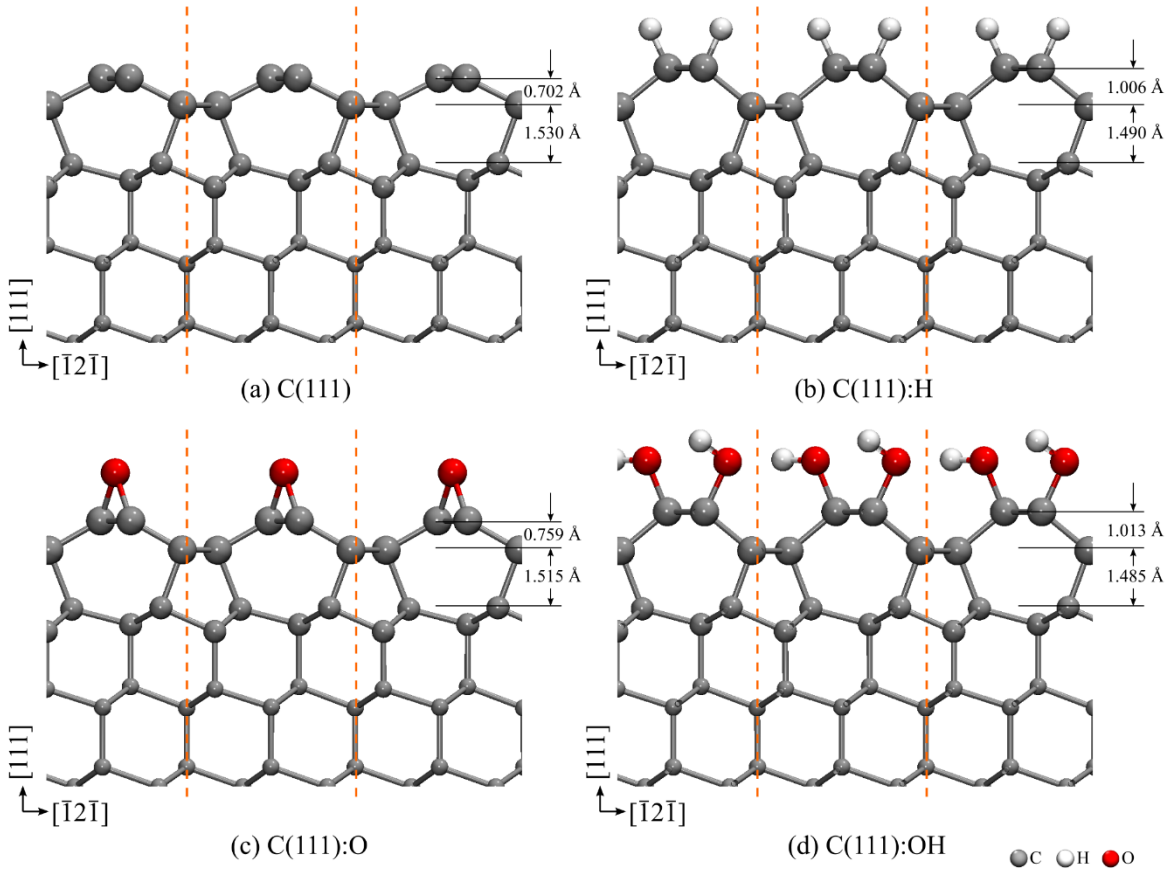

Fig. 8.1. Optimized geometries of the (a) non-terminated and (b) H-, (c) O-, and (d) OH-terminated C(111) surfaces.

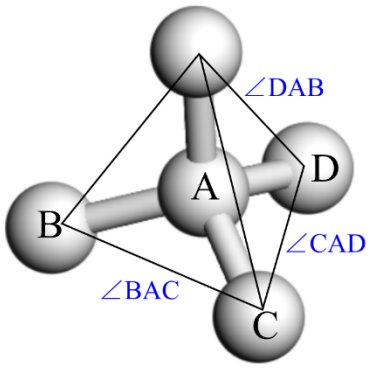

Fig. 8.2. Definition of the three tripod angles of a given central atom.

Table 8.1. Effect of surface termination on the geometry of the C(111) surface

	C(111)	C(111):H	C(111):O	C(111)*OH
bond length (Å)				
C_{L1}- $C_{L1'}$	1.442	1.565	1.467	1.593
C_{L1}- C_{L2}	1.548	1.596	1.536	1.583
C_{L2}- $C_{L2'}$	1.562	1.595	1.560	1.596
C_{L2}- C_{L3}	1.632	1.587	1.617	1.584
tripod angle sum (degree)				
C_{L1}:($C_{L1'}$, $C_{L1''}$, C_{L2})	353.4	341.0	351.0	340.3
C_{L2}:(C_{L1}, $C_{L2'}$, $C_{L2''}$)	350.6	340.7	349.0	340.1

8.2. Graph Neural Network Interatomic Potential for Diamond Surfaces with H, O, and OH

I constructed a GNN interatomic potential to perform large-scale and long-timescale simulations of the clean and H-, O-, and OH-terminated C(111) surfaces. The final dataset contains a total of 16390 structures, of which 90% and 10% have been used for training and testing, respectively. The dataset contains all the structures used in the construction of GNN_CH potential discussed in Chapter 7, with the addition of C(111) and C(100) slabs terminated with H, O, and OH and their interface with H_2, O_2, OH, and H_2O molecules. Moreover, a reactive dataset constructed from NEB simulations of the diamond oxidation discussed in Chapters 5 and 6 has been added. The energy and force RMS errors of the test set are 3.0 meV/atom and 99.5 meV/Å, respectively. Pre-production validation has been performed by simulating the clean and H-, O-, and O-terminated stepped C(111) surface [C(442)] (Fig. 8.3) at increasing temperatures with a constant heating rate of 10 K/ps up to 2000 K. A total of 400 structures across the temperature range were selected for the validation. The comparison of DFT and GNN energies and forces are shown in Fig. 8.4. The energy and force RMS errors of the pre-production validation are 6.4 meV/atom and 86.0 meV/Å, respectively, showing good accuracy. The sampled MD trajectories of the pre-production validation have no extrapolated atomic environment which guarantees the reliability of the interatomic potential. From here on, the interatomic potential will be referred to as GNN_CHO.

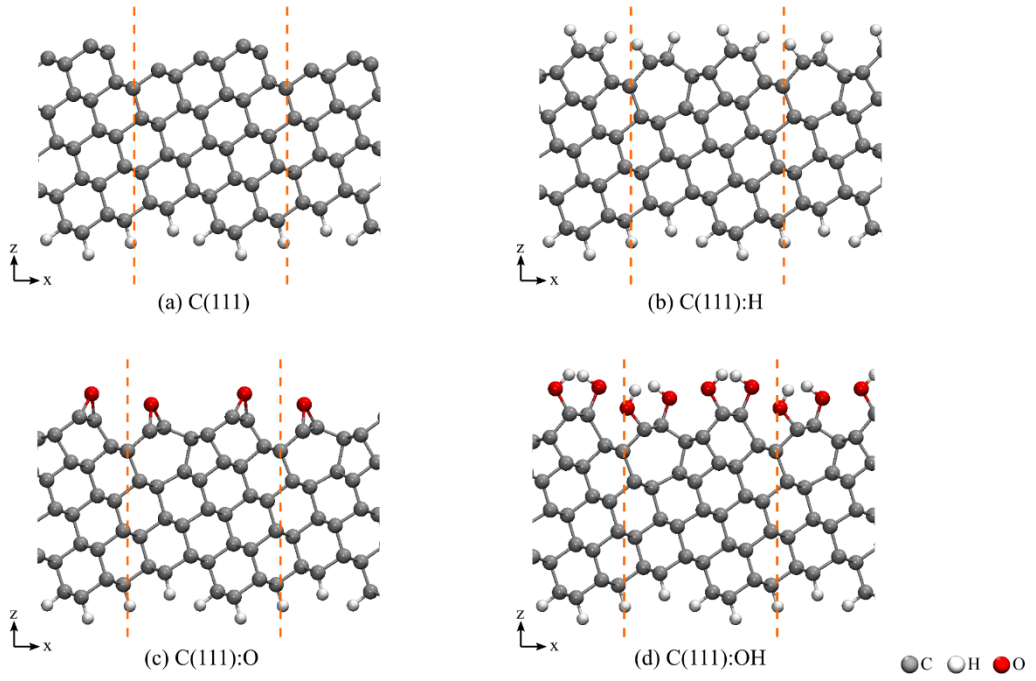

Fig. 8.3. Pre-production validation dataset includes (a) non-terminated, (b) H-, (c) O-, and (d) OH-terminated stepped C(111) surfaces [C(442)]

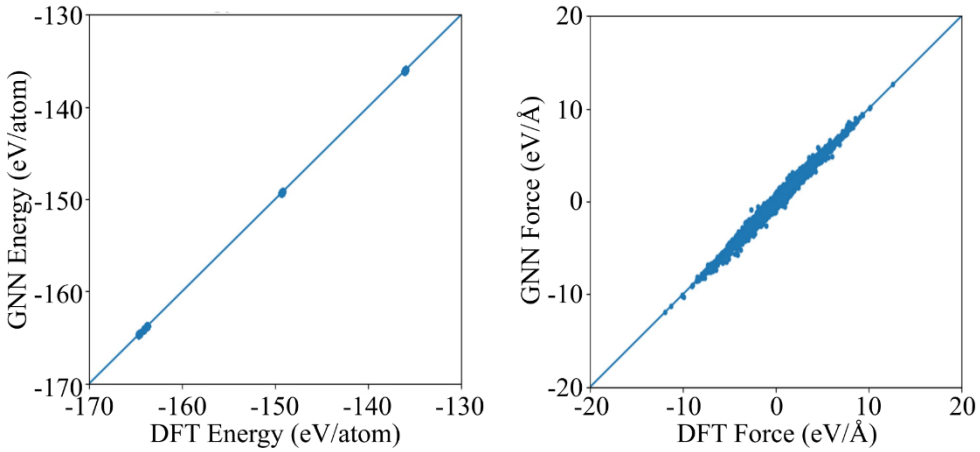

Fig. 8.4. Comparison of the DFT and GNN energies and forces for the pre-production validation dataset, with energy and force RMSEs of 6.4 meV/atom and 86.0 eV/Å, respectively.

8.3. Comparison of GNN and ReaxFF Interatomic Potentials in Describing the Oxidative Etching of Diamond (111) and (100) Surfaces

In this section, I present a comparison of the accuracy of the developed GNN interatomic potential with the ReaxFF interatomic potential (Srinivasan et al., 2015) in depicting the oxidative etching reactions on the C(111) and C(100) surfaces. The initial CO desorption reaction from the oxygen-terminated C(111) surface [C(111)(1×1):O_{ML}] surface is exothermic, while all subsequent CO desorption reactions are endothermic. Following the desorption of the first two CO molecules, the geometry of the carbonyl pairs relaxes, revealing a distinct pattern of high and low activation energies associated with the desorption of the first and second CO from a carbonyl pair.

Figure 8.5 shows that the GNN interatomic potential can accurately reproduce the DFT calculated activation and reaction energies with a mean absolute error (MAE) of 0.169 eV. Conversely, the ReaxFF interatomic potential failed to reproduce the DFT calculated activation and reaction energies in both qualitative and quantitative terms. Specifically, the desorption reaction energies of the second half of the carbonyl pair (reactions 4, 6, 8) are all exothermic, with negative activation energies. The initial states of these reactions are defined by a CO molecule adsorbed on the π-reconstructed second-layer atoms. The ReaxFF interatomic potential suggests that this structure is unstable, and that the CO will desorb through a non-activated reaction. Additionally, when considering the reverse reaction, the ReaxFF interatomic potential predicts that CO will not adsorb on the π-reconstructed second-layer atoms. The predicted activation and reaction energies of the ReaxFF interatomic potential exhibit poor

agreement with DFT, yielding a significantly higher MAE of 2.050 eV compared to the GNN interatomic potential.

The CO desorption reaction from the oxygen-terminated C(100) surface [C(100)(1×1):O_{ML}] is characterized by a decrease in activation energies after the initial CO desorption and the creation of a vacancy site. Figure 8.6 shows that the GNN interatomic potential can accurately reproduce the DFT calculated activation and reaction energies, with an MAE of 0.249 eV. The ReaxFF can reproduce the DFT calculations qualitatively, except for the first CO desorption reaction where the activation energy is lower compared to the second. However, the predicted activation and reaction energies have a poor agreement with DFT in general, with a much higher MAE of 0.945 eV compared to the GNN interatomic potential.

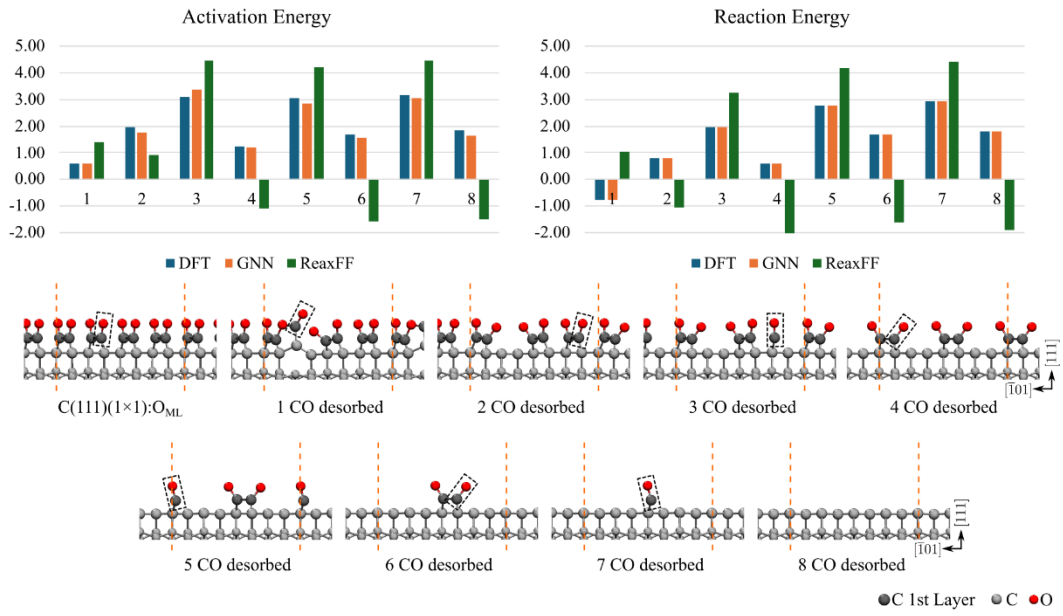

Fig. 8.5. CO desorption activation and reaction energies on the C(111)(1×1):O_{ML} calculated using DFT, GNN, and ReaxFF

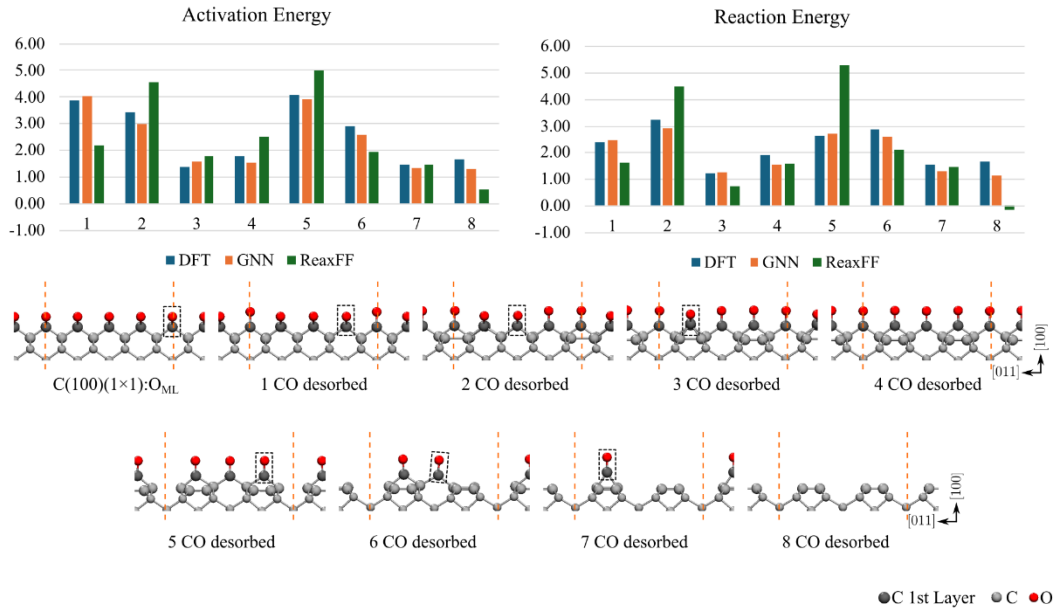

Fig. 8.6. CO desorption activation and reaction energies on the C(100)(1×1):O_{ML} calculated using DFT, GNN, and ReaxFF

8.4. Effect Of Dangling Bond Saturation in Suppressing the C(111) Graphitization

In this section, I conducted a constant heating rate simulation of the clean and H-, O-, and OH-terminated stepped C(111) surfaces [C(443] using the GNN_CHO potential. Figure 8.7 shows that at T = 1800 K, the top two bilayers of the clean stepped C(111) surface underwent partial graphitization. In comparison, graphitization has been suppressed on all the terminated surfaces. Upon further heating, the step edges of the O- and OH-terminated stepped C(111) surfaces began to oxidize at T = 2000 K through O-induced C-C bond breaking at the steps, followed by carbonyl formation and CO and CO_2 desorption. In contrast, the H-terminated stepped C(111) surface remains stable and damage-free (Fig. 8.8). These simulations demonstrate that while O and OH can effectively suppress graphitization, O atoms will promote surface damage through oxidative etching at high temperatures. Therefore, among the terminating species considered, the H atom shows the greatest potential in preventing thermal degradation of the C(111) surface.

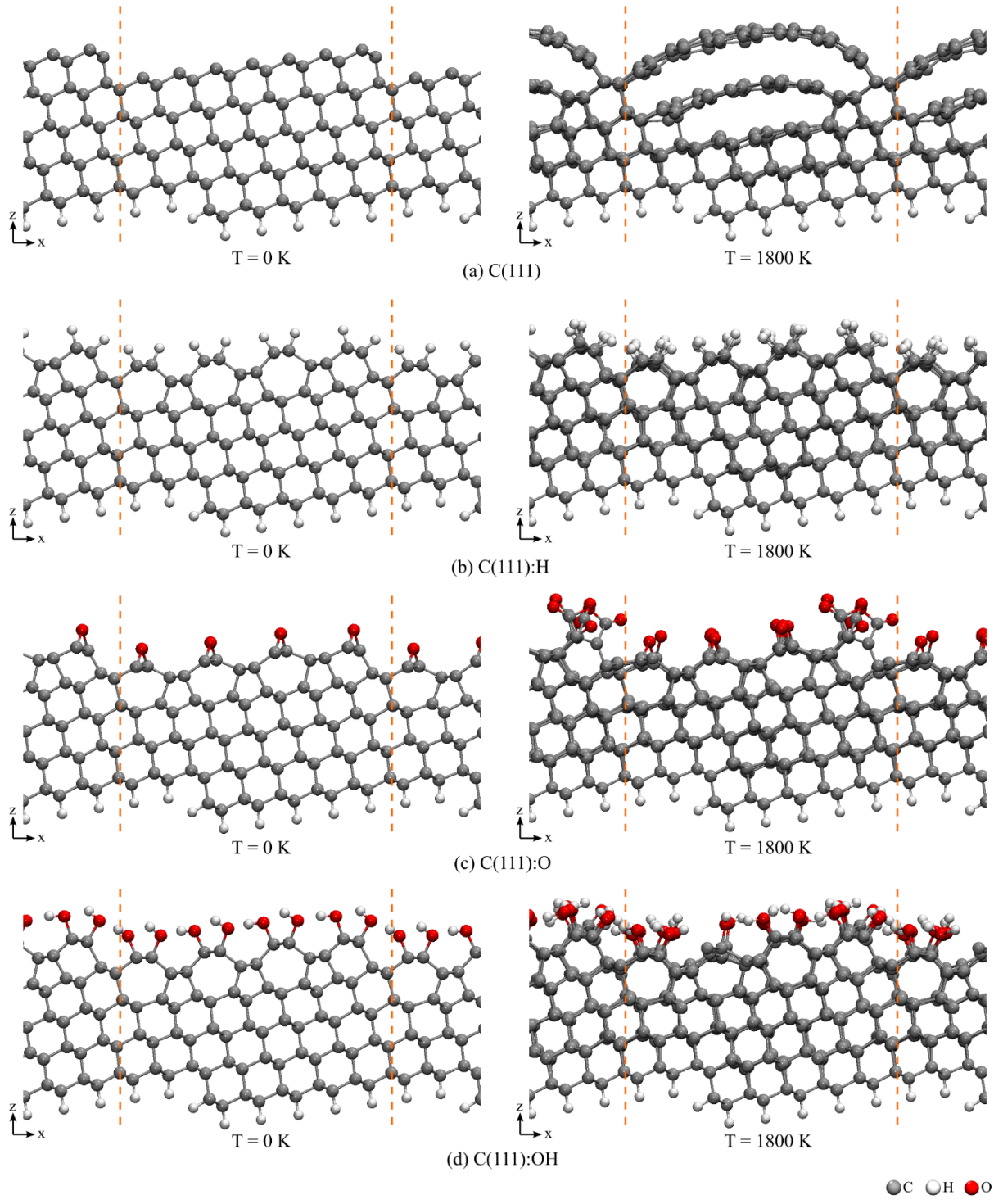

Fig. 8.7. Constant heating rate simulation of the (a) clean and (b) H-, (c) O-, and (d) OH-terminated stepped C(111) surfaces [C(443)].

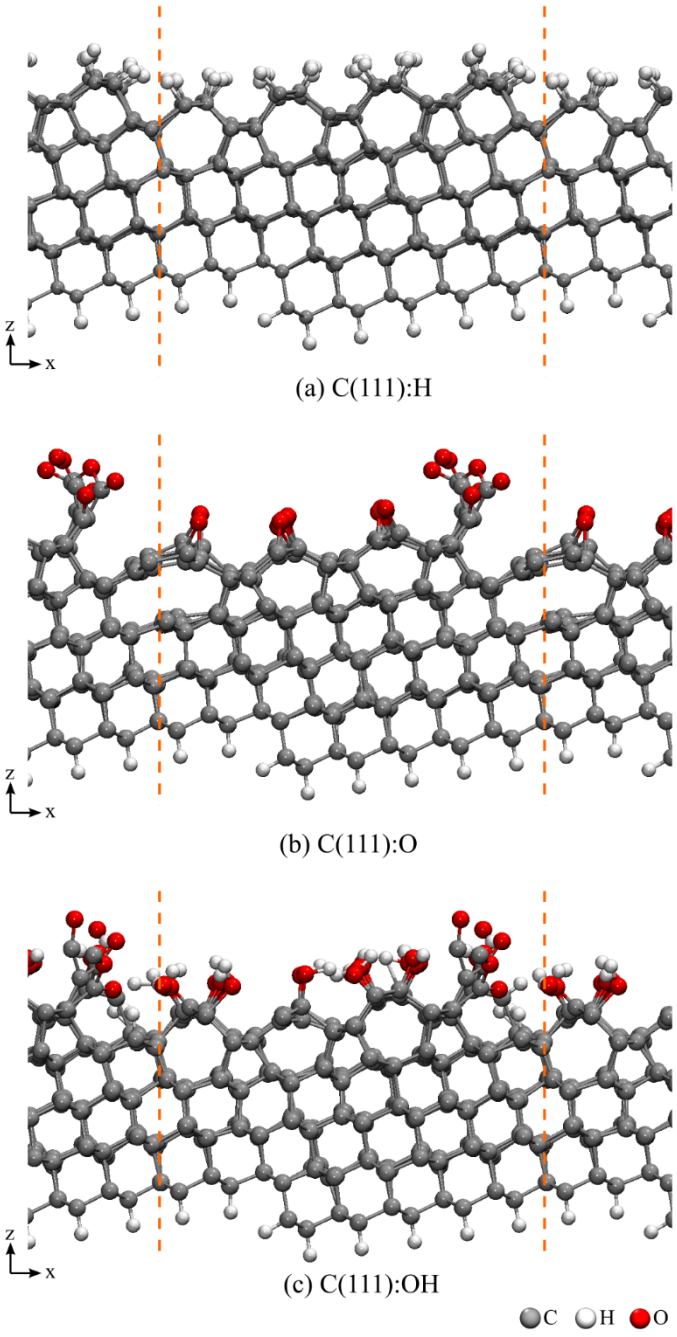

Fig. 8.8. Comparison of the (a) H-, (b) O-, and (c) OH-terminated stepped C(111) surface at T = 2000 K.

8.5. Thermal Degradation of C(111) Surface with Triangular Island and Pit

To further investigate the effect of H termination in graphitization suppression, I constructed a more physically realistic model of clean and H-terminated C(111) surfaces with triangular island and pit features. The sides of the triangle are oriented along the {110} directions. This model reflects the 3-fold symmetry of the C(111) surface observed on the triangular overgrowth and hollow octahedral faces of diamond microcrystals, as well as in the etched pits on the C(111) surface oxidized with oxygen and water (Fig. 8.9) (de Theije et al., 2000; Kvasnytsya, 2021).

The C(111) surface model features an equilateral triangular island and pit, with a side length of approximately 30 Å (Fig. 8.10a). The surface is heated at a constant heating rate up to T = 1500 K. At 500 K, the terrace adjacent to one of the island's vertices begins to graphitize, as shown by lighter-colored spheres arranged in 6-member rings (Fig. 8.10b). Complete graphitization of the island is observed by T = 1500 K (Fig. 8.10d). The edges of the graphitized island remain attached to the surface through covalent bonds. On the other hand, the surface atoms on the pit start to reconstruct into π-bonded chains at T = 500 K as shown by lighter-colored spheres arranged in chains (Fig. 8.10b). Initially, the π-bonded chains run along both the $[\bar{1}01]$ and the $[01\bar{1}]$ directions. At T = 1000 K, all the π-bonded chains on the pit run uniformly along the $[\bar{1}01]$ direction (Fig. 8.10c). The simulation shows that the island is more susceptible to graphitization compared to the pit. This is because the sides of the island essentially behaved as stepped C(111) models, making them more susceptible to graphitization due to the dangling bonds at the edges. Furthermore, given that graphitization is facilitated on

the vertices of the island, it can be deduced that islands with narrow terrace areas will exhibit greater susceptibility to graphitization compared to those with larger terrace areas.

The simulation also demonstrates the potential for preferential graphitization of asperities on the C(111) surface. Similar to step edges and island vertices, asperity edges contain dangling bonds that can facilitate graphitization. This concept can be applied to the mechanical and chemical refinement of diamond surfaces. By preheating the diamond surface before polishing, the inter-layer bonding between the asperity atoms can be weakened as they transition from sp^3 to sp^2 hybridization, transforming the inter-layer bonds from covalent to van der Waals. Consequently, a layer-by-layer material removal mechanism will be facilitated, leading to an enhancement in surface finish and polishing rate.

Next, I investigated the effect of H-termination on the C(111) island and pit (Fig. 8.10e). Fig. 8.10f shows there are no thermally degraded atoms at T = 1500 K, which is strikingly different from the non-terminated C(111) surface at the same temperature (Figure 8.10d). The simulation results indicate that saturating the dangling bond is an effective approach to preventing the thermal wear of diamonds, even on graphitization-prone surface features such as island vertices and narrow terraces. This effect is observable at temperatures lower than 1500 K, which is below the temperature at which oxidation begins (i.e., 2000 K as discussed in Section 8.4), implying that graphitization suppression will be equally effective when using O or OH as terminating species.

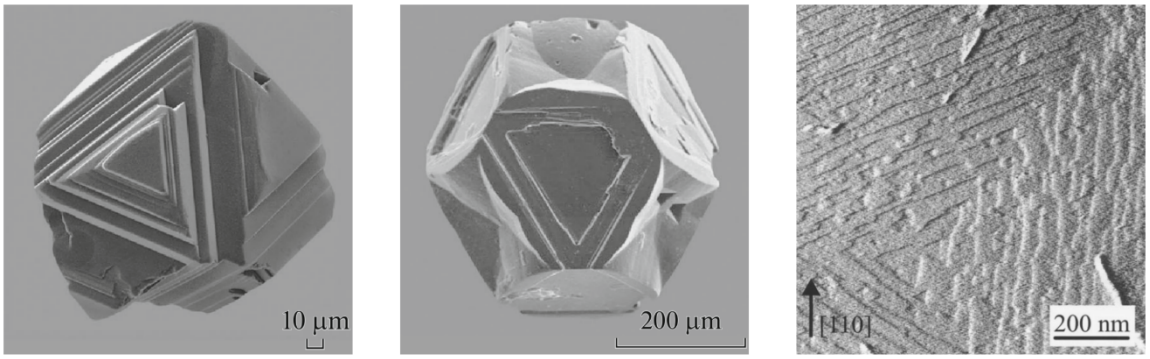

(a) C(111) with overgrowth (b) Hollow C(111) (c) C(111) with pits

Fig. 8.9. SEM images of diamond microcrystals with (a) overgrowth and (b) hollow octahedral faces and (c) oxidized diamond (111) surface with triangular etched pits.

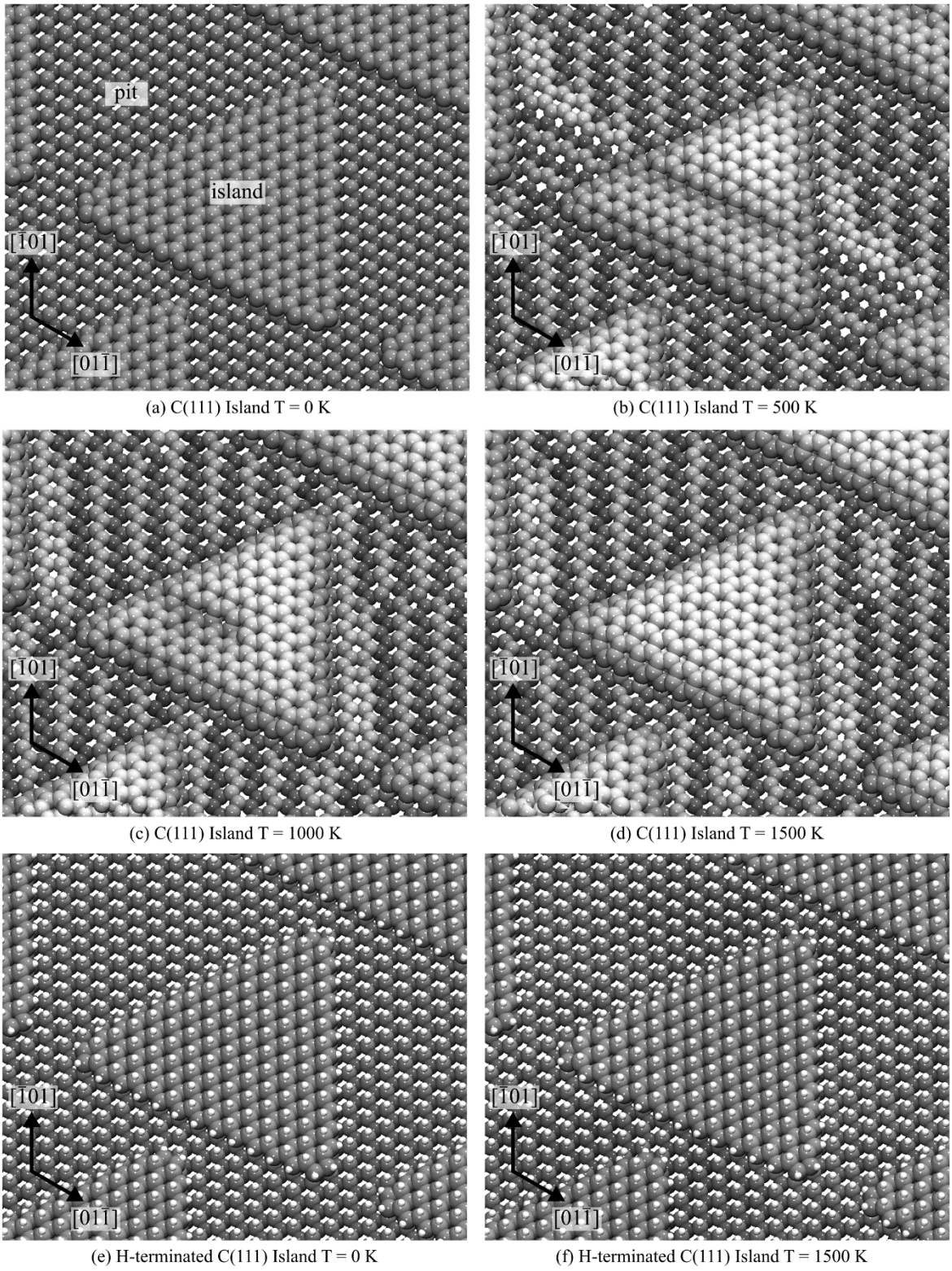

Fig. 8.10. Comparison of the surface morphologies of the clean and H-terminated C(111) surface islands heated up to 1500 K.

8.6. Preferential Graphitization of Non-Terminated C(111) Surface Atoms

In the previous sections, I have shown that the C(111) surface fully terminated by H-atoms has a higher resistance to graphitization. In this section, I investigated what will occur when the C(111) surface is only partially terminated by H atoms.

I constructed a (14×8) supercell model of C(111) surface with partial termination of H atoms (Fig. 8.11). The simulation is performed in three phases. In the first phase, the surface was heated up to T = 2400 K. By the end of this phase, the non-terminated part of the C(111) surface had undergone graphitization, while the terminated parts remained intact, and the H atoms did not desorb. To investigate further, I employed the nudged elastic band (NEB) method to calculate the activation energies of the bilayer exfoliation of the C(111) surface and the H_2 desorption from non-reconstructed and reconstructed C(111) surfaces (Fig. 8.12). The activation energies of H_2 desorption from C(111) surfaces are higher compared to bilayer exfoliation of the C(111) surface. This result confirms that preferential graphitization of the non-terminated surface could occur without the desorption of H_2 from the terminated surfaces when heated in vacuum conditions.

In the second phase, the surface is simulated at a constant temperature of T = 2400 K to determine the stability of the partially graphitized surface at this temperature. After 100 ps, no significant changes in the structure of the C(111) surface are observed. Finally, in the third phase, an annealing simulation is performed, during which the surface is cooled until it reaches T = 300 K. The graphitized surface remains in its sp^2 state and does not reattach to the C(111) surface. Additionally, the bilayer beneath the graphitized atoms undergoes π-bonding

reconstruction, rendering it non-reactive to the graphene above it. As a result, this structure can be considered at least metastable at room temperature.

Based on the findings, I propose a novel method for producing graphene-on-diamond through epitaxial graphene self-assembly on the C(111) surface (Fig. 8.13). The process begins with the passivation of an atomically flat C(111) surface through exposure to hydrogen plasma. Subsequently, preferential removal of the H atoms from specific areas can be achieved using a pulsed laser, a technique already proven effective for graphene (Zhang et al., 2012; Costantini et al., 2024). Lastly, the material is heated until epitaxial graphene is formed. This proposed method offers several advantages over current techniques for fabricating graphene-on-diamond devices. Firstly, the process is significantly simpler as it eliminates the need for a metal catalyst or pre-fabrication of graphene followed by transfer onto the diamond. Secondly, due to the covalent bonding of graphene edges into the diamond, the resulting device will exhibit greater resilience to mechanical and thermal stresses compared to conventional devices where graphene is simply held on top of the diamond by van der Waals forces. Lastly, the use of the pulsed laser hydrogen removal technique enables precise control over the dimensions of the graphene on top of the diamond. Apart from this application, this approach could be employed in the microfabrication of an all-carbon circuit board, with the diamond surface serving as the non-conducting area and the epitaxial graphene as the conducting circuit traces.

The self-assembly process of epitaxial graphene on diamond holds significant promise as it could lead to a shift from silicon-based to carbon-based electronics. Silicon-based electronic devices are nearing their theoretical and technical constraints, prompting the pursuit of alternative technologies. Carbon nanotubes, graphene, and diamond-based electronic

devices have exhibited remarkable performance in comparison to conventional devices (Avouris, 2002, 2010; Wort and Balmer, 2008). The idea of an all-carbon circuit board further suggests the possibility of developing devices from a single elemental material (Avouris et al., 2007; Williams et al., 2021).

Carbon-based electronics offer the potential for not only higher performance but also increased sustainability, biocompatibility, and environmental safety. These characteristics make them a promising component for the development of carbon-neutral technologies, contributing to a more sustainable and eco-friendly future.

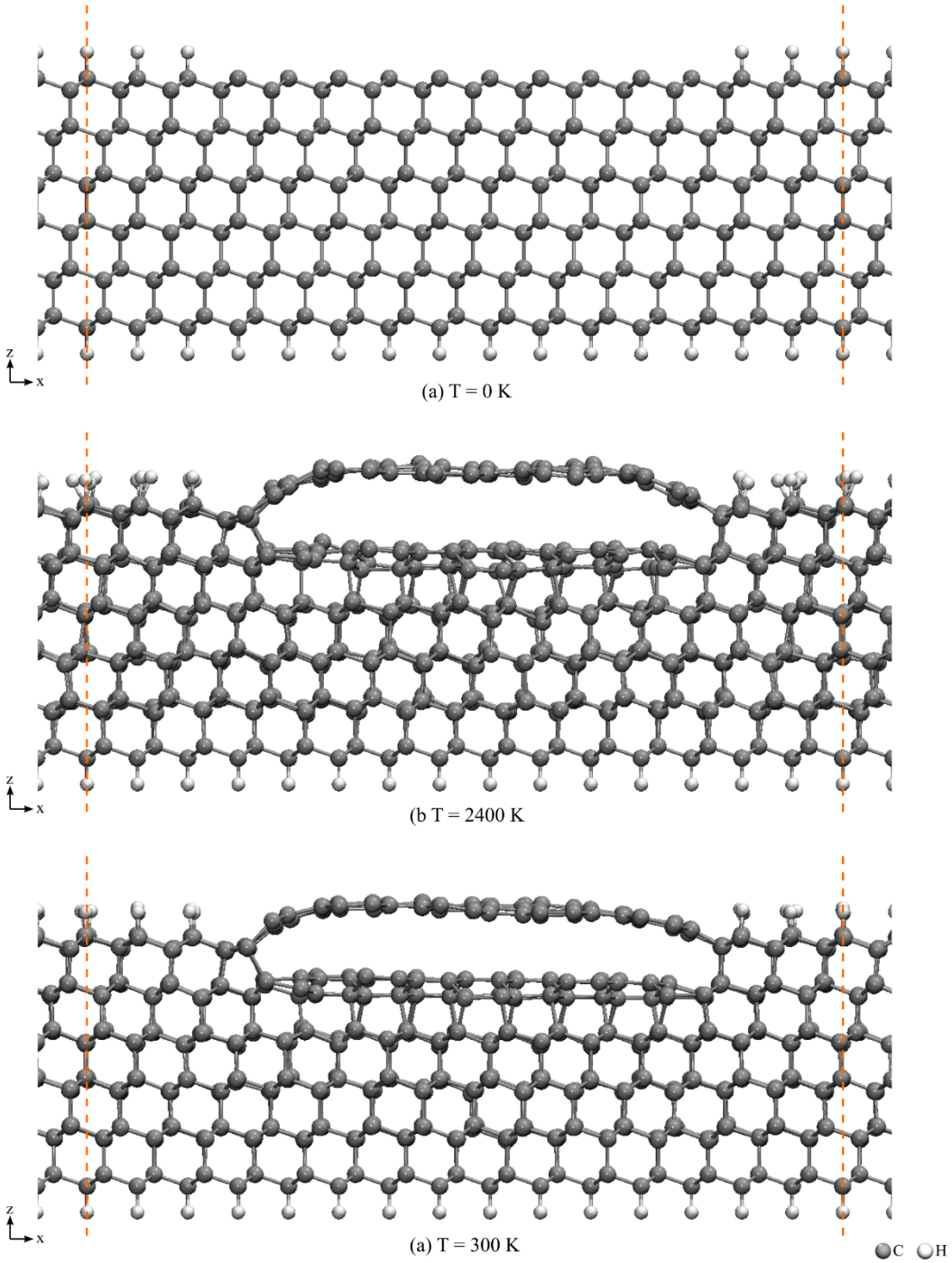

Fig. 8.11. Self-assembly of epitaxial graphene on the partially H-terminated C(111) surface. (a) initial structure, (b) surface heated up to T = 2400 K, (c) cooling down up to T = 300 K.

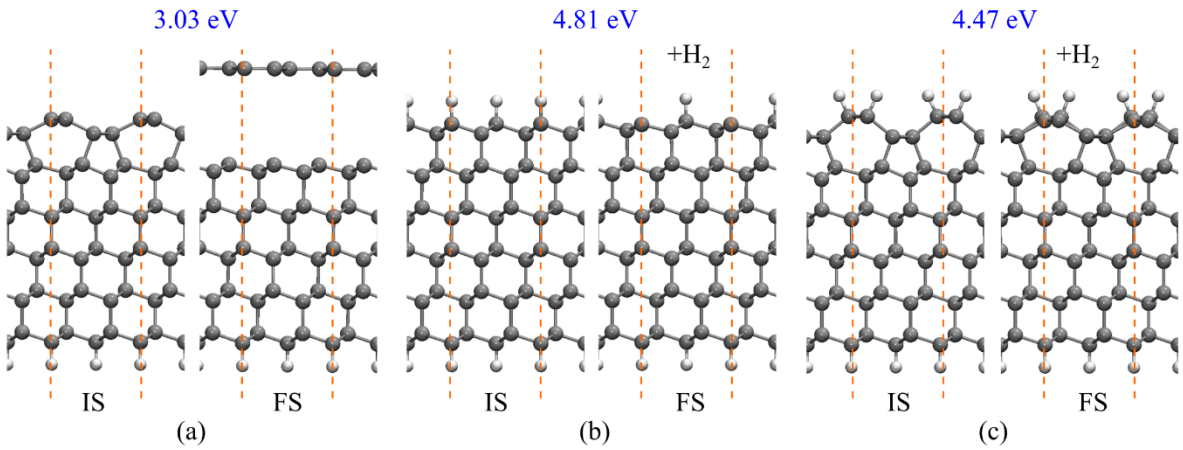

Fig. 8.12. Activation energies of (a) bilayer exfoliation reaction, and H_2 desorption reactions from (b) unreconstructed and (c) reconstructed C(111) surfaces.

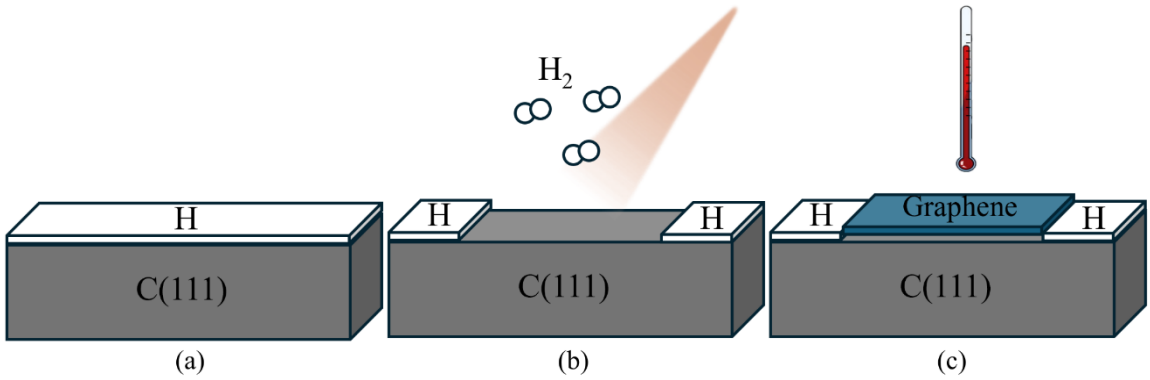

Fig. 8.13. Proposed method of graphene-on-diamond device fabrication by self-assembly of epitaxial graphene. (a) From the H-terminated C(111) surface, (b) pulsed laser can be used to precisely remove hydrogen from selected areas. (c) Heating the material will selectively graphitize the non-H-terminated parts of the surface.

8.7. Effect of Dangling Bond Saturation in the Interfacial Interaction of the Diamond (111) and Nickel (111) Surfaces

Experiments and theoretical calculations indicate that hydrogen termination reduces the friction force between diamond and diamond-like films (Fontaine et al., 2004; Okubo et al., 2015). Additionally, studies have demonstrated that vibrational cutting of iron by diamond in an oxygen atmosphere can reduce the wear of diamond tools (X. Zhang et al., 2019). These findings suggest that terminating species such as H and O could potentially be utilized to minimize interfacial interactions and decrease the wear of diamond tools and materials. In this section, I investigated this phenomenon by simulating the interaction between the C(111) surface and Ni(111) slab with and without surface terminations. I developed an interface model of the C(111) and Ni(111) using orthorhombic simulation cells, incorporating 12 and 4 atomic layers of diamond and nickel, respectively. To determine the optimized geometry of the interface, I systematically calculated the total energies of the structures with the Ni slab translated on a 10×5-grid that spans along the $[\bar{1}2\bar{1}]$ and $[\bar{1}01]$ directions, at various interfacial distances. The relaxed geometries and interface distances are shown in Figure 8.14. In addition, I calculated the interface interaction energy E_{inter} using the equation

$$E_{inter} = \frac{E_{sys} - (E_{dia} - E_{Ni})}{N} \tag{8.1}$$

where E_{sys}, E_{sys}, and E_{sys} are the total energies of the interface, C(111), and Ni(111), respectively and N is the number of surface atoms. In this formula, a negative energy value means that the interaction is energetically favorable.

The C(111)-Ni(111) interface has an equilibrium distance of 1.854 Å and an interaction energy of -2.113 eV. Terminating the dangling bonds increases the equilibrium distances and reduces the interaction energies (Table 8.2). The highest reduction in interaction energy ΔE_{inter} is H-termination (0.760 eV), followed by O-termination (0.747 eV) and OH-termination (0.703 eV). Next, I calculated the 2-dimensional potential energy surface of the C(111)-Ni(111) interface while translating the Ni(111) slab across the C(111) surface without relaxation (Fig. 8.15). Positive values of ΔE mean a decrease in energetic stability compared to the most energetically stable interface structure, while high standard deviations mean rough sliding interaction. The results show that the sliding motion between the C(111) and Ni(111) will result in ΔE as high as 0.56 eV with a standard deviation of 0.15 eV. Terminating the dangling bonds reduces the ΔE and standard deviation of energy. In particular, H-termination results in an energetically flat potential energy surface with a maximum ΔE of only 0.043 eV and a standard deviation of 0.013 eV. Therefore, sliding Ni(111) across the H-terminated C(111) surface will not cause significant changes in the interaction energies and the sliding interaction is generally smooth. A less significant effect can also be observed on the OH-terminated C(111) surface, while the O-terminated C(111) surface shows the least potential energy smoothing effect. To investigate further, I performed NEB simulations to calculate the reaction energies of sliding Ni(111) on the clean and H-terminated C(111) surfaces along the $[\bar{1}2\bar{1}]$ and $[\bar{1}01]$ directions (Fig. 8.16). The NEB simulation allows the relaxation of interface atoms, providing a more accurate description of the interfacial energies during sliding. The simulations show that the activation energies of the sliding reaction of Ni(111) on clean C(111) along the $[\bar{1}2\bar{1}]$ and $[\bar{1}01]$ directions are 0.479 and 0.489 eV, respectively. This is reduced to 0.032 eV and 0.025 eV, respectively, when Ni(111) slides on the H-terminated C(111) surface. These results suggest that the H-termination of the C(111) surface presents a promising approach in diamond-metal lubrication.

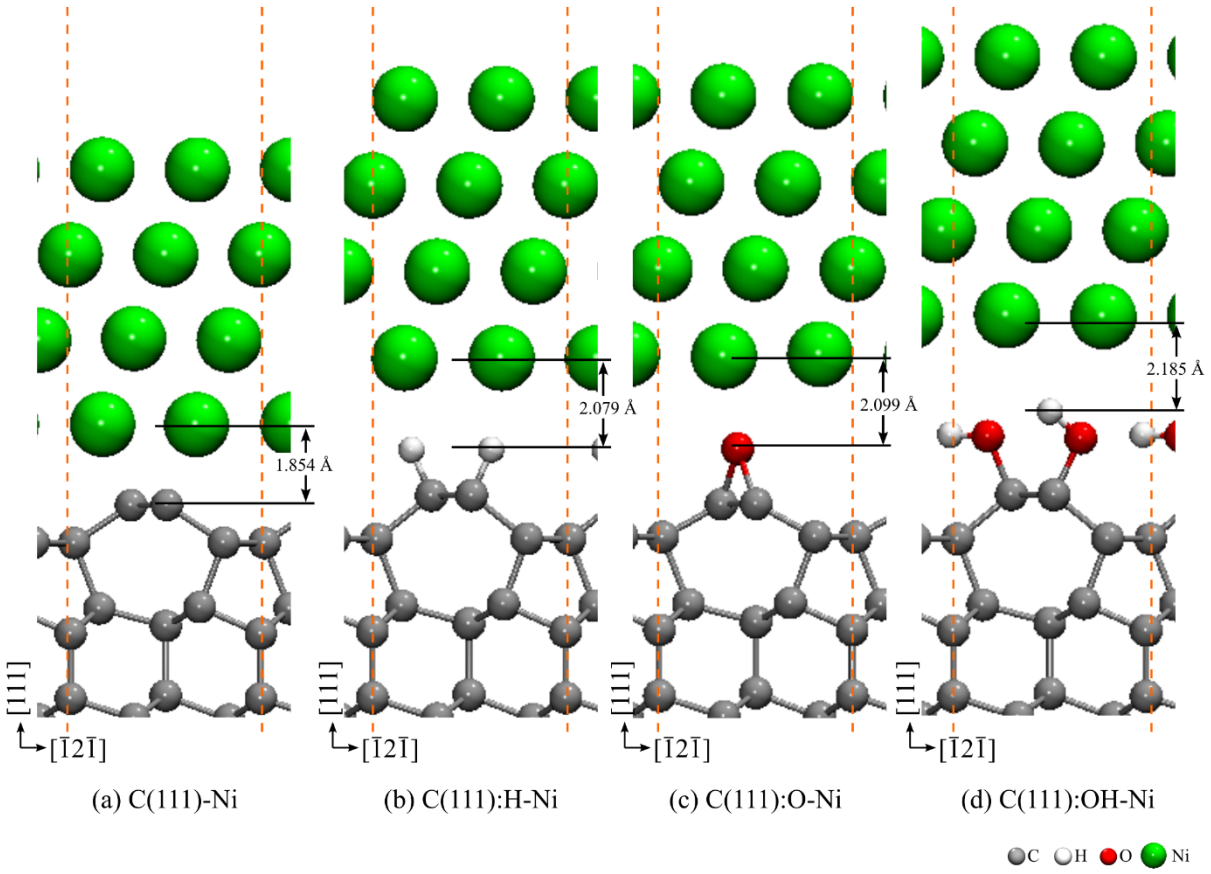

Fig. 8.14. Optimized geometries of the (a) clean, (b) H-, (c) O-, and (d) OH-terminated C(111)-Ni(111) interface.

Table 8.2. Effect of Surface Termination on the Interface Distance d_{inter} and Energy E_{inter} of the C(111)-Ni(111) Interface

Interface Model	d_{inter} (Å)	Δd_{inter} (Å)	E_{inter}(eV/atom)	ΔE_{inter}(eV/atom)
C(111)-Ni	1.854	---	-1.057	---
C(111):H-Ni	2.079	0.225	-0.297	0.760
C(111):O-Ni	2.099	0.246	-0.310	0.747
C(111):OH-Ni	2.185	0.331	-0.354	0.703

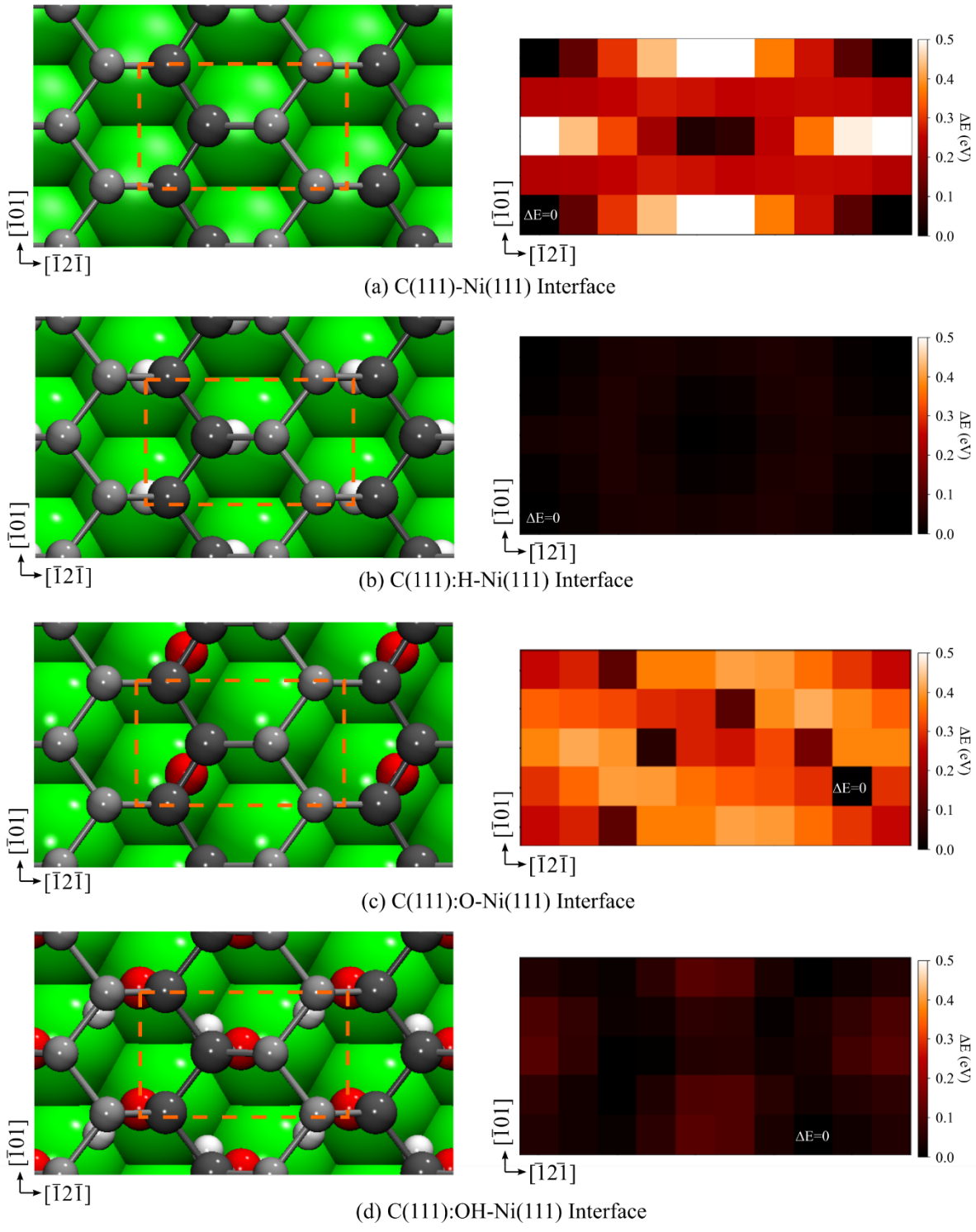

Fig. 8.15. Optimized geometries of the (a) clean, (b) H-, (c) O-, and (d) OH-terminated C(111)-Ni(111) interface with the 2-dimensional potential energy surfaces.

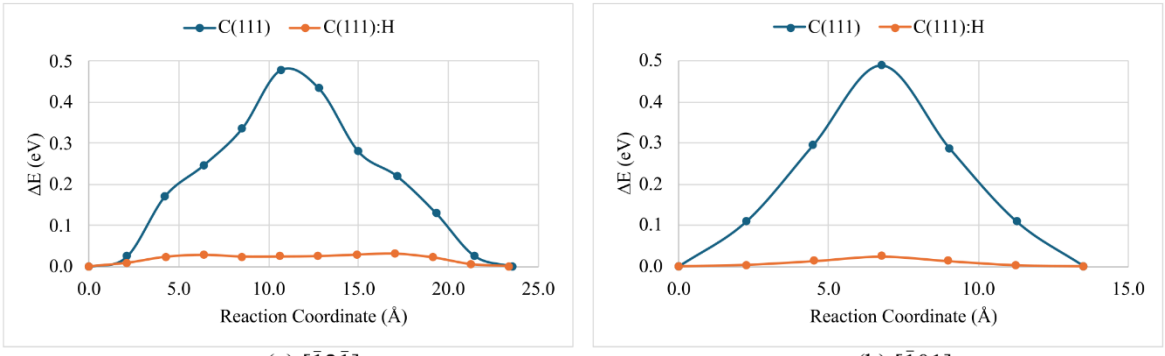

(a) $[\bar{1}2\bar{1}]$ (b) $[\bar{1}01]$

Fig. 8.16. Reaction path of Ni(111) sliding on the clean and H-terminated C(111) surfaces along the (a) $[\bar{1}2\bar{1}]$ and (b) $[\bar{1}01]$ directions.

CHAPTER 9

SUMMARY, CONCLUSIONS, FUTURE WORKS, AND RECOMMENDATIONS

9.1. Summary

Diamond materials possess a unique combination of mechanical, electronic, thermal, and quantum properties, making them suitable for several conventional and advanced technologies. Oxidation and thermal degradation are two fundamental reactions used for etching, modifying, shaping, and forming diamond surfaces. The presence of surface dangling bonds significantly influences the stability and chemical reactivity of diamond surfaces. By employing density functional theory and machine learning molecular dynamics simulations, I have gained an atomic-level understanding that I used to address fundamental questions about diamond surfaces and develop innovative methods and solutions for the technological applications of diamond materials.

9.1.1. On the Oxidative Etching Mechanism of the Diamond (100) Surface

I investigated the oxidation process of the C(100) surface, starting from the adsorption of O_2 to the etching of the first layer atoms and subsequent surface stabilization using reaction path calculations, vibrational mode analysis, and electronic analysis. The following are the critical points of this chapter:

1. The bridge site adsorption is the most energetically stable O adsorption configuration on an ideal surface. However, on surfaces with defects such as vacancies and steps, the bridge site adsorption is only metastable, and the top site adsorption becomes the most energetically stable. This phenomenon accounts for the presence of both carbonyl and ether groups in experimental observations. By applying this principle, the quality of a C(100) surface can be assessed based on the ratio of these functional groups. A higher ether-to-carbonyl ratio suggests a more atomically flat surface.

2. The thermal desorption spectra from the oxidative etching of the C(100) surface exhibit significant width. This is attributable to the wide range of CO desorption activation energies. In the presence of an ideal row of ether, the initial CO desorption activation energy is notably high. However, forming a point defect serving as a nucleation site reduces the activation energy for successive etching along the [011] direction.

3. The experimentally observed shallow stepped surface morphology of oxidized C(100) surface can be explained by the stabilization of steps through dimerization and O adsorption. Because of this, atoms on steps can practically obtain the same stability as the terrace atoms.

9.1.2. On the Origin of the Surface Facet Dependence in the Oxidative Etching of the Diamond (111) and (100) Surfaces

I extended my study of the oxidative etching mechanism to include the C(111) surface. While the C(100) surface is currently the most used surface facet in advanced technologies, the C(111) surface has unique properties that could be useful in other applications. Understanding the difference in the oxidative etching mechanism of these two surfaces will directly impact the CVD growth and diamond device fabrication methods. The key results of this chapter are as follows:

1. The C(111) surface exhibits lower chemical reactivity towards oxygen than the C(100) surface. Triplet O_2 interaction with the C(111) surface is repulsive, whereas the interaction is attractive on the C(100) surface. The molecular and dissociative adsorption energies on the C(111) surface are lower than the C(100) surface.

2. As the C(111) surface is oxidized, carbonyl groups are formed with the C=O bonding with atoms on different layers. This causes the carbonyl orientation to be inclined, which causes high steric repulsion. Consequently, when a neighboring atom is removed through CO desorption, the remaining atoms in the vicinity stabilize. This leads to the surface being etched in a staggered order, resulting in a rough oxidized surface morphology. In contrast, the C=O of the carbonyl on the C(100) surface remains upright, causing less steric repulsion and leading to improved energetic stability, particularly at monolayer coverage.

9.1.3. On the Origin of the Surface Facet Dependence in the Thermal Degradation of the Diamond (111) and (100) Surfaces

Along with oxidation, thermal degradation or graphitization is a fundamental reaction on diamond tools and devices. Graphitization is generally undesirable; hence, graphitization suppression is an active area of research. In this chapter, I investigated the atomic-level mechanism of the thermal degradation of the C(111) and C(100) surfaces. The following are the highlights of this chapter:

1. The C(111) surface is more susceptible to thermal degradation compared to the C(100) surface. This is because only one bond per atom needs to be broken to exfoliate a bilayer from the C(111) surface. In contrast, the same process requires breaking two bonds per atom for the C(100) surface. For this reason, the C(100) surface thermally degrades at a higher temperature.

2. The stepped surfaces are more susceptible to thermal degradation compared to flat surfaces. This is caused by the dangling bonds at the step edges, which facilitate sp^2-sp^3 rehybridization.

3. The C(111) surface thermally degrades by bilayer exfoliation and formation of graphene. In contrast, the C(100) surface thermally degrades by forming amorphous carbon and carbon chain structures.

9.1.4. On the Suppression and Control of Diamond Graphitization and Lubrication by Dangling Bond Saturation

In the preceding chapters, I have studied the oxidation and thermal degradation properties of diamond surfaces and developed fundamental theories that elucidate experimental observations. I have applied these theories in this chapter to propose novel solutions to essential issues in diamond technologies. The main results are as follows:

1. Dangling bond saturation using H atoms will improve the graphitization resistance of the C(111) surface, including surface features such as step edges, narrow terraces, and asperities. Termination by O and OH could also improve the graphitization resistance, but it will degrade the surface through oxidation at higher temperatures.

2. Heating the C(111) surface before polishing can preferentially graphitize islands and asperities, weakening interlayer bonds. This practical approach could significantly enhance the polishing effectiveness and efficiency.

3. When a C(111) surface is partially terminated with H atoms, heating the surface will selectively graphitize the areas without H-termination. This innovative strategy can be used to epitaxially grow graphene directly on the C(111) surface without catalysts, opening up exciting possibilities for developing all-carbon devices.

4. Dangling bond saturation also chemically passivates the C(111) surface, as shown in the diamond-nickel interface interaction energy reduction. In addition, it smoothens the

potential energy of the sliding motion between the diamond and nickel. Therefore, surface termination is a good strategy for lubricating diamonds sliding on metals.

9.2. Conclusions

The surface facet dependence in diamond oxidation and thermal degradation is an intrinsic property resulting from the difference in the number of surface dangling bonds, the orientation of surface functional groups, and the number of interlayer bonds. This property's electronic and atomic-level mechanisms have been elucidated, leading to insights applicable to diamond etching, polishing, and device fabrication. Terminating the C(111) surface with H, O, and OH is an effective approach for inhibiting graphitization and reducing interaction energy at the C(111)-Ni(111) interface. Partially saturating the surface dangling bonds will preferentially graphitize the C(111) surface. Based on this principle, a novel design concept of epitaxial graphene self-assembly for graphene-on-diamond devices and all-carbon circuit boards has been proposed. This opens a new paradigm in diamond device design and fabrication, accelerating the industrialization and widespread use of next-generation diamond technologies.

9.3. Future Works

I intend to pursue two other studies that will expand the discoveries and conclusions of this work and significantly impact the diamond device and diamond tool industry. First, since I discovered a fundamental difference between the oxidation of the C(111) and C(100) surfaces,

a natural extension of this work is to predict the distinct vibrational modes of surface species and compare them with experiments. This will allow for the surface chemistry and electrical characteristics to be precisely adjusted to meet the demands of the particular technology, thereby revolutionizing the way we design and optimize materials. I will use machine learning molecular dynamics to perform large-scale simulations necessary for the realistic modeling of etched surface morphologies, defects, and reconstructions. Second, I also discovered that surface passivation, especially by H atoms, shows good promise in lubricating the diamond-metal interface. To further evaluate its applicability in actual experiments and industrial conditions, finite temperature and pressure simulations must be performed, potentially leading to the development of more efficient and sustainable industrial processes.

In the near future, I am particularly excited about studying diamond growth and nanodiamond applications in biotechnology. These research areas are relatively unexplored and hold immense potential for groundbreaking discoveries and applications. In particular, experiments reveal that creating a diamond with the (111) surface facet using CVD is substantially more difficult than creating a diamond with the (100) facet. First-principles simulation of CH_4 and CH_3 reactions on the C(111) and C(100) surfaces will aid in elucidating the origins of surface facet dependence in diamond growth, potentially leading to the development of a more successful technique of synthesizing the C(111) surface. Furthermore, nanodiamonds have become a powerful tool in targeted drug delivery and medical quantum sensing because their unique fluorescent property enables precise monitoring of their position even when inside human cells. Studying the oxidation and thermal degradation of nanodiamonds and their interaction with organic compounds and proteins using first principles and machine learning molecular dynamics has the potential to accelerate the development of these technologies.

9.4. Recommendations

I conclude this paper with two recommendations for experimental scientists and engineers. Firstly, this study has highlighted potential methods to enhance diamond polishing and diamond-metal lubrication through controlled graphitization and surface passivation. I encourage researchers with access to relevant equipment to validate this study's findings through experimentation. Whether confirming or contradictory, the results of these experiments will aid theoretical and computational materials scientists in refining the modeling of the diamond surface and interfaces. Secondly, this study presents a groundbreaking approach to growing graphene directly on the C(111) surface. To achieve this precisely, a laser-driven hydrogen desorption technique for diamonds must be developed. Although designing and constructing the required equipment and optimizing experimental conditions will demand considerable effort, I want to highlight that the potential benefits far exceed the associated costs. This novel graphene-on-diamond fabrication approach could profoundly impact the transition from silicon to carbon-based electronics and play a pivotal role in sustainability and carbon neutrality.

APPENDIX

A1. Convergence Test of Adsorption Energy for Slab Thickness

The adsorption energies for various configurations have been calculated for 8, 12, 16, and 20-layer slab models. The adsorption energy on 8-layer slab model is converged to within $\sim 10^{-3}$eV for O_2 molecule adsorption on reconstructed C(100) surface adsorption (Fig. S1 and S2) and to within $\sim 10^{-2}$eV for monolayer O atom adsorption (Fig. S3 and S4).

Table A1. O_2 molecular adsorption energies on clean C(100)-(2×1) for slab models with various thickness

Slab Model	Adsorption Energy (eV)	Absolute Difference Relative to 8 Layer Slab (eV)
8 Layers	-2.668	0.000
12 Layers	-2.669	0.001
16 Layers	-2.663	0.005
20 Layers	-2.665	0.003

Table A2. O_2 metastable adsorption energies on clean C(100)-(2×1) for slab models with various thickness

Slab Model	Adsorption Energy (eV)	Absolute Difference Relative to 8 Layer Slab (eV)
8 Layers	-0.779	0.000
12 Layers	-0.785	0.006
16 Layers	-0.778	0.001
20 Layers	-0.783	0.004

Table A3. Adsorption Energy per O atom on C(100)-(1×1):O_{top} for slab models with various thickness

Slab Model	Adsorption Energy (eV)	Absolute Difference Relative to 8 Layer Slab (eV)
8 Layers	-4.490	0.000
12 Layers	-4.512	0.022
16 Layers	-4.526	0.036
20 Layers	-4.550	0.060

Table A4. Adsorption Energy per O atom on C(100)-(1×1):O_{bridge} for slab models with various thickness

Slab Model	Adsorption Energy (eV)	Absolute Difference Relative to 8 Layer Slab (eV)
8 Layers	-5.238	0.000
12 Layers	-5.261	0.023
16 Layers	-5.269	0.030
20 Layers	-5.281	0.043

A2. Band Structure Calculations for Different Slab Thickness

The band structures for clean C(100)-(2×1) and C(100)-(1×1) with monolayer O on top and bridge sites were calculated using 8, 12, 16, and 20-layer model slabs. A thicker 20-layer slab is necessary to properly describe the energy bands.

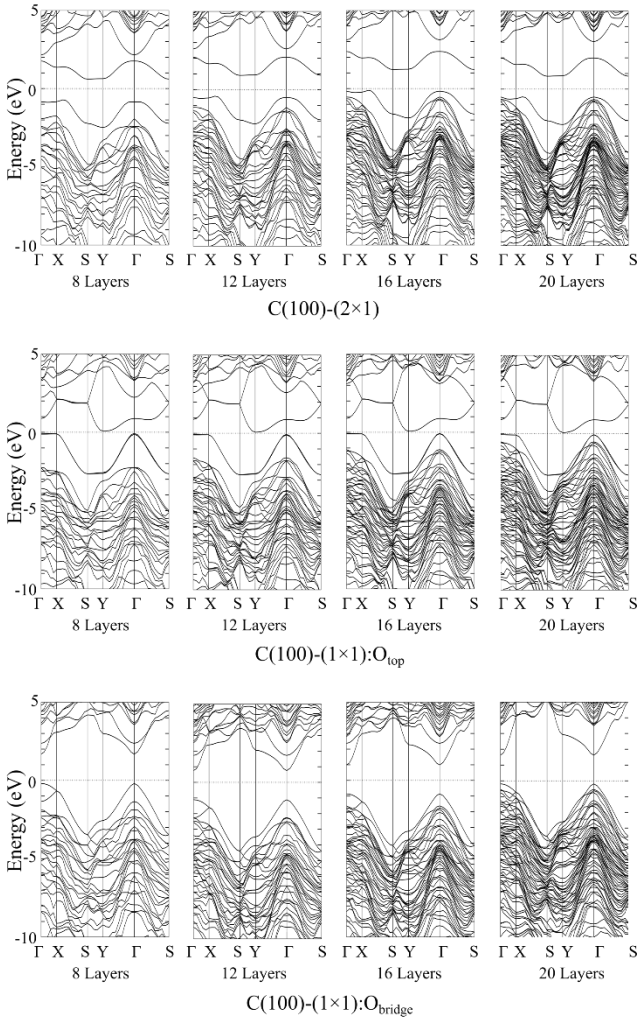

Fig. A1. Band structures of the clean C(100)-(2×1) surface and oxygenated C(100)-(1×1):O_{top} and C(100)-(1×1):O_{bridge} surfaces for 8, 12, 16, and 20-layer slab models. The Fermi level is set to zero eV.

A3. CO Desorption Reaction from Flat and Etched Diamond Surfaces on Various Sites

For every surface model presented in Chapter 6, we considered several CO desorption sites and presented the reactions with the lowest activation energy in the main text. All the CO desorption reaction sites considered in this study are presented in this supplementary document.

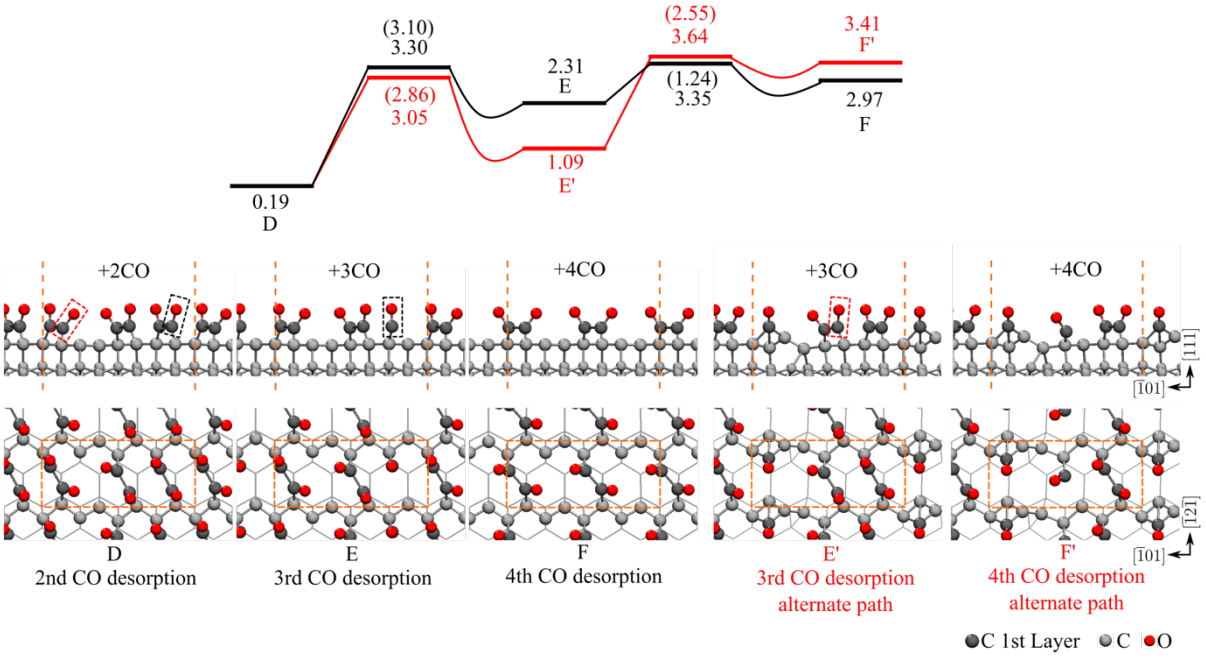

Fig. A2. Alternate reaction path to CO desorption reactions D to F described in Figure 6.9.

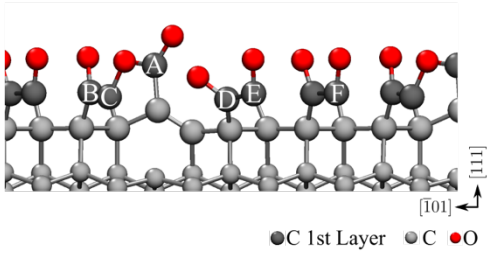

	Activation Energy (eV)	Reaction Energy (eV)
A	1.96	1.07
B	3.39	0.37
C	3.38	1.08
D	3.19	0.69
E	2.11	0.57
F	2.42	1.46

Fig. A3. CO desorption activation energies and reaction energies from various locations on the C(111)-(1×1):O surface with 1 CO desorbed (Fig. 6.9 C).

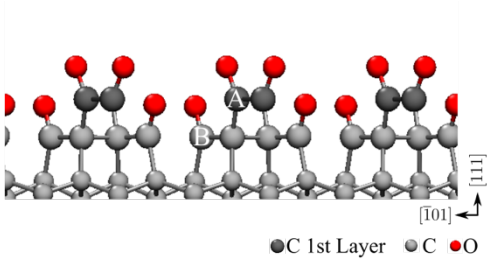

	Activation Energy (eV)	Reaction Energy (eV)
A	0.64	0.70
B	3.23	1.52

Fig. A4. CO desorption activation energies and reaction energies from various locations on the C(111)-(1×1):O surface with 4 CO desorbed and 2 O_2 adsorbed (Fig. 6.12 H).

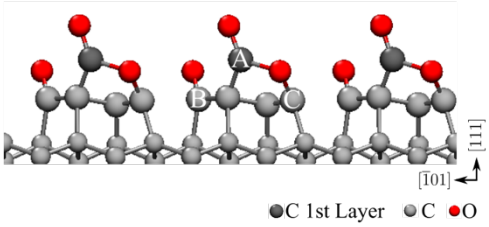

	Activation Energy (eV)	Reaction Energy (eV)
A	2.83	2.86
B	3.14	2.73
C	3.07	3.00

Fig. A5. CO desorption activation energies and reaction energies from various locations on the C(111)-(1×1):O surface with 5 CO desorbed and 2 O_2 adsorbed (Fig. 6.12 J).

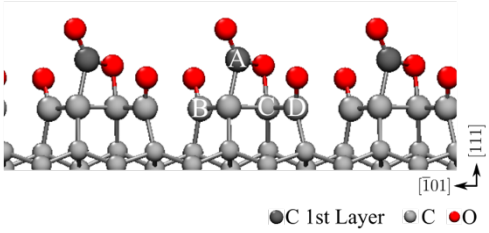

	Activation Energy (eV)	Reaction Energy (eV)
A	2.53	2.52
B	2.37	0.39
C	1.81	0.61
D	1.23	0.34

Fig. A6. CO desorption activation energies and reaction energies from various locations on the C(111)-(1×1):O surface with 6 CO desorbed and 3 O_2 adsorbed (Fig. 6.12 K).

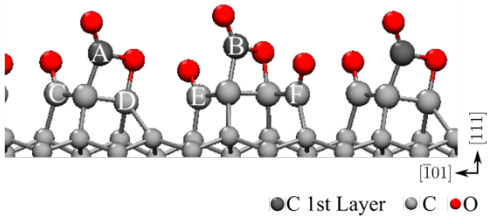

	Activation Energy (eV)	Reaction Energy (eV)
A	2.33	2.22
B	3.40	2.89
C	2.99	0.16
D	1.86	0.35
E	4.29	2.01
F	2.79	2.01
G	3.30	1.62

Fig. A7. CO desorption activation energies and reaction energies from various locations on the C(111)-(1×1):O surface with 7 CO desorbed and 3 O_2 adsorbed (Fig. 6.12 L).

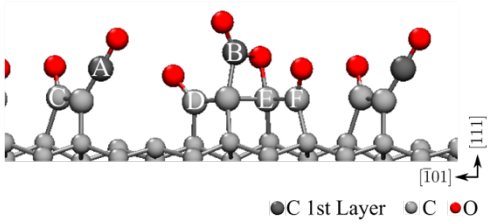

	Activation Energy (eV)	Reaction Energy (eV)
A	3.06	2.81
B	3.62	2.98
C	3.43	3.37
D	4.22	2.24
E	2.81	1.87
F	3.22	1.73

Fig. A8. CO desorption activation energies and reaction energies from various locations on the C(111)-(1×1):O surface with 8 CO desorbed and 3 O_2 adsorbed (Fig. 6.12 M).

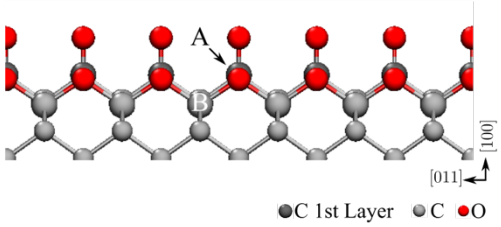

	Activation Energy (eV)	Reaction Energy (eV)
A	4.04	2.34
B	4.32	3.01

Fig. A9. CO desorption activation energies and reaction energies from various locations on the C(100)-(1×1):O surface with 4 CO desorbed and 2 O_2 adsorbed (Fig. 6.13 H).

A4. Learning Database of the Graph Neural Network Interatomic Potential

The database of structures and target energies and forces used in training the graph neural network interatomic potential is shown in this section. We consider 10 equilibrium structure models shown in Fig. A10. For each equilibrium structure, additional structures were generated by randomization of atomic coordinates and annealing at various temperatures. The total number of energy data and force components per structure model is shown in Table A5. The details of the database construction method are discussed in the main text.

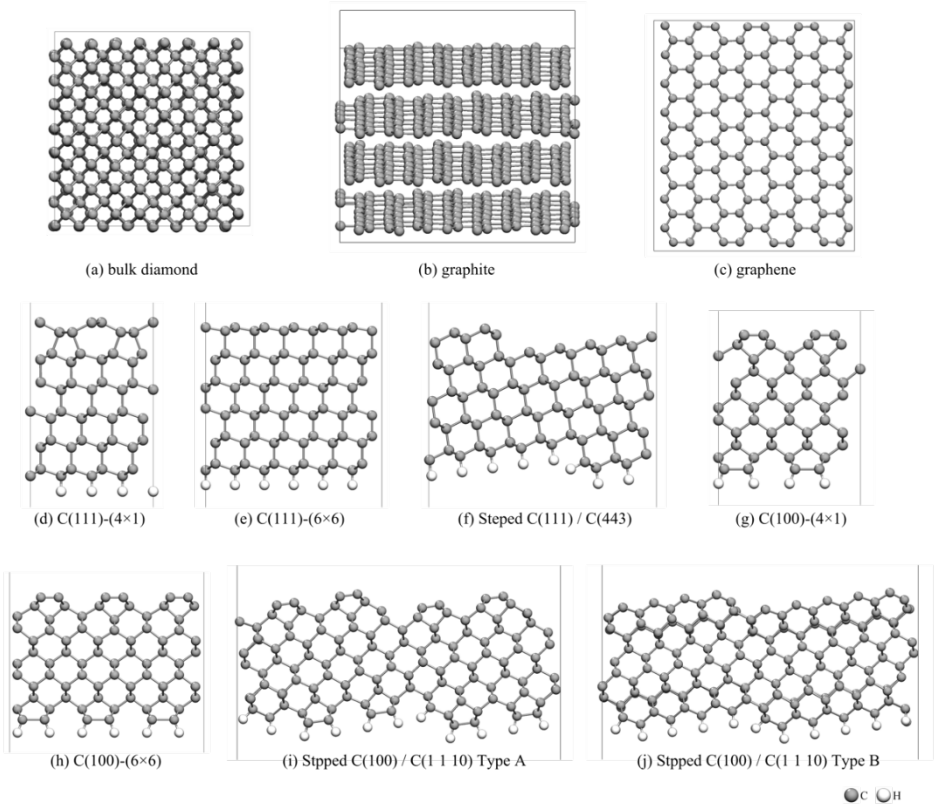

Fig. A10. Equilibrium structures used in training the GNN interatomic potential. Additional structures were generated by randomization of the atomic coordinates and annealing of the structures at various temperatures.

Table A5. Database of structures and target energies and forces used in training the GNN interatomic potential. Each structure sample contains a total energy data and each atom on the structure contains force components along x, y, and z directions.

Structure Model	No. of Atoms per Structure	No. of Samples / Energy Data	No. of Force Components
(a) Bulk Diamond	512	20	30720
(b) Graphite	512	10	15360
(c) Graphene	128	10	3840
(d) C(111)-(4×1)	52	3000	468000
(e) C(111)-(6× 6)	468	54	75816
(f) Stepped C(111)	468	40	56160
(g) C(100)-(4×1)	52	3000	468000
(h) C(100)-(6× 6)	468	133	186732
(i) Stepped C(100) Type A	500	25	37500
(j) Stepped C(100) Type B	528	10	15840

References

Aharonovich, I., Greentree, A.D., Prawer, S., 2011. Diamond photonics. Nat. Photonics 5, 397–405. https://doi.org/10.1038/nphoton.2011.54

Aida, H., Ikejiri, K., Kim, S.-W., Koyama, K., Kawamata, Y., Kodama, H., Sawabe, A., 2016. Overgrowth of diamond layers on diamond microneedles: New concept for freestanding diamond substrate by heteroepitaxy. Diam. Relat. Mater. 66, 77–82. https://doi.org/10.1016/j.diamond.2016.03.019

Aizawa, H., Morikawa, Y., Tsuneyuki, S., Fukutani, K., Ohno, T., 2002. A density-functional study of the atomic structures and vibrational spectra of NO/Pt(1 1 1). Surf. Sci. 514, 394–403. https://doi.org/10.1016/S0039-6028(02)01658-8

Aizawa, H., Tsuneyuki, S., 1998. First-principles study of CO bonding to Pt(111): validity of the Blyholder model. Surf. Sci. 399, L364–L370. https://doi.org/10.1016/S0039-6028(98)00042-9

Alfonso, D.R., Drabold, D.A., Ulloa, S.E., 1995. Phonon modes of diamond (100) surfaces from ab initio calculations. Phys. Rev. B 51, 1989–1992. https://doi.org/10.1103/PhysRevB.51.1989

Ali, B., Litvinyuk, I.V., Rybachuk, M., 2021. Femtosecond laser micromachining of diamond: Current research status, applications and challenges. Carbon 179, 209–226. https://doi.org/10.1016/j.carbon.2021.04.025

Amaratunga, G.A.J., 2002. A Dawn for Carbon Electronics? Science 297, 1657–1658. https://doi.org/10.1126/science.1075868

Avouris, P., 2010. Graphene: Electronic and Photonic Properties and Devices. Nano Lett. 10, 4285–4294. https://doi.org/10.1021/nl102824h

Avouris, P., 2002. Carbon nanotube electronics. Chem. Phys. 281, 429–445. https://doi.org/10.1016/S0301-0104(02)00376-2

Avouris, P., Chen, Z., Perebeinos, V., 2007. Carbon-based electronics. Nat. Nanotechnol. 2, 605–615. https://doi.org/10.1038/nnano.2007.300

Awschalom, D.D., Epstein, R., Hanson, R., 2007. The Diamond Age Diamond Age of Spintronics. Sci. Am. 297, 84–91. https://doi.org/10.1038/scientificamerican1007-84

Babinec, T.M., Hausmann, B.J.M., Khan, M., Zhang, Y., Maze, J.R., Hemmer, P.R., Lončar, M., 2010. A diamond nanowire single-photon source. Nat. Nanotechnol. 5, 195–199. https://doi.org/10.1038/nnano.2010.6

Bartók, A.P., Csányi, G., 2015. Gaussian approximation potentials: A brief tutorial introduction. Int. J. Quantum Chem. 115, 1051–1057. https://doi.org/10.1002/qua.24927

Batzner, S., Musaelian, A., Sun, L., Geiger, M., Mailoa, J.P., Kornbluth, M., Molinari, N., Smidt, T.E., Kozinsky, B., 2022. E(3)-equivariant graph neural networks for data-efficient and accurate interatomic potentials. Nat. Commun. 13, 2453. https://doi.org/10.1038/s41467-022-29939-5

Becke, A.D., 1992. Density-functional thermochemistry. I. The effect of the exchange-only gradient correction. J. Chem. Phys. 96, 2155–2160. https://doi.org/10.1063/1.462066

Behler, J., 2021. Four Generations of High-Dimensional Neural Network Potentials. Chem. Rev. 121, 10037–10072. https://doi.org/10.1021/acs.chemrev.0c00868
Behler, J., Parrinello, M., 2007. Generalized Neural-Network Representation of High-Dimensional Potential-Energy Surfaces. Phys. Rev. Lett. 98, 146401. https://doi.org/10.1103/PhysRevLett.98.146401
Bishop, C.M., 2006. Pattern recognition and machine learning, Information science and statistics. Springer, New York.
Björkman, H., Rangsten, P., Hjort, K., 1999. Diamond microstructures for optical micro electromechanical systems. Sens. Actuators Phys. 78, 41–47. https://doi.org/10.1016/S0924-4247(99)00202-2
Bobzin, K., 2017. High-performance coatings for cutting tools. CIRP J. Manuf. Sci. Technol. 18, 1–9. https://doi.org/10.1016/j.cirpj.2016.11.004
Bokhonov, B.B., Dudina, D.V., Sharafutdinov, M.R., 2021. Graphitization of synthetic diamond crystals: A morphological study. Diam. Relat. Mater. 118, 108563. https://doi.org/10.1016/j.diamond.2021.108563
Born, M., Jordan, P., 1925. Zur Quantenmechanik. Z. Für Phys. 34, 858–888. https://doi.org/10.1007/BF01328531
Born, M., Oppenheimer, R., 1927. Zur Quantentheorie der Molekeln. Ann. Phys. 389, 457–484. https://doi.org/10.1002/andp.19273892002
Bradac, C., Gao, W., Forneris, J., Trusheim, M.E., Aharonovich, I., 2019. Quantum nanophotonics with group IV defects in diamond. Nat. Commun. 10, 5625. https://doi.org/10.1038/s41467-019-13332-w
Bradley, C.E., Randall, J., Abobeih, M.H., Berrevoets, R.C., Degen, M.J., Bakker, M.A., Markham, M., Twitchen, D.J., Taminiau, T.H., 2019. A Ten-Qubit Solid-State Spin Register with Quantum Memory up to One Minute. Phys. Rev. X 9, 031045. https://doi.org/10.1103/PhysRevX.9.031045
Brazhkin, V.V., Lyapin, A.G., Popova, S.V., Klyuev, Yu.A., Naletov, A.M., 1998. Mechanical properties of the 3D polymerized, sp2–sp3 amorphous, and diamond-plus-graphite nanocomposite carbon phases prepared from C60 under high pressure. J. Appl. Phys. 84, 219–226. https://doi.org/10.1063/1.368021
Breeze, J.D., Salvadori, E., Sathian, J., Alford, N.M., Kay, C.W.M., 2018. Continuous-wave room-temperature diamond maser. Nature 555, 493–496. https://doi.org/10.1038/nature25970
Brinksmeier, E., Preuss, W., 2012. Micro-machining. Philos. Trans. R. Soc. Math. Phys. Eng. Sci. 370, 3973–3992. https://doi.org/10.1098/rsta.2011.0056
Bryan, J.B., 1979. Design and construction of an ultraprecision 84 inch diamond turning machine. Precis. Eng. 1, 13–17. https://doi.org/10.1016/0141-6359(79)90071-0
Bundy, F.P., 1980. The P, T phase and reaction diagram for elemental carbon, 1979. J. Geophys. Res. Solid Earth 85, 6930–6936. https://doi.org/10.1029/JB085iB12p06930
Car, R., Parrinello, M., 1985. Unified Approach for Molecular Dynamics and Density-Functional Theory. Phys. Rev. Lett. 55, 2471–2474. https://doi.org/10.1103/PhysRevLett.55.2471
Casstevens, J.M., 1983. Diamond turning of steel in carbon-saturated atmospheres. Precis. Eng. 5, 9–15. https://doi.org/10.1016/0141-6359(83)90063-6

Ceperley, D.M., Alder, B.J., 1980. Ground State of the Electron Gas by a Stochastic Method. Phys. Rev. Lett. 45, 566–569. https://doi.org/10.1103/PhysRevLett.45.566

Chadi, D.J., 1987. Stabilities of single-layer and bilayer steps on Si(001) surfaces. Phys. Rev. Lett. 59, 1691–1694. https://doi.org/10.1103/PhysRevLett.59.1691

Chen, M., Pierstorff, E.D., Lam, R., Li, S.-Y., Huang, H., Osawa, E., Ho, D., 2009. Nanodiamond-mediated delivery of water-insoluble therapeutics. ACS Nano 3, 2016–2022. https://doi.org/10.1021/nn900480m

Chen, X., Li, J., 2020. Superlubricity of carbon nanostructures. Carbon 158, 1–23. https://doi.org/10.1016/j.carbon.2019.11.077

Chen, X., Zhang, W., 2017. Diamond nanostructures for drug delivery, bioimaging, and biosensing. Chem. Soc. Rev. 46, 734–760. https://doi.org/10.1039/C6CS00109B

Chow, E.K., Zhang, X.-Q., Chen, M., Lam, R., Robinson, E., Huang, H., Schaffer, D., Osawa, E., Goga, A., Ho, D., 2011. Nanodiamond Therapeutic Delivery Agents Mediate Enhanced Chemoresistant Tumor Treatment. Sci. Transl. Med. 3, 73ra21-73ra21. https://doi.org/10.1126/scitranslmed.3001713

Chow, L., Wang, H., Kleckley, S., Daly, T.K., Buseck, P.R., 1995. Fullerene formation during production of chemical vapor deposited diamond. Appl. Phys. Lett. 66, 430–432. https://doi.org/10.1063/1.114046

Correa, A.A., Bonev, S.A., Galli, G., 2006. Carbon under extreme conditions: Phase boundaries and electronic properties from first-principles theory. Proc. Natl. Acad. Sci. 103, 1204–1208. https://doi.org/10.1073/pnas.0510489103

Costantini, R., Giampietri, A., Marchiani, D., Betti, M.G., Jeong, S., Ito, Y., Morgante, A., Dell'Angela, M., Mariani, C., 2024. Controlled laser-induced dehydrogenation of free-standing graphane probed by pump–probe X-ray photoemission. Appl. Surf. Sci. 644, 158784. https://doi.org/10.1016/j.apsusc.2023.158784

Davies, G., Evans, T., Ditchburn, R.W., 1997. Graphitization of diamond at zero pressure and at a high pressure. Proc. R. Soc. Lond. Math. Phys. Sci. 328, 413–427. https://doi.org/10.1098/rspa.1972.0086

de Theije, F.K., Roy, O., van der Laag, N.J., van Enckevort, W.J.P., 2000. Oxidative etching of diamond. Diam. Relat. Mater. 9, 929–934. https://doi.org/10.1016/S0925-9635(99)00239-3

De Vita, A., Galli, G., Canning, A., Car, R., 1996. Graphitization of diamond (111) studied by first principles molecular dynamics. Appl. Surf. Sci., Proceedings of the Fifth International Conference on the Formation of Semiconductor Interfaces 104–105, 297–303. https://doi.org/10.1016/S0169-4332(96)00161-4

Deringer, V.L., Bartók, A.P., Bernstein, N., Wilkins, D.M., Ceriotti, M., Csányi, G., 2021. Gaussian Process Regression for Materials and Molecules. Chem. Rev. 121, 10073–10141. https://doi.org/10.1021/acs.chemrev.1c00022

Dong, Y., Wu, X., Martini, A., 2013. Atomic roughness enhanced friction on hydrogenated graphene. Nanotechnology 24, 375701. https://doi.org/10.1088/0957-4484/24/37/375701

Enriquez, J.I., Muttaqien, F., Michiuchi, M., Inagaki, K., Geshi, M., Hamada, I., Morikawa, Y., 2021. Oxidative etching mechanism of the diamond (100) surface. Carbon 174, 36–51. https://doi.org/10.1016/j.carbon.2020.11.057

Enriquez, J.I.G., Halim, H.H., Yamasaki, T., Michiuchi, M., Inagaki, K., Geshi, M., Hamada, I., Morikawa, Y., 2024a. Origin of the surface facet dependence in the thermal degradation of the diamond (111) and (100) surfaces in vacuum investigated by machine learning molecular dynamics simulations. Carbon 226, 119223. https://doi.org/10.1016/j.carbon.2024.119223

Enriquez, J.I.G., Yamasaki, T., Michiuchi, M., Inagaki, K., Geshi, M., Hamada, I., Morikawa, Y., 2024b. Origin of the Surface Facet Dependence in the Oxidative Etching of the Diamond (111) and (100) Surfaces from First-Principles Calculations. J. Phys. Chem. C. https://doi.org/10.1021/acs.jpcc.3c08378

Erdemir, A., Martin, J.M., 2018. Superior wear resistance of diamond and DLC coatings. Curr. Opin. Solid State Mater. Sci. 22, 243–254. https://doi.org/10.1016/j.cossms.2018.11.003

Evans, C., Bryan, J.B., 1991. Cryogenic Diamond Turning of Stainless Steel. CIRP Ann. 40, 571–575. https://doi.org/10.1016/S0007-8506(07)62056-3

Evans, T., James, P.F., 1964. A Study of the Transformation of Diamond to Graphite. Proc. R. Soc. Lond. Ser. Math. Phys. Sci. 277, 260–269.

Fedak, W.A., Prentis, J.J., 2009. The 1925 Born and Jordan paper "On quantum mechanics." Am. J. Phys. 77, 128–139. https://doi.org/10.1119/1.3009634

Fontaine, J., Belin, M., Le Mogne, T., Grill, A., 2004. How to restore superlow friction of DLC: the healing effect of hydrogen gas. Tribol. Int., Novel Carbons in Tribolgy 37, 869–877. https://doi.org/10.1016/j.triboint.2004.07.002

Frauenheim, Th., Köhler, Th., Sternberg, M., Porezag, D., Pederson, M.R., 1996. Vibrational and electronic signatures of diamond surfaces. Thin Solid Films, Atom dynamics of thin films and surfaces: theory and simulations 272, 314–330. https://doi.org/10.1016/0040-6090(95)06956-9

Frenklach, M., Huang, D., Thomas, R.E., Rudder, R.A., Markunas, R.J., 1993. Activation energy and mechanism of CO desorption from (100) diamond surface. Appl. Phys. Lett. 63, 3090–3092. https://doi.org/10.1063/1.110217

Frenklach, M., Spear, K.E., 1988. Growth mechanism of vapor-deposited diamond. J. Mater. Res. 3, 133–140. https://doi.org/10.1557/JMR.1988.0133

Fu, C.-C., Lee, H.-Y., Chen, K., Lim, T.-S., Wu, H.-Y., Lin, P.-K., Wei, P.-K., Tsao, P.-H., Chang, H.-C., Fann, W., 2007. Characterization and application of single fluorescent nanodiamonds as cellular biomarkers. Proc. Natl. Acad. Sci. 104, 727–732. https://doi.org/10.1073/pnas.0605409104

Fujii, M.N., Tanaka, M., Tsuno, T., Hashimoto, Y., Tomita, H., Takeuchi, S., Koga, S., Sun, Z., Enriquez, J.I., Morikawa, Y., Mizuno, J., Uenuma, M., Uraoka, Y., Matsushita, T., 2023. Atomic Imaging of Interface Defects in an Insulating Film on Diamond. Nano Lett. 23, 1189–1194. https://doi.org/10.1021/acs.nanolett.2c04176

Furushiro, N., Tanaka, H., Higuchi, M., Yamaguchi, T., Shimada, S., 2010. Suppression mechanism of tool wear by phosphorous addition in diamond turning of electroless nickel deposits. CIRP Ann. 59, 105–108. https://doi.org/10.1016/j.cirp.2010.03.058

Gicquel, A., Silva, F., Rond, C., Derkaoui, N., Brinza, O., Achard, J., Lombardi, G., Tallaire, A., Michau, A., Wartel, M., Hassouni, K., 2014. Ultrafast Deposition of Diamond by

Plasma-Enhanced CVD, in: Comprehensive Hard Materials. Elsevier, pp. 217–268. https://doi.org/10.1016/B978-0-08-096527-7.00047-7
Gilmer, J., Schoenholz, S.S., Riley, P.F., Vinyals, O., Dahl, G.E., 2017. Neural Message Passing for Quantum Chemistry. https://doi.org/10.48550/ARXIV.1704.01212
Giustino, F., 2014. Materials modelling using density functional theory: properties and predictions, 1st ed. ed. Oxford University Press, Oxford.
Goodfellow, I., Bengio, Y., Courville, A., 2016. Deep learning, Adaptive computation and machine learning. The MIT press, Cambridge, Mass.
Greentree, A.D., Fairchild, B.A., Hossain, F.M., Prawer, S., 2008. Diamond integrated quantum photonics. Mater. Today 11, 22–31. https://doi.org/10.1016/S1369-7021(08)70176-7
Grenville-Wells, H.J., 1952. The graphitization of diamond and the nature of cliftonite. (With Plate XXVI). Mineral. Mag. J. Mineral. Soc. 29, 803–816. https://doi.org/10.1180/minmag.1952.029.216.01
Grimme, S., 2006. Semiempirical GGA-type density functional constructed with a long-range dispersion correction. J. Comput. Chem. 27, 1787–1799. https://doi.org/10.1002/jcc.20495
Grimme, S., 2004. Accurate description of van der Waals complexes by density functional theory including empirical corrections. J. Comput. Chem. 25, 1463–1473. https://doi.org/10.1002/jcc.20078
Gruber, A., Dräbenstedt, A., Tietz, C., Fleury, L., Wrachtrup, J., Borczyskowski, C. von, 1997. Scanning Confocal Optical Microscopy and Magnetic Resonance on Single Defect Centers. Science 276, 2012–2014. https://doi.org/10.1126/science.276.5321.2012
Hamada, I., 2014. van der Waals density functional made accurate. Phys. Rev. B 89, 121103. https://doi.org/10.1103/PhysRevB.89.121103
Hamada, I., Otani, M., Sugino, O., Morikawa, Y., 2009. Green's function method for elimination of the spurious multipole interaction in the surface/interface slab model. Phys. Rev. B 80, 165411. https://doi.org/10.1103/PhysRevB.80.165411
Hamann, D.R., 1996. Generalized Gradient Theory for Silica Phase Transitions. Phys. Rev. Lett. 76, 660–663. https://doi.org/10.1103/PhysRevLett.76.660
Hammer, B., Scheffler, M., 1995. Local Chemical Reactivity of a Metal Alloy Surface. Phys. Rev. Lett. 74, 3487–3490. https://doi.org/10.1103/PhysRevLett.74.3487
Hayashi, T., Morikawa, Y., Nozoye, H., 2001. Adsorption state of dimethyl disulfide on Au(111): Evidence for adsorption as thiolate at the bridge site. J. Chem. Phys. 114, 7615–7621. https://doi.org/10.1063/1.1360245
Hébert, C., Scorsone, E., Bendali, A., Kiran, R., Cottance, M., Girard, H.A., Degardin, J., Dubus, E., Lissorgues, G., Rousseau, L., Mailley, P., Picaud, S., Bergonzo, P., 2014. Boron doped diamond biotechnology: from sensors to neurointerfaces. Faraday Discuss. 172, 47–59. https://doi.org/10.1039/C4FD00040D
Henkelman, G., Uberuaga, B.P., Jónsson, H., 2000. A climbing image nudged elastic band method for finding saddle points and minimum energy paths. J. Chem. Phys. 113, 9901–9904. https://doi.org/10.1063/1.1329672

Hicks, M.-L., Pakpour-Tabrizi, A.C., Jackman, R.B., 2019. Diamond Etching Beyond 10 μm with Near-Zero Micromasking. Sci. Rep. 9, 15619. https://doi.org/10.1038/s41598-019-51970-8

Hitchiner, M.P., Wilks, J., 1984. Factors affecting chemical wear during machining. Wear 93, 63–80. https://doi.org/10.1016/0043-1648(84)90178-9

Hoffmann, R., 1988. A chemical and theoretical way to look at bonding on surfaces. Rev. Mod. Phys. 60, 601–628. https://doi.org/10.1103/RevModPhys.60.601

Hohenberg, P., Kohn, W., 1964. Inhomogeneous Electron Gas. Phys. Rev. 136, B864–B871. https://doi.org/10.1103/PhysRev.136.B864

Hoover, W.G., 1985. Canonical dynamics: Equilibrium phase-space distributions. Phys. Rev. A 31, 1695–1697. https://doi.org/10.1103/PhysRevA.31.1695

Hossain, M.Z., Kubo, T., Aruga, T., Takagi, N., Tsuno, T., Fujimori, N., Nishijima, M., 1999. Chemisorbed states of atomic oxygen and its replacement by atomic hydrogen on the diamond (100)-(2×1) surface. Surf. Sci. 436, 63–71. https://doi.org/10.1016/S0039-6028(99)00609-3

Iacobucci, S., Alippi, P., Calvani, P., Girolami, M., Offi, F., Petaccia, L., Trucchi, D.M., 2016. Electronic structure of hydrogenated diamond: Microscopical insight into surface conductivity. Phys. Rev. B 94, 045307. https://doi.org/10.1103/PhysRevB.94.045307

Ibach, H., Ibach, H., Mills, D.L., 1982. Electron energy loss spectroscopy and surface vibrations. Academic Press, New York.

Imanishi, S., Horikawa, K., Oi, N., Okubo, S., Kageura, T., Hiraiwa, A., Kawarada, H., 2019. 3.8 W/mm RF Power Density for ALD Al2O3-Based Two-Dimensional Hole Gas Diamond MOSFET Operating at Saturation Velocity. IEEE Electron Device Lett. 40, 279–282. https://doi.org/10.1109/LED.2018.2886596

Inaba, M.(稲葉優文), Muta, T.(牟田 翼), Kobayashi, M.(小林幹典), Saito, T.(斎藤俊輝), Shibata, M.(柴田将暢), Matsumura, D.(松村大輔), Kudo, T.(工藤拓也), Hiraiwa, A.(平岩篤), Kawarada, H.(川原田洋), 2016. Hydrogen-terminated diamond vertical-type metal oxide semiconductor field-effect transistors with a trench gate. Appl. Phys. Lett. 109, 033503. https://doi.org/10.1063/1.4958889

Irifune, T., Sumiya, H., 2014. Nanopolycrystalline Diamond without Binder and its Application to Various High-Pressure Apparatus, in: Comprehensive Hard Materials. Elsevier, pp. 173–191. https://doi.org/10.1016/B978-0-08-096527-7.00045-3

John, P., Polwart, N., Troupe, C.E., Wilson, J.I.B., 2002. The oxidation of (100) textured diamond. Diam. Relat. Mater., 12th European Conference on Diamond, Diamond-Like Materials, Carbon Nanotubes, Nitrides & Silicon Carbide 11, 861–866. https://doi.org/10.1016/S0925-9635(01)00673-2

Jonsson, H., Mills, G., Jacobsen, K.W., 1998. Nudged elastic band method for finding minimum energy paths of transitions, in: Classical and Quantum Dynamics in Condensed Phase Simulations. WORLD SCIENTIFIC, pp. 385–404. https://doi.org/10.1142/9789812839664_0016

Kanada, S., Nagai, M., Ito, S., Matsumoto, T., Ogura, M., Takeuchi, D., Yamasaki, S., Inokuma, T., Tokuda, N., 2017. Fabrication of graphene on atomically flat diamond (111) surfaces using nickel as a catalyst. Diam. Relat. Mater., Special Issue “27th

International Conference on Diamond and Carbon Materials – DCM 2016" 75, 105–109. https://doi.org/10.1016/j.diamond.2017.02.014
Kasu, M., 2016. Diamond field-effect transistors for RF power electronics: Novel NO2 hole doping and low-temperature deposited Al2O3 passivation. Jpn. J. Appl. Phys. 56, 01AA01. https://doi.org/10.7567/JJAP.56.01AA01
Kawabata, Y., Taniguchi, J., Miyamoto, I., 2004. XPS studies on damage evaluation of single-crystal diamond chips processed with ion beam etching and reactive ion beam assisted chemical etching. Diam. Relat. Mater. 13, 93–98. https://doi.org/10.1016/j.diamond.2003.09.005
Kawarada, H., Tsuboi, H., Naruo, T., Yamada, T., Xu, D., Daicho, A., Saito, T., Hiraiwa, A., 2014. C-H surface diamond field effect transistors for high temperature (400 °C) and high voltage (500 V) operation. Appl. Phys. Lett. 105, 013510. https://doi.org/10.1063/1.4884828
Kern, G., Hafner, J., 1998. Ab initio molecular-dynamics studies of the graphitization of flat and stepped diamond (111) surfaces. Phys. Rev. B 58, 13167–13175. https://doi.org/10.1103/PhysRevB.58.13167
Kitabayashi, Y., Kudo, T., Tsuboi, H., Yamada, T., Xu, D., Shibata, M., Matsumura, D., Hayashi, Y., Syamsul, M., Inaba, M., Hiraiwa, A., Kawarada, H., 2017. Normally-Off C–H Diamond MOSFETs With Partial C–O Channel Achieving 2-kV Breakdown Voltage. IEEE Electron Device Lett. 38, 363–366. https://doi.org/10.1109/LED.2017.2661340
Kittel, C., 1996. Introduction to solid state physics, 7th ed. ed. Wiley, New York.
Kleimeier, N.F., Haarlammert, T., Witte, H., Schühle, U., Hochedez, J.-F., BenMoussa, A., Zacharias, H., 2010. Autocorrelation and phase retrieval in the UV using two-photon absorption in diamond pin photodiodes. Opt. Express 18, 6945–6956. https://doi.org/10.1364/OE.18.006945
Klimeš, J., Bowler, D.R., Michaelides, A., 2011. Van der Waals density functionals applied to solids. Phys. Rev. B 83, 195131. https://doi.org/10.1103/PhysRevB.83.195131
Kohn, W., Sham, L.J., 1965. Self-Consistent Equations Including Exchange and Correlation Effects. Phys. Rev. 140, A1133–A1138. https://doi.org/10.1103/PhysRev.140.A1133
Koizumi, S., Umezawa, H., Pernot, J., Suzuki, M. (Eds.), 2018. 4 - Key technologies for device fabrications and materials characterizations, in: Power Electronics Device Applications of Diamond Semiconductors, Woodhead Publishing Series in Electronic and Optical Materials. Woodhead Publishing, pp. 219–294. https://doi.org/10.1016/B978-0-08-102183-5.00004-2
Koizumi, S., Watanabe, K., Hasegawa, M., Kanda, H., 2001. Ultraviolet Emission from a Diamond pn Junction. Science 292, 1899–1901. https://doi.org/10.1126/science.1060258
Komanduri, R., Shaw, M.C., 1975. Wear of synthetic diamond when grinding ferrous metals. Nature 255, 211–213. https://doi.org/10.1038/255211a0
Komlenok, M.S., Kononenko, V.V., Ralchenko, V.G., Pimenov, S.M., Konov, V.I., 2011. Laser Induced Nanoablation of Diamond Materials. Phys. Procedia, Lasers in Manufacturing 2011 - Proceedings of the Sixth International WLT Conference on Lasers in Manufacturing 12, 37–45. https://doi.org/10.1016/j.phpro.2011.03.103

Krüger, P., Pollmann, J., 1995. Dimer Reconstruction of Diamond, Si, and Ge (001) Surfaces. Phys. Rev. Lett. 74, 1155–1158. https://doi.org/10.1103/PhysRevLett.74.1155

Kvasnytsya, V.M., 2021. Morphology of Diamond Crystals and Mechanism of Their Growth. J. Superhard Mater. 43, 75–84. https://doi.org/10.3103/S1063457621020076

Lee, J.G., 2016. Computational Materials Science: an Introduction, Second Edition, 2nd edition. ed. CRC Press, Boca Raton.

Lee, S.-T., Apai, G., 1993. Surface phonons and CH vibrational modes of diamond (100) and (111) surfaces. Phys. Rev. B 48, 2684–2693. https://doi.org/10.1103/PhysRevB.48.2684

Li, L., Zhao, X., 2011. Dangling bond-induced graphitization process on the (111) surface of diamond nanoparticles. J. Chem. Phys. 134, 044711. https://doi.org/10.1063/1.3528726

Li, Y., Jiang, J.-W., 2023. Vacancy defects impede the transition from peapods to diamond: a neuroevolution machine learning study. Phys. Chem. Chem. Phys. 25, 25629–25638. https://doi.org/10.1039/D3CP03862A

Li, Z.J., Fang, F.Z., Gong, H., Zhang, X.D., 2013. Review of diamond-cutting ferrous metals. Int. J. Adv. Manuf. Technol. 68, 1717–1731. https://doi.org/10.1007/s00170-013-4970-5

Lieberman, M.A., Lichtenberg, A.J., 2005. Principles of Plasma Discharges and Materials Processing, 1st ed. Wiley. https://doi.org/10.1002/0471724254

Lin, H.-H., Lee, H.-W., Lin, R.-J., Huang, C.-W., Liao, Y.-C., Chen, Y.-T., Fang, J.-M., Lee, T.-C., Yu, A.L., Chang, H.-C., 2015. Tracking and Finding Slow-Proliferating/Quiescent Cancer Stem Cells with Fluorescent Nanodiamonds. Small 11, 4394–4402. https://doi.org/10.1002/smll.201500878

Liu, N., Sugimoto, K., Yoshitaka, N., Yamada, H., Sun, R., Kawai, K., Arima, K., Yamamura, K., 2022. Effects of polishing pressure and sliding speed on the material removal mechanism of single crystal diamond in plasma-assisted polishing. Diam. Relat. Mater. 124, 108899. https://doi.org/10.1016/j.diamond.2022.108899

Loh, K.P., Xie, X.N., Yang, S.W., Zheng, J.C., 2002. Oxygen Adsorption on (111)-Oriented Diamond: A Study with Ultraviolet Photoelectron Spectroscopy, Temperature-Programmed Desorption, and Periodic Density Functional Theory. J. Phys. Chem. B 106, 5230–5240. https://doi.org/10.1021/jp0139437

Long, R., Dai, Y., Guo, M., 2008. Characterization of diamond (100) surface with oxygen termination. Appl. Surf. Sci. 254, 2851–2855. https://doi.org/10.1016/j.apsusc.2007.10.045

Lu, S., Fan, D., Chen, C., Mei, Y., Ma, Y., Hu, X., 2020. Ground-state structure of oxidized diamond (100) surface: An electronically nearly surface-free reconstruction. Carbon 159, 9–15. https://doi.org/10.1016/j.carbon.2019.12.003

Lucca, D.A., Klopfstein, M.J., Riemer, O., 2020. Ultra-Precision Machining: Cutting With Diamond Tools. J. Manuf. Sci. Eng. 142, 110817. https://doi.org/10.1115/1.4048194

Ma, T., Hu, Y.-Z., Wang, H., Li, X., 2007. Microstructural and stress properties of ultrathin diamondlike carbon films during growth: Molecular dynamics simulations. Phys. Rev. B 75, 035425. https://doi.org/10.1103/PhysRevB.75.035425

Mainwood, A., 2000. Recent developments of diamond detectors for particles and UV radiation. Semicond. Sci. Technol. 15, R55. https://doi.org/10.1088/0268-1242/15/9/201

Market Study on Diamond Tools: Europe & North America Together Account for Over 50% Market Share [WWW Document], n.d. . Persistence Mark. Res. URL https://www.persistencemarketresearch.com/market-research/diamond-tools-market.asp (accessed 4.26.24).

Markham, M., Twitchen, D., 2020. The diamond quantum revolution. Phys. World 33, 39. https://doi.org/10.1088/2058-7058/33/4/31

Mehedi, H., Arnault, J.-C., Eon, D., Hébert, C., Carole, D., Omnes, F., Gheeraert, E., 2013. Etching mechanism of diamond by Ni nanoparticles for fabrication of nanopores. Carbon 59, 448–456. https://doi.org/10.1016/j.carbon.2013.03.038

Mermin, N.D., 1965. Thermal Properties of the Inhomogeneous Electron Gas. Phys. Rev. 137, A1441–A1443. https://doi.org/10.1103/PhysRev.137.A1441

Mildren, R.P., Butler, J.E., Rabeau, J.R., 2008. CVD-diamond external cavity Raman laser at 573 nm. Opt. Express 16, 18950–18955. https://doi.org/10.1364/OE.16.018950

Mildren, R.P., Downes, J.E., Brown, J.D., Johnston, B.F., Granados, E., Spence, D.J., Lehmann, A., Weston, L., Bramble, A., 2011. Characteristics of 2-photon ultraviolet laser etching of diamond. Opt. Mater. Express 1, 576–585. https://doi.org/10.1364/OME.1.000576

Monkhorst, H.J., Pack, J.D., 1976. Special points for Brillouin-zone integrations. Phys. Rev. B 13, 5188–5192. https://doi.org/10.1103/PhysRevB.13.5188

Morikawa, Y., Ishii, H., Seki, K., 2004. Theoretical study of n-alkane adsorption on metal surfaces. Phys. Rev. B 69, 041403. https://doi.org/10.1103/PhysRevB.69.041403

Morofushi, Y., Matsushita, H., Miki, N., 2011. Microscale patterning of single crystal diamond by thermochemical reaction between sidero-metal and diamond. Precis. Eng. 35, 490–495. https://doi.org/10.1016/j.precisioneng.2011.03.003

Nagai, M., Nakamura, Y., Yamada, T., Tabakoya, T., Matsumoto, T., Inokuma, T., Nebel, C.E., Makino, T., Yamasaki, S., Tokuda, N., 2020. Formation of U-shaped diamond trenches with vertical {111} sidewalls by anisotropic etching of diamond (110) surfaces. Diam. Relat. Mater. 103, 107713. https://doi.org/10.1016/j.diamond.2020.107713

Nagai, M., Nakanishi, K., Takahashi, H., Kato, H., Makino, T., Yamasaki, S., Matsumoto, T., Inokuma, T., Tokuda, N., 2018. Anisotropic diamond etching through thermochemical reaction between Ni and diamond in high-temperature water vapour. Sci. Rep. 8, 6687. https://doi.org/10.1038/s41598-018-25193-2

Nakanishi, K., Kuroshima, H., Matsumoto, T., Inokuma, T., Tokuda, N., 2016. Atomically flat diamond (100) surface formation by anisotropic etching of solid-solution reaction of carbon into nickel. Diam. Relat. Mater. 68, 127–130. https://doi.org/10.1016/j.diamond.2016.06.011

Narulkar, R., Bukkapatnam, S., Raff, L.M., Komanduri, R., 2009. Graphitization as a precursor to wear of diamond in machining pure iron: A molecular dynamics investigation. Comput. Mater. Sci. 45, 358–366. https://doi.org/10.1016/j.commatsci.2008.10.007

Nimmagadda, R.R., Joshi, A., Hsu, W.L., 1990. Role of microstructure on the oxidation behavior of microwave plasma synthesized diamond and diamond-like carbon films. J. Mater. Res. 5, 2445–2450. https://doi.org/10.1557/JMR.1990.2445

O'Bannon, E., Xia, G., Shi, F., Wirth, R., King, A., Dobrzhinetskaya, L., 2020. The transformation of diamond to graphite: Experiments reveal the presence of an intermediate linear carbon phase. Diam. Relat. Mater. 108, 107876. https://doi.org/10.1016/j.diamond.2020.107876

Ogawa, S., Yamada, T., Ishizduka, S., Yoshigoe, A., Hasegawa, M., Teraoka, Y., Takakuwa, Y., 2012. Vacuum Annealing Formation of Graphene on Diamond C(111) Surfaces Studied by Real-Time Photoelectron Spectroscopy. Jpn. J. Appl. Phys. 51, 11PF02. https://doi.org/10.1143/JJAP.51.11PF02

Okubo, H., Oshima, K., Tuboi, R., Tadokoro, C., Sasaki, S., 2015. Effects of Hydrogen on Frictional Properties of DLC Films. Tribol. Online 10, 397–403. https://doi.org/10.2474/trol.10.397

Otani, M., Sugino, O., 2006. First-principles calculations of charged surfaces and interfaces: A plane-wave nonrepeated slab approach. Phys. Rev. B 73, 115407. https://doi.org/10.1103/PhysRevB.73.115407

Paci, J.T., Schatz, G.C., Minton, T.K., 2011. Theoretical Studies of the Erosion of (100) and (111) Diamond Surfaces by Hyperthermal O(3P). J. Phys. Chem. C 115, 14770–14777. https://doi.org/10.1021/jp201563m

Paszke, A., Gross, S., Massa, F., Lerer, A., Bradbury, J., Chanan, G., Killeen, T., Lin, Z., Gimelshein, N., Antiga, L., Desmaison, A., Köpf, A., Yang, E., DeVito, Z., Raison, M., Tejani, A., Chilamkurthy, S., Steiner, B., Fang, L., Bai, J., Chintala, S., 2019. PyTorch: An Imperative Style, High-Performance Deep Learning Library. https://doi.org/10.48550/ARXIV.1912.01703

Paul, E., Evans, C.J., Mangamelli, A., McGlauflin, M.L., Polvani, R.S., 1996. Chemical aspects of tool wear in single point diamond turning. Precis. Eng. 18, 4–19. https://doi.org/10.1016/0141-6359(95)00019-4

Perdew, J.P., Burke, K., Ernzerhof, M., 1996. Generalized Gradient Approximation Made Simple. Phys. Rev. Lett. 77, 3865–3868. https://doi.org/10.1103/PhysRevLett.77.3865

Perdew, J.P., Chevary, J.A., Vosko, S.H., Jackson, K.A., Pederson, M.R., Singh, D.J., Fiolhais, C., 1992. Atoms, molecules, solids, and surfaces: Applications of the generalized gradient approximation for exchange and correlation. Phys. Rev. B 46, 6671–6687. https://doi.org/10.1103/PhysRevB.46.6671

Petrini, D., Larsson, K., 2008. Theoretical Study of the Thermodynamic and Kinetic Aspects of Terminated (111) Diamond Surfaces. J. Phys. Chem. C 112, 3018–3026. https://doi.org/10.1021/jp709625a

Petrini, D., Larsson, K., 2007. A Theoretical Study of the Energetic Stability and Geometry of Hydrogen- and Oxygen-Terminated Diamond (100) Surfaces. J. Phys. Chem. C 111, 795–801. https://doi.org/10.1021/jp063383h

Pham, T.N., Hamamoto, Y., Inagaki, K., Son, D.N., Hamada, I., Morikawa, Y., 2020. Insight into Trimeric Formation of Nitric Oxide on Cu(111): A Density Functional Theory Study. J. Phys. Chem. C 124, 2968–2977. https://doi.org/10.1021/acs.jpcc.9b08569

Pierson, H.O., 1993. 13 - CVD Diamond, in: Pierson, H.O. (Ed.), Handbook of Carbon, Graphite, Diamonds and Fullerenes. William Andrew Publishing, Oxford, pp. 302–336. https://doi.org/10.1016/B978-0-8155-1339-1.50018-9

Prawer, S., Greentree, A.D., 2008. Diamond for Quantum Computing. Science 320, 1601–1602. https://doi.org/10.1126/science.1158340

Proynov, E.I., Ruiz, E., Vela, A., Salahub, D.R., 1995. Determining and extending the domain of exchange and correlation functionals. Int. J. Quantum Chem. 56, 61–78. https://doi.org/10.1002/qua.560560808

Raymakers, J., Haenen, K., Maes, W., 2019. Diamond surface functionalization: from gemstone to photoelectrochemical applications. J. Mater. Chem. C 7, 10134–10165. https://doi.org/10.1039/C9TC03381E

Reed, B.P., Bathen, M.E., Ash, J.W.R., Meara, C.J., Zakharov, A.A., Goss, J.P., Wells, J.W., Evans, D.A., Cooil, S.P., 2022. Diamond (111) surface reconstruction and epitaxial graphene interface. Phys. Rev. B 105, 205304. https://doi.org/10.1103/PhysRevB.105.205304

Rowe, P., Deringer, V.L., Gasparotto, P., Csányi, G., Michaelides, A., 2020. An Accurate and Transferable Machine Learning Potential for Carbon [WWW Document]. arXiv.org. https://doi.org/10.1063/5.0005084

Rubanov, S., Suvorova, A., Popov, V.P., Kalinin, A.A., Pal'yanov, Yu.N., 2016. Fabrication of graphitic layers in diamond using FIB implantation and high pressure high temperature annealing. Diam. Relat. Mater., 9th International Conference on New Diamond and Nano Carbons – NDNC 2015 63, 143–147. https://doi.org/10.1016/j.diamond.2015.11.017

Rutter, M.J., Robertson, J., 1998. Ab initio calculation of electron affinities of diamond surfaces. Phys. Rev. B 57, 9241–9245. https://doi.org/10.1103/PhysRevB.57.9241

Schrödinger, E., 1926. An Undulatory Theory of the Mechanics of Atoms and Molecules. Phys. Rev. 28, 1049–1070. https://doi.org/10.1103/PhysRev.28.1049

Seal, M., 1958. Graphitization and Plastic Deformation of Diamond. Nature 182, 1264–1267. https://doi.org/10.1038/1821264a0

Shenderova, O.A., 2014. Production of Nanodiamond Particles, in: Comprehensive Hard Materials. Elsevier, pp. 143–171. https://doi.org/10.1016/B978-0-08-096527-7.00044-1

Shikata, S., 2016. Single crystal diamond wafers for high power electronics. Diam. Relat. Mater., Special Issue "26th International Conference on Diamond and Carbon Materials – DCM 2015" 65, 168–175. https://doi.org/10.1016/j.diamond.2016.03.013

Shikata, S., Tanno, T., Teraji, T., Kanda, H., Yamada, T., Kushibiki, J., 2018. Precise measurements of diamond lattice constant using Bond method. Jpn. J. Appl. Phys. 57, 111301. https://doi.org/10.7567/JJAP.57.111301

Shimada, S., Tanaka, H., Higuchi, M., Yamaguchi, T., Honda, S., Obata, K., 2004. Thermo-Chemical Wear Mechanism of Diamond Tool in Machining of Ferrous Metals. CIRP Ann. 53, 57–60. https://doi.org/10.1016/S0007-8506(07)60644-1

Shockley, W., 1976. Electrons and holes in semiconductors, with applications to transistor electronics. R. E. Krieger Pub. Co, Huntington, N.Y.

Skokov, S., Weiner, B., Frenklach, M., 1994. Molecular-dynamics study of oxygenated (100) diamond surfaces. Phys. Rev. B 49, 11374–11382. https://doi.org/10.1103/PhysRevB.49.11374

Slater, J.C., 1951. A Simplification of the Hartree-Fock Method. Phys. Rev. 81, 385–390. https://doi.org/10.1103/PhysRev.81.385

Song, Y., Zou, W., Lu, Q., Lin, L., Liu, Z., 2021. Graphene Transfer: Paving the Road for Applications of Chemical Vapor Deposition Graphene. Small 17, 2007600. https://doi.org/10.1002/smll.202007600

Sque, S.J., Jones, R., Briddon, P.R., 2006. Structure, electronics, and interaction of hydrogen and oxygen on diamond surfaces. Phys. Rev. B 73, 085313. https://doi.org/10.1103/PhysRevB.73.085313

Srinivasan, S.G., van Duin, A.C.T., Ganesh, P., 2015. Development of a ReaxFF Potential for Carbon Condensed Phases and Its Application to the Thermal Fragmentation of a Large Fullerene. J. Phys. Chem. A 119, 571–580. https://doi.org/10.1021/jp510274e

STATE Code [WWW Document], n.d. URL http://www-cp.prec.eng.osaka-u.ac.jp/puki_state/ (accessed 5.13.23).

Stekolnikov, A.A., Furthmüller, J., Bechstedt, F., 2002. Absolute surface energies of group-IV semiconductors: Dependence on orientation and reconstruction. Phys. Rev. B 65, 115318. https://doi.org/10.1103/PhysRevB.65.115318

Strobel, P., Riedel, M., Ristein, J., Ley, L., 2004. Surface transfer doping of diamond. Nature 430, 439–441. https://doi.org/10.1038/nature02751

Sumiya, H., Harano, K., Tamasaku, K., 2015. HPHT synthesis and crystalline quality of large high-quality (001) and (111) diamond crystals. Diam. Relat. Mater. 58, 221–225. https://doi.org/10.1016/j.diamond.2015.08.006

Tersoff, J., 1988. Empirical interatomic potential for silicon with improved elastic properties. Phys. Rev. B 38, 9902–9905. https://doi.org/10.1103/PhysRevB.38.9902

Thomas, R.E., Rudder, R.A., Markunas, R.J., 1992. Thermal desorption from hydrogenated and oxygenated diamond (100) surfaces. J. Vac. Sci. Technol. Vac. Surf. Films 10, 2451–2457. https://doi.org/10.1116/1.577983

Thompson, A.P., Aktulga, H.M., Berger, R., Bolintineanu, D.S., Brown, W.M., Crozier, P.S., In 'T Veld, P.J., Kohlmeyer, A., Moore, S.G., Nguyen, T.D., Shan, R., Stevens, M.J., Tranchida, J., Trott, C., Plimpton, S.J., 2022. LAMMPS - a flexible simulation tool for particle-based materials modeling at the atomic, meso, and continuum scales. Comput. Phys. Commun. 271, 108171. https://doi.org/10.1016/j.cpc.2021.108171

Thoms, B.D., Butler, J.E., 1995. HREELS and LEED of : the 2 × 1 monohydride dimer row reconstruction. Surf. Sci. 328, 291–301. https://doi.org/10.1016/0039-6028(95)00039-9

Thornton, A.G., Wilks, J., 1980. The wear of diamond tools turning mild steel. Wear 65, 67–74. https://doi.org/10.1016/0043-1648(80)90009-5

Tiwari, A.K., Goss, J.P., Briddon, P.R., Wright, N.G., Horsfall, A.B., Jones, R., Pinto, H., Rayson, M.J., 2011. Calculated electron affinity and stability of halogen-terminated diamond. Phys. Rev. B 84, 245305. https://doi.org/10.1103/PhysRevB.84.245305

Tokuda, N., Ogura, M., Matsumoto, T., Yamasaki, S., Inokuma, T., 2016. Influence of substrate misorientation on the surface morphology of homoepitaxial diamond (111) films. Phys. Status Solidi A 213, 2051–2055. https://doi.org/10.1002/pssa.201600082

Toros, A., Kiss, M., Graziosi, T., Mi, S., Berrazouane, R., Naamoun, M., Vukajlovic Plestina, J., Gallo, P., Quack, N., 2020. Reactive ion etching of single crystal diamond by inductively coupled plasma: State of the art and catalog of recipes. Diam. Relat. Mater. 108, 107839. https://doi.org/10.1016/j.diamond.2020.107839

Toros, A., Kiss, M., Graziosi, T., Sattari, H., Gallo, P., Quack, N., 2018. Precision micro-mechanical components in single crystal diamond by deep reactive ion etching. Microsyst. Nanoeng. 4, 1–8. https://doi.org/10.1038/s41378-018-0014-5

Tran, D.T., Fansler, C., Grotjohn, T.A., Reinhard, D.K., Asmussen, J., 2010. Investigation of mask selectivities and diamond etching using microwave plasma-assisted etching. Diam. Relat. Mater., Proceedings of Diamond 2009, The 20th European Conference on Diamond, Diamond-Like Materials, Carbon Nanotubes and Nitrides, Part 2 19, 778–782. https://doi.org/10.1016/j.diamond.2010.02.001

Tran, N.V., Righi, M.C., 2022. Ab initio insights into the interaction mechanisms between H2, H2O, and O2 molecules with diamond surfaces. Carbon 199, 497–507. https://doi.org/10.1016/j.carbon.2022.07.056

Tully, J.C., 2000. Perspective on "Zur Quantentheorie der Molekeln." Theor. Chem. Acc. 103, 173–176. https://doi.org/10.1007/s002149900049

Ueda, K., Kasu, M., Yamauchi, Y., Makimoto, T., Schwitters, M., Twitchen, D.J., Scarsbrook, G.A., Coe, S.E., 2006. Diamond FET using high-quality polycrystalline diamond with f/sub T/ of 45 GHz and f/sub max/ of 120 GHz. IEEE Electron Device Lett. 27, 570–572. https://doi.org/10.1109/LED.2006.876325

Uemura, M., 2004. An analysis of the catalysis of Fe, Ni or Co on the wear of diamonds. Tribol. Int., Novel Carbons in Tribolgy 37, 887–892. https://doi.org/10.1016/j.triboint.2004.07.004

Umezawa, H., 2018. Recent advances in diamond power semiconductor devices. Mater. Sci. Semicond. Process., Wide band gap semiconductors technology for next generation of energy efficient power electronics 78, 147–156. https://doi.org/10.1016/j.mssp.2018.01.007

Umezawa, H., Mokuno, Y., Yamada, H., Chayahara, A., Shikata, S., 2010. Characterization of Schottky barrier diodes on a 0.5-inch single-crystalline CVD diamond wafer. Diam. Relat. Mater., NDNC 2009 19, 208–212. https://doi.org/10.1016/j.diamond.2009.11.001

Vanderbilt, D., 1990. Soft self-consistent pseudopotentials in a generalized eigenvalue formalism. Phys. Rev. B 41, 7892–7895. https://doi.org/10.1103/PhysRevB.41.7892

Wang, C.Z., Ho, K.M., Shirk, M.D., Molian, P.A., 2000. Laser-Induced Graphitization on a Diamond (111) Surface. Phys. Rev. Lett. 85, 4092–4095. https://doi.org/10.1103/PhysRevLett.85.4092

Wang, H., Lee, D.-K., Chen, K.-Y., Chen, J.-Y., Zhang, K., Silva, A., Ho, C.-M., Ho, D., 2015. Mechanism-Independent Optimization of Combinatorial Nanodiamond and Unmodified Drug Delivery Using a Phenotypically Driven Platform Technology. ACS Nano 9, 3332–3344. https://doi.org/10.1021/acsnano.5b00638

Wang, J., Wan, L., Chen, J., Yan, J., 2015. Anisotropy of synthetic diamond in catalytic etching using iron powder. Appl. Surf. Sci. 346, 388–393. https://doi.org/10.1016/j.apsusc.2015.04.022

Williams, N.X., Bullard, G., Brooke, N., Therien, M.J., Franklin, A.D., 2021. Printable and recyclable carbon electronics using crystalline nanocellulose dielectrics. Nat. Electron. 4, 261–268. https://doi.org/10.1038/s41928-021-00574-0

Willman, J.T., Nguyen-Cong, K., Williams, A.S., Belonoshko, A.B., Moore, S.G., Thompson, A.P., Wood, M.A., Oleynik, I.I., 2022. Machine learning interatomic potential for simulations of carbon at extreme conditions. Phys. Rev. B 106, L180101. https://doi.org/10.1103/PhysRevB.106.L180101

Wort, C.J.H., Balmer, R.S., 2008. Diamond as an electronic material. Mater. Today 11, 22–28. https://doi.org/10.1016/S1369-7021(07)70349-8

Wu, Y., Lin, Y., Bol, A.A., Jenkins, K.A., Xia, F., Farmer, D.B., Zhu, Y., Avouris, P., 2011. High-frequency, scaled graphene transistors on diamond-like carbon. Nature 472, 74–78. https://doi.org/10.1038/nature09979

Yamada, T., Yoshikawa, H., Uetsuka, H., Kumaragurubaran, S., Tokuda, N., Shikata, S., 2007. Cycle of two-step etching process using ICP for diamond MEMS applications. Diam. Relat. Mater., Proceedings of Diamond 2006, the 17th European Conference on Diamond, Diamond-Like Materials, Carbon Nanotubes, Nitrides and Silicon Carbide 16, 996–999. https://doi.org/10.1016/j.diamond.2006.11.023

Yamazaki, Y., Ishikawa, K., Mizuochi, N., Yamasaki, S., 2007. Etching Damage in Diamond Studied Using an Energy-Controlled Oxygen Ion Beam. Jpn. J. Appl. Phys. 46, 60. https://doi.org/10.1143/JJAP.46.60

Yan, X., Wei, J., An, K., Liu, J., Chen, L., Zhang, X., Li, C., 2021. Graphitization of CVD diamond grain boundaries during transient heat treatment. Diam. Relat. Mater. 116, 108433. https://doi.org/10.1016/j.diamond.2021.108433

Yu, J., Liu, G., Sumant, A.V., Goyal, V., Balandin, A.A., 2012. Graphene-on-Diamond Devices with Increased Current-Carrying Capacity: Carbon sp2-on-sp3 Technology. Nano Lett. 12, 1603–1608. https://doi.org/10.1021/nl204545q

Yu, X., Zhou, J., Zhang, S., Cao, Z., Kong, Y., Chen, T., 2019. High frequency H-diamond MISFET with output power density of 182 mW/mm at 10 GHz. Appl. Phys. Lett. 115, 192102. https://doi.org/10.1063/1.5125771

Zaitsev, A.M., Bergman, A.A., Gorokhovsky, A.A., Huang, M., 2006. Diamond light emitting diode activated with Xe optical centers. Phys. Status Solidi A 203, 638–642. https://doi.org/10.1002/pssa.200521125

Zhai, W., Srikanth, N., Kong, L.B., Zhou, K., 2017. Carbon nanomaterials in tribology. Carbon 119, 150–171. https://doi.org/10.1016/j.carbon.2017.04.027

Zhang, H., Miyamoto, Y., Rubio, A., 2012. Laser-induced preferential dehydrogenation of graphane. Phys. Rev. B 85, 201409. https://doi.org/10.1103/PhysRevB.85.201409

Zhang, X., Deng, H., Liu, K., 2019. Oxygen-shielded ultrasonic vibration cutting to suppress the chemical wear of diamond tools. CIRP Ann. 68, 69–72. https://doi.org/10.1016/j.cirp.2019.04.026

Zhang, Z., Wu, H., Sang, L., Huang, J., Takahashi, Y., Wang, L., Imura, M., Koizumi, S., Koide, Y., Liao, M., 2019. Single-crystal diamond microelectromechanical resonator

integrated with a magneto-strictive galfenol film for magnetic sensing. Carbon 152, 788–795. https://doi.org/10.1016/j.carbon.2019.06.072

Zheng, J.C., Xie, X.N., Wee, A.T.S., Loh, K.P., 2001. Oxygen-induced surface state on diamond (100). Diam. Relat. Mater., 11th European Conference on Diamond, Diamond-like Materials, Carbon Nanotubes, Nitrides and Silicon Carbide 10, 500–505. https://doi.org/10.1016/S0925-9635(00)00439-8

Zou, L., Yin, J., Huang, Y., Zhou, M., 2018. Essential causes for tool wear of single crystal diamond in ultra-precision cutting of ferrous metals. Diam. Relat. Mater. 86, 29–40. https://doi.org/10.1016/j.diamond.2018.04.012

Zupan, A., Perdew, J.P., Burke, K., Causà, M., 1997. Density-gradient analysis for density functional theory: Application to atoms. Int. J. Quantum Chem. 61, 835–845. https://doi.org/10.1002/(SICI)1097-461X(1997)61:5<835::AID-QUA9>3.0.CO;2-X